Production, Calibration and Performance of the Scintillation Detectors for the IceCube Surface Array Enhancement

Shefali

picture credit: Marc Jacquart

Production, Calibration and Performance of the Scintillation Detectors for the IceCube Surface Array Enhancement

Zur Erlangung des akademischen Grades eines
DOKTORS DER NATURWISSENSCHAFTEN (Dr. rer. nat.)
von der KIT-Fakultät für Physik des
Karlsruher Instituts für Technologie (KIT)

angenommene

DISSERTATION

von

Shefali (M.Sc.)
aus Sonepat, Haryana, Indien

Tag der mündlichen Prüfung:	01.08.2025
Referent:	Prof. Dr. Engel, Ralph
Korreferent:	Prof. Dr. Simon, Frank
Betreuer:	Dr. Haungs, Andreas

To my parents,
who chose courage over caution and believed in my path,
even when it led far from theirs.

To my brother,
for being my loudest cheerleader and my quietest strength.

To my sister-in-law,
whose steady encouragement carried me further than she knows.

To Agastya, my beloved nephew,
whose laughter and curiosity brightened even the hardest days.

Abstract

The IceCube Surface Array Enhancement (SAE) represents a significant upgrade to the IceCube Neutrino Observatory's surface cosmic-ray detection capabilities, targeting the energy region in the cosmic-ray spectrum around the knee (PeV energies). This work covers the production, calibration, and on-ice commissioning of the scintillation detectors equipped with temperature-sensitive Silicon Photomultipliers (SiPMs). As part of the detector preparation, a dedicated pre-calibration framework was developed to ensure uniform detector performance, including natural radioactive background suppression and energy response validation. Following this, the first final-configuration station (Station 0) was deployed at the South Pole in early 2023 with fully updated scintillation modules and readout electronics, expanding the observable dynamic range and improving data acquisition fidelity.

During commissioning, a robust SiPM gain calibration across the three gain channels covering the entire South Pole temperature range enabled reliable conversion of raw ADC data into physical Minimum Ionizing Particle (MIP) units. Post-deployment studies confirmed excellent detector uniformity and nanosecond-level timing precision, critical for accurate reconstruction of the air-shower front and effective background suppression. A scalable data processing pipeline was established to integrate scintillator data with coincident IceTop and radio detector events, enabling unified hybrid event reconstruction.

Furthermore, a data-driven air-shower reconstruction approach was developed, incorporating temporal pulse cleaning and a L2 reconstruction that leverages IceTop's core position estimates to overcome single-station limitations. A realistic zenith-dependent signal variance model reflecting near-Poisson fluctuations was introduced, improving signal weighting in Lateral Distribution Function (LDF) fits. For the single-station setup, the reconstruction achieved a space-angle resolution of 2.3° overall with Station 0, improving to 1.2° for showers with cores near the station, which is particularly relevant for studies of lower-energy cosmic-rays. Timing resolution studies further demonstrated excellent performance with zenith-dependent timing behaviour and a reconstructed shower front resolution of approximately 7 ns for scintillation pairs separated by 5 m.

Preliminary comparisons of the reconstructed shower size, S_{125}, between scintillators and IceTop revealed a factor of ≈ 3 pointing to the difference in the two detectors' response due to the scintillation detector's lower energy threshold and higher sensitivity to the electromagnetic component of the air-showers. Preliminary seasonal analyses with measured signals suggest evolving detector response linked to snow accumulation effects, highlighting the need for ongoing calibration improvements.

Collectively, these results demonstrate the technical readiness and scientific potential of the SAE scintillator modules for long-term cosmic-ray observations at the South Pole. The enhanced surface array promises improved sensitivity and precision for probing the astrophysical origins and acceleration mechanisms of high-energy cosmic rays, particularly in the crucial knee region of the spectrum.

Zusammenfassung

Herstellung, Kalibrierung und Leistungsfähigkeit der Szintillationsdetektoren für das IceCube Surface Array Enhancement

Das IceCube Surface Array Enhancement (SAE), bestehend aus Szintillationsdetektoren und Radioantennen, stellt eine bedeutende Erweiterung der Fähigkeiten des IceCube Neutrino-Observatoriums und des bestehenden Oberflächenarrays IceTop zur Detektion kosmischer Strahlung an der Oberfläche dar und zielt auf den Bereich um das sogenannte Knie im Spektrum der primären kosmischen Strahlung (PeV-Energien). Diese Arbeit umfasst die Herstellung, Kalibrierung und Inbetriebnahme der am Südpol stationierten Szintillationsdetektoren, die mit temperaturempfindlichen Silizium-Photomultipliern (SiPMs) ausgestattet sind. Eine spezielle Vorkalibrierung wurde entwickelt, um eine einheitliche Detektorleistung zu gewährleisten, einschließlich der Unterdrückung des natürlichen radioaktiven Hintergrunds und der Validierung des Energieverhaltens. Die erste Station in der endgültigen Konfiguration (Station 0) wurde Anfang 2023 mit vollständig modernisierten Szintillationsmodulen und Ausleseelektronik am Südpol aufgestellt, wodurch der dynamische Bereich erweitert und die Genauigkeit der Datenerfassung verbessert wurde. Eine robuste SiPM-Verstärkungskalibrierung für alle drei Verstärkungskanäle sowie eine Temperaturkorrektur ermöglicht eine zuverlässige Umwandlung der ADC-Rohdaten in physikalische MIP-Einheiten (Minimum Ionizing Particle). Erste Studien nach dem Aufbau bestätigen die hervorragende Gleichförmigkeit des Detektors und die zeitliche Präzision im Nanosekundenbereich, die für die präzise Rekonstruktion der Schauerfront und die Unterdrückung des Hintergrunds entscheidend ist. Es wurde eine skalierbare Datenprozessierungs-Pipeline eingerichtet, um Szintillatordaten mit koinzidenten IceTop- und Radiodetektormessungen zu integrieren, was eine einheitliche hybride Ereignisrekonstruktion ermöglicht.

Es wurde ein datengesteuerter Ansatz zur Rekonstruktion von Luftschauern entwickelt, der eine zeitliche Impulsbereinigung und einen weiteren Rekonstruktionsschritt beinhaltet, der die Schätzungen der Ankunftsorte der Schauer von IceTop nutzt, um die Beschränkungen einer einzelnen Station zu überwinden. Es wurde ein realistisches, zenitwinkelabhängiges Modell der Signalvarianz eingeführt, das annähernd Poissonsche Fluktuationen widerspiegelt und die Signalgewichtung in den Anpassungen der lateralen Verteilungsfunktion (LDF) verbessert. Mit dieser Rekonstruktion wurde eine Raumwinkelauflösung von insgesamt 2,3° erreicht, die sich bei Schauerachsen in Stationsnähe auf 1,2° verbesserte, was insbesondere Studien zur kosmischen Strahlung mit niedrigen Energien zugute kommt. Studien zur Zeitauflösung zeigen außerdem eine hervorragende Leistung der Detektoren im Zeitverhalten und einer rekonstruierten Schauerfrontauflösung nahe 7 ns.

Vorläufige Vergleiche der rekonstruierten Schauergröße S_{125} zwischen Szintillatoren und IceTop ergaben einen Faktor von $\sim$3, was auf den Unterschied in der Antwort der beiden Detektortypen auf den Luftschauer weist, der auf die niedrigere Energieschwelle des Szintillationsdetektors und die höhere Empfindlichkeit für die elektromagnetische Komponente zurückzuführen ist. Saisonale Analysen deuten darauf hin, dass sich das Ansprechverhalten

des IceTop-Detektors in Abhängigkeit von der Schnee-Akkumulation verändert, was auf die Möglichkeiten der neuen Detektoren im Monitoring der Schneedicke hindeutet.

Insgesamt zeigen die Ergebnisse dieser Arbeit die technologische Qualität und das wissenschaftliche Potenzial der SAE-Szintillatormodule für langfristige Beobachtungen der kosmischen Strahlung am Südpol. Der verbesserte Oberflächendetektor bei IceCube verspricht eine höhere Empfindlichkeit und Präzision bei der Messung ausgedehnter Luftschauer und damit zur Erforschung der astrophysikalischen Ursprünge und Beschleunigungsmechanismen der hochenergetischen kosmischen Strahlung, insbesondere im wichtigen Kniebereich des Spektrums.

Contents

1 Introduction **1**

2 High-energy cosmic-ray physics **3**
2.1 Cosmic-Ray Sources and Propagation . . . 3
2.2 Extensive Air Showers . . . 5
2.3 Cosmic-Ray Energy Spectrum . . . 7
2.4 Detection Techniques . . . 8

3 IceCube Neutrino Observatory **13**
3.1 Scientific Research at IceCube . . . 13
3.2 Instrumentation . . . 16
3.3 Future of IceCube . . . 20
3.4 Surface Array Enhancement (SAE) . . . 23

4 Scintillation detectors: Series production **31**
4.1 Scintillators as Particle Detectors . . . 31
4.2 Series Production . . . 40
4.3 Test Bench for Scintillators' Validation . . . 46
4.4 Scintillation Detector Validation . . . 59

5 Commissioning and Calibration of the first SAE station **67**
5.1 Prototype Station . . . 67
5.2 Station 0 . . . 68
5.3 Commissioning and Calibration of Station 0 . . . 69
5.4 SAE data processing . . . 83

6 Data-driven Reconstruction of Air Showers **91**
6.1 Air Shower Reconstruction . . . 91
6.2 Single Station Simulations . . . 96
6.3 Data-driven Reconstruction Parametrization . . . 97

7 First Performance Studies **111**
7.1 Directional Resolution . . . 111
7.2 Timing Resolution . . . 114
7.3 S_{125} Reconstruction and Comparison to IceTop . . . 117

8 Summary **123**

A Supplementary Measurements: Pre-Calibration **127**
A.1 SiPM calibration: Disqualified unit . . . 127
A.2 Field Tests: Low Temperature measurements . . . 128
A.3 Radioactive Source Measurements . . . 129
A.4 Local Radioactivity Measurements . . . 130

B Supplementary Measurements: On-Ice Calibration and comissioning **131**
B.1 Baseline Studies . . . 131
B.2 Time offset: Radio-IT . . . 132
B.3 Time offset: Radio-Scint . . . 133
B.4 Temperature Co-relation . . . 134
B.5 SAE-IT Coincidences . . . 136

C Supplementary material: Data Driven Parametrization **137**
C.1 EMG-Gaussian Time bin model . . . 137
C.2 Slope vs Measured Signal . . . 138
C.3 More examples of LDF Binned Data . . . 139

Acknowledgements **149**

Chapter 1

Introduction

Cosmic-rays were discovered over a century ago through a series of pioneering experiments, including underwater measurements by Domenico Pacini [1] and high-altitude balloon flights by Victor Hess [2]. These studies established that ionising radiation has an extraterrestrial origin, marking the birth of cosmic-ray physics, a field that later evolved into the broader discipline of high-energy astroparticle-physics. Since then, cosmic-ray research has achieved significant milestones, including surveying the cosmic-ray energy spectrum across approximately eleven orders of magnitude which revealed spectral features like the knee and ankle [3, 4], identifying primary and secondary particle components using balloon and satellite detectors which provided insights into the cosmic-ray composition [5, 6], detection of ultra-high energy cosmic rays [7, 8], as well as finding evidence for anisotropies in the arrival directions of cosmic-rays [9]. These achievements have provided valuable insights into the possible astrophysical origins of cosmic rays and the physical mechanisms behind their acceleration and propagation. Despite these advances, many fundamental questions remain open, including the origins of the highest-energy cosmic rays, the mechanisms responsible for their acceleration, and the details of their propagation through the cosmos to Earth. Features observed in the cosmic-ray energy spectrum, their composition, and anisotropy studies provide crucial experimental input for addressing these unresolved questions.

The primary sources of galactic cosmic rays are believed to be supernovae, supported by direct detections up to $\sim 100\,\mathrm{TeV}$ [3], using satellite and balloon experiments operating at high altitudes. However, at higher energies, starting around the so-called "knee" (near $\sim 3\,\mathrm{PeV}$), surface detection becomes indispensable due to the rapidly falling flux. Detection covering this energy region is critical, as it can provide information regarding the transition in the origin or acceleration mechanisms of cosmic-rays. Surface arrays enable the indirect reconstruction of cosmic-ray properties by sampling the Extensive Air Showers (EAS) generated when these high-energy particles interact with the Earth's atmosphere.

Several major ground-based observatories have been built to study cosmic rays with high to ultra-high energies. In the Northern Hemisphere, KASCADE-Grande [10], Grapes-3 [11], and Telescope Array [12] are some examples, while in the Southern Hemisphere, the Pierre Auger Observatory [13] and the IceCube Neutrino Observatory [14] play a central role. These facilities differ in design and altitude, but together offer complementary coverage of the sky and the entire energy spectrum starting from a few TeV. This thesis focuses on the IceCube Neutrino Observatory, a hybrid detector that contributes significantly to cosmic-ray studies through its surface component, IceTop [15]. Situated at the South Pole, IceCube benefits from an atmospheric depth that allows extensive air showers to have shower maxima near or even below the surface. This unique location enables IceTop to probe cosmic rays in the energy range covering the knee. By combining surface measurements from IceTop with data from the In-Ice component, IceCube enhances its sensitivity to the mass composition of primary cosmic rays,

allowing for more precise reconstruction of their mass-sensitive parameters. Since its deployment, the IceTop array has experienced non-uniform snow accumulation at an average rate of approximately 20 cm/yr [16]. This accumulation leads to increased detection thresholds due to signal attenuation, posing challenges to data quality. To mitigate these effects and improve cosmic-ray measurements through complementary detection channels, an upgrade of IceTop with hybrid stations equipped with scintillation and radio detectors has been proposed [17] and is called the Surface Array Enhancement (SAE). These detectors are designed to be adjustable in height to prevent snow coverage and are proposed to be positioned along the footprint of IceTop. A prototype station for this enhancement has been operational at the South Pole since 2020. Over the following years, the station underwent multiple upgrades, culminating in its final configuration in 2023, since referred to as Station 0. Furthermore, two additional stations were deployed during the 2024-25 Antarctic summer. A comprehensive description of the scientific motivation, infrastructure, and latest results of IceCube, including the SAE, is provided in Chapter 3 of this thesis. By restoring the fidelity of surface signals and incorporating detectors with complementary sensitivity to the electromagnetic and muonic components of air showers, the SAE will enhance the precision of shower reconstruction, improve sensitivity to lower-energy and inclined events, and enable cross-calibration across detector systems, key for advancing long-term studies of cosmic rays with the IceCube Observatory.

Within the scope of this thesis, 99 scintillation detectors were produced and calibrated, of which 56 were designated for deployment at the South Pole. So far, 24 of these detectors have been installed on site, and 32 are ready for deployment. The remaining detectors have contributed to research and development stations [18] at major cosmic-ray observatories worldwide, including the Telescope Array (TA) and the Pierre Auger Observatory. The validation and calibration of these detectors required an in-depth characterisation of their performance in the production environment, followed by the development of a dedicated test bench tailored for this purpose. These production and calibration procedures are detailed in Chapter 4. Notably, eight of the scintillation detectors produced and validated in this work were ultimately integrated into the final configuration of Station 0. Chapter 5 describes the on-ice calibration performed with these Station 0 detectors, alongside the scalable data processing pipeline partially developed during this thesis to prepare an air-shower measurement dataset for the prototype station.

A data-driven reconstruction of air-shower parameters was carried out to optimise the reconstruction methods previously reliant on simulation-derived inputs. This work is elaborated on in Chapter 6. Subsequently, the first performance studies of the Station 0, using data collected throughout 2023, are presented in Chapter 7. An outlook on the potential impact of a single Surface Array Enhancement (SAE) station within the broader IceCube surface programme and a summary of the work within the scope of the thesis can be found in Chapter 8.

Chapter 2

High-energy cosmic-ray physics

Cosmic rays are highly energetic, ionised atomic particles that travel through space and arrive at Earth from both galactic and extragalactic sources [19, 20]. They are primarily composed of protons (about 90%), followed by helium nuclei (alpha particles) and heavier nuclei. A smaller fraction consists of electrons, positrons, and other subatomic particles. In addition to these charged particles, cosmic rays also include neutral messengers such as gamma rays and neutrinos, which travel undeflected by magnetic fields, providing direct insights into their sources of origin. These particles travel at velocities approaching the speed of light and can reach energies exceeding 10^{20} eV, which is many orders of magnitude higher than those achievable by the current human-made particle accelerators.

The discovery of cosmic rays was a result of several key experiments in the early 20^{th} century. In 1911, Domenico Pacini demonstrated that radiation levels decreased underwater, suggesting an origin external to the Earth [1]. Shortly after, in 1912, Victor Hess conducted balloon experiments that showed increasing ionisation rates with altitude, providing strong evidence for an extraterrestrial source of this radiation [2]. Together, these discoveries marked the beginning of the field of high-energy astroparticle-physics.

After nearly a century since the conception of the field, many fundamental questions remain unsolved pertaining to the origins of cosmic rays, their acceleration mechanisms, as well as their composition. This chapter will briefly discuss the possible sources and mechanisms of propagation of cosmic rays. It will also cover their interaction processes with Earth's atmosphere, resulting in extensive air showers and their detection methods.

2.1 Cosmic-Ray Sources and Propagation

Cosmic rays are inferred to originate from high-energy astrophysical processes, where particles are accelerated to relativistic energies via mechanisms such as shock acceleration. After acceleration, these particles propagate through interstellar and intergalactic space, and a fraction of them reach Earth, where they interact with the atmosphere, initiating extensive air showers. This section outlines the dominant source classes, the acceleration mechanisms responsible for energizing cosmic rays, and the propagation effects that shape the spectrum observed on Earth.

While the exact origin of cosmic rays is still under investigation, their energy spectrum and observed anisotropies point to a transition from predominantly galactic sources at lower energies to extragalactic origins above approximately 10^{18} eV. Within the Milky Way, supernova remnants (SNRs) [4] are the leading candidates for accelerating cosmic rays up to $\sim 10^{15-17}$ eV. The shock waves generated in these explosions provide favourable conditions for diffusive shock acceleration. Beyond a certain energy, the magnetic field of the Galaxy is no longer strong

enough to contain cosmic rays. This can be understood in terms of the Larmor radius:

$$R_L = \frac{E}{ZeB}, \tag{2.1}$$

where R_L is the Larmor radius, E is the particle energy, Z the charge number, e the elementary charge, and B the magnetic field strength. When R_L exceeds the size of the Galactic disk (ranging from $\sim 220\,\mathrm{pc}$ in thin regions to $\sim 2.6\,\mathrm{kpc}$ in thick regions [21]), cosmic rays can escape, pointing to a transition from galactic to extragalactic sources.

Thus, at ultra-high energies, exceeding roughly $10^{18}\,\mathrm{eV}$, the sources are believed to be of extragalactic origin. This is because they are energetic enough to escape the galactic magnetic field. Active galactic nuclei (AGNs), which harbor supermassive black holes at their centres, can accelerate particles through powerful jets and accretion-driven shocks. Gamma-ray bursts (GRBs) [22], among the most energetic explosions in the universe, and large-scale structure formation shocks are also considered viable candidates for producing the highest-energy cosmic rays.

The acceleration of cosmic rays is often explained by the first-order Fermi acceleration mechanism [23]. This process involves charged particles repeatedly crossing a shock front, where they are scattered and reflected by irregularities in the magnetic field structure. Each crossing can increase the particle's energy, resulting in a cumulative energy gain over multiple reflections. The efficiency of this mechanism depends on the inhomogeneous and turbulent nature of the shock environment. The energy gain per cycle is proportional to the particle's energy, making the mechanism efficient and capable of producing a power-law energy spectrum:

$$\frac{dN}{dE} \propto E^{-\gamma},$$

For a strong, non-relativistic shock front, this yields a factor of 2 [23]. However, after propagation effects are taken into account, including energy-dependent escape from the Galaxy, the observed spectrum becomes steeper. The maximum energy that a particle can achieve through this acceleration process is constrained by the Hillas criterion [24], which limits the particle confinement time within the acceleration region. This criterion can be expressed as $E_{max} = qBR$, where $E_{\max}$ is the maximum achievable energy, q is the particle charge, B is the magnetic field strength, and R is the characteristic size of the acceleration region. The Hillas criterion ensures that the particle's Larmor radius remains smaller than the size of the accelerator, enabling efficient confinement and acceleration. After their acceleration, the cosmic rays undergo a complex journey through the universe that significantly shapes their properties before they reach Earth. Their propagation is influenced by deflections due to the galactic and extragalactic magnetic fields, with the degree of deflection depending on their energy and charge. At lower energies, this scattering effectively randomises their arrival directions, making it difficult to trace them back to their sources. Only the most energetic cosmic rays, especially neutral particles like neutrinos and photons, can travel largely unperturbed, retaining directional information about their origins. Additionally, cosmic rays interact with the cosmic microwave background (CMB) and interstellar matter, leading to energy loss processes such as pion production and photo-disintegration at the highest energies. This energy suppression leads to a theoretical upper limit on the energies of cosmic rays that can reach Earth from distant sources, a phenomenon known as the Greisen–Zatsepin–Kuzmin (GZK) cutoff (6×10^{19} eV) [25, 26].

To model the transport of cosmic rays, various propagation frameworks such as the diffusion model and leaky-box approximation are employed. These models describe how cosmic rays scatter, interact, and escape from the Galaxy. In particular, the leaky-box model assumes that cosmic rays are confined in a "box" (the Galaxy) and can escape with a probability that

increases with energy. This model naturally predicts a steepening of the energy spectrum from the source index of $\gamma \approx 2$ to an observed index of ~ 2.7, due to the energy-dependent escape time. The particles with lower charge-to-mass ratios (like protons) leak out earlier than heavier nuclei (like iron), and a gradual shift in composition is expected with increasing energy. This gives rise to the observed "knee" feature in the cosmic-ray spectrum at $\sim 3\,\mathrm{PeV}$ (discussed in Sec. 2.3), marking the point where light nuclei begin to escape (see Fig. 2.2). As energy increases further, a second knee appears, associated with the leakage of heavier elements. This interpretation is consistent with the mass composition measurements, which show an increasing dominance of iron group elements near the second knee. Ultimately, beyond the "ankle" region, extragalactic sources dominate, characterized by a hardening of the spectrum and a change in composition.

2.2 Extensive Air Showers

Upon entering the Earth's atmosphere, a high-energy cosmic ray initiates a cascade of secondary particles, generally upon interaction with a nitrogen or oxygen molecule higher up in the atmosphere [20, 19]. This process is referred to as Extensive Air Showers (EAS), where the primary particle's energy is redistributed among millions of secondary particles. Consequently, the generated shower properties depend on the energy, direction, and mass of the primary cosmic ray particle. The first interaction in Earth's atmosphere typically results in the production of pions, kaons, neutrons, and other hadrons [19], as shown in Fig. 2.1. These secondaries continue the tertiary and so on, particle production, resulting in three main components:

- **Hadronic Component:** Comprised of secondary hadrons such as pions, kaons, and nuclear fragments. This component dominates the early stages of the shower and serves as the primary energy reservoir, feeding other components with each interaction generation. The lateral spread of this component is relatively narrow, concentrated near the shower core, due to the short interaction lengths and high inelasticity of hadronic collisions.

- **Electromagnetic Component:** Neutral pions (π^0) rapidly decay into two photons,

$$\pi^0 \to \gamma + \gamma. \tag{2.2}$$

  Each photon initiates an electromagnetic sub-cascade via pair production and bremsstrahlung. This component carries the majority ($\sim 98\%$) of the shower energy and defines much of the lateral spread of the EAS.

- **Muonic Component:** Charged pions and kaons decay into muons and neutrinos:

$$\pi^{\pm} \to \mu^{\pm} + \nu_{\mu}(\bar{\nu}_{\mu}) \tag{2.3}$$

$$K^{\pm} \to \mu^{\pm} + \nu_{\mu}(\bar{\nu}_{\mu}) \tag{2.4}$$

  where muons, due to their relatively long lifetime and minimal energy loss in the atmosphere, cover large distances, reaching the Earth's surface and even penetrate underground detectors. Neutrinos escape detection in most experiments due to their weak interaction cross-section, effectively carrying away a portion of the primary energy.

The air shower propagates along the direction of the primary particle until a maximum number of secondary particles is reached. The depth at which this maximum is achieved is called X_{max}. It is sensitive to the energy and mass of the primary and can be characterised by the Heitler-Matthews model [29]. The Heitler model describes the electromagnetic cascade as a binary

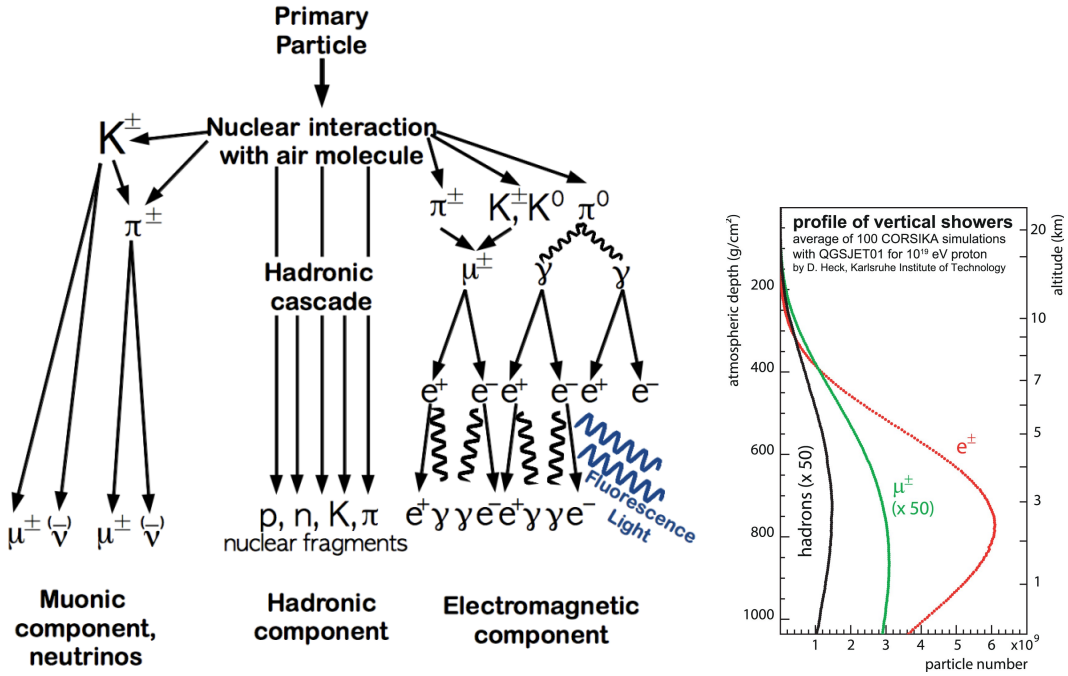

Figure 2.1: Left: Schematic of an extensive air shower showing its main components—electromagnetic, hadronic, and muonic [27]. Right: Longitudinal development profiles of different particle types [28].

splitting process occurring every interaction length λ, with particle energy halving at each step until a critical energy E_c is reached in the atmosphere, resulting in

$$X_{\max} \propto \lambda \ln\left(\frac{E_0}{E_c}\right) \tag{2.5}$$

Matthews extended this to hadronic showers by modelling pion production. Each hadronic interaction produces charged ($\pi^{\pm}$) and neutral pions (π^0), with π^0 decaying promptly into photons, initiating electromagnetic sub-showers, while charged pions continue hadronic interactions or decay into muons. Applying the superposition principle for a nucleus of mass number A, the shower maximum scales as

$$X^A_{\max} = X^p_{\max} - \lambda \ln A, \tag{2.6}$$

explaining the shallower development (smaller $X_{\max}$) and larger muon content of showers initiated by heavier primaries. The transverse momentum imparted in interactions, along with multiple Coulomb scattering, leads to a lateral spread of the shower as it develops longitudinally (2.1 (right)). At ground level, this results in a disk-like distribution of particles, with a dense core and gradually decreasing density toward the periphery. Due to these variations in particle production height and scattering processes, the timing of arrival of particles is varied, giving the shower front a thickness, which is broader further away from the shower core. The electromagnetic component of a shower experiences the greatest lateral spread due to its much larger scattering cross-section. Low-energy muons also undergo significant lateral spreading because of Coulomb scattering. The particle density as a function of radial distance from the shower axis can be described by a Lateral Distribution Function (LDF). Heavier primaries tend to produce broader lateral distributions and a higher muon-to-electron ratio due to their increased hadronic activity [20]. These features of air showers can be used to reconstruct the primary energy, mass composition, and arrival direction of cosmic rays, and are crucial for optimizing hadronic interaction and shower propagation models.

2.3 Cosmic-Ray Energy Spectrum

The incident flux of cosmic rays with energies 1 GeV on Earth's atmosphere is approximately $1\mathrm{m}^{-2}\mathrm{s}^{-1}$. This rate exhibits a rapid decline with increasing primary particle energy, reaching values as low as $1\mathrm{km}^{-2}\mathrm{yr}^{-1}$ at energies of approximately 10^7GeV. The cosmic-ray flux has been observed over a broad range of energies from $\sim$ 1 GeV to 10^{11} GeV and beyond, using various direct and indirect detection methods since their discovery in the early 20th century. The energy dependence of the incident cosmic-ray flux can provide key insights into their acceleration mechanisms and propagation through the Galaxy and beyond. Empirical data from various detectors consistently show that the differential flux follows a power-law dependence:

$$\frac{dN}{dE} \propto E^{-\gamma}, \tag{2.7}$$

where γ is the spectral index. Figure 2.2 compiles measurements from leading global experiments, covering the energy range of $\sim 10^4$ GeV to $\sim 10^{11}$ GeV. The flux is scaled by $E^{2.6}$ to highlight deviations from a simple power law. These deviations, manifesting as distinct spectral features, indicate changes in the underlying composition and origin of the cosmic-ray primaries.

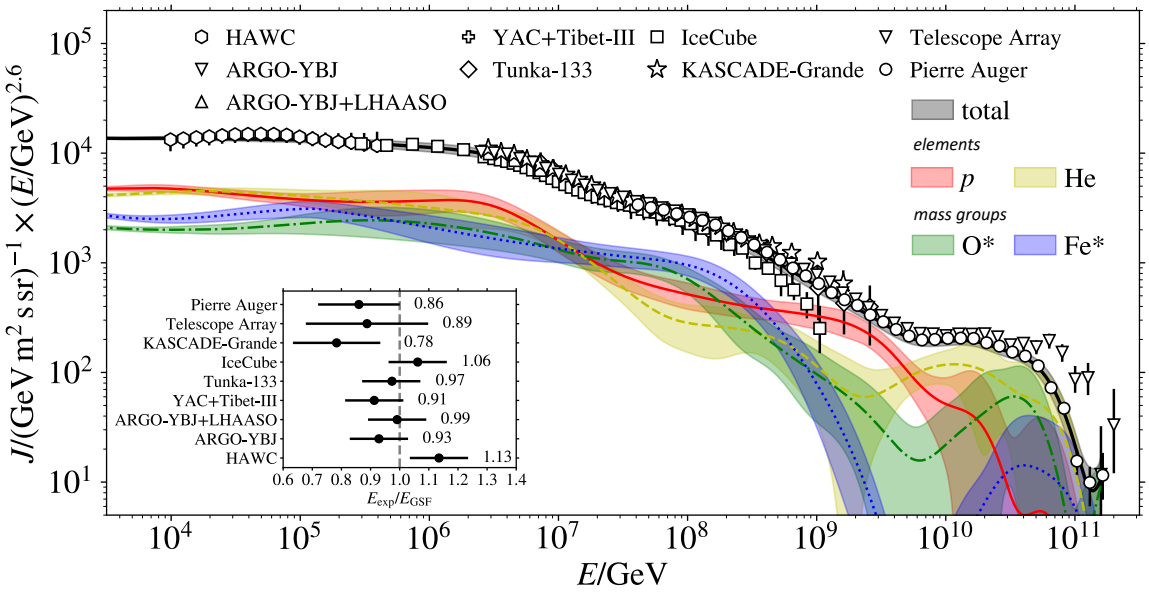

Figure 2.2: The observed flux of cosmic rays using information from many different experiments[4].The flux has been scaled with a factor of $E^{2.6}$ to make the individual features distinctly visible. The solid black line shows the Global Spline Fit to the energy spectrum and composition. Coldred curves represent simulated contributions from different mass groups.

At energies up to a few hundred TeV, cosmic rays are measured using direct detection techniques, primarily via balloon- or satellite-borne experiments. A power-law spectrum with a spectral index of $\gamma \approx 2.7$ [3] is observed with these measurements. At higher energies, the flux becomes too low for direct measurements due to limitations on the detector size deployable in air-borne experiments. Ground-based indirect detection methods, such as extensive air shower (EAS) arrays, are therefore employed for higher energy cosmic rays.

As shown in Fig. 2.2, a prominent steepening in the cosmic-ray spectrum occurs at $\sim 3\times10^6$ GeV, known as the *knee*, where the spectral index increases from $\gamma \approx 2.7$ to $\gamma \approx 3.1$ [30]. This feature can be interpreted as the energy ceiling for standard galactic accelerators, particularly for protons. Due to their higher charge Z, heavier nuclei can be accelerated to

proportionally higher energies, producing a sequence of spectral cutoffs that scales with rigidity, a phenomenon known as the Peters cycle [31]. Experimental results from KASCADE, KASCADE-Grande support this interpretation, observing a shift from lighter to heavier composition across this energy range [32]. At higher energies, around 10^8 GeV, the spectrum steepens again to $\gamma \approx 3.2$, forming the so-called *second knee*. This is often attributed to the suppression of the heaviest galactic nuclei, marking the final turnover in the Peters cycle and potentially signalling the upper limit of conventional galactic acceleration mechanisms, supported by the Pierre Auger Observatory findings [33].

A hardening of the spectrum back to $\gamma \sim 2.7$ is observed at approximately 3×10^9 GeV, forming a feature known as the *ankle*. Early interpretations suggested that this dip was caused by e^+e^- pair production of extragalactic protons interacting with the cosmic microwave background (CMB)[34]. However, composition measurements from experiments like the Pierre Auger Observatory indicate a mixed or heavy-dominated composition at these energies [35], challenging pure proton models. The ankle is now broadly understood as the transition point from galactic to extragalactic cosmic rays.

Finally, the flux exhibits a marked suppression above $\sim 10^{11}$ GeV. This is found to be consistent with the Greisen–Zatsepin–Kuzmin (GZK) suppression [25, 26]. This suppression arises from energy losses suffered by ultra-high-energy protons via pion production in interactions with cosmic microwave background (CMB) photons, limiting their propagation distance to ∼100–150 Mpc. For heavier nuclei, the dominant energy loss mechanism is photodisintegration. While this feature may alternatively reflect the maximum acceleration capability of extragalactic sources, current observational data favour models involving a mixed composition and charge-dependent source energy limits [35].

2.4 Detection Techniques

2.4.1 Direct Detection

Direct detection techniques are used for studying cosmic rays (CRs) at energies up to $\sim$ 100 TeV [36]. These methods rely on high-precision instruments deployed on satellites or balloon-borne platforms that can directly sample incoming cosmic-ray particles above the atmosphere. The main categories of instruments used are: (1) Magnetic spectrometers, such as AMS-02 (Alpha Magnetic Spectrometer) [5] and PAMELA [6]. These devices use magnetic fields and tracking systems to determine the rigidity and charge sign of particles; (2) Calorimeter-based detectors, like DAMPE (DArk Matter Particle Explorer) [37], and CREAM (Cosmic Ray Energetics and Mass) experiment [38], which measure the total energy of particles through full absorption; (3) Time-of-flight systems and Cherenkov or transition radiation detectors, used in experiments like *ATIC* (Advanced Thin Ionization Calorimeter) [36] and *TRACER* [39] (Transition Radiation Array for Cosmic Energetic Radiation), which measure the particle velocity and Lorentz factor. When combined with measurements of rigidity or energy, these quantities allow the determination of the particle's mass and hence its identity.

Despite their precision, direct detection methods are fundamentally constrained by the small geometrical acceptance and limited payload mass of space- and balloon-based experiments. In addition, as mentioned previously, the steeply falling flux of cosmic rays at higher energies makes it unfeasible to extend these techniques further into the PeV range and above, due to insufficient exposure time and the impracticality of scaling detector mass accordingly.

2.4.2 Indirect Detection

At energies above $\sim$ 1 PeV, the cosmic-ray flux are measured indirectly by observing the cascades of secondary particles (EAS) produced when a primary particle enters the Earth's

atmosphere. Indirect detection relies on measuring various components of the EAS using large arrays of ground-based detectors and atmospheric instruments. Using the measured particle densities and their temporal and spatial distributions, fundamental properties like the energy, direction, and mass composition of the primary cosmic ray can be reconstructed. Figure 2.3 shows a schematic overview of the different detection methods used to observe air shower components. The main detection channels and their physical observables will be discussed in the following sections.

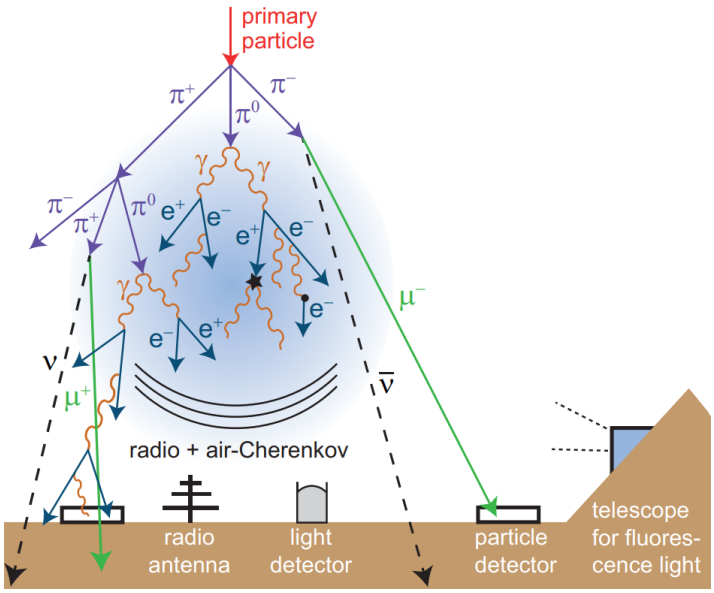

Figure 2.3: Illustration of the main components of an extensive air shower and the corresponding detection techniques [28].

Particle Detectors

The electromagnetic and muonic components of extensive air showers (EAS) can be sampled using arrays of particle detectors deployed at the Earth's surface. Two principal technologies are commonly used, namely, Water Cherenkov Detectors (WCD) and Scintillation Detectors (SD).

WCDs generally consist of large tanks filled with ultra-pure water or ice, instrumented with photomultiplier tubes (PMTs). They are used in major experiments like the Pierre Auger Observatory [40] and IceCube's IceTop array [15]. When a charged particle traverses through a medium with refractive index n at a speed v exceeding the phase velocity of light in that medium, it emits Cherenkov radiation [41] at an angle θ_C given by

$$\cos\theta_C = \frac{1}{\beta n},$$

where $\beta = \frac{v}{c}$ is the particle's velocity relative to the speed of light in vacuum. This radiation is collected by the PMTs in the WCD detectors. Due to their longer path lengths, muons generate more Cherenkov light than electrons or photons, making WCDs relatively more sensitive to the muonic component of the shower. These detectors are therefore often calibrated in units of *Vertical Equivalent Muon* (VEM), which is defined as the average signal produced by a single vertical muon traversing the detector.

Scintillation detectors are composed of plastic scintillator bars that emit light when traversed by charged particles. This light is captured via wavelength-shifting fibres and read out by

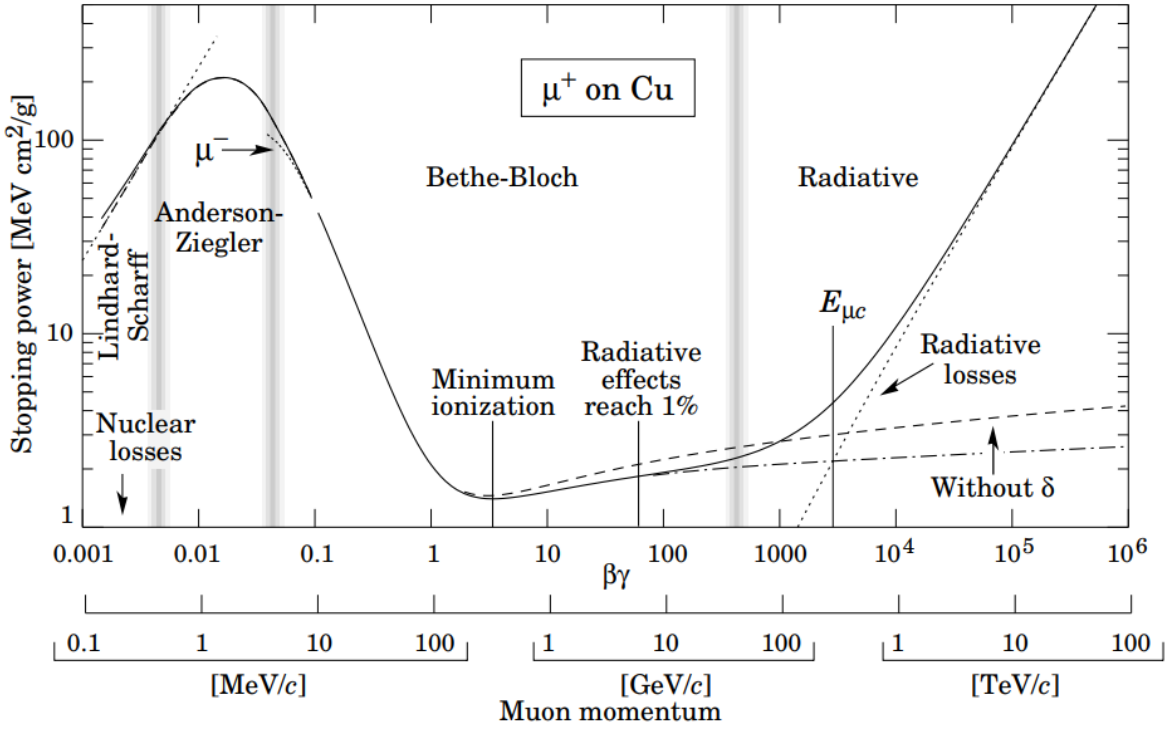

Figure 2.4: Bethe-Bloch energy loss curve for muons traversing a medium. The minimum ionizing region can be found in the $\beta\gamma \sim 3 - 3.5$region [42].

PMTs (e.g., in AugerPrime [13]) or silicon photomultipliers (SiPMs) (e.g. in IceCube Surface Array Enhancement [17], which are the focus of this thesis). SDs are sensitive to both the electromagnetic and muonic component of the shower. The energy deposited in scintillators is governed by the *Bethe-Bloch equation*, which describes the average energy loss per unit distance due to ionisation:

$$-\left\langle \frac{dE}{dx} \right\rangle = 0.307 \, \frac{\text{MeV}}{\text{g cm}^2} \cdot \frac{z^2 Z}{A} \cdot \frac{1}{\beta^2} \left[\frac{1}{2} \ln \left(\frac{2 m_e c^2 \beta^2 \gamma^2 W_{\max}}{I^2} \right) - \beta^2 - \frac{\delta(\beta\gamma)}{2} \right], \tag{2.8}$$

where z and M are the charge and mass of the incident particle, $\beta = v/c$, $\gamma = (1 - \beta^2)^{-1/2}$, Z and A are the atomic number and mass of the target material, I is the mean excitation potential, and $\delta(\beta\gamma)$ accounts for the density effect correction. The maximum energy transfer in a single collision is given by:

$$W_{\max} = \frac{2 m_e c^2 \beta^2 \gamma^2}{1 + 2\gamma m_e / M + (m_e/M)^2}. \tag{2.9}$$

Charged particles with $\beta\gamma \sim 3$–4 are referred to as *Minimum Ionising Particles* (MIPs), as they deposit the least energy per unit distance. These particles, typically high-energy muons or relativistic electrons, are used for SD calibration in units of MIP, where one MIP corresponds to the charge deposited by a single MIP. Figure 2.4 presents Bethe-Bloch energy loss curve for muons traversing matter. The dependence of the stopping power $\left(-\frac{dE}{dx}\right)$ on the particle's kinetic energy is plotted.

To improve the separation of shower components, buried scintillator detectors can be used, such as the Underground Muon Detectors (UMDs) planned for the AugerPrime upgrade. These suppress the electromagnetic component and can provide a direct measurement of the muonic content of the shower, thereby enhancing sensitivity to primary composition.

Fluorescence Detectors (FD)

Fluorescence detectors observe ultraviolet light emitted by atmospheric nitrogen molecules excited by air-shower particles. This light is proportional to the energy deposit along the shower path, making FDs a nearly calorimetric energy estimator. The Pierre Auger Observatory operates 27 fluorescence telescopes [40] with a field of view of $\sim 180°$ in azimuth and 0°–30° in elevation. A key observable from FD measurements is the depth of shower maximum, $X_{\max}$, which is composition-sensitive. This method provides a very accurate measurement of the longitudinal profile of the air shower as the emission is isotropic in nature and can be detected in all directions, although the energy threshold is quite high for these detectors. Due to the low duty cycle ($\sim 15\%$) for the necessity of clear, moonless nights, the measurements with FDs are limited.

Air-Cherenkov Detectors

Air-Cherenkov detectors observe the Cherenkov radiation emitted by relativistic charged particles in the EAS as they traverse the Earth's atmosphere. When these particles move faster than the speed of light in air, they emit a cone of coherent light in the optical to near-UV range. This Cherenkov light can be detected using optical telescopes equipped with fast photodetectors, typically arranged in large arrays that monitor large portions of the sky. Similar to fluorescence detectors, air-Cherenkov instruments provide valuable information about the longitudinal development of the shower and enable energy reconstruction based on the intensity and angular distribution of the emitted light. Their operation is also constrained to moonless, clear nights due to the low intensity of Cherenkov light, which makes them sensitive to atmospheric conditions. Notable experiments that utilise such detectors include the imaging atmospheric Cherenkov telescopes (IACTs) used primarily for gamma-ray astronomy, such as H.E.S.S. [43], MAGIC [44], and VERITAS [45], as well as IceAct, which is a planned array of Imaging Air Cherenkov Telescopes on the surface of IceCube [46].

Radio Detection

Radio emission from extensive air showers (EAS) is primarily generated by the electromagnetic component of the shower as it propagates through the atmosphere. Two mechanisms are responsible for this emission: the *geomagnetic effect* [47], where electrons and positrons in the shower are deflected in opposite directions by the Earth's magnetic field, creating a time-varying transverse current; and the *Askaryan effect* [48], which arises from a negative charge excess due to ionisation and annihilation processes, leading to coherent radio emission radially polarised with respect to the shower axis. These emissions can be detected using arrays of radio antennas. Because the radio signal is produced by the electromagnetic portion of the EAS, it carries significant information about the primary energy, making radio detection a promising technique for high-precision energy reconstruction. A major advantage is the high duty cycle, as radio measurements are not restricted by daylight or normal weather conditions, but adverse conditions like thunderstorms can have an effect. However, the combined contributions of the geomagnetic and Askaryan mechanisms introduce complexity in signal modelling and increase the challenge of accurate error estimation. Despite these challenges, radio detection is rapidly maturing into a powerful complementary method for cosmic-ray studies. Current and upcoming experiments such as AERA at the Pierre Auger Observatory, RNO-G [49], and IceCube Surface Array Enhancement (SAE) [50] as well as the proposed Radio Surface Array for IceCube-Gen2 are advancing this technique using dense antenna grids operating in the 30–80 MHz and 60–400 MHz frequency bands, respectively.

Chapter 3

IceCube Neutrino Observatory

The IceCube Neutrino Observatory is a three-dimensional array of optical sensors instrumenting one cubic kilometer of clear Antarctic ice at the geographic South Pole [51]. A precursor experiment to IceCube that instrumented the deep antarctic ice was AMANDA [52]. IceCube consists of an in-ice array, which primarily detects neutrino interactions deep within the Antarctic ice, and a surface component called IceTop, designed primarily for cosmic-ray studies, as well as veto against atmospheric background for the in-ice counterpart.

Since its full deployment and commissioning in 2011, IceCube has remained the world's largest neutrino observatory, utilizing the exceptionally clear Antarctic ice to explore fundamental questions in astroparticle physics. This chapter will cover the science conducted at IceCube, including its instrumentation, major scientific results to date, and future directions for the observatory.

3.1 Scientific Research at IceCube

IceCube's primary objective is the detection of high-energy astrophysical neutrinos, enabling the study of their origins and their fundamental interactions. However, its capabilities extend beyond this central goal, contributing to several key areas in astrophysics, particle physics, and cosmology. These include cosmic-ray physics, indirect dark matter searches, and tests of Beyond the Standard Model (BSM) physics, such as neutrino oscillations, Lorentz invariance violation, and searches for exotic particles [51].

As shown in Fig. 3.1, high-energy messengers such as cosmic rays, neutrinos, and gamma rays reach Earth carrying unique insights into extreme astrophysical environments. Their distinct interaction mechanisms reveal critical information about the universe's most energetic processes. Multi-messenger astronomy, which combines these observations, enables a more holistic understanding of such phenomena. IceCube plays a central role by detecting both neutrinos and cosmic rays, and by partnering with a global network of observatories to help pinpoint and investigate potential neutrino sources. The main research areas and key results are summarized below.

Neutrino Astronomy

Neutrinos are weakly interacting particles that travel vast distances unimpeded, carrying direct information from their sources. These high-energy neutrinos interact with nucleons in the Antarctic ice via charged-current (CC) or neutral-current (NC) deep inelastic scattering [51]. The resulting secondary particles travel faster than the speed of light in ice, emitting Cherenkov radiation, which is detected by IceCube's in-ice array. These measurements allow

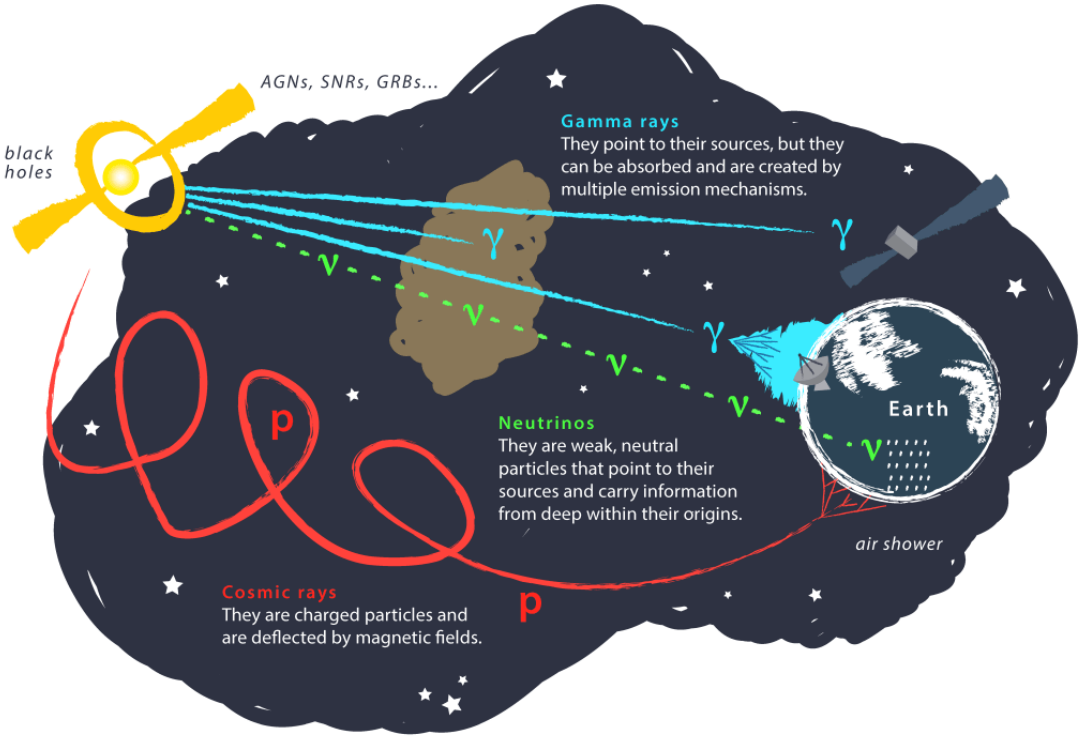

Figure 3.1: Demonstration of multi-messenger particle propagation; neutrinos travel undeflected and unscattered, pointing back to their sources. Image adapted from IceCube Research News [53].

the reconstruction of the neutrino's energy, direction, and possible sources of origin, opening a new window into the study of cosmic accelerators such as supernova remnants, active galactic nuclei, and gamma-ray bursts.

Key Results

- Soon after IceCube was operational in its final configuration, the collaboration reported the observation of a diffuse flux of high-energy neutrinos based on the events measured in 2011, named *Bert* and *Ernie* with reconstructed energies of 1.04 and 1.14 PeV [54] providing the first evidence of highest energy astrophysical neutrinos at the time. The observed power-law spectrum and isotropic distribution further supported an extragalactic origin [55].

- A major breakthrough followed in 2017 with the detection of a muon neutrino with an energy of 290 TeV in directional coincidence with the flaring blazar TXS 0506+056. This observation was supported by gamma-ray telescopes Fermi-LAT and MAGIC, and provided the first evidence for a high-energy neutrino source [56, 57]. This marked the first observation of a multi-messenger event with IceCube.

- In 2021, a cascade event of 6.05 PeV was detected by IceCube, which was consistent with the long predicted Glashow resonance [58] expected to have 6.3 PeV, which should arise from an electron anti-neutrino interacting with an atomic electron. This was an important result in favor of the Standard Model in particle physics in an experimentally unexplored energy regime so far.

- In 2022, IceCube identified the Seyfert galaxy NGC 1068 (also known as M77) as a high-energy neutrino source in the TeV range, based on a spatial clustering of cascade events in a time-integrated analysis using template fitting. The excess rejected the background-only hypothesis at $4.2\,\sigma$, marking a key detection of an extragalactic source [59].
- The Milky Way was confirmed as the high-energy neutrino source with 4.5 σ in 2023 with 10 years of cascade data, analysed using an unbinned maximum-likelihood stacking method, with spatial template fitting [60]. This will facilitate a critical test of the Galactic Cosmic-Ray propagation models. Figure 3.2 presents a multi-wavelength view of the Milky Way's Galactic Plane.

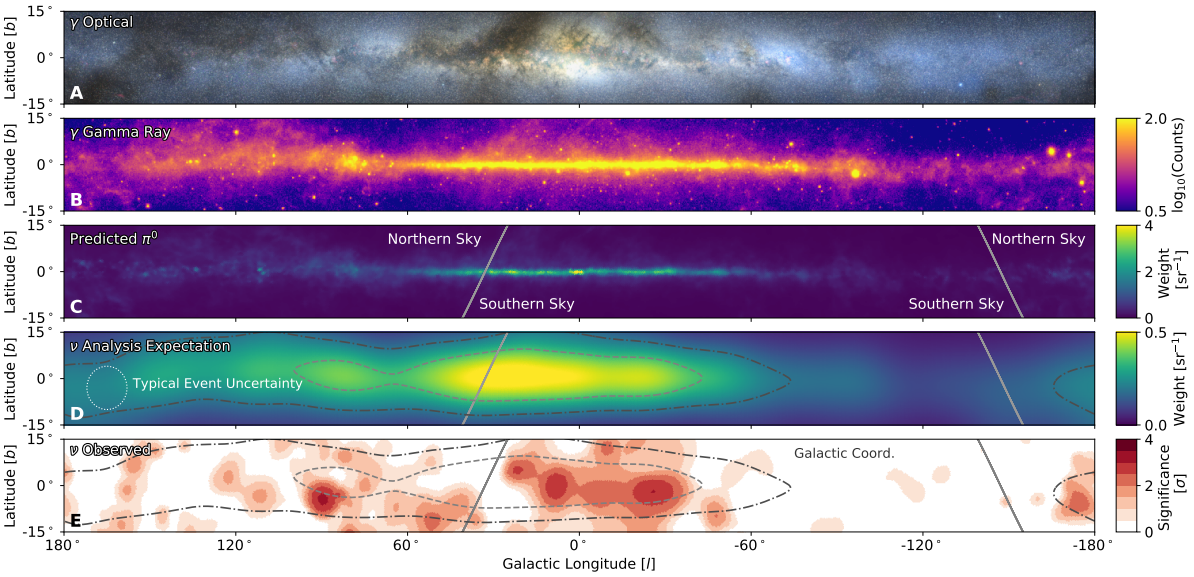

Figure 3.2: Multi-wavelength view of the Galactic Plane. The different panels show (A) optical image, (B) gamma-ray intensity, (C) predicted π^0 decay neutrino emission, (D) The emission template from C, after including the detector sensitivity to cascade-like neutrino events and the angular uncertainty of a typical signal event, and (E) observed neutrino significance sky map. The correlation between the predicted and observed distributions supports the Galactic origin of the detected neutrinos [60].

Cosmic Ray Studies

Cosmic rays, which are predominantly protons and heavier nuclei, are deflected by magnetic fields, making it challenging to trace their origins. Upon striking the Earth's atmosphere, they produce extensive air showers. The electromagnetic and muonic components of air showers are detectable by IceTop [15]. This allows for measurements of cosmic-ray energy spectra and composition, advancing our understanding of cosmic-ray sources and propagation. IceCube is one of the major contributors to cosmic ray measurements in the Southern Hemisphere in the PeV-EeV energy range.

Key Results

- Observation of anisotropies in the arrival directions of cosmic rays can reveal possible cosmic-ray sources and the magnetic fields they propagate through. IceCube reported the first anisotropy studies of large and small scale structures from the Southern Hemisphere, observed within the energy range of 10 TeV to 1 PeV [61]. These studies were recently updated with 12 years of IceCube data, confirming the change in angular structure of the CR-anisotropy in the 100-300 TeV range [9].

- IceTop has measured the cosmic-ray energy spectrum from approximately 250 TeV to 1 EeV, covering the transition region between Galactic and extragalactic cosmic rays. These measurements reveal a clear steepening at the "knee" around 3-5 PeV and suggest a second softening at higher energies near $10^{17}\,eV$ [62]. The results are consistent with northern hemisphere observations and extend our understanding to the southern sky.

- By combining IceTop surface signals with deep in-ice muon measurements, IceCube has conducted detailed studies of the cosmic-ray mass composition across a wide energy range. The data indicate a trend toward heavier primaries above the knee, with a gradual shift from proton-dominated to iron-dominated cosmic rays [62].

- A combined IceTop and in-ice analysis measured the average multiplicity of TeV muons in air showers for primary energies between 2.5 and 100 PeV. The results were used to test and validate the hadronic interaction models underlying air-shower simulations, revealing notable deviations from predictions by Sibyll 2.1, QGSJet-II.04, and EPOS-LHC [63].

Multi-Messenger Astronomy

As mentioned previously, IceCube operates as a multi-messenger observatory with a detector up-time exceeding 99%, enabling near-continuous monitoring of the southern sky for high-energy astrophysical events. Many potential neutrino sources, such as jetted and non-jetted AGNs, novae, and gamma-ray bursts, are predicted to emit both neutrinos and electromagnetic radiation through hadronic interactions. Although IceCube is sensitive to PeV gamma-ray emission [64], no such events have been detected to date. To identify possible counterparts, IceCube issues real-time neutrino alerts that trigger rapid follow-up observations by gamma-ray telescopes such as VERITAS, MAGIC, and H.E.S.S. [65, 56]. It also responds to alerts from the broader astronomical community to perform targeted searches. Through these coordinated efforts and collaborations with other neutrino detectors (e.g., KM3NeT, Baikal-GVD), electromagnetic observatories, and gravitational wave detectors, IceCube plays a central role in advancing multi-messenger astrophysics. The confirmation of TXS 0506+056 as a high-energy neutrino source was a major multi-messenger observation using IceCube data.

Beyond the Standard Model Physics

IceCube's sensitivity to high-energy neutrinos allows it to probe a range of phenomena beyond the Standard Model. Precision tests of Lorentz Invariance Violation (LIV) using atmospheric muon neutrinos led to some of the tightest constraints in the neutrino sector, limiting dimension-four LIV coefficients to the 10^{-28} level [66]. Extensive searches for eV-scale sterile neutrinos, utilizing 10.7 years of data and refined event classification, found no significant signal and set strong limits on mixing parameters [67]. Dark matter searches targeting neutrinos from WIMP annihilation in the Earth's core have resulted in competitive constraints on the spin-independent WIMP-nucleon cross-section for masses above 100 GeV [68]. Additionally, IceCube continues to explore other beyond Standard Model scenarios, including non-standard neutrino interactions, magnetic monopoles, and exotic particles, capitalizing on its vast detection volume and energy reach.

3.2 Instrumentation

Fig. 3.3 illustrates the complete 3-dimensional instrumentation of the IceCube Neutrino Observatory. The primary components include the surface array called IceTop and the In-Ice array.

At the center of the In-Ice array lies DeepCore, a more densely instrumented sub-array designed to lower the detector's energy threshold to O(10) GeV. Additionally, all operations and data acquisition are coordinated from the IceCube Laboratory (ICL) located on the surface.

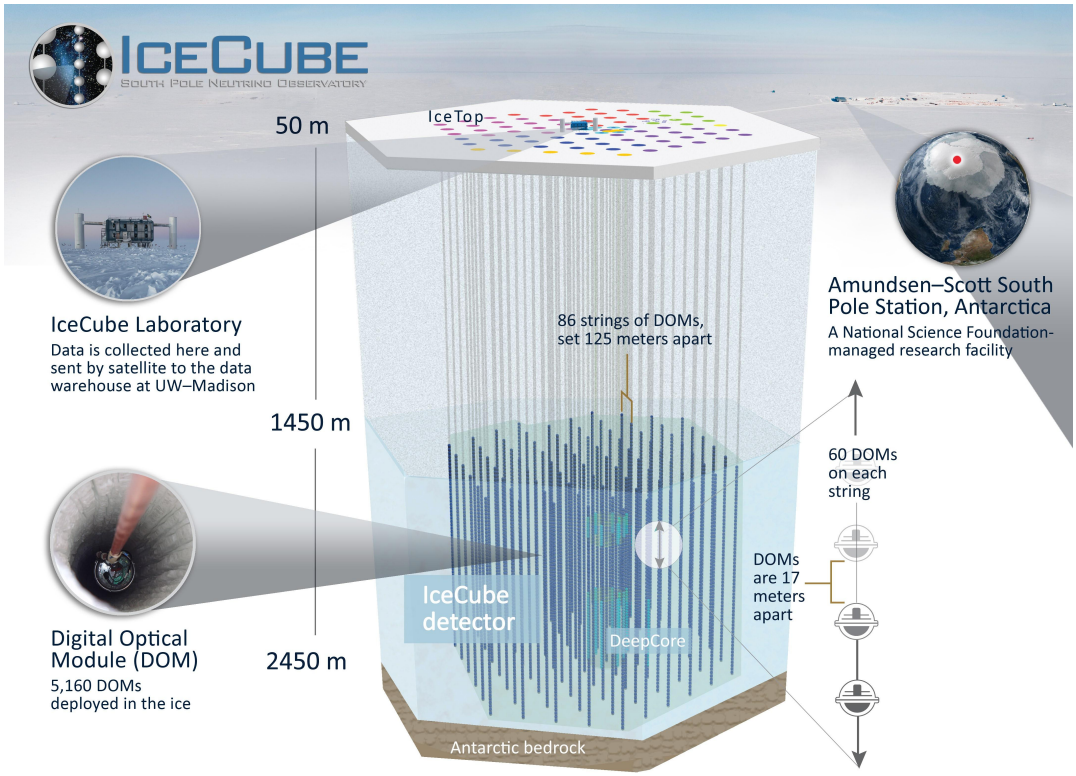

Figure 3.3: A 3-dimensional illustration of the IceCube Neutrino Observatory. All the main components of the observatory are visible in the illustration. It was taken from [14]

3.2.1 In-Ice Array

The in-ice array of IceCube comprises 86 vertical strings deployed between depths of 1450 m and 2450 m beneath the Antarctic surface. Each string hosts 60 Digital Optical Modules (DOMs) arranged in a hexagonal grid, as illustrated in Fig. 3.4. For 78 of the total strings, the DOMs are vertically spaced at 17 m, and the inter-string spacing is approximately 125 m. This forms the main in-ice array. The rest of the 8 strings are part of the DeepCore array. The full instrumented volume is about 1 km^3, enabling neutrino detection across a wide energy range from tens of GeV up to a few PeV [51].

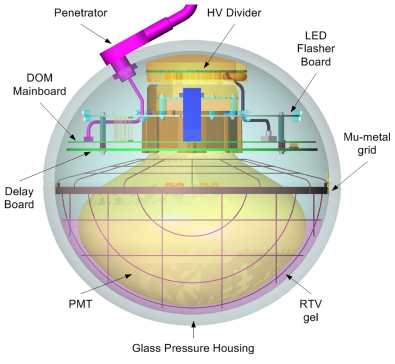

Figure 3.4: Schematic of a Digital Optical Module (DOM). These are the primary light sensors used in IceCube.

The detection units, or Digital Optical Modules (DOMs), are spherical Cherenkov detectors containing a downward-facing 10-inch photomultiplier tube (PMT), enclosed in a pressure-resistant glass housing along with digitizing electronics. Each DOM functions as a self-contained sensor, capable of detecting single photons with a gain of 10^7 and nanosecond-level timing resolution. DOMs can also register delayed

photons up to 6.4 μs, for which both the hit time and waveform are stored. Data are transmitted to the IceCube Laboratory (ICL) every second, with internal buffering allowing storage for up to 10 s in case of communication interruptions. To enhance light collection and Single Photo-Electron (SPE) resolution, each PMT is shielded from the geomagnetic field using a mu-metal cage. A comprehensive description of the DOM design and functionality is available in [51].

3.2.2 DeepCore

Eight specialized strings, along with seven central strings from the main in-ice array, make up the DeepCore sub-array. Designed to extend IceCube's sensitivity to lower energies, DeepCore features a denser configuration. The bottom 50 DOMs on each of the 8 dedicated strings are deployed with a vertical spacing of just 7 m, while the remaining 10 DOMs are located above 2000 m depth and spaced 10 m apart to form a veto layer [51]. The average inter-string distance in DeepCore is reduced to 72 m. This configuration lowers the energy threshold to a O(1-10) GeV, enabling studies of atmospheric neutrino oscillations, searches for signals from low-mass dark matter candidates, such as WIMP annihilation products, and searches for astrophysical sources of sub-TeV neutrinos [51, 69].

3.2.3 Surface Array: IceTop

The surface component of IceCube is known as IceTop [15]. It comprises 162 cylindrical, ice-filled tanks, each instrumented with two Digital Optical Modules (DOMs) similar to those used in the in-ice array. The two DOMs in each tank are operated at different gain settings to extend the dynamic range of the detector. Each tank is filled with approximately 0.9 m of clear ice and is deployed directly on the surface of the ice, which lies at an elevation of about 2.8 km above sea level. The tanks are arranged in pairs, forming 81 IceTop stations. These stations are distributed over a footprint roughly matching that of the in-ice string array, with an average inter-station spacing of 10 m. In the region above DeepCore, the IceTop tanks are more densely packed to match the in-ice configuration and is referred to as the in-fill region. A picture of the deployed IceTop tanks and the array layout is shown in Fig. 3.5.

IceTop plays a crucial role in the study of cosmic rays and serves as a veto for atmospheric muons that can mimic neutrino events in the in-ice array. It is sensitive to both the electromagnetic and muonic components of extensive air showers and covers the energy range from PeV to EeV, corresponding to the transition region between galactic and extragalactic cosmic-ray sources. Additionally, due to the elevation of the array corresponding to a vertical atmospheric depth of 690 g/cm^2, the air showers observed with IceTop have their shower maxima close to or even below the detectors, providing increased sensitivity to the primary particle mass [70]. Finally, thanks to its unique design, the high-energy muons produced in air showers can be studied in detail as they pass through the in-ice instrumentation, leveraging the three-dimensional nature of the observatory [71].

For the cosmic-ray studies, the calibrated data from the IceTop tanks is reconstructed using a three-step method [15]. This provides the information about the incoming direction (θ, ϕ), the position of the shower core (x, y), and the energy of the primary particle (E_{CR}).

- **Step 1:** The lateral distribution of the measured charge is fit to determine the shower core position using a Double Logarithmic Parabola (DLP) function:

$$S(r) = S_{\text{ref}} \left(\frac{r}{R_{\text{ref}}} \right)^{-\beta - \kappa \log_{10}(R_{\text{ref}})} \tag{3.1}$$

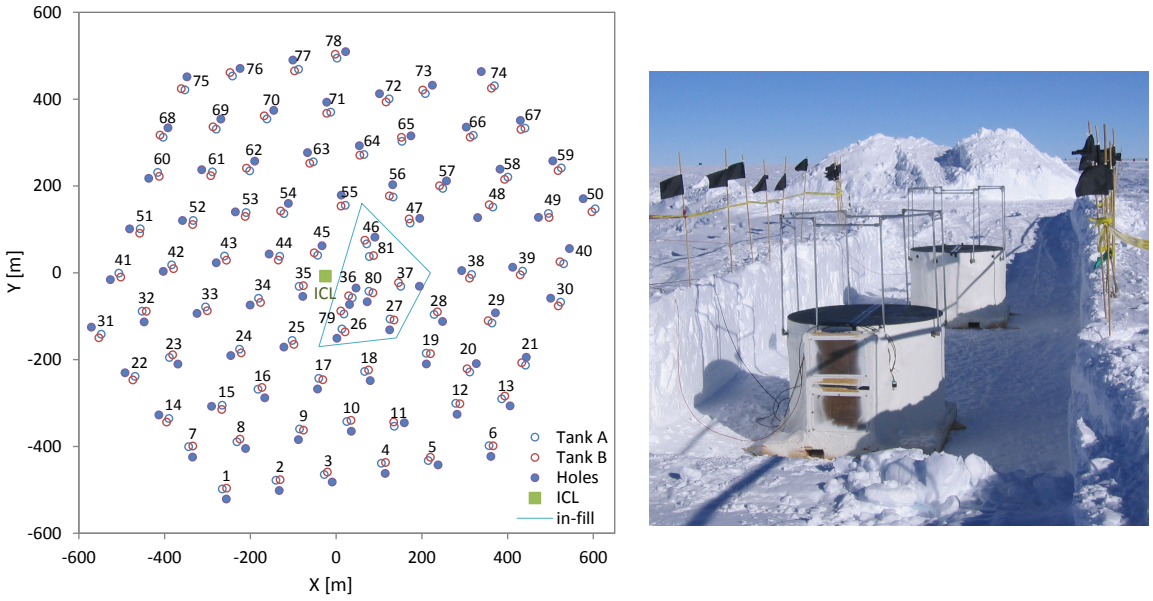

Figure 3.5: Left: Overhead view of the IceTop surface array, aligned with the footprint of the in-ice strings. Right: IceTop station with two tanks deployed in 2011.

where $S(r)$ is the expected signal at distance r from the shower axis, S_{ref} is the signal at a reference distance R_{ref} (typically 125 m), β is a slope parameter related to the shower age, and κ accounts for the curvature in the lateral distribution. Simultaneously, a seed for the direction reconstruction is obtained using a curved shower front approximation:

$$t(r) = ar^2 + b\left[1 - \exp\left(-\frac{r^2}{2\sigma^2}\right)\right] \tag{3.2}$$

where $t(r)$ is the time delay at distance r from the shower axis, and a, b, and σ are fit parameters describing the curvature and spread of the shower front.

- **Step 2:** A simultaneous fit of the lateral distribution and a curved shower front timing model by maximizing the combined log-likelihood of both the timing and charge distributions is performed in several iterations. In addition to the signal charges and times, the likelihood function also takes into account stations that did not trigger.

- **Step 3:** The output of the previous step is used to estimate the energy of the primary cosmic ray. This estimate is based on the reconstructed signal at a reference distance of 125 m from the shower core, denoted S_{125}, which serves as an energy proxy.

The agreement of S_{125} using the reconstruction and the true energy from the simulation set is shown in Fig. 3.6. This reconstruction framework forms the basis for the determination of high-level observables such as the cosmic-ray energy spectrum and mass composition.

The core and angular resolutions using the IceTop reconstruction as a function of energy are shown in Fig. 3.7. The core resolution ranges from 6-20 m with the minimum at the highest efficiency of 3 PeV. The angular resolution similarly reaches an optimal value of 0.2° at full efficiency and ranges upto 1°. The resolution worsens at higher energies for two main reasons: (1) air showers begin to exceed the physical size of the array, leading to incomplete sampling, and (2) signal saturation occurs in the tanks near the core [62].

Although IceTop has been successfully operational since the beginning of IceCube, its location on the surface of the ice introduces challenges. Over the years, non-uniform accumulation

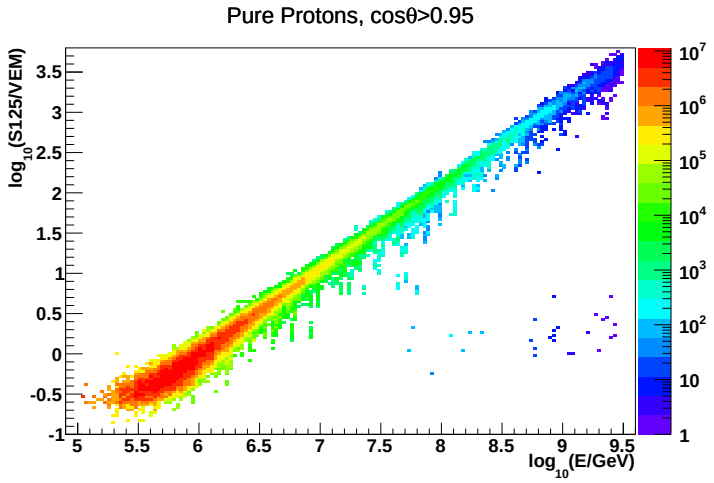

Figure 3.6: The reconstructed energy estimate S_{125} versus the true energy is presented. The color gradient indicates the density of events.

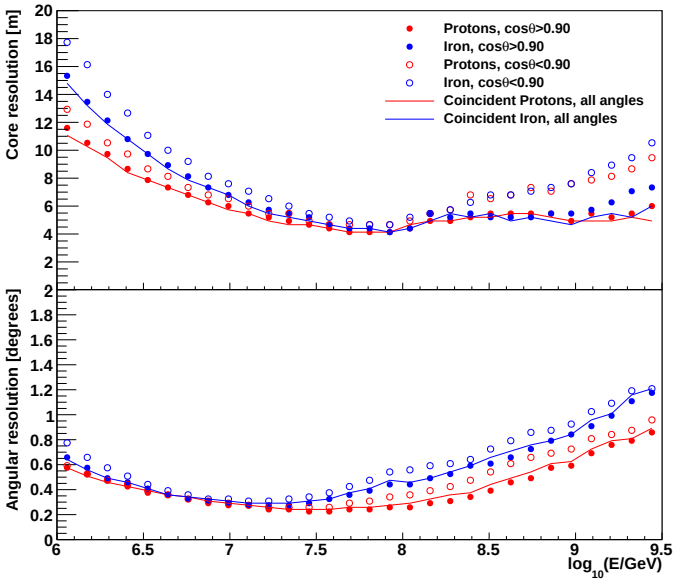

Figure 3.7: Performance of the IceTop reconstruction for simulated cosmic-ray showers: core resolution (top), angular resolution (bottom).

of snow on the IceTop stations at an average rate of approximately 20 cm/year has been observed [16]. This accumulation leads to signal attenuation in the ice, which increases the uncertainties in energy and mass determination from IceTop data. Several efforts have been made to study and correct for this snow-induced attenuation [16]. However, this is a non-trivial task, as the snow corrections rely on two yearly measurements of the snow depth, and the attenuation in the snow can vary depending on the particle traversing, with muons experiencing significantly less attenuation. The snow accumulation throughout the period from 2012 to 2023 is shown in Fig. 3.8.

3.3 Future of IceCube

IceCube has been operating successfully for over 14 years, making significant contributions to the field of astroparticle physics. With a remarkable annual uptime of $> 99\%$, the detector

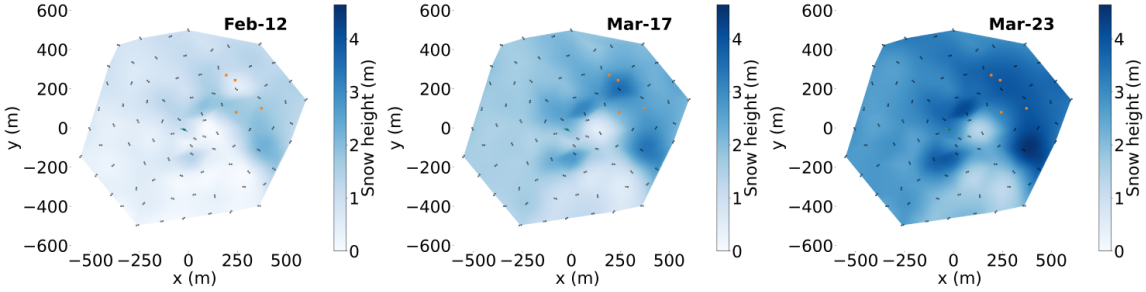

Figure 3.8: Snow accumulation on IceTop tanks measured from 2012 to 2023.Taken from [16].

has proven to be highly reliable, especially impressive given its remote location at the South Pole. Building on this success and the scientific results, a series of upgrades and expansions are currently underway to further enhance IceCube's capabilities.

3.3.1 IceCube Upgrade

IceCube in-ice array is set to undergo a major enhancement with the deployment of seven new strings in the bottom central region of the array, spanning depths from 2150 to 2425 m. This region features exceptionally clear glacial ice and a minimal background from atmospheric muons [72]. Figure 3.9 presents a schematic layout of the planned upgrade configuration. Deployment is scheduled for the Antarctic summer of 2025/2026.

The new strings will host a total of 700 advanced optical sensors, with each string arranged with a vertical spacing of 3 m between modules and 20 m horizontal spacing between adjacent strings. The geometry is optimized to enhance sensitivity to low-energy neutrinos, particularly in the GeV energy range. Two types of next-generation Digital Optical Modules (DOMs) will be featured in the physics region of the upgrade: mDOM [73], and D-Egg [74]. These modules will serve as prototypes for the planned IceCube-Gen2 extension. A new design of the original DOMs, called pDOM will be included in the calibration region to improve current understanding of their in-situ response [75]. The upgrade will also include a selection of novel calibration instruments such as the pencil beam, acoustic pinger, and POCAM, designed to reduce systematic uncertainties and support scalable calibration strategies for the full IceCube array.

A primary scientific objective of the IceCube Upgrade is to improve the precision of neutrino oscillation measurements. In particular, it is expected to provide world-leading sensitivity to tau neutrino appearance, enabling stringent tests of the unitarity of the Pontecorvo-Maki-Nakagawa-Sakata (PMNS) matrix. Any observed deviation from unitarity could indicate the presence of new physics beyond the Standard Model. As already mentioned, the upgrade will lower the energy threshold to $0(\text{GeV})$ for astrophysical neutrino source searches. Furthermore, advancements in calibration and detector design will enhance IceCube's overall sensitivity and support more precise analyses of existing archival data.

3.3.2 IceCube Gen2

Following the Upgrade, a major expansion is planned, increasing the instrumented volume from 1 km^3 to 8 km^3 called IceCube-Gen2 [76]. This enhancement is designed to significantly improve the sensitivity and accuracy of high-energy neutrino detection. The upgrade will involve the deployment of 120 new detection strings within the Antarctic ice. Each string will host 80 next-generation optical modules, arranged with a horizontal spacing of 240 meters. These advanced sensors, planned to be tested as a part of the IceCube Upgrade, will be capable

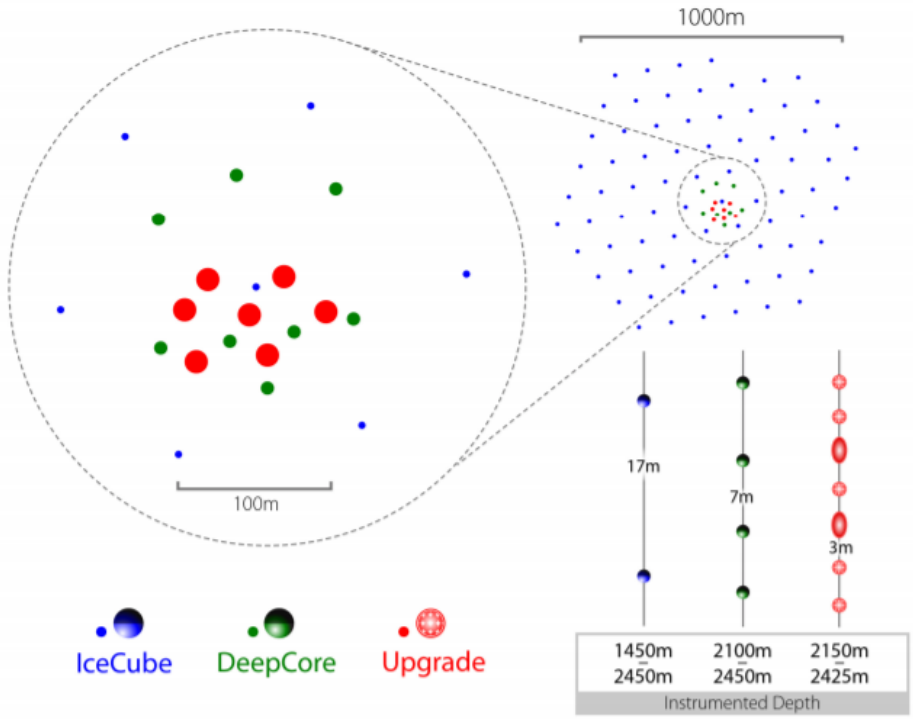

Figure 3.9: Schematic view of the planned IceCube Upgrade string deployment. The Upgrade strings are marked in red, while the deepcore strings in the vicinity are shown in green. The strings from the main in-ice array are in blue, respectively. This image was taken from [16].

of collecting four times more light than the IceCube current modules. As a result, the neutrino detection rate is expected to increase by an order of magnitude, dramatically expanding the observatory's discovery potential.

The enhanced in-ice detector will be complemented by a surface array of hybrid stations combining scintillation detectors and radio antennas. These will improve cosmic-ray background rejection and support the calibration and interpretation of deep-ice events by exceptional veto against atmospheric background. This surface array will be analogous to the Surface Array Enhancement layout (Sec. 3.4). Additionally, a large-scale in-ice radio array covering 500 km^2 will target the detection of ultra-high-energy neutrinos in the 10 PeV to 100 EeV range, probing some of the most extreme environments in the universe. Fig. 3.10 presents an aerial schematic of IceCube with all the planned upgrades. In addition, Fig. 3.11 presents a description of all the sub-systems that will be included in the full IceCube-Gen2.

By increasing the number and quality of neutrino detections, IceCube-Gen2 will significantly advance our understanding of where and how high-energy cosmic neutrinos are produced, shedding light on astrophysical neutrino sources, such as active galactic nuclei and gamma-ray bursts. The observatory will also probe the mechanisms behind cosmic ray acceleration and offer unique insights into the fundamental properties of neutrinos, such as their cross sections at ultra-high energies and potential interactions beyond the Standard Model. Furthermore, IceCube's expanded capabilities will enhance its role in multi-messenger astronomy, correlating neutrino detections with gravitational waves and gamma rays. The new in-ice radio array will open a window onto the ultra-high-energy universe, enabling the detection of the most energetic neutrinos ever observed and providing clues to the nature of the most extreme astrophysical phenomena.

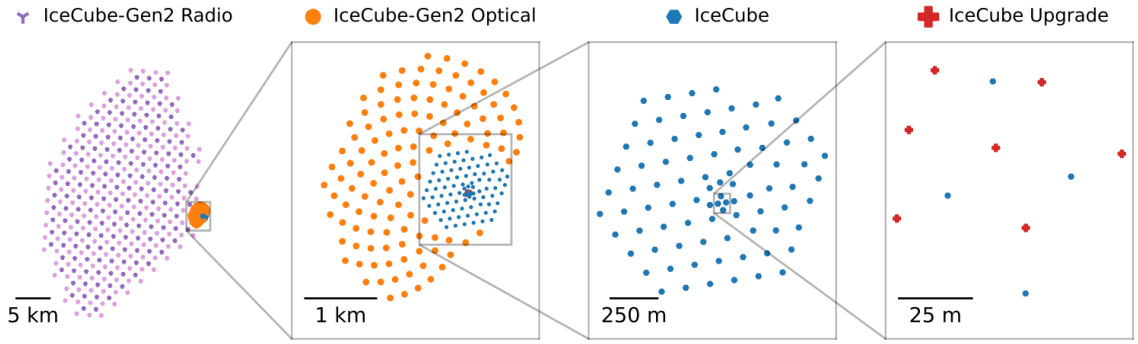

Figure 3.10: Layout of the IceCube-Gen2 detector array showing the increasing levels of zoom from the full IceCube-Gen2 Radio array (purple) to the IceCube Upgrade (red). Also shown are the IceCube-Gen2 Optical (orange), which will each host a surface array station, and existing IceCube (blue) components. Each panel highlights the spatial scale and density of detector instrumentation.

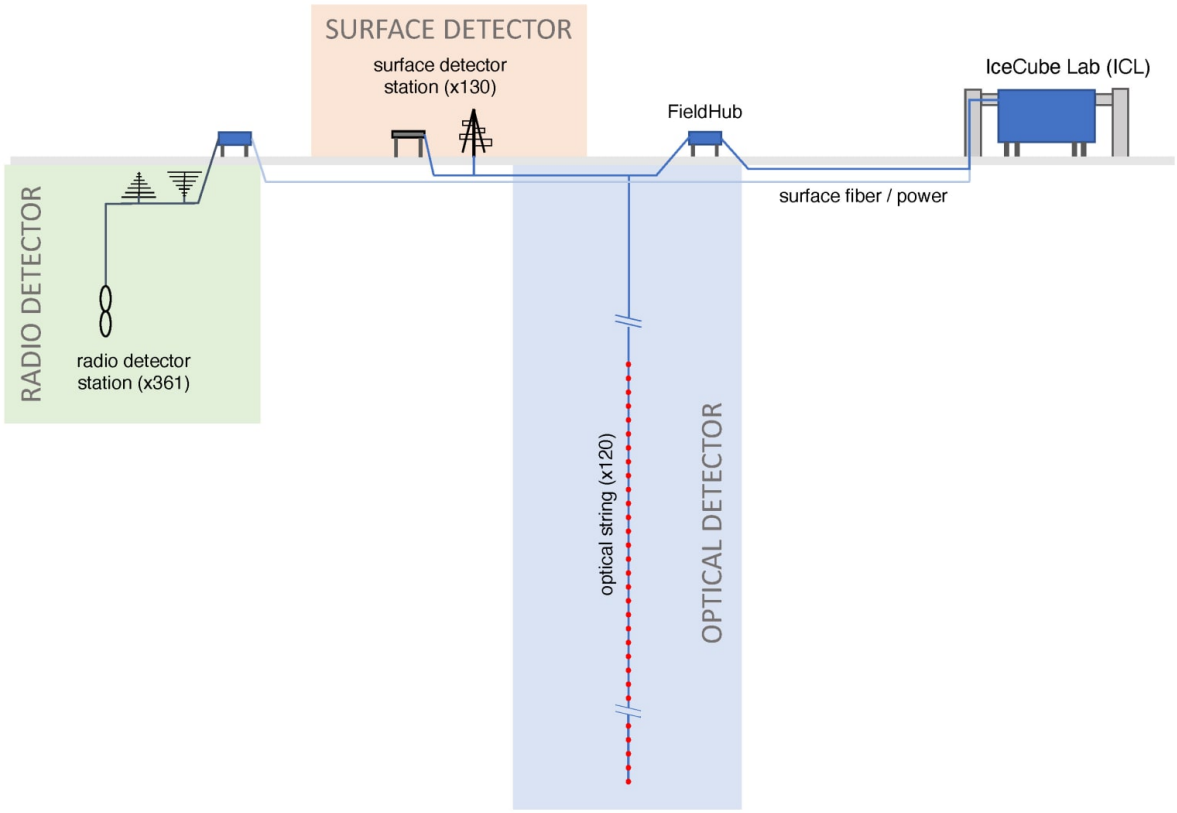

Figure 3.11: Schematic of the system architecture of IceCube-Gen2 [76].

3.4 Surface Array Enhancement (SAE)

An extension of IceTop, called the Surface Array Enhancement (SAE), has been proposed to enhance its performance as a cosmic ray detector and improve its capabilities for vetoing atmospheric background [77], and is the main topic of this work. The enhancement will consist of 32 hybrid detector stations, each equipped with 8 scintillation detectors, 3 radio antennas, and a central data acquisition (DAQ) system. Figure 3.12 illustrates the proposed layout, where SAE stations are distributed in a complementary triangular pattern covering the existing IceTop footprint. The inset shows the layout of a single SAE station. The chosen

geometry for the SAE has been optimized to minimize trenching required for new cabling, while also maintaining a uniform distribution of the stations [78].

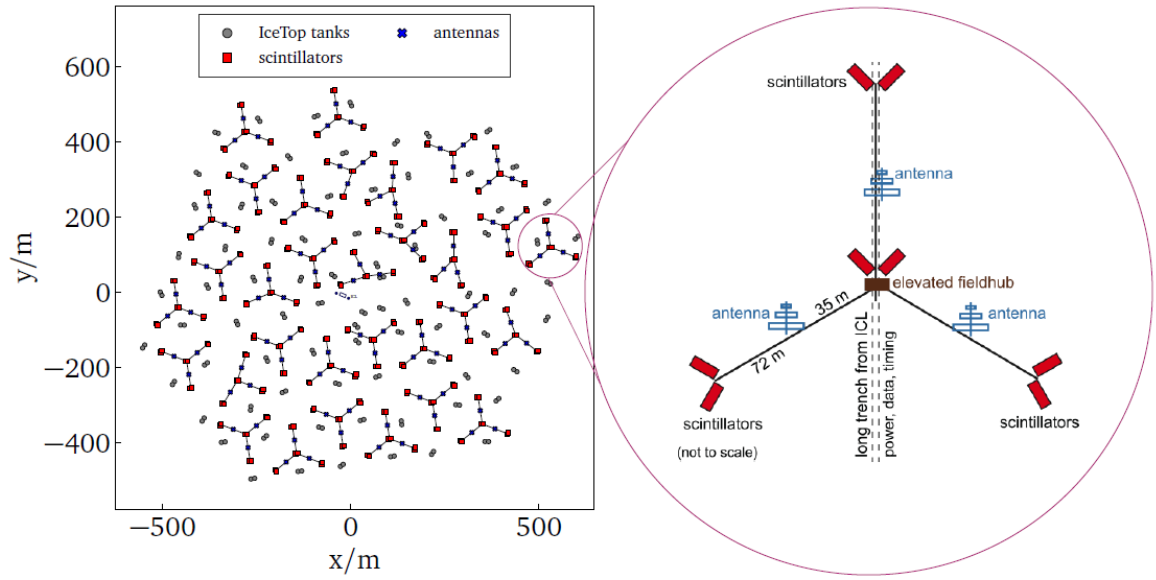

Figure 3.12: The planned geometry of the Surface Array Enhancement. IceTop tanks are shown in grey, SAE scintillation detectors in red, and radio antennas in blue. The inset highlights the layout of an individual SAE station, with the central DAQ also distinguishable in maroon.

Each SAE station adopts a triangular geometry, with scintillator detectors arranged in pairs. One pair is placed on each arm of the triangle, and an additional pair is placed at the center. Each scintillator pair is placed at a distance of 5m and 90 degrees to each other. The radio antennas are positioned midway along each arm, approximately 35 m from the central point. The central DAQ unit, referred to as the field hub, is also located at the center of the station. All components are mounted on elevatable platforms to mitigate the impact of snow accumulation to avoid the known issue for the IceTop tanks.

3.4.1 Science Case

The scientific motivations for the Scintillator Array Enhancement (SAE) are outlined below. For a more comprehensive discussion, refer to [17, 79].

- **Improved Calibration**: Coincident observations with scintillators allow for a better understanding and correction of snow-related effects on IceTop signals. This enables consistent calibration across a range of energies, zenith angles, and core distances, thereby reducing systematic uncertainties in air-shower reconstructions. In addition, scintillation detectors will facilitate a cross calibration with the IceTop tanks, which will improve the energy calibration for the past 13 years of IceCube data.

- **Enhanced Cosmic-Ray Measurements**: The increased detector density lowers the detection threshold and improves sensitivity to showers with cores outside the main array. The complementary responses of IceTop (muonic and electromagnetic), scintillators (muonic and electromagnetic), and radio antennas (sensitive to the electromagnetic emission) provide improved mass composition measurements. This multi-component approach also enhances constraints on the validity of hadronic interaction models.

- **Gamma-Ray Detection**: Gamma-ray showers produce slightly stronger radio signals and about ten times fewer muons than cosmic-ray showers, making the combination of radio and muon detectors ideal for photon searches. The Galactic Center, a promising PeV photon source, is continuously visible from the South Pole at a zenith angle of 61 degrees.

- **Enhanced Veto Capabilities**: The denser array improves atmospheric background rejection, boosting IceCube's sensitivity to neutrinos in the 100 TeV–PeV range. The high timing resolution of scintillators allows for fast and precise correlation with in-ice events, enabling efficient vetoing of background muons. In addition, the observation of the very inclined showers with the radio antenna will further facilitate veto against showers with cores outside the array.

- **Test Bed for IceCube-Gen2 Surface Array**: The SAE serves as a prototype for the Gen2 (3.3.2) surface array, which will include both scintillators and radio antennas. It provides a platform to test long-term detector performance and data acquisition in South Pole conditions, and helps optimize detector layout, triggering, and readout systems.

3.4.2 Station Overview

The central DAQ of an SAE station provides power, communication, and timing to the scintillation and radio detectors as shown in Fig. 3.13. Scintillator signals are digitized by a custom readout board called the microDAQ (described in detail in Chapter 4), located inside each detector, and are read out continuously. To limit the volume and minimize noisy data, Radio antennas are read out only when a chosen trigger condition is met. The trigger condition requires a coincidence of signals above threshold in a minimum number of scintillators (typically five) within a defined time window. This trigger is generated and distributed by the central DAQ, prompting the recording of the radio data. Both data streams are first stored locally at the central DAQ. After a measurement run is complete, the data are transferred to the surface DAQ in the IceCube Lab(ICL) over a 1 Gbit fiber link using a White Rabbit (WR) layer, and subsequently sent via satellite to IceCube servers. Power is supplied from the ICL and distributed by the central DAQ, with DC-DC converters providing the required voltages for detectors and antennas. Timing is maintained with sub-nanosecond precision through the WR-system [80], with a WR switch installed at the ICL and a WR-LEN module integrated into the central DAQ.

The scintillation detectors of the SAE are the primary focus of this work and will be discussed in detail in the following chapter. The other components of the surface array, namely the radio antennas and the central DAQ, are briefly described in the subsequent sections.

Radio Detectors

The radio detectors chosen for the Surface Array Enhancement (SAE) are dual-polarization Log-Periodic Dipole Array (LPDA) antennas, based on the SKALA-2 design developed by the SKA collaboration for their low-frequency array [81]. These antennas employ a unique arrangement of multiple dipoles to achieve uniform gain across a broad frequency range of 50–650 MHz, with omnidirectional coverage from zenith down to 60°. Frequencies above 350 MHz are filtered out by the front-end electronics (RadioTADs) located in the central data acquisition (DAQ) system to avoid interference from a nearby communication channel operating at 360.2 MHz.

Each polarization channel passes through a Low Noise Amplifier (LNA) mounted directly on the antenna, which pre-amplifies the signal with a gain of 40 dB before transmission to the DAQ. The antennas are mounted on wooden structures that can be elevated to mitigate snow

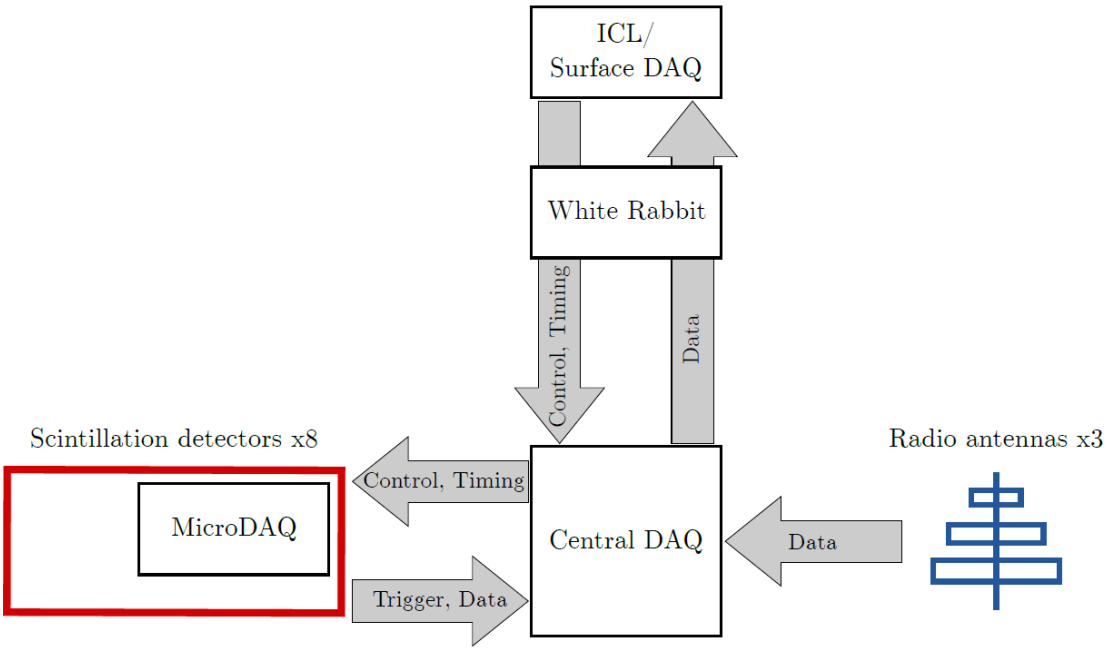

Figure 3.13: Overview of the DAQ of the SAE station

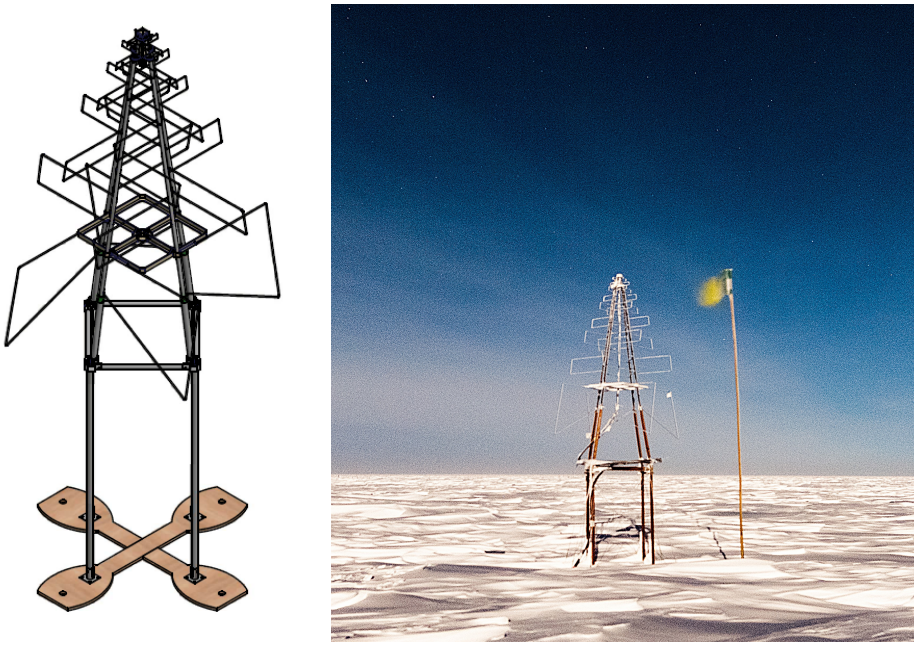

Figure 3.14: Left: A 3D illustration of the LPDA antennas with the custom wooden mount. The base plates are designed to maintain a stable structure, as the inclination of the antennas is crucial for accurate measurements and must remain fixed. Right: A photograph of one of the deployed radio antennas at the South Pole, taken in 2020 by the winterover Yuya Makino.

accumulation. Mahogany wood was specifically selected for its durability under South Pole conditions. A wooden mount is preferred to minimize electromagnetic interference and signal distortion, ensuring the clean detection of faint radio signals. Figure 3.14 shows a 3D design of the radio antenna with the mount. It also presents a picture of one of the deployed radio antennas at the South Pole. A more detailed discussion on the radio detectors of the SAE is available in [50, 82].

Central DAQ

The central DAQ is housed in a metallic box called the FieldHub, which is lined with styrofoam insulation for protection from the low ambient temperatures. The FieldHub also contains a dedicated enclosure for fiber housing and an eBox, which provides power to the central DAQ. The eBox is shared with another surface experiment, IceACT, a prototype for an array of optical Cherenkov telescopes aimed at detecting air showers and cross-calibrating surface detectors [46]. The FieldHub is an *R&D* design developed for the surface array of IceCube-Gen2. It is mounted on a metallic structure with four poles to elevate the Hub above the snow. Fig. 3.15 shows a deployed FieldHub at the South Pole, with an inside view of its components.

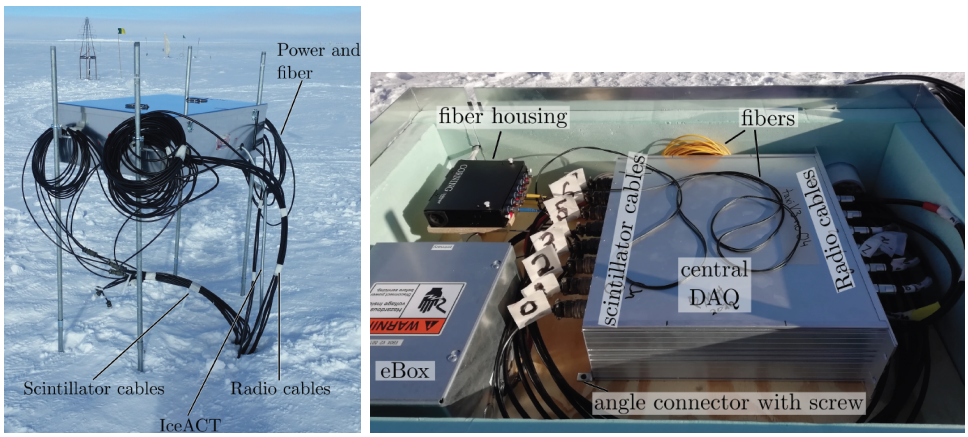

Figure 3.15: Left: An elevated FieldHub deployed at the South Pole, showing cables from the scintillation and radio detectors, as well as power and communication fiber connections. Right: Inside view of the FieldHub, displaying the eBox, fiber housing, and central DAQ components. The cables connecting the detectors to the DAQ are also visible.

The central DAQ consists of a TAXI board, a fanout board, three RadioTADs, and a WR-LEN. Fig. 3.16(a) shows a fully assembled central DAQ with the components labeled clearly. The core of the central DAQ is the TAXI board [83], which was developed as a modular, transportable test array to address the challenges of astroparticle detection in extreme environments. The main components of the TAXI system used in the SAE are an ARM-based microcontroller (Stamp9G45), an FPGA (Xilinx Spartan 6: XC6SLX45), a DC-DC converter, and DRS4 sampling chips. These components are visible in Fig. 3.16(b). The microcontroller serves as the on-site computing unit, running a Linux environment to manage communication between various SAE electronic components. The DRS4 chips act as a ring buffer, storing the analog radio data that has passed through the LNAs and RadioTADs (the radio front-end electronics). This data is digitized by a 14-bit ADC [50].

The RadioTADs (Fig. 3.16(c)) are specialized electronics boards designed to filter, amplify, and convert the single-ended signals from the antennas into differential pairs. Each board includes low-pass and high-pass filters that isolate the desired frequency band (70-350 MHz), amplify the signal, and provide power to the Low-Noise Amplifiers (LNAs), ensuring optimal signal integrity for further processing by the DRS4 chips in the TAXI system [50].

The fanout board facilitates the connection between the TAXI board and the eight scintillation detectors. It connects to the FPGA of the TAXI board via two-pin headers. The timing signals (PPS and 10 MHz) coming from the WR-LEN are split on the fanout board and distributed to both the TAXI board and the scintillation detectors. The WR-LEN acts as a slave to the WR-switch situated at the ICL, which in turn receives its timing from GPS, providing nanosecond precision. A detailed description of how the components of the station communicate with each other and with the infrastructure is presented in the block diagram shown in Fig. 3.17.

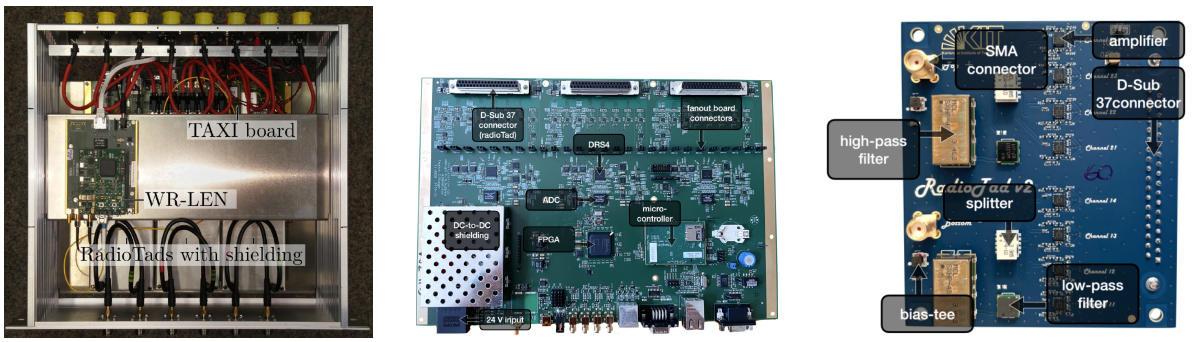

(a) (b) (c)

Figure 3.16: Components of the central DAQ system. (a) A fully assembled TAXI with the TAXI board, WR-LEN, RadioTADs, and fanout board with shielding. (b) The TAXI board with all its main components. (c) A RadioTAD board with labelled components.

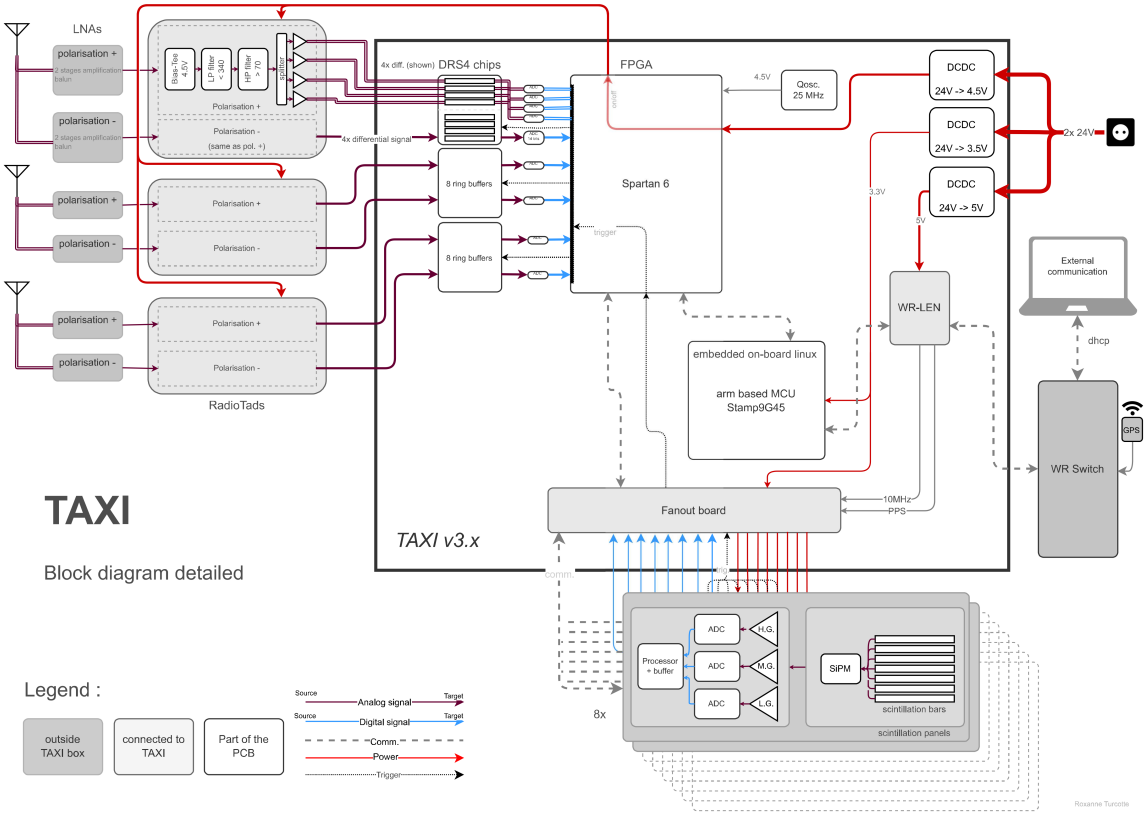

Figure 3.17: Block diagram of the communication and power flow between the TAXI and the SAE detectors.

3.4.3 Current status and timeline of the SAE

The Surface Array Enhancement (SAE) was first proposed in 2016, followed by several prototyping stages. In 2023, the first station in its final configuration was deployed, and it serves as the focus of this thesis. More recently, during the Antarctic summer of 2025, two new stations were deployed. Four additional stations produced within the scope of this thesis are foreseen to be deployed in the upcoming deployment seasons. Below is a timeline outlining the key developments leading to the full implementation of the Surface Array Enhancement. All deployments occurred during the Antarctic summers, primarily in the December–January

period.

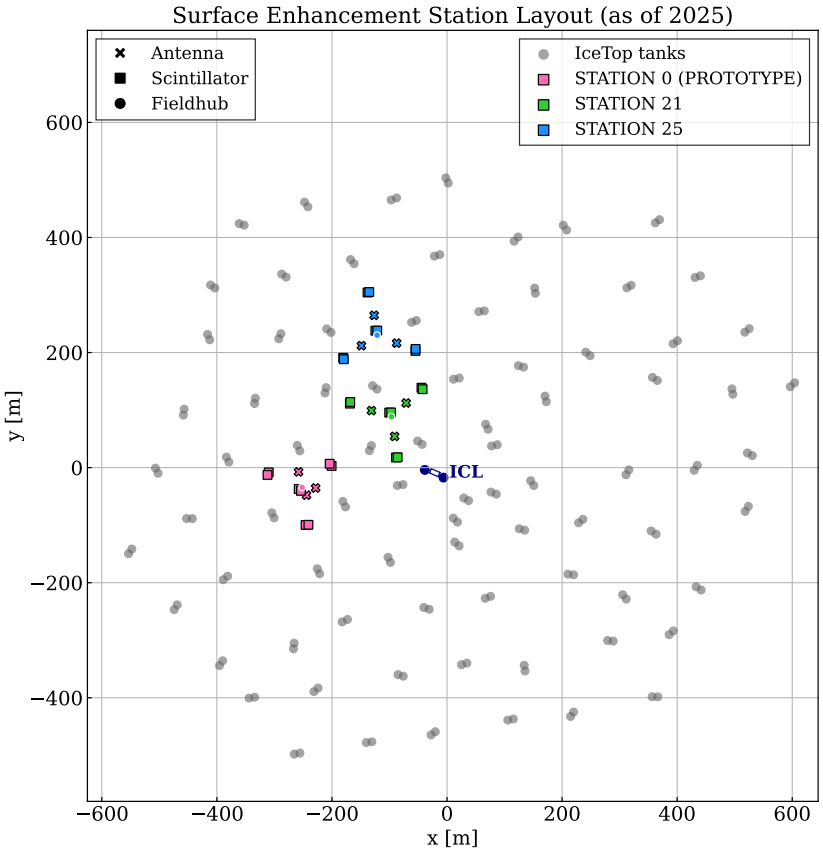

Figure 3.18: Layout of the three deployed stations of the IceCube SAE.

- **2017/18:** Two proof-of-concept stations, each with seven scintillation detectors, were installed at the IceCube site using an older central DAQ [77]. Each station's scintillators were equipped with two different/competing DAQ systems.

- **2018/19:** One of the two stations was modified by adding two radio antennas and updating the central DAQ accordingly [84].

- **2019/2020:** The first complete **Prototype Station** with three antennas, eight scintillation detectors, and one FieldHub was deployed. The version of the TAXI DAQ used was TAXI V3.0. The deployed station geometry was slightly different, especially for the radio antennas [85]. Fig. 3.19 shows a picture of the Prototype Station. The station components were raised ≈ 1.5 m above the snow height.

- **2021/22:** The central DAQ was upgraded to TAXI v3.2 to mitigate radio frequency interference (RFI) emissions identified in the 70-100 MHz range. The edges of the scintillation detectors were sealed with aluminum tape to correct for light leaks observed during analysis [85].

- **2022/2023:** The scintillation detectors of the Prototype Station were completely replaced with updated (final) versions, and the radio antenna mount was also updated. This configuration became the first SAE station in its final detector configuration, referred to as **Station 0** in this work.

- **2024/2025:** Two additional stations in the planned configuration, namely station 21 and 25, were deployed (Layout shown in Fig. 3.18). Maintenance of Station 0 was also carried out, which included raising the scintillation detectors and updating the mount of the third antenna.

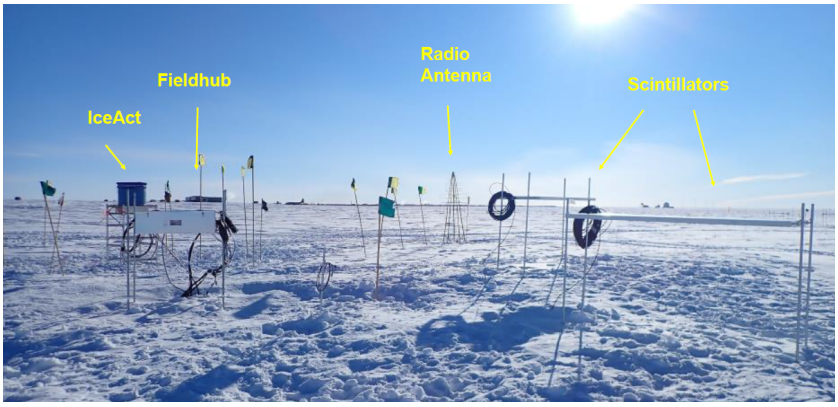

Figure 3.19: The prototype station at the South Pole in a picture taken in 2020.

Chapter 4

Scintillation detectors: Series production

Scintillation detectors are among the most widely used instruments for identifying secondary cosmic-ray particles. As discussed in the previous chapter, they are a key component of the Surface Array Enhancement (SAE), where they measure extensive air showers in conjunction with radio antennas and Ice-Cherenkov tanks to enable multi-component particle detection.

Section 4.1 provides a detailed description of the working principles of scintillation detectors, with particular emphasis on the detectors developed for the SAE. Since the production of these detectors constituted a major part of this work, Section 4.2 outlines the procedures followed during their series production. Given the scale of the production effort, establishing consistent test setups and standardized procedures was essential for ensuring detector uniformity and performance. These considerations are addressed in Section 4.3, which discusses the development of a dedicated pre-calibration and test environment to evaluate detector response under controlled conditions. Finally, the validation measurements performed to qualify the detectors for deployment are presented in Section 4.4. These results demonstrate the readiness of the SiPM-based scintillation modules developed and produced at KIT [86]. This chapter thus covers both the detection mechanism and the practical aspects of producing and validating scintillation detectors for the SAE, including the setup, procedures, and quality control measures that ensured a successful large-scale deployment.

4.1 Scintillators as Particle Detectors

This section begins with an overview of the detection principle underlying scintillation detectors, providing the necessary theoretical background for understanding their operation. Building on this foundation, the design and development of the scintillation detectors intended for the SAE are presented in detail.

4.1.1 Scintillation Mechanism

Scintillation is a luminescence process in which certain materials emit light in response to interaction with ionizing radiation. Such materials, known as scintillators, convert the energy deposited by charged particles into detectable visible or near-visible light. The spectral characteristics of this emitted light depend on the intrinsic properties of the material. This property is exploited to detect secondary particles generated in extensive air showers, thus allowing to indirectly detect them. In the context of extensive air showers, the primary sources of ionization are Minimally Ionizing Particles (MIPs), which are typically (high-energy) muons and

electrons produced during the shower development. The coincidence detection of these MIPs across spatially distributed detector arrays allows the reconstruction of shower properties (e.g., direction, energy, core location) through timing and amplitude measurements.

Scintillators are broadly categorised into two types: *organic* and *inorganic*. These categories differ primarily in their scintillation mechanisms and constituent materials. In this work, we focus on *plastic scintillators*, a type of organic scintillator chosen for the SAE. Composed of hydrocarbon-based polymers containing aromatic ring structures [87], plastic scintillators typically produce fast pulses with decay times of the order of a few nanoseconds (e.g., 2–5 ns), making them ideal for applications requiring fast timing response.

In organic scintillators, this process is governed by the electronic structure of the molecules, particularly the presence of aromatic rings which are stable, cyclic molecular structures with delocalized π-electrons. When a charged particle passes through the scintillator and deposits energy via ionization, it excites these π-electrons to higher energy states. As the electrons return to their ground state, the energy is released in the form of ultraviolet or visible photons, which constitute the scintillation light [88]. Figure 4.1a illustrates the excitation and emission processes involving π-energy levels in organic molecules. These molecules exhibit both *singlet (S_i)* and *triplet (T_i)* electronic states with distinct spin configurations. The de-excitation of these states leads to light emission via several channels. They can be distinguished by their timing relative to the initial excitation:

- **Prompt fluorescence**: Occurs within nanoseconds (ns) of excitation and constitutes the primary signal in most applications.
- **Phosphorescence**: Involves transitions from triplet to singlet states and occurs on much longer timescales (ms-s).
- **Delayed fluorescence**: Arises from thermal or triplet-triplet annihilation processes, and is typically suppressed in practical detector systems.

Prompt fluorescence arising from $S_1 \rightarrow S_0$ transitions dominates the detectable signal with typical emission wavelengths in the ultraviolet (UV) region around 350 nm for plastic scintillator material. The other two components are generally suppressed in the detector design. For typical scintillation detectors, the quantum yield η, defined as the number of photons generated per deposited energy, is $\approx 10^4$ photons/MeV [88].

A key property of scintillators is the *Stokes shift*, defined as the difference in energy between the absorbed (E_{abs}) and emitted (E_{em}) photons (illustrated in Fig. 4.1b).

$$\Delta E = E_{\text{abs}} - E_{\text{em}} = hc\left(\frac{1}{\lambda_{\text{abs}}} - \frac{1}{\lambda_{\text{em}}}\right) \tag{4.1}$$

where h is Planck's constant, c is the speed of light, and λ are the wavelengths of absorption and emission peaks, respectively. Since the emitted light typically has a lower energy than the absorbed radiation (typically by an order of $0.2 - 0.4$ MeV), the emission spectrum is red-shifted (shifted to longer wavelengths). This shift minimizes self-absorption by ensuring that the emitted photons are less likely to be reabsorbed, thereby increasing the effective optical attenuation length within the scintillator volume. A large Stokes shift is therefore desirable as it promotes efficient light transport within the scintillator material and ultimately improves detector performance.

Although the Stokes shift is naturally present in organic scintillators, the initial emission is typically in the near-ultraviolet (near-UV) range (300–400 nm), which is still subject to significant absorption within the scintillator material itself. To overcome this and further enhance the light output, the base scintillator material is usually doped with one or more

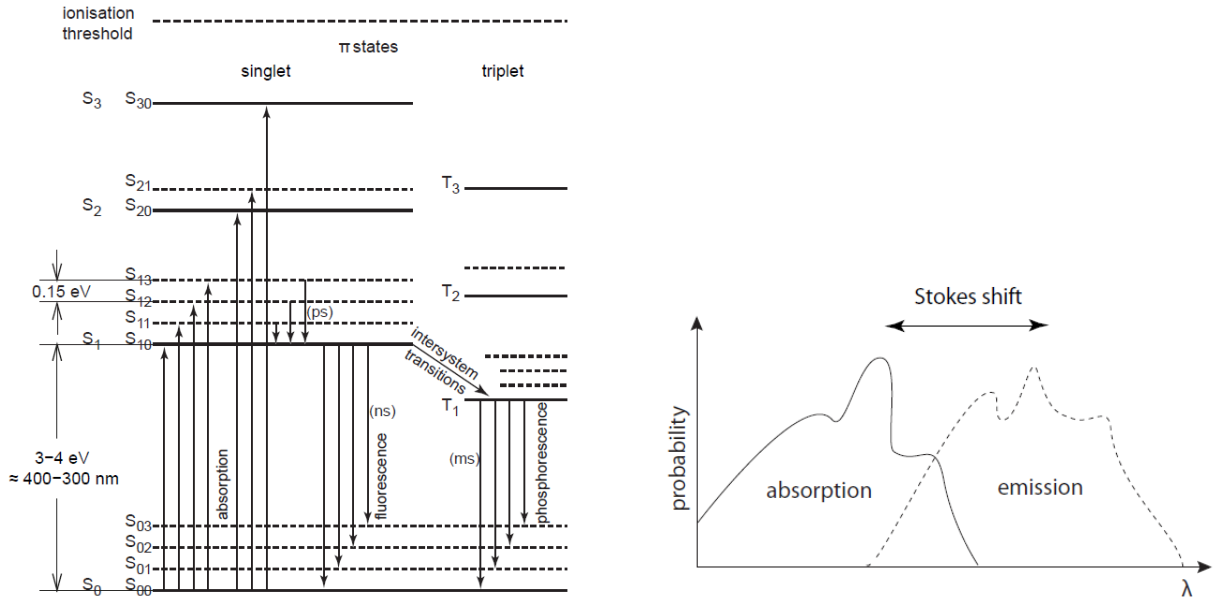

Figure 4.1: (a) Energy-level diagram of singlet and triplet states in organic scintillators indicating excitation and emission pathways. (b) Illustration of the Stokes shift, representing the spectral difference between absorption and emission maxima. Images adapted from [88].

wavelength-shifting fluorescent agents. This additional wavelength shifting marks the second step in the scintillation detectors' working mechanism.

The *primary fluor*, often referred to as the *first dopant*, is added to improve the light yield through the mechanism of *Förster resonance energy transfer (FRET)* [88]. This process relies on a spectral overlap between the emission spectrum of the base scintillator and the absorption spectrum of the primary fluor. The energy is non-radiatively transferred from the base material to the fluor, which then emits light at a longer wavelength, typically in the violet region (370-420 nm). The efficiency of the FRET transfer is given by:

$$E_{\text{FRET}} = \frac{R_0^6}{R_0^6 + r^6} \tag{4.2}$$

where R_0 is the Förster radius ($\approx$ 2-6 nm) i.e., the distance at which the energy transfer efficiency is 50% [89], and r is the donor-acceptor separation.

To shift the light further into the visible spectrum, a *secondary fluor* (or *second dopant*) is often employed. This fluor absorbs the violet emission from the primary fluor and re-emits it in the blue region (420-450 nm), which is better matched to the sensitivity range of common photo-detectors and has improved transmission properties in plastic media.

This multi-step wavelength shifting strategy not only improves the overall light yield but also facilitates efficient light collection and detection by reducing self-absorption and optimizing spectral compatibility with photo-detectors. The entire process is summarized in Fig. 4.2.

The detection efficiency of common photodetectors such as Silicon PhotoMultipliers (SiPMs) and PhotoMultiplier Tubes (PMTs) typically peaks in the wavelength range of 400–500 nm, corresponding to blue to green light. To optimize this spectral match and further improve light collection, wavelength-shifting (WLS) fibers are often embedded or coupled to the scintillator. These fibers, commonly made from materials such as *Y-11* (a type of green-emitting fiber), absorb the blue emission from the secondary fluor and re-emit it in the green region. This final shift ensures optimal transmission through the fiber and maximum sensitivity at the

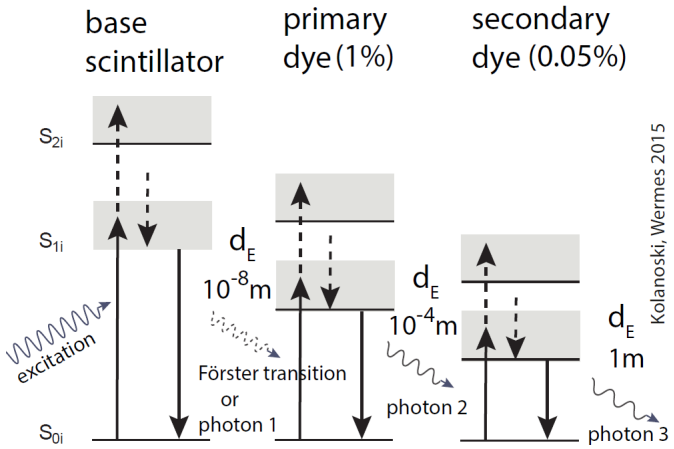

Figure 4.2: The mechanism of light emission at a higher wavelength with minimal re-absorption is shown as a three-step process. The base material radiatively transfers the emission to the first dopant, which then absorbs and re-emits it at a higher wavelength via the second dopant. The average spatial distance is indicated by d_E, which is smaller for the base to primary flour. Image from [88].

photo-detector level, thus enhancing the overall efficiency of the detection system.

4.1.2 Scintillator Readout Techniques

A final and crucial step of the scintillation detection is to convert the optical photons generated in the scintillation material into electrical signals. Secondary photon detectors are employed for this purpose. Common types of photodetectors include Photomultiplier Tubes (PMTs), Photodiodes, Charge-Coupled Devices (CCDs), and Silicon Photomultipliers (SiPMs) [88]. Each device offers trade-offs in gain, timing resolution, sensitivity, and operational complexity. In this work, we utilize SiPMs, which were selected for the readout of the SAE scintillators. Their compact size, low operating voltage, insensitivity to magnetic fields, and excellent timing resolution make them highly suitable for scintillator-based detection systems in high-energy physics. In addition, they are suitable for low temperature measurements due to their gain dependence and are sturdy for the adverse South Pole conditions.

Silicon Photomultipliers (SiPMs) are solid-state photodetectors composed of an array of Avalanche Photodiodes (APDs) operating in Geiger mode [90]. Due to this configuration, they are also referred to as Multi-Pixel Photon Counters (MPPCs). Each array consists of thousands of microcells (N), where each microcell comprises a single APD connected in series with a quenching resistor (R_q). All microcells are connected in parallel and share a common anode and cathode. When a photon strikes a microcell, it generates an electron-hole pair. If the applied bias voltage (V_{bias}) exceeds the breakdown voltage (V_{br}), a condition known as *overvoltage* (V_{ov}), the carrier initiates a self-sustaining avalanche. This produces a current pulse with a charge given approximately by:

$$Q_{cell} = C_{cell} * (V_{bias} - V_{br}) = C_{cell} * V_{ov}, \tag{4.3}$$

where C_{cell} is the cell capacitance, typically ranging from 20-100 pF. The over-voltage is usually set between $2 - 5\,V$. The integrated quenching resistor limits the avalanche and resets the microcell for subsequent photon detection by stopping the discharge and allowing the cell to recharge with a recovery time, $\tau = R_q * C_{cell}$, which is generally of the order of 10 ns. Figure 4.3(a) illustrates the working principle of an APD, showing the internal semiconductor structure and electric field profile. Figures 4.3(b) and 4.3(c) show a schematic representation

of an SiPM composed of multiple APD microcells, and a microscope image of a real SiPM array, respectively.

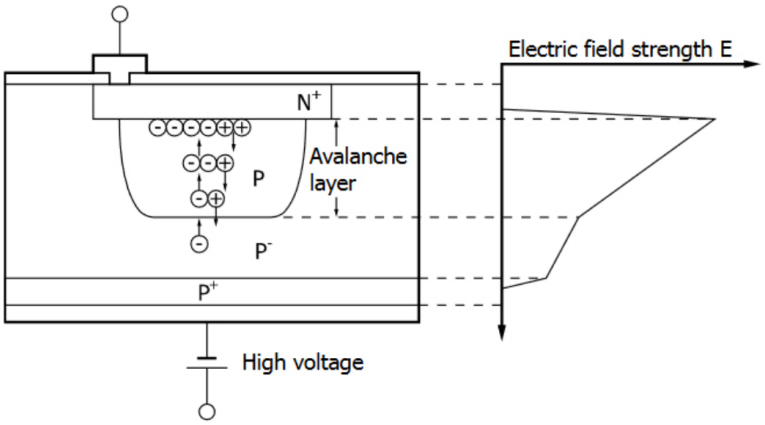

(a) Working principle of an Avalanche Photodiode (APD), showing the semiconductor structure, avalanche layer, and the electric field profile responsible for charge multiplication.

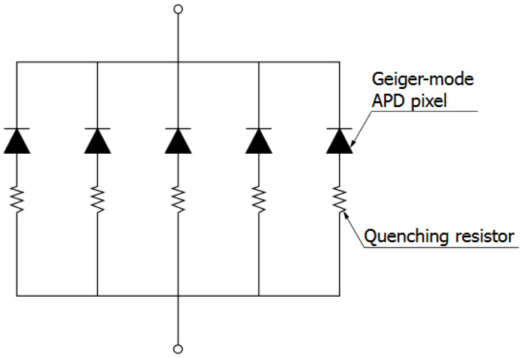

(b) Schematic of a Silicon Photomultiplier (SiPM), consisting of a matrix of APD microcells, each with an integrated quenching resistor.

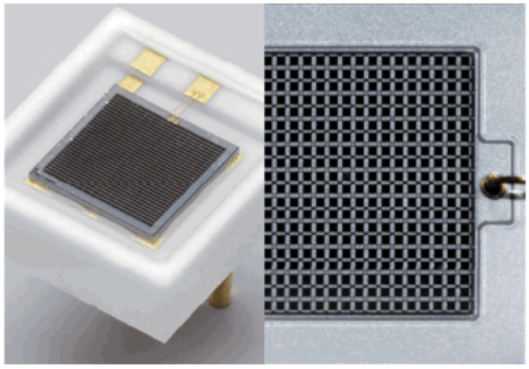

(c) Image of an SiPM chip, showing the regular grid of microcells responsible for single-photon detection.

Figure 4.3: (a) Internal operation of an APD; (b) SiPM circuit schematic; (c) Image of an SiPM device with hundreds of microcells [91].

The SiPMs provide a high gain per detected photon, of the order of $G = \frac{Q_{cell}}{e} \approx 10^6$ (where e is the elementary charge), enabling the detection of single photons. The Photon Detection Efficiency (PDE) of a Silicon Photomultiplier (SiPM) is given by

$$\mathrm{PDE}(\lambda, V_{\mathrm{ov}}) = \mathrm{QE}(\lambda) \times \varepsilon_{\mathrm{geom}} \times P_{\mathrm{Geiger}}(V_{\mathrm{ov}}), \tag{4.4}$$

where $\mathrm{QE}(\lambda)$ represents the wavelength-dependent quantum efficiency (typically peaking at 400–500 nm), $\varepsilon_{\mathrm{geom}}$ is the geometrical fill factor (50–70%) [91], and $P_{\mathrm{Geiger}}(V_{\mathrm{ov}})$ denotes the avalanche triggering probability that increases with overvoltage V_{ov}. PDE values generally range from 20% to 50%, optimized for the blue emission region of plastic scintillators. However, increasing V_{ov} also elevates noise contributions, including dark counts (thermally generated avalanches occurring at rates of 10^5–10^6 Hz/mm^2 at room temperature), optical crosstalk (secondary photon-induced avalanches in neighboring microcells), and afterpulsing (delayed avalanches due to trapped carriers). Furthermore, the SiPM breakdown voltage varies with temperature at approximately 20–50 mV/°C, which affects gain and PDE, necessitating thermal stabilization or active bias compensation for reliable operation.

Table 4.1 summarizes the key characteristics of common photodetector technologies for scintillator readout. It underscores the distinct advantages of SiPMs, such as compactness, low-

voltage operation, and magnetic field insensitivity, while noting their higher dark noise and temperature sensitivity compared to traditional photomultiplier tubes (PMTs).

Table 4.1: Comparison of photodetector technologies for scintillator readout.

Parameter	**PMTs**	**Photodiodes**	**CCDs**	**SiPMs**
Gain	10^6–10^7	∼1	N/A (imaging)	10^6
Operating Voltage	1000–2000 V	<100 V	<50 V	20–70 V
PDE Peak Wavelength (nm)	300–500 (UV–blue)	Broad	Broad (silicon)	400–500 (blue region)
Timing Resolution	∼1 ns	10–100 ns	ms range (slow)	100 ps–few ns
Size / Form Factor	Bulky, fragile tubes	Compact	Bulky optics	Compact, solid-state
Magnetic Field Sensitivity	Highly sensitive	Insensitive	Insensitive	Insensitive
Noise (Dark Count Rate)	Low	Very low	Very low	Moderate to high
Temperature Dependence	Moderate	Low	Low	High (requires compensation)

4.1.3 SAE Scintillators

Building on the working mechanism of scintillation detectors described in the previous section, this section will focus on their specific design for deployment at the South Pole as part of the Surface Array Enhancement (SAE). One of the installed scintillation detectors is shown in Fig. 4.4. More details on the hardware design and operation of the scintillators can be found in [85][77].

Figure 4.4: One of the deployed scintillation detectors of the Prototype station at the South Pole. Picture taken in January 2021.

Scintillator In-lay

The base unit of a scintillation detector is referred to as the *in-lay*. Each inlay consists of 16 plastic scintillator bars, fabricated at Fermilab [92, 93]. These bars are made of polystyrene (PS) as the base scintillation material, doped with 1% PPO and 0.3% POPOP as the primary and secondary fluors, respectively. Two kidney-shaped holes run longitudinally through each bar (Fig. 4.5 (right)) to accommodate wavelength-shifting (WLS) fibers, which collect the scintillation light generated in the bars. To enhance internal light reflection and guide photons efficiently to the WLS fibers, the bars are coated with a reflective titanium dioxide (TiO_2) layer of thickness 0.25 ± 0.13 mm. Each bar has dimensions of 0.05 m × 0.01 m × 1.875 m, resulting in a total active detector area of 1.5 m^2.

The WLS fibers used are Kuraray Y-11(300) [94], which absorb blue scintillation light ($\approx 430\,nm$) and re-emit it at longer wavelengths in the green region (peak at 476 nm) [94]. The emission spectrum of the scintillation material as well as the WLS fibres is presented in Fig. 4.6. The fibers have an attenuation length of approximately $4\,m$. A total of 32 fibers are routed symmetrically through the bars to ensure uniform light collection and signal response, as shown

Figure 4.5: Left: In-lay of the detector. Fibers are routed symmetrically with bends on either side in a way that ensures uniform light collection by keeping the length of each fiber the same. Right: Cross-section of a scintillator bar showing the two kidney-shaped holes for fiber routing.

in Fig. 4.5 (left). Fibers are routed in a special configuration with large bends at the ends to minimize stress and to achieve equal lengths, which in turn contributes to the uniformity of the detection unit. Some extra slack in the fibre length before coupling to the SiPM is intentional. This allows the emitted light from the WLS fibers to spread more uniformly in time and space, which in turn helps mitigate the effect of particles hitting the detector close to the SiPM, which would otherwise cause a sharp, localized signal and compromise the spatial uniformity of the response.

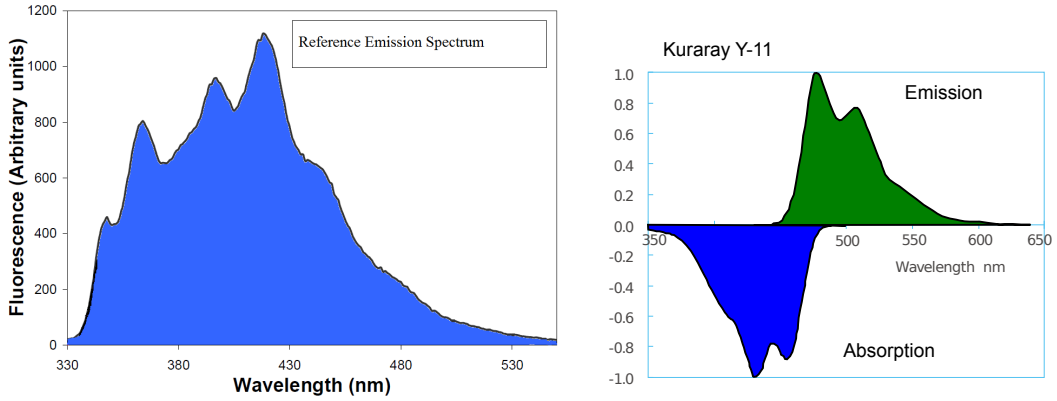

Figure 4.6: Left: The emission spectrum of the extruded scintillation bars used in the SAE scintillators. Right: The emission spectrum of the WLS fibres after absorption from the scintillation bars [95].

Scintillator readout: SiPM

The WLS fibers are coupled to a silicon photomultiplier (SiPM) using a PMMA optical coupler. The fibre bunch is glued onto the active area of the SiPM as shown in Fig. 4.7. This configuration results in minimal positional sensitivity in the detectors, since all light from the fibers is summed onto a single SiPM without individual readout.(left). The SiPMs used are Hamamatsu S13360-6025PE [90], which are multi-pixel photon counters (MPPCs) with a photosensitive area of 6×6 mm^2 and a pixel pitch of 25 μm. This SiPM features 57600 microcells. Each SiPM is mounted on a small PCB alongside a temperature sensor. This assembly is referred to as a *cookie board* (Fig. 4.7(right)) [96].

SiPM readout board: uDAQ

Electrical signals from the SiPMs are read out by a microprocessor-based acquisition board called the microDAQ or uDAQ [85], shown in Fig. 4.8. This board digitizes the analog information from the SiPMs, enabling fast response times and controlling the data rate to support the future veto for the IceTop and in-ice components. Recording analog waveforms from every

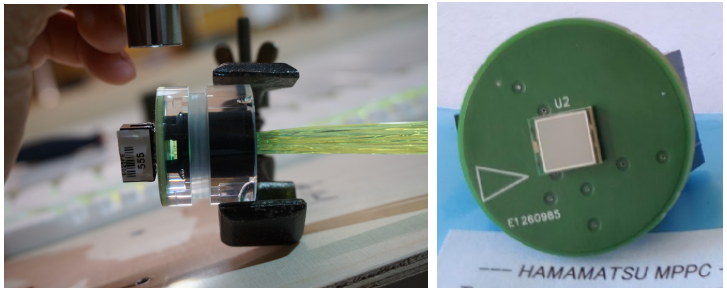

Figure 4.7: Left: Shows the coupled fibres to the SiPM. The clear acrylic holding structure is the PMMA coupler. The extruded pins on the left are the connectors from the SiPM and the temperature sensor. Right: A cookie board incorporating the SiPM and a temperature sensor for temperature readout.

single hit would generate enormous amounts of data and significantly slow down processing. Digitizing the output directly at the detectors helps avoid this issue. The final version of the uDAQs deployed in the SAE scintillation detectors is the uDAQ v4.1a. A schematic of this readout board is provided in Fig. 4.9. The temperature from the temperature sensor of the cookie boards is also read out and converted to Kelvin units using the uDAQ. The SiPM signal is amplified through three gain channels for a wider dynamic range and shaped using a linear RLC network. The shaped output signal, V_{out}, features a flat top of approximately 100 ns and returns to baseline within about 500 ns. Its amplitude is linearly proportional to the number of detected photoelectrons. The signal is digitized using 12-bit sample-and-hold ADCs, with tunable (but interlinked) sampling delays across channels. The timing information is extracted using a discriminator and a 180 MHz counter linked to the White Rabbit, resulting in 5.5 ns resolution. This resolution is further improved to $\sim$1 ns using a chain of eight delay lines. When the signal crosses the threshold, a trigger is sent to the central DAQ to read out radio antennas, in case of a coincidence in trigger from a defined multiplicity of scintillators (often used 5 or more) within a configurable coincidence window (currently used 1 μs). uDAQ supports two acquisition modes:

- **Hitbuffer Mode**: In this mode, for each particle interaction, the timestamp, the charge of the pulse for all three amplifications, and whether the measured pulse was CPU-triggered or signal over threshold are recorded. A CPU-triggered pulse called the Fixed Rate Trigger (FRT) is also saved per second to facilitate baseline studies.

- **Histogram Mode**: In this mode, the charge of the pulses is saved as a histogram in the buffer of the microprocessor, so this charge histogram is already built on uDAQ, allowing longer measurement runs for calibration purposes.

Detector Shielding

For mechanical stability, the scintillation bars are supported first by a wooden plate and additionally using Styrofoam sheets, which provide both cushioning and a lightweight structural base (Fig. 4.10a). To prevent any light contamination, the entire detector assembly is made light-tight using a black ESD (Electrostatic Discharge) foil. The foil is vacuum sealed, and the edges are welded. Since SiPMs are extremely sensitive to even single incident photons, ensuring complete light isolation is crucial to avoid false signals or elevated noise caused by external photons. Any stray light entering the system could be indistinguishable from true scintillation events, thereby compromising the integrity of the data. The light-tight assembly is enclosed in an aluminum casing, which provides additional mechanical protection and also

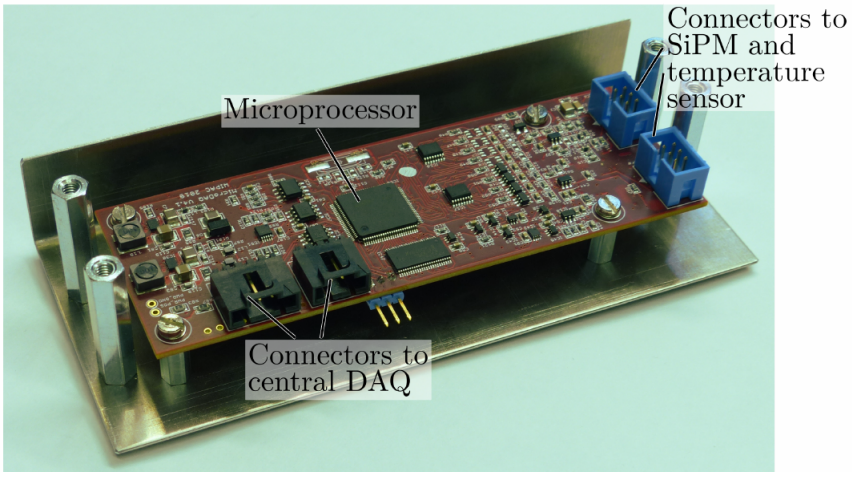

Figure 4.8: A picture of a microprocessor-based uDAQ v4.1a used for SiPM readout. The power supply and communication to the central DAQ of a single detector are established using the black connectors. The blue connectors are coupled to the temperature and SiPM sensors on the cookie board.

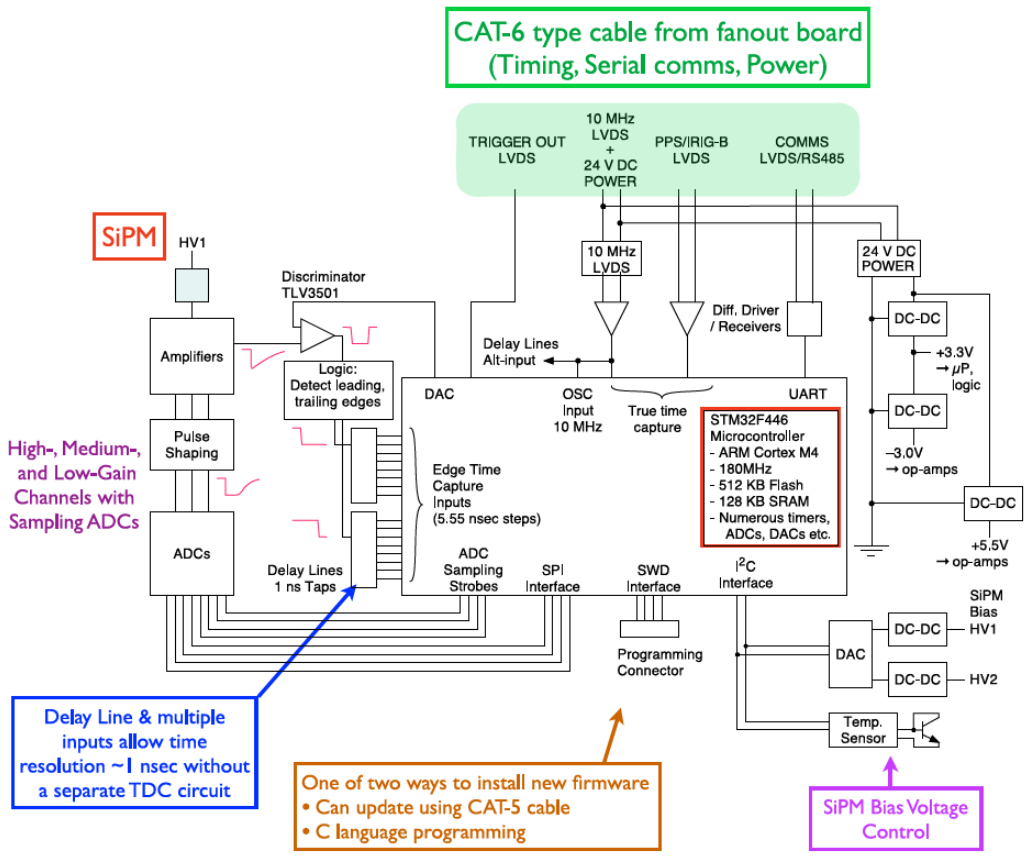

Figure 4.9: Schematic explaining the signal processing from the cookie board by the uDAQ. Both temperature and SiPM signals are processed by the uDAQ. The signal from the SiPM is amplified in three gain channels and shaped using an RLC network. The timing is maintained using the discriminator output.

serves as the electrical ground. Power and communication cables are routed through dedicated connectors mounted on the casing, maintaining both signal integrity and environmental

sealing. Fig. 4.10b shows the light-tight scintillators placed in the aluminum housing.

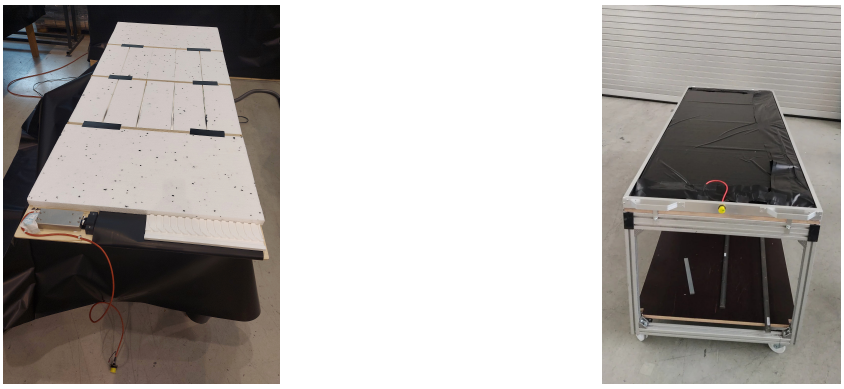

(a) **(b)**

Figure 4.10: (a) Scintillator inlay with styrofoam to add a safety layer to the scintillation bars and optical fibers. (b) A scintillator (placed on a movable table) after being vacuum sealed in the ESD foil and coupled to the aluminum casing.

4.2 Series Production

As part of this thesis work, a total of 99 scintillation panels were produced and tested for deployment in the period from 2021 to 2022. These included scintillation detectors for seven stations destined for the South Pole, four R&D stations, and additional panels reserved for future deployments. A production effort of this scale requires a well-defined, multi-step process and the collaboration of an entire team. The main steps involved in the production chain have been defined as follows.

- **Component Testing:** The electrical components of the scintillation detectors, SiPM and uDAQ, are tested before incorporating them in the final assembly. The SiPMs are tested in a dark chamber, called the SPOCK(Single PhOton Calibration Stand at KIT) [96], to investigate for dark-spectrum irregularities, if any, as well as the dark-current response to variable voltage, which would exhibit the SiPM's breakdown behavior. The uDAQs are tested for communication and functionality in the whole temperature range of $+40$ to $-70°C$. Only components that pass these quality checks proceed to the next production step.

- **In-lay Preparation:** The second step involves the preparation of the scintillation detector inlay. This preparation involves gluing the SiPMs to the PMMA coupler, in parallel to preparing the scintillation bars on the wooden base and routing the optical fibers through them. The process concludes with the precise coupling of the fiber bundle to the SiPM's active area and takes 2 days to complete. This step was carried out with the help of Murat Toron and Michael Riegel.

- **Mechanical Assembly:** During the final assembly of the detectors, the uDAQs are installed and connected to the cookie boards. Styrofoam sheets are added on top of the scintillator bars for support. The modules are then sealed to ensure light tightness by using a black ESD foil, which is vacuum sealed, followed by welding the foil edges. The entire structure is placed in an aluminum casing, with the main cable connection via a military grade plug for output. This is followed by riveting and gluing of the casing edges to complete the mechanical enclosure, making it water/moisture tight as well.

- **Performance Validation:** Each completed module undergoes a rigorous validation, which includes histogram measurements, hit buffer measurements, threshold scans, and coincidence measurements to trigger the radio counterpart. These procedures verify the signal quality and confirm the operational readiness of the detectors.

(a)

(b)

Figure 4.11: Fully assembled scintillation detectors during the qualification phase. (a) Production overview. Various stages of series production are presented with pictures. (b)33 scintillation detectors post production in the validation stage.

Contributions were made to all stages of the production process throughout this work (Fig. 4.11a). In particular, the calibration of the SiPMs and the qualification of each scintillation module were carried out independently. Figure 4.11b shows 33 fully assembled scintillation detector modules ready for the final stage of testing and verification. The following sub-sections will present more details on the single-component calibration as well as the full module verification.

4.2.1 SiPM Calibration

Since the Silicon Photomultipliers (SiPMs) constitute the core photodetectors in the SAE scintillator modules, ensuring their operational integrity is critical. Comprehensive investigations into the temperature dependence of SiPM performance parameters such as photon detection efficiency (PDE), dark count rate (DCR), crosstalk probability, and afterpulsing for the chosen SiPM model have been conducted in earlier dedicated studies [97]. Consequently, the focus

during series production was on verifying the baseline functionality and electrical behavior of individual SiPMs under dark conditions and at room temperature.

The measurement campaign employed the setup illustrated in Fig. 4.12, incorporating an analog front-end readout board named IceARM, developed at KIT for initial scintillator characterization [96], and also used at the South Pole for the first prototype station [77]. The IceARM board is capable of acquiring analog waveforms from the SiPMs with high fidelity. Communication and control were facilitated via an RS485 interface, with a Python-based control firmware executed on a local host computer. This interface enabled remote configuration of the SiPM bias voltage and acquisition parameters. A TTI EL302D dual-output power supply of $\pm 5\,\mathrm{V}$ was used to operate the IceARM board, and an oscilloscope was employed to visualize the analog output from the SiPMs. The SiPM, along with the readout board, was placed inside a light-tight chamber called SPOCK, and all measurements were performed in the dark conditions with no incident light and at room temperature. The results of the tests performed to evaluate SiPM performance are discussed in the following sub-sections.

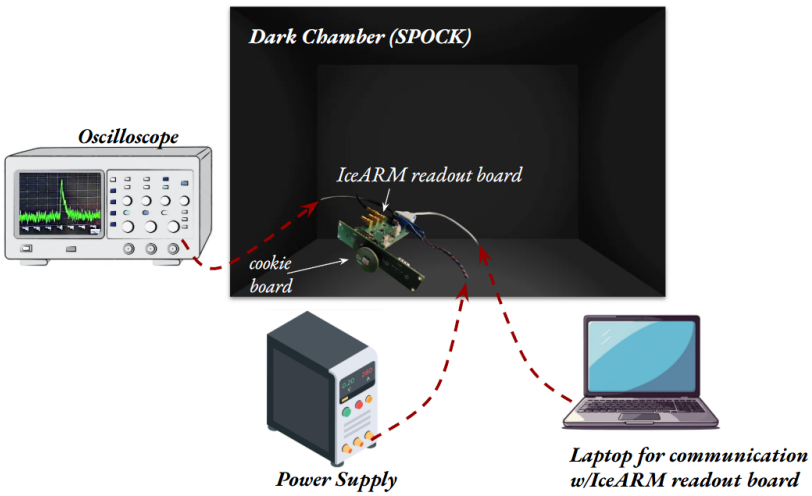

(a) Diagram of the measurement setup and associated components.

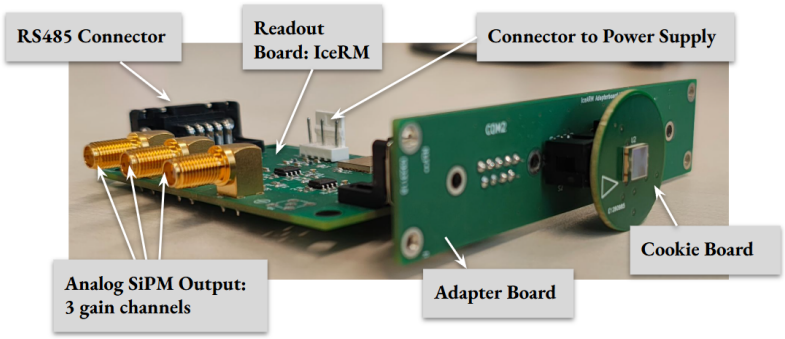

(b) Close-up of the IceARM readout board and its components.

Figure 4.12: Measurement setup used for the SiPM calibration is presented. The IceARM board, along with the SiPM board, was placed inside a light-tight chamber called SPOCK. An oscilloscope was used to analyze the analog signals from the high-gain of the readout board. (a) Presents a diagram of the setup and the components used; (b) shows a close-up of the IceARM readout board and its respective components. An adapter board is used for the connection between SiPM board and the readout board [96].

Dark Spectrum

The initial stage of SiPM calibration involved analyzing thermally generated pulses under dark conditions. Waveforms were captured using a Teledyne LeCroy high-bandwidth digital oscilloscope, triggered at $\approx$ 5 mV threshold corresponding to approximately a single photo-electron (1 p.e) event for the SiPM. Both single-peak charge spectrum and the persistence mode charge spectrum acquisition were employed to characterize the temporal response and assess the SiPMs' performance. Single event traces (Fig. 4.13) were exported as CSV data and analyzed using a custom Python script. The waveform was modeled with a bi-exponential function (4.5) describing the avalanche buildup and quenching behavior.

$$f(t) = \begin{cases} 0, & \text{for } t < t_0 \\ A\left(1 - e^{-\frac{t-t_0}{\tau_{\text{rise}}}}\right) e^{-\frac{t-t_0}{\tau_{\text{fall}}}}, & \text{for } t \geq t_0 \end{cases} \tag{4.5}$$

In this equation, A corresponds to the amplitude of the thermally generated dark spectrum peak, and τ_{rise} and τ_{fall} correspond to the rise and fall time of the peak, respectively. A fit to this functional form yields a rise time τ_{rise} of approximately 4.6 ns and a fall time τ_{fall} of about 49.9 ns for the presented waveform in Fig. 4.13. These values are consistent with expectations for the S13360 series SiPMs, taking into account the influence of analog front-end shaping and electronics response. The fitted peak amplitude of 9.8 mV indicates a clean isolated dark count. The absence of a long tail or secondary components implies that high time-resolution triggering is feasible at the sub-nanosecond level if proper leading-edge discriminators are used.

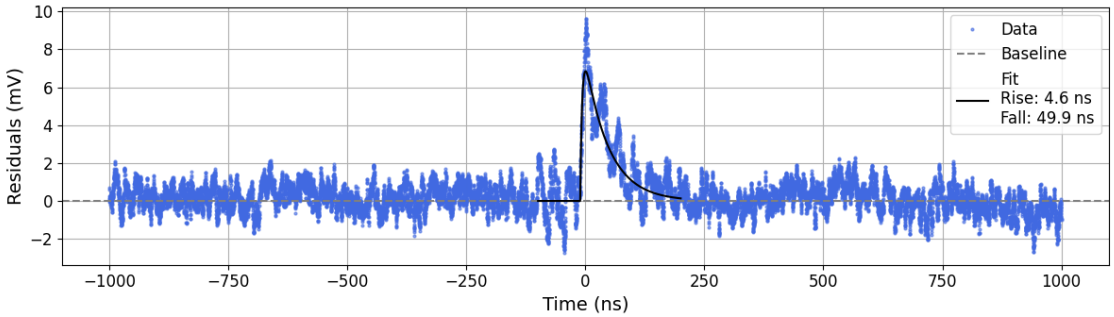

Figure 4.13: Single event dark pulse waveform from a Hamamatsu S13360-6025PE SiPM. The blue trace is oscilloscope data, while the black curve is a fit performed to the data using a bi-exponential pulse shape. Extracted parameters: rise time $\tau_{\text{rise}} = 4.6$ ns, fall time $\tau_{\text{fall}} = 49.9$ ns. Fluctuations in the baseline of ± 2 mV are observed, which suggest origins in the electronics of the measurement setup.

To assess statistical stability and noise behavior, the oscilloscope was also operated in the persistence mode, capturing thousands of dark pulses overlaid on a single screen (Fig. 4.14). In this view, each waveform trace is color-coded by frequency of occurrence (red corresponds to the most frequent and violet corresponds to the least frequent). The vertically collimated nature of the leading edge confirms low jitter and a highly reproducible breakdown initiation. The trailing edge shows consistent exponential decay, slightly broadened due to analog noise and minor baseline fluctuations.

The absence of distinct higher-amplitude tracks suggests that prompt optical crosstalk is minimal, while the lack of post-pulse echoes or delayed shoulders indicates negligible after-pulsing activity. The noise band with a vertical spread of ± 2 mV around the baseline agrees with the baseline fluctuations seen in single event traces. These findings collectively demonstrate that the SiPM is operating in a clean, low-noise breakdown regime under dark conditions, with

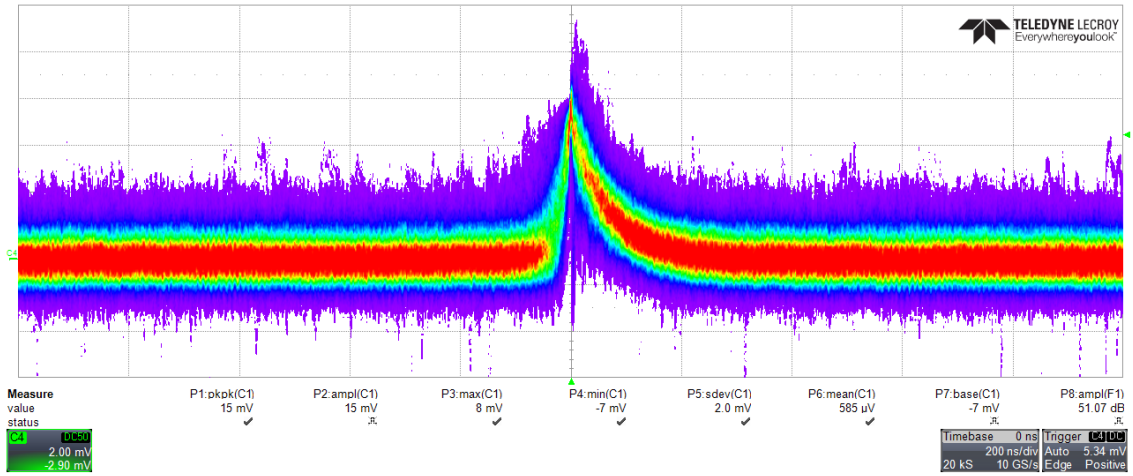

Figure 4.14: Persistence-mode oscilloscope capture of dark pulses. Each waveform is overlaid with color indicating frequency of occurrence (red = most frequent). The narrow, consistent leading edge confirms reproducible timing response, while the symmetric decay suggests low correlated noise and minimal after-pulsing.

good gain uniformity and minimal correlated noise.

Current-Voltage (IV) Characteristics

The second stage of SiPM calibration involved characterizing the dark current response to reverse bias voltage. For each of the 99 SiPMs, reverse IV measurements were performed across the 55–75 V range in 0.1 V increments. To ensure statistical reliability, each measurement was repeated three times. Fig. 4.15 demonstrates consistent IV behavior across all 99 SiPMs. The color bar represents the tested SiPM-IDs. Low leakage current below breakdown and a sharp rise in current, indicating avalanche onset, is clearly visible. The plotted data points represent the mean measured current, while the error bars denote the standard deviation across the three repetitions. These uncertainties were propagated into the fitting procedure.

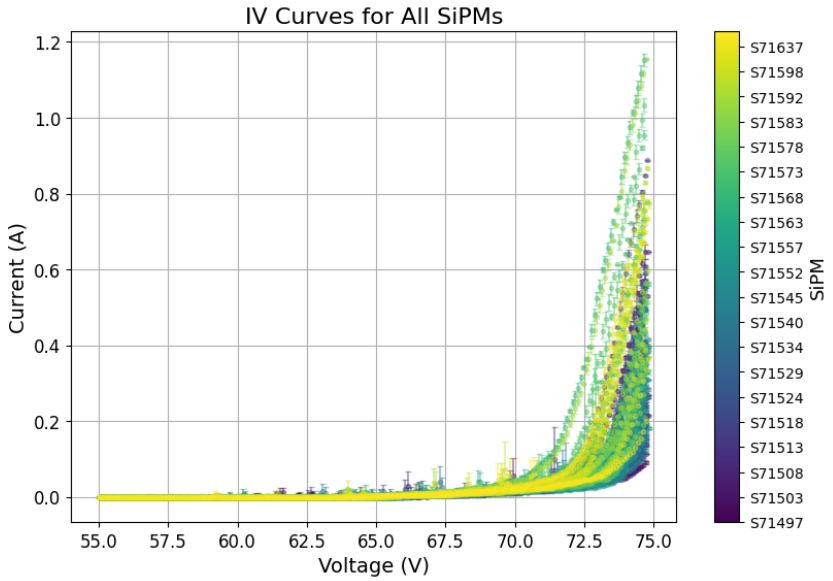

Figure 4.15: IV curves for 99 SiPMs. Each SiPM was measured 3 times, and the error bars represent the measured deviation in these repetitions.

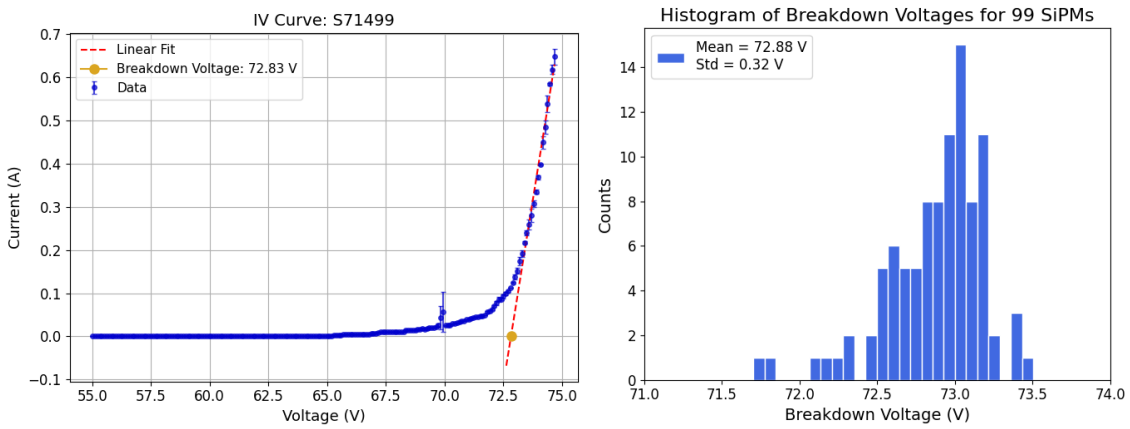

(a) **(b)**

Figure 4.16: Reverse IV characterization of the SiPMs. (a) Fit to post-breakdown region of one SiPM (b) Histogram of breakdown voltages. The SiPMs are observed to behave uniformly with their breakdown voltages in the range of 71.7-73.5 V

A linear fit was performed on the post-breakdown region, using the standard deviation at each point as weights. The intersection of this linear region with the pre-breakdown baseline defines V_{bd}. Fig. 4.16a shows the breakdown voltage (V_{bd}) extraction for one of the SiPMs, namely S71499. This procedure is carried out for all the SiPMs. The histogram in Fig. 4.16b shows a mean breakdown voltage of 72.88 V with a standard deviation of 0.32 V. The narrow distribution between 71.7-73.5 V highlights the uniformity of the SiPMs. Deviations from the mean are attributed to variations in room temperature during measurements, as V_{bd} is known to be temperature-sensitive. The observed uniform slope of the IV curves above breakdown indicates stable avalanche gain and consistent quenching resistor values across the SiPMs. In addition, post-breakdown, linearity, and tight error bars suggest reliable device response and reproducibility in the measurement procedure.

Out of 100 tested SiPMs, one (1%) was excluded due to a premature current rise before the expected breakdown region, likely indicating a defect or leakage path. The IV characteristics for this SiPM is shown in Appendix A.1. This analysis confirms a 99% success rate in device qualification based on IV performance.

4.2.2 uDAQ validation

The uDAQs undergo preliminary testing post-production before being sent to KIT for scintillator assembly [98]. To further evaluate the robustness of the uDAQs under thermal stress, a series of tests are conducted pre-assembly. A climate (temperature) chamber from Vötsch [99] was used for these measurements. Figure 4.17 shows the temperature chamber used during testing with the uDAQs placed inside. The details regarding the uDAQ validation tests are mainly from [100]. The validation measurements are as follows:

- The uDAQs were first subjected to two temperature cycles in a temperature chamber, ranging from +40 °C to −70 °C. No external electrical connections were added during these cycles, as the primary objective was to assess the mechanical reliability of the solder joints under repeated thermal expansion and contraction. Silica gel packets were placed inside the chamber to absorb any moisture during the temperature cycling.

- Secondly, a communication stability test was conducted on each of the uDAQs. During this phase, the devices were reprogrammed using the uDAQ firmware, and the print-time

diagnostic function was executed on each module to verify consistent communication performance.

- Finally, throughout the thermal cycling process, both a 30-second hitbuffer measurement and a histogram measurement were performed using the uDAQ software. A pulser provided periodic test signals to evaluate the above-threshold response. Communication and data acquisition were handled by a previously temperature-tested central DAQ system (TAXI), located outside the climate chamber and connected via external feedthroughs. Acquisition was controlled by a bash script, and a dedicated processing script was used to verify data integrity by computing checksums [101] for each binary data frame to identify any corrupted files. Although the short acquisition duration did not yield statistically significant results, the presence of valid, uncorrupted data confirmed proper communication and functional operation of the system during the tests.

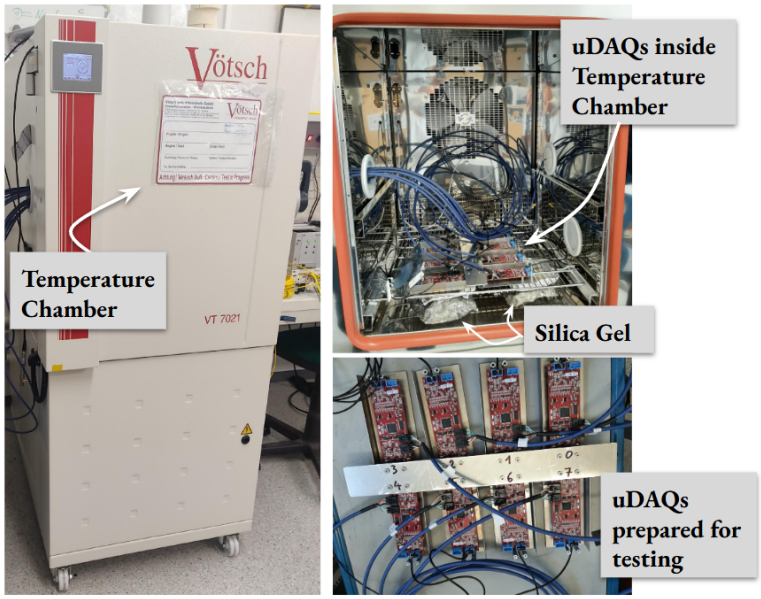

Figure 4.17: Photograph of the Vötsch VT7021 climate chamber with uDAQs placed inside for thermal cycling. The uDAQs are tested in batches of eight. A temperature-tested central DAQ system is used to perform communication measurements in a configuration similar to that deployed at the South Pole. The central DAQ is located outside the chamber.

4.3 Test Bench for Scintillators' Validation

Following the assembly of the scintillation detectors, a validation procedure was conducted to ensure their functionality and quality. Since Karlsruhe does not share the atmospheric and topographic conditions of the intended deployment site, *South Pole*, investigatory measurements were carried out at KIT to assess detector performance under local conditions and to define the requirements for a suitable test bench post production. These preliminary studies focused on analyzing the charge histograms measured by the scintillation detectors to identify the interaction peak corresponding to Minimum Ionizing Particles (MIPs).

The first measurements were conducted in the SPOCK lab, where the SiPM and uDAQ systems underwent validation. These tests aimed to assess environmental noise levels, considering the lab's location within a concrete building and its proximity to other experimental setups. Figure 4.18a shows the measurement setup in the SPOCK lab, which included a TAXI and a

WR-Node controlled by a WR-switch to provide timing synchronization. A voltage of +24 V was supplied using a dedicated power box, and the TAXI system was controlled via Ethernet. The tested scintillators were placed on top of the SPOCK chamber, replicating the full data acquisition chain as expected at the South Pole post-deployment.

Figure 4.18b shows a charge histogram recorded in this environment using a newly assembled panel. Although the histogram displays recorded particle hits and the expected low-ADC peak from the Fixed Rate Trigger (FRT) around 250 ADCs, the characteristic MIP peak was not clearly discernible. This suggested either an elevated environmental background noise or a malfunctioning detector.

In contrast, Figure 4.18c displays a reference histogram obtained from a previously validated prototype panel, measured at the Physical Sciences Lab (PSL) in Wisconsin under a similar configuration but with significantly improved shielding, using a custom freezing container. Before deployment, all scintillation panels are calibrated in this facility at low temperatures. The reference measurement shown here was performed at room temperature (approximately 25°C), comparable to the conditions at KIT. It represents a 110-second acquisition in histogram mode. The resulting charge spectrum exhibits the expected features: a small initial peak from the FRT, followed by a sharp rise due to integrated dark noise and ambient electromagnetic background, decaying exponentially. The prominent peak near 700 ADC units corresponds to the MIP signal, which is expected to follow a Landau-like distribution, characteristic of energy deposition from charged particles in scintillation material.

As shown by the observed and expected histogram in Fig. 4.18, the histogram obtained at KIT using the newly assembled scintillation detectors indicated a significant level of background contamination or the possibility of the detector not working as expected. This prompted a series of follow-up tests in different environments to determine whether the new panels were operating correctly. For this purpose, two newly manufactured scintillation detectors in 2021 and one older panel originally deployed in the 2017 South Pole prototype station and known to have successfully recorded air shower data, were tested under varied conditions. The 2017 panel, which used an older SiPM and readout board, was upgraded with the uDAQ V4.1a for these investigations. The motivation behind using a previously functional panel was to have a comparison in identical environments between the two generations and observe if their behavior differed outside of expectation.

Field Tests

The 3 panels were tested in a series of field tests. These included low temperature measurements in a freezing facility and measurements conducted in a remote location near a lake. The measurements conducted in each configuration are summarized in the Table 4.2. The main findings from the histogram measurements of the field tests for the 3 panels are discussed below. The details of the supplementary measurements will be included in the Appendix A.2.

Low-temperature measurements (at −10 °C and −20 °C) were carried out in a freezer facility at the Thermodynamics Department of KIT [102]. Figure 4.19 shows the experimental setup inside the freezer, located in the basement of the building. The three scintillators were arranged in a hodoscope configuration and connected to the TAXI data acquisition system. The scintillators are referred to as panels 0, 1, and 2 from bottom to top, with the top panel (panel 2) being the 2017 benchmark panel. A 70 m cable was used to connect each scintillator to the TAXI. A portable power supply provided a +24 V bias, while a White Rabbit switch and node ensured PPS-precise timing.

Figure 4.20 presents charge histograms measured at −10 °C for the three panels using the high-gain channel. All three panels show a clear pedestal and visible SPE peaks, while the MIP peak is suppressed. The measured gain at this temperature for the three panels is 20, 28,

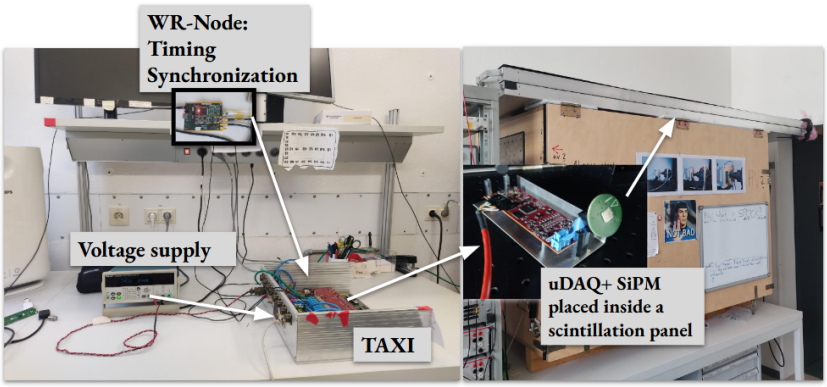

(a)

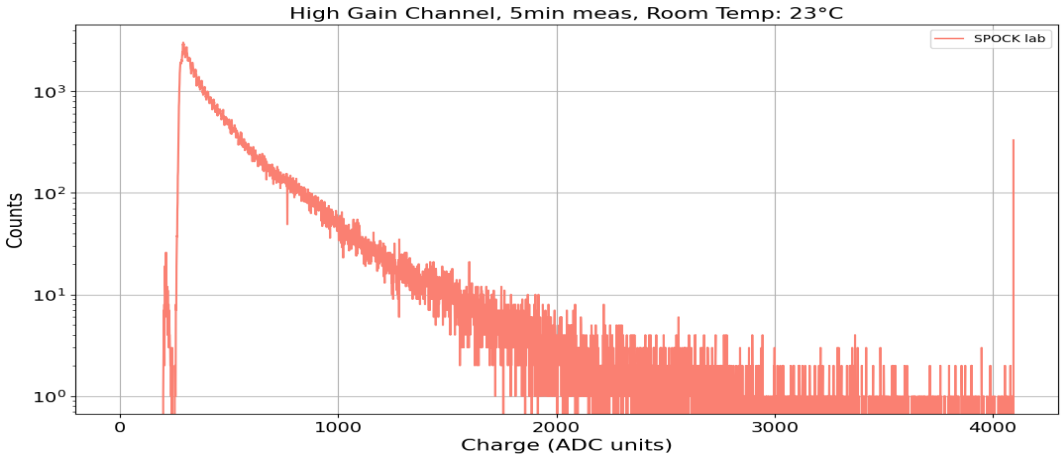

(b)

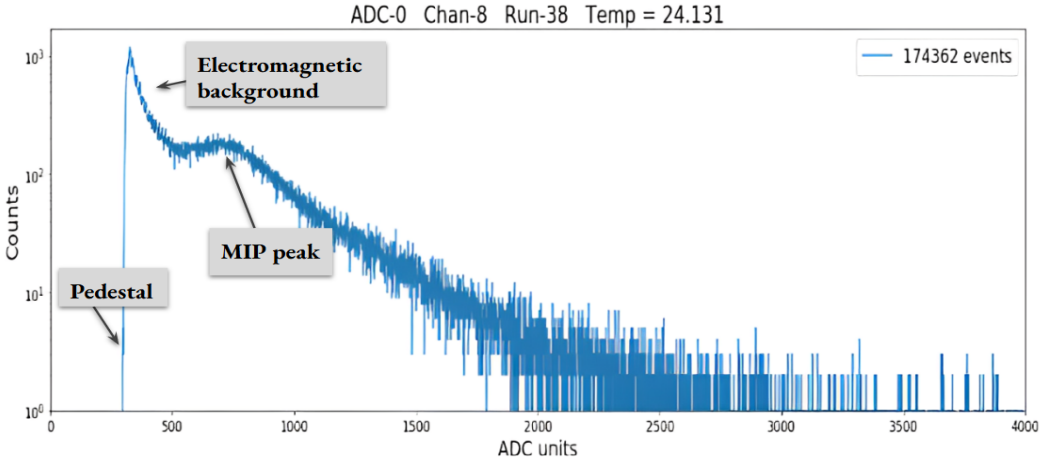

(c)

Figure 4.18: Validation and comparison of scintillator panel performance. (a) Measurement setup in the SPOCK lab at KIT. The panel is placed on the SPOCK chamber and connected via the full acquisition chain, including a TAXI, WR-Node, and +24 V power supply. (b) Charge histogram recorded with a newly assembled panel at KIT under local lab conditions. The MIP peak is barely visible, likely due to the environmental background. (c) Reference charge histogram from a validated prototype measured at PSL. The MIP peak is clearly visible, showing expected energy loss behavior.

and 25 ADC units, respectively. The 2017 panel (topmost) uses a 50 μm-pitch Hamamatsu SiPM, which exhibits lower gain compared to the 2021 panels. To highlight the features of the charge histograms, a scaled version is also shown where the counts are multiplied by ADC^3.

Table 4.2: Overview of measurements conducted during the field tests

Configuration	Type	Description
Low Temp and Lake	Long Histogram meas.	5-minute Histogram measurements at settings: AUXDAC2650, DAC1350
Low Temp and Lake	Long Hitbuffer meas.	5-minute long Hitbuffer meas.s at settings: AUXDAC2650, DAC1350
Low Temp and Lake	Short Histogram meas.	120s long histogram meas. at different DAC threshold values: 0, 1200-1500 in 50 ADC steps, and 4095 DAC units
Low Temp and Lake	Voltage Scan	120s long hitbuffer meas. for a range of AUXDAC values (corresponding to bias voltage):2550-2700 in ADC units
Low Temp	Threshold Scan	110s long Hitbuffer measurements covering the entire threshold range of 0 to 4095 ADCs

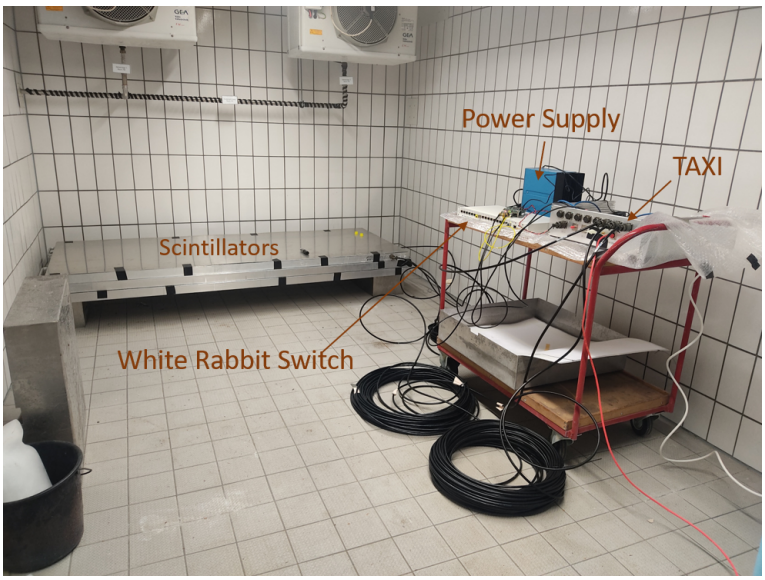

Figure 4.19: Measurement setup for the low-temperature tests in the freezer facility.

After scaling, the MIP bump in the 2017 panel becomes distinguishable, benefiting from the additional shielding provided by the lower two (2021) panels. Although the MIP bump is also present in the 2021 panels, it is less pronounced. The suppression is attributed to the location of the freezer facility, which, being underground and surrounded by concrete, provides significant shielding from cosmic rays and minimizes background contributions.

The low temperature measurements aimed to characterize the SiPM gain at low temperatures by resolving the single photoelectron (SPE) peaks. The gain of a SiPM is inversely proportional to temperature, so the spacing between adjacent SPE peaks directly provides the gain. An increase in gain at lower temperatures results in a shift of the MIP peak in the charge spectrum to higher ADC channels. Figure 4.21 shows the SPE peaks for one of the 2021 panels at both temperatures. Gaussian fits were performed for each peak, and the distance between adjacent means yields the gain. The gain increases by approximately 1.4 ADC units with a 10 °C drop in temperature, confirming the expected temperature dependence.

The measured gains for all three panels at both temperatures are summarized in Table 4.3.

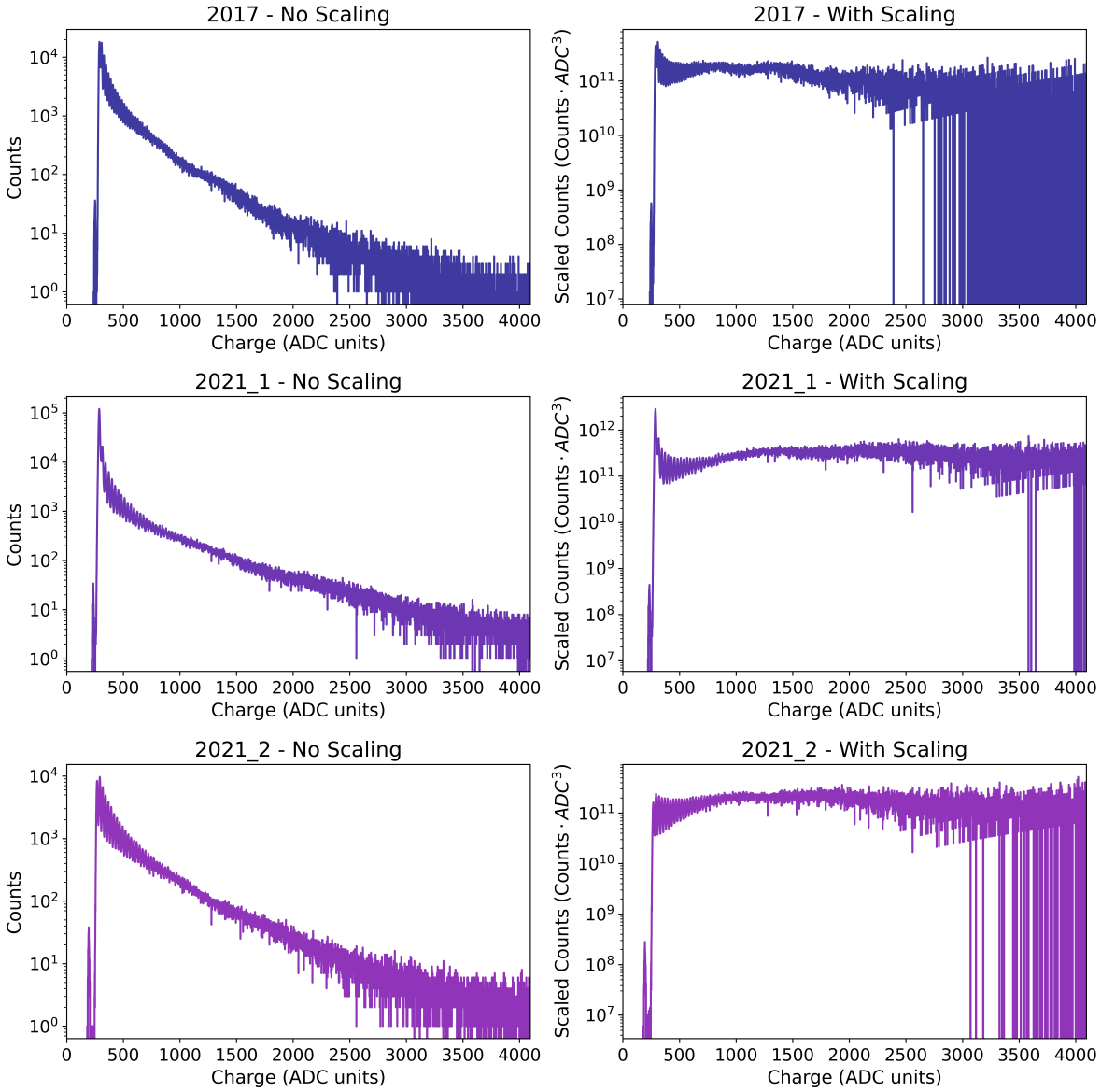

Figure 4.20: Charge histograms for the three scintillator panels at $-10\,^{\circ}\mathrm{C}$, both unscaled and scaled (counts $\times\, ADC^3$) to enhance feature visibility.

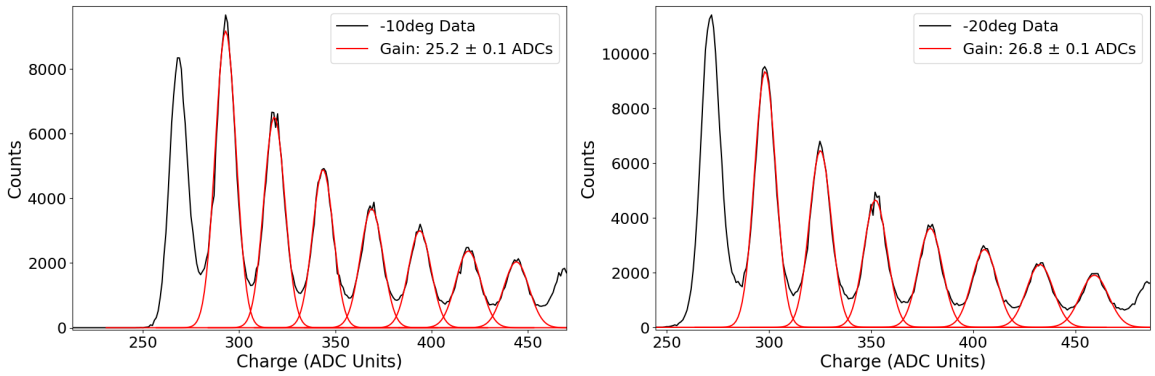

Figure 4.21: SPE peaks for one of the 2021 panels at $-10\,^{\circ}\mathrm{C}$ and $-20\,^{\circ}\mathrm{C}$.

These measurements confirm the expected functionality of the detectors at low temperatures, although elevated background noise was observed.

Table 4.3: Measured SiPM gain at $-10\,°C$ and $-20\,°C$

Panel ID	Gain at $-10\,°C$ (ADC)	Gain at $-20\,°C$ (ADC)
2017, P0	20 ± 0.1	21.8 ± 0.1
2021, P1	28.1 ± 0.2	29.4 ± 0.1
2021, P2	25.2 ± 0.1	26.8 ± 0.1

Lake Measurements were conducted at ambient conditions (approximately $22\,°C$) following the completion of low-temperature testing. These measurements were carried out at a remote location near Eggenstein, a small lake at a distance of $12\,km$ from the north campus of the Karlsruhe Institute of Technology (KIT). The site was chosen to minimize environmental and anthropogenic background, such as electromagnetic interference and secondary radiation from nearby infrastructure, which could otherwise compromise the quality of the recorded data.

To ensure consistency and facilitate comparison with previous measurements, the experimental procedure was replicated as closely as possible. The full setup, shown in Fig. 4.22, was installed within a "mobile laboratory" van. This vehicle served both as a means of transportation and as a controlled environment for operating the sensitive scintillation detectors. Power for the data acquisition system was provided via the van's onboard battery, eliminating the need for external power sources and thereby reducing the risk of introducing electrical noise or grounding issues.

A direct interface between the TAXI data acquisition system and a laptop allowed for real-time monitoring and data logging. The scintillation detectors were arranged in a hodoscope configuration, with the 2017 panel placed on the bottom in these measurements. To reduce background from ground-level radiation and to replicate the geometry of laboratory measurements, the detector assembly was elevated on a non-conductive wooden support and positioned in an open area near the lake, as illustrated in Fig. 4.22.

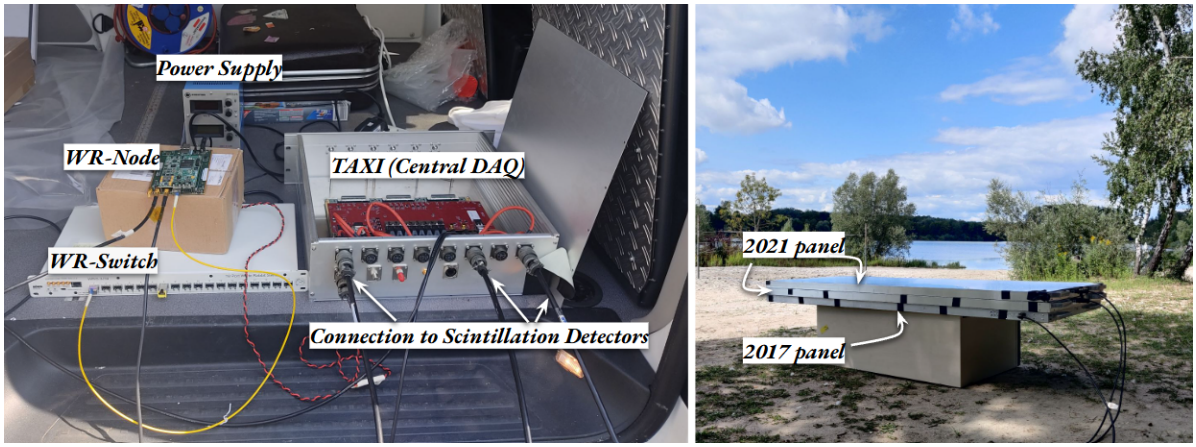

Figure 4.22: Left: Measurement setup housed in the mobile laboratory van. Right: Scintillation detectors positioned on a wooden support in hodoscope configuration near the lake shore.

A representative charge spectrum (presented in high gain) from all three scintillation detectors during a 5-minute measurement interval is shown in Fig. 4.23. The scaled version is also included to show the MIP peak clearly. The previously visible background peak before the MIP peak is not observed in these measurements. The remote location proved effective in suppressing background noise, enabling the clear identification of the characteristic peak associated with minimally ionizing particles (MIPs) in all three detector modules. The visibility

of the MIP peak under these conditions validated the suitability of the site for the calibration measurements.

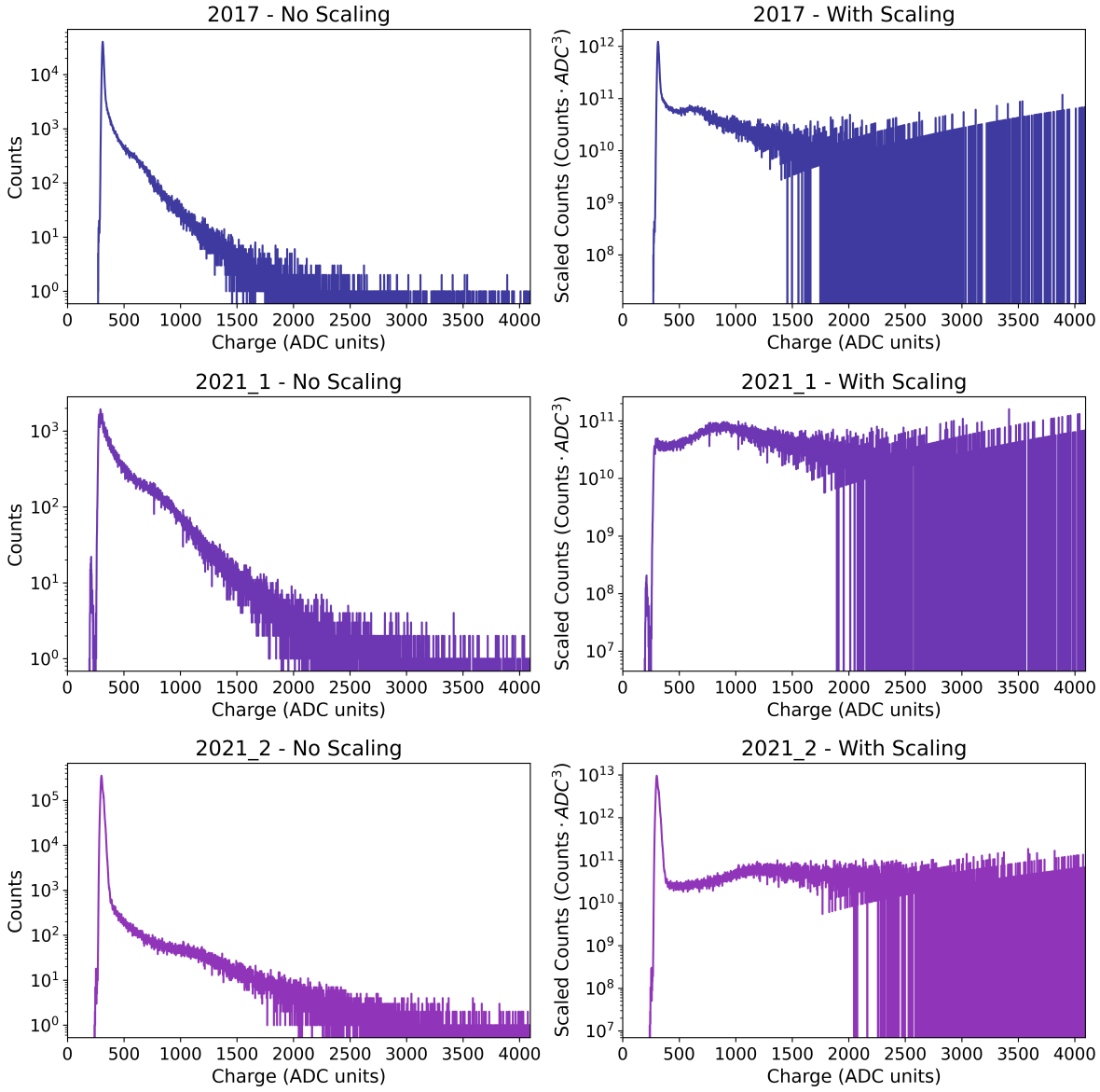

Figure 4.23: Charge distribution recorded over a 5-minute interval during the lake test campaign for all three scintillation detectors. The MIP peak is clearly visible, indicating a low-background measurement environment.

The combined results from the field tests represent an important step toward establishing a reliable and scalable test procedure for quality assurance during the mass production phase of scintillation detectors.

Radioactive source measurements

During the field measurements, an elevated level of background contamination was verified for the original laboratory setup. This background is likely due to natural radioactivity originating from trace concentrations of radioactive nuclides like uranium (U), thorium (Th), and potassium (K) present in nearby concrete walls and infrastructure. These isotopes emit gamma rays and beta particles that can interact with scintillation detectors, introducing low-energy elec-

tromagnetic contamination. In addition, electromagnetic interference from nearby electronic equipment could be an additional source of RFI.

To investigate the mitigation of such background and simultaneously validate the detector response to known radiation sources, dedicated measurements were carried out. These were designed to (i) test the effectiveness of passive shielding using lead absorbers and (ii) cross-check the expected detector response to MIPs by simulations [78] with experimental data.

From simulations performed in [78], an expected energy deposition profile for different incident particles was deduced. As shown in Fig. 4.24, muons, electrons, and photons at 0° incidence exhibit characteristic profiles, with muons at GeV energies depositing approximately 1.7 MeV, serving as a reference for validating the experimental measurements. Low-energy electrons are fully absorbed and exhibit energy deposition correlated with their incident energy. Above several MeV, they begin to mimic MIP-like ionization behaviour. The energy deposited by photons varies significantly depending on the dominant interaction process: photoelectric effect at low energies, visible as a separate band at low energies, Compton scattering at intermediate energies, and pair production at higher energies.

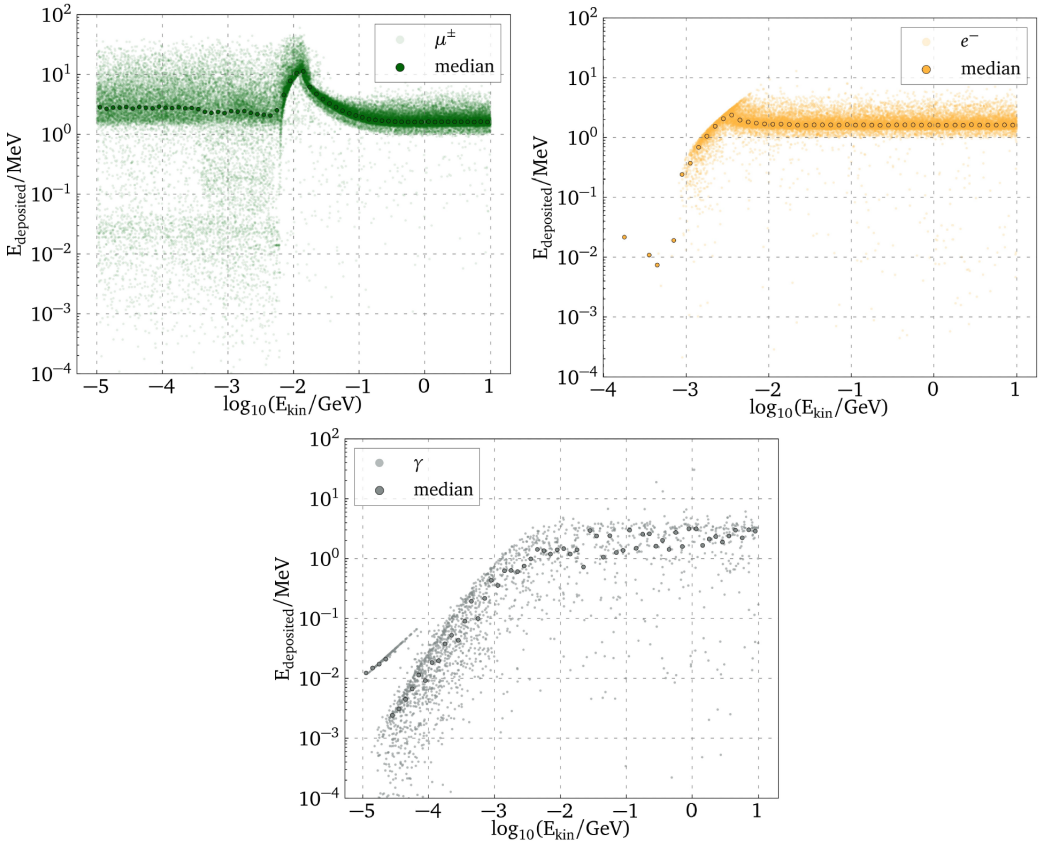

Figure 4.24: Simulated energy deposition in the scintillator for vertically injected muons, electrons, and photons [78]. The MIP energy plateau is clearly visible for muons at GeV energies.

Measurements with radioactive sources were conducted in two separate campaigns: the first in July 2022 (ambient temperature: $\approx 20°C$) and the second in January 2023 (ambient temperature: $\approx 10°C$). The 2022 campaign served as the primary measurement set for the test bench, while the 2023 campaign complemented the initial study by providing crucial data for validating energy deposition profiles. Two scintillator panels with IDs 173 and 174 were employed in both campaigns to have a consistent detector response. This work was done in close collaboration with Laura Lehmann, who conducted a detailed analysis of the campaigns as part of her bachelor's thesis [103].

The radioactive sources used in both campaigns were selected from a limited inventory approved for use in the designated measurement buildings. The selection was further constrained to sources whose decay produces gamma rays in the energy range of 1-4 MeV. This choice was motivated by the expected energy deposition ($\approx 1.7\,\mathrm{MeV}$) of minimum ionizing particles (MIPs). A summary of the sources used during both campaigns is presented in Table 4.4.

Table 4.4: Summary of radioactive source measurements conducted during the 2022 and 2023 measurement campaign.

Year	Source	Decay Mode	Radiation Type	Energy (MeV)
2022	Cs-137	Beta$^-$ decay (^{137}Cs $\rightarrow$ ^{137m}Ba)	Gamma from isomeric transition	0.662
2022	Na-22	Beta$^+$ decay + electron capture	Positron annihilation and ^{22}Ne* de-excitation	0.511, 1.275
2022	Am-Be	α from Am-241 + ^{9}Be $\rightarrow$ ^{12}C* + n	Gamma from ^{12}C* and Neutrons (broad spectrum)	~4.4
2023	Co-60	Beta$^-$ decay (^{60}Co $\rightarrow$ ^{60}Ni*)	Gamma from Ni-60* de-excitation	1.17, 1.33
2023	Na-22	Beta$^+$ decay + electron capture	Positron annihilation and ^{22}Ne* de-excitation	0.511, 1.275

The measurement setup used during the 2022 campaign is shown in Fig. 4.25. Panel 173 was fully covered with lead shielding, with Panel 174 placed directly on top. Additional plastic sheets loaded with boron carbide were included as an extra shielding layer to mitigate the neutron background, as a neutron-emitting source was also considered in these measurements.

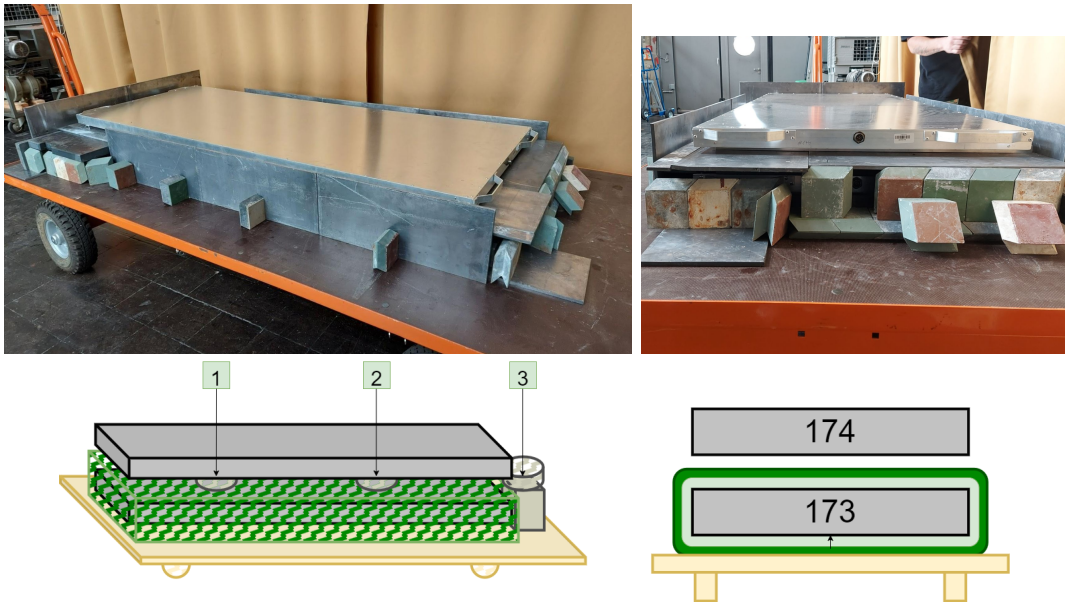

Figure 4.25: Measurement setup from the 2022 campaign showing scintillator panels 173 and 174 with shielding layers.

The radioactive sources were placed at three distinct positions: two positions covered different parts of the detector with active scintillation bars, and a third position was in front of the fiber bundle, as shown in the schematic of Fig. 4.25. In all cases, the source was placed within the lead shielding assembly and in close proximity to Panel 173. This setup allowed for direct comparison of gamma detection by the detectors with and without shielding.

The first two positions were selected to verify the uniformity and efficiency of the scintillation detector, while the third position aimed to assess how much of the scintillation enhancement effect is lost when incident particles do not traverse the scintillator material but instead enter the WSL fiber bundle directly.

It is important to note that the plastic scintillator panels do not exhibit a sharp photopeak from the radioactive sources. Due to the low atomic number (low-Z) of the scintillator material,

the probability for photoelectric absorption of MeV-range gamma rays is low. Instead, the dominant interaction mechanism is Compton scattering, resulting in a continuous spectrum of deposited energies up to the Compton edge. This edge represents the maximum energy transfer to an electron during a single scattering event and can be calculated as:

$$E_C = E_\gamma \left(1 - \frac{1}{1 + \frac{2E_\gamma}{m_e c^2}}\right),$$

where $m_e c^2 \approx 0.511\,\text{MeV}$ is the electron rest energy. In our measurements, the Compton edge is the most prominent feature in the charge spectra, consistent with expectations for plastic scintillators in this energy range, and confirms that only partial energy deposition is detected in these materials.

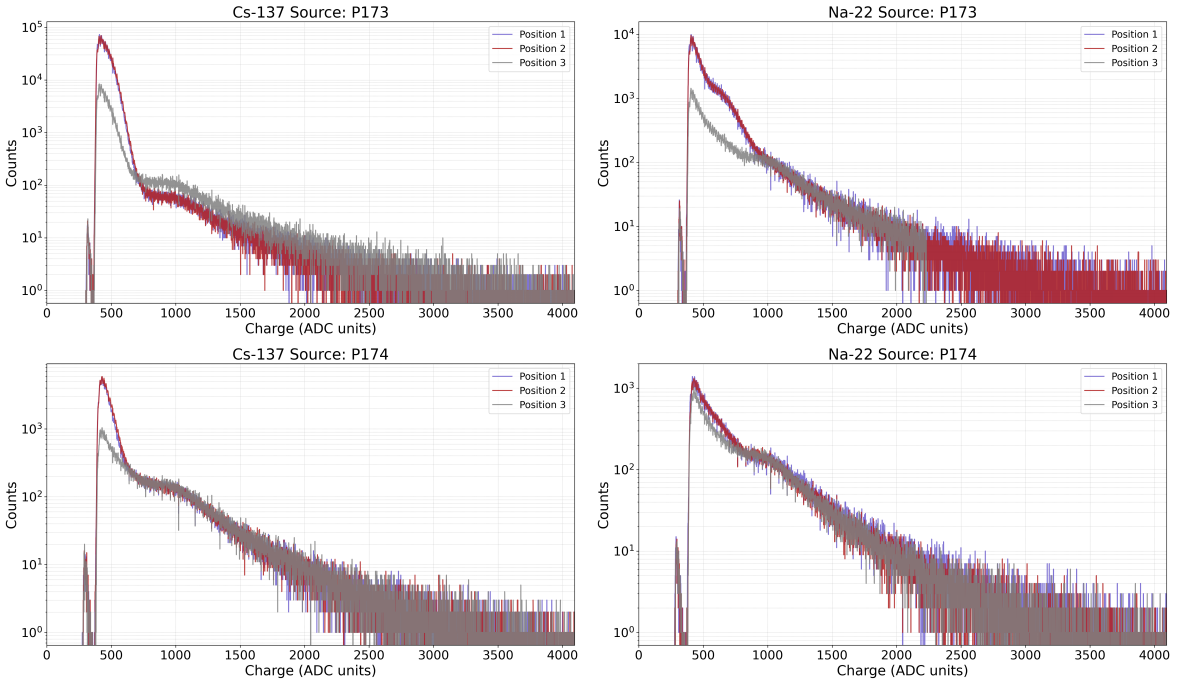

Figure 4.26: Charge Histogram observed by P173, and 174 with and without radioactive sources in the vicinity. The Compton edges energy deposit from the Cs-137, and Na-22 sources are well observed.

Figure 4.26 presents the measured charge histograms for Panel 173 and Panel 174 under various configurations during the 2022 measurements, both with and without the presence of radioactive sources. The neutron source Compton edges were observed to be smeared out, covering the entire range from the region before and after the expected MIP peak. This was also because it was too powerful and simply saturated the detectors. These measurements were therefore excluded from further analysis. The observed charge spectrum from the AmBe source measurements is presented in Appendix A.3. The main observations from the Na-22 and Cs-137 measurements are summarized below:

1. For the Cs-137 and Na-22 sources, the Compton edges are distinctly visible in Panel 173. Note the 2 peaks expected from the Na-22 decay chain as discussed in 4.4. In contrast, these edges are only marginally discernible in Panel 174. Nevertheless, the MIP peak remains similarly distinguishable in both panels at approx. 1200 ADC units.

2. Measurements at position 3 exhibit a significantly lower deposited charge, suggesting reduced interaction of the incident particles with the scintillator material.

3. The charge histograms obtained at positions 1 and 2 exhibit a high degree of overlap, indicating a uniform response of the scintillation detector across these positions.

4. The MIP peak visibility appeared to be higher even for panel 174, which was shielded only from below. This suggests increased background contamination originating from the ground, consistent with the high traces of ^{40}K in the soil. ^{40}K emits beta electrons and gamma rays in the 0.5–1.35 MeV range. Potassium levels in the Karlsruhe region are indeed elevated [104].

From these measurements, it was clear that lead absorbers would be a crucial part of the test bench for the series production validation. The measurements were subsequently repeated in 2023 (see Fig. 4.27) using Co-60 and Na-22 sources. In this campaign, two source positions were selected for charge histogram measurements, with both panels placed within a lead shielding enclosure to reduce background interference. The combined data from these 2023 measurements, together with the 2022 dataset, formed the basis for a dedicated analysis of the deposited energy.

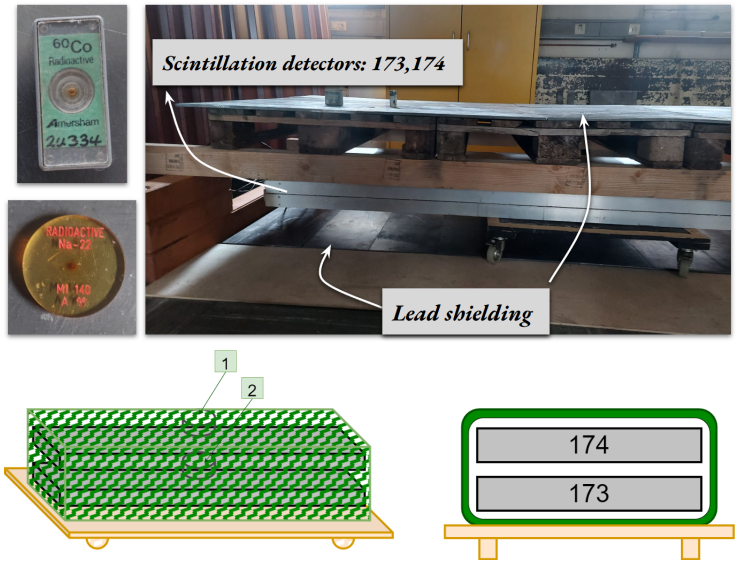

Figure 4.27: Measurement setup from the 2023 campaign showing scintillator panels 173 and 174 with lead shielding.

For all measurement configurations, the MIP peak and Compton edge were extracted by fitting the charge histograms. A Landau function of the form

$$L(E) = \frac{a\sigma}{\sqrt{2\pi}} \exp\left(-\frac{x + \exp(-x)}{2}\right) \tag{4.6}$$

was employed to fit the MIP peak, while Gaussian fits

$$f(x) = \frac{1}{\sqrt{2\pi}\sigma} \exp\left(-\frac{(x-\mu)^2}{2\sigma^2}\right) \tag{4.7}$$

were applied to both the Compton edge region and the pedestal. A modified Gaussian fit for the Compton edge was explored during [103], but it proved very sensitive to the fit parameters. Fig. 4.28 presents a histogram with the corresponding fits to the MIP, pedestal, and Compton edges to extract the mean values from measurements performed with the radioactive sources. From these fits, the MIP peak and Compton edge positions were determined in ADC units. In line with conventions in the nuclear physics community, the Compton edge was defined as 66–80% of the mean obtained from the Gaussian fit.

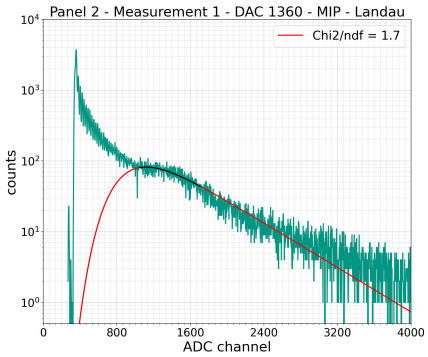

(a) Background measurement (no source).

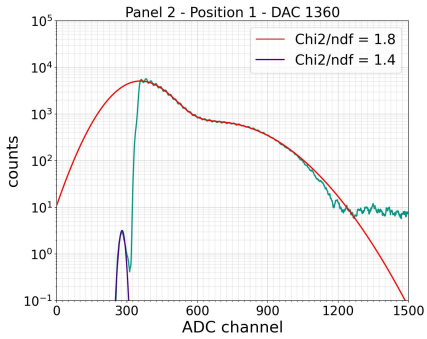

(b) Na-22 source at position 1.

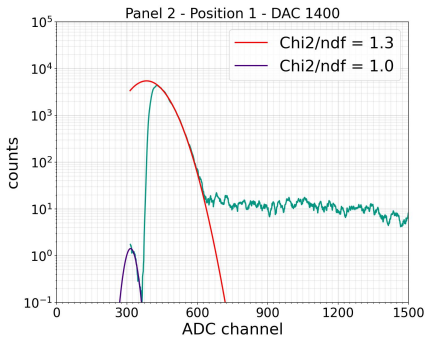

(c) Cs-137 source at position 1 (average).

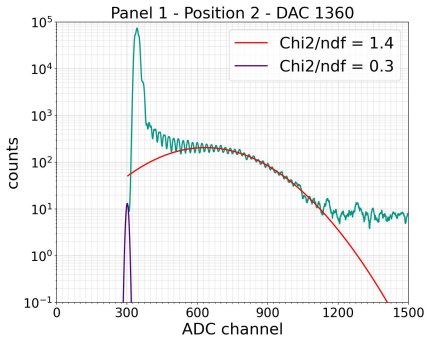

(d) Co-60 source at position 2 (average).

Figure 4.28: Charge spectra for different source configurations measured during the 2023 campaign.

Using the known photopeak energies and consequently deducing the Compton edge energies from literature as calibration points for the radioactive sources, a linear fit was performed to establish the relationship between ADC values corresponding to all fit peaks and deposited energy. Figure 4.29 shows the results of this calibration.

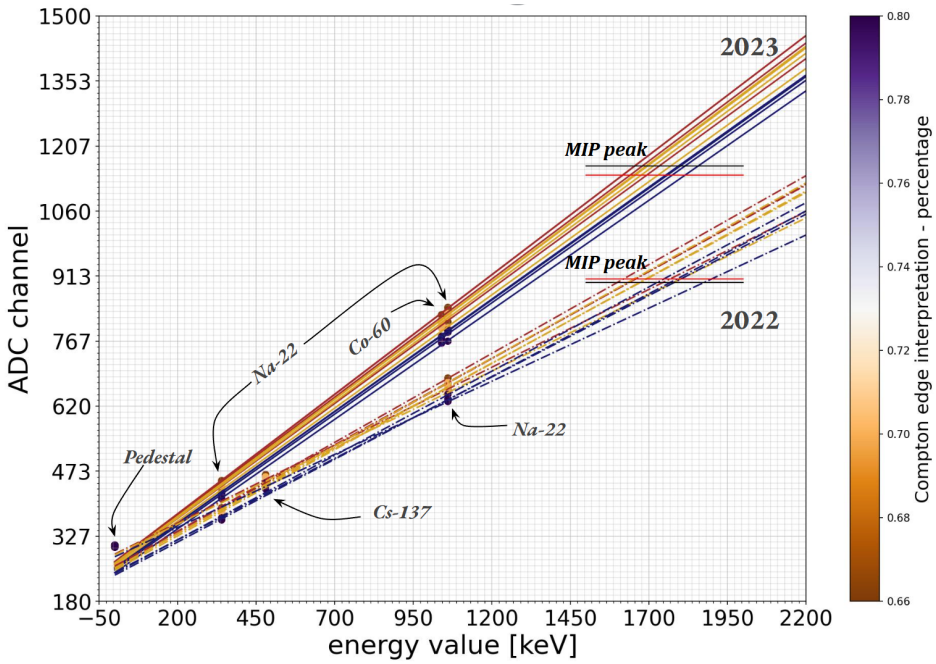

Figure 4.29: Measurement results from radioactive sources (2022–2023). The MIP deposited energy is derived using known Compton edge energies of the sources. The slope variation is attributed to differences in ambient temperature during the measurements [103]. Colored fits span the full range, assuming Compton edge contributions from 66% to 80%.

The weighted mean of the measured ADC channel for the MIP is distributed across an energy band of $E_{MIP} = 1500\,\text{keV} - 2000\,\text{keV}$ and is compared with the calculated linear ADC-energy relations for illustration. Figure 4.29 presents the calibration results, displaying linear fits of the various measurements that form a band matching the assumed values of the MIP peak. These fits account for the entire range with lowest assumed Compton edge contribution of 66% to the highest of 80%. Both measurement series are shown and differ primarily due to temperature fluctuations, which influence the ADC channel readings due to changes in SiPM gain. The 2023 measurements were carried out in the winter months with a room temperature of 10°, while the 2022 measurements were at $\sim 25°$. The MIP region aligns with the calculated linear regression band. Table 4.5 summarizes the calculations for the MIP energy levels, confirming the assumed energy range of $E_{MIP} = 1500\,\text{keV} - 2000\,\text{keV}$. Furthermore, the MIP energy range can be constrained by considering a 70% interpretation of the Compton edges, resulting in a range from $E_{MIP} = 1631\,\text{keV}$ to $1803\,\text{keV}$.

Table 4.5: MIP Peak identification for all measurements with the MIP ADC values taken from either the measurements without source, with Cs137 or Co60. The highlighted values considering the 70% interpretation of the Compton edge represent the best evaluated results [103].

		2022		2023	
Calculation method		Without source	Cs137	Without source	Co60
Panel1-1	66%	1636.7 keV	1658.7 keV	1732.7 keV	1692.6 keV
	70%	**1671.8 keV**	**1694.1 keV**	**1769.2 keV**	**1728.5 keV**
	80%	1779.5 keV	1802.9 keV	1856.6 keV	1814.5 keV
Panel1-2	66%	1598.4 keV	1619.9 keV	1678.8 keV	1639.8 keV
	70%	**1631.3 keV**	**1653.1 keV**	**1714.5 keV**	**1674.9 keV**
	80%	1725.6 keV	1748.2 keV	1814.7 keV	1773.3 keV
Panel2-1	66%	-	-	1654.9 keV	1616.3 keV
	70%	-	-	**1690.9 keV**	**1651.7 keV**
	80%	-	-	1794.1 keV	1752.9 keV
Panel2-2	66%	-	-	1654.1 keV	1615.6 keV
	70%	-	-	**1695.6 keV**	**1656.3 keV**
	80%	-	-	1799.5 keV	1758.2 keV
Panel1-1-30min	66%	1634.9 keV	1656.7 keV	-	-
	70%	**1668.9 keV**	**1691.0 keV**	-	-
	80%	1766.9 keV	1789.9 keV	-	-
Panel2-1-30min	66%	1743.6 keV	1768.1 keV	-	-
	70%	**1777.7 keV**	**1802.5 keV**	-	-
	80%	1874.4 keV	1900.5 keV	-	-

In Conclusion The measurements and simulations consistently show that cosmic-ray-induced MIPs deposit a mean energy of 1.7 MeV in the scintillator, validating the detector calibration and confirming its ability to identify relativistic particles even in shielded environments. The shielding effectively suppresses low-energy backgrounds without affecting MIP detection, ensuring that the simulation accurately predicts the detector response and supports its reliable operation for future deployments.

Final Test Setup

Utilising the insights from the measurements discussed, the final calibration setup for the scintillation detectors, intended for the surface array upgrade, was housed within an all-metal-walled structure to minimise RFI from the surrounding laboratory environment. To further reduce the influence of natural radioactive backgrounds, additional lead shielding has been incorporated as a layer of 1 cm thick lead sheets placed below and above a wooden holding structure. A movable wooden tray with wheels was used as a mount to slide the scintillation detectors between the lead layers by placing them on the tray and sliding them into place. Due to the required compactness of the two layers to avoid radiation from the sides, only two scintillation detectors can be tested in this setup at a time. Figure 4.30 shows the complete setup.

Figure 4.30: Left: The metal-walled building housing the test setup. Right: The lead-shielded configuration, allowing for simultaneous testing of two panels using a sliding mechanism.

One of the histogram measurements from this setup is shown in Fig. 4.31. With the lead shielding in place, the MIP peak becomes more distinct, highlighting the significant natural radioactivity background in the unshielded measurements. The station deployed at the South Pole during the 2022-23 Antarctic summer was tested using this setup. Additionally, six more stations for the SAE were validated using this test setup.

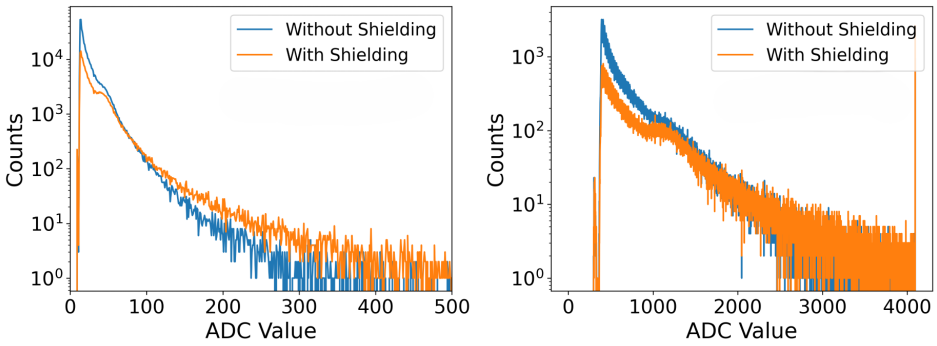

Figure 4.31: Left: Medium channel histogram. Right: High channel histogram. The orange curves represent measurements without lead shielding, while the blue curves correspond to measurements with shielding in place.

4.4 Scintillation Detector Validation

Post-assembly, each scintillation detector underwent a comprehensive series of validation measurements to verify its performance. This section details the measurements performed with the six-station scintillation detectors manufactured for deployment at the South Pole. Subsequent production campaigns will employ a similar validation structure. A summary of the

validation measurements is provided in Table 4.6. Measurements were conducted in batches of eight scintillation detectors (equivalent to one station), with an average duration of three days per station. These measurements were conducted in the duration of 16th August to 21st September 2022. The measurements were carried out using TAXI-20 (version V3.2). [1].

Measurement	Description	Settings
Histogram (w/ shielding)	Two 5-minute histogram measurements with shielding to calibrate the MIP peak under low-background conditions.	DAC 1350; AUX-DAC 2650
Histogram (w/o shielding)	Two 5-minute histogram measurements without shielding to characterize the unshielded detector response.	DAC 1350; AUX-DAC 2650
Hitbuffer (w/ shielding)	Two 5-minute hitbuffer measurements with shielding to monitor hit rates under minimal background noise.	DAC 1350; AUX-DAC 2650
Hitbuffer (w/o shielding)	Two 5-minute hitbuffer measurements without shielding to study background rejection using coincident hits across detectors.	DAC 1350; AUX-DAC 2650
Threshold Scans (w/o shielding)	110-second hitbuffer measurements with incremental threshold scans to characterize noise and optimize thresholds.	DAC: 0-4095, step size 10 DAC
Shower Trigger/Air Shower (w/o shielding)	Radio-triggering measurements under unshielded conditions with multiplicity varied from 1 to 8 in a hodoscope setup to assess trigger efficiency.	DAC 1400, AUX-DAC 2650; DAC 4095 , AUXDAC 2650

Table 4.6: Summary of validation measurements conducted for each station, including key settings.

As shown in Fig. 4.32, two configurations were employed for the validation measurements: shielded and unshielded. In the shielded configuration (4.32 (right)), two scintillation detectors were tested simultaneously within the lead setup, while in the unshielded configuration (4.32 (left)), all eight detectors were positioned in a hodoscope condition and measurements were performed in parallel. A brief discussion of the measurement results is summarized in the following subsections.

Histogram measurements

Figure 4.33 shows the histogram measurements performed with (left) (2 at a time) and without (right) (all 8 stacked vertically) lead shielding for all scintillation detectors of station 1. The detectors, labeled SD1 through SD8, were vertically stacked from bottom (SD1) to top (SD8) for the unshielded measurement. This is shown in the left plot, and it is evident that the background suppression in the valley region (roughly between 300-700 ADC units) between the pedestal and MIP peak improves with increasing detector height. This effect is likely due to partial self-shielding, as the intermediate scintillators in the stack absorb ambient low-energy gamma rays and beta electrons, thereby reducing the background contribution in the upper detectors. In contrast, the right plot shows a uniform overlap of the histograms for all scintillators when measured in the lead setup in groups of 2, indicating that the external lead shielding uniformly suppressed background contributions across all the scintillation detectors. The slight pedestal shifts across detectors are attributed to variations in detector gain and the associated bias voltage settings, which can vary per module.

[1]Two firmware versions of the uDAQ system were utilized: uDAQv4.1-chw-tjb-3sec-to-20210202.bin for histogram mode, and udaq4.1-bin-cobs-mar_14_2022.bin for hitbuffer mode measurements

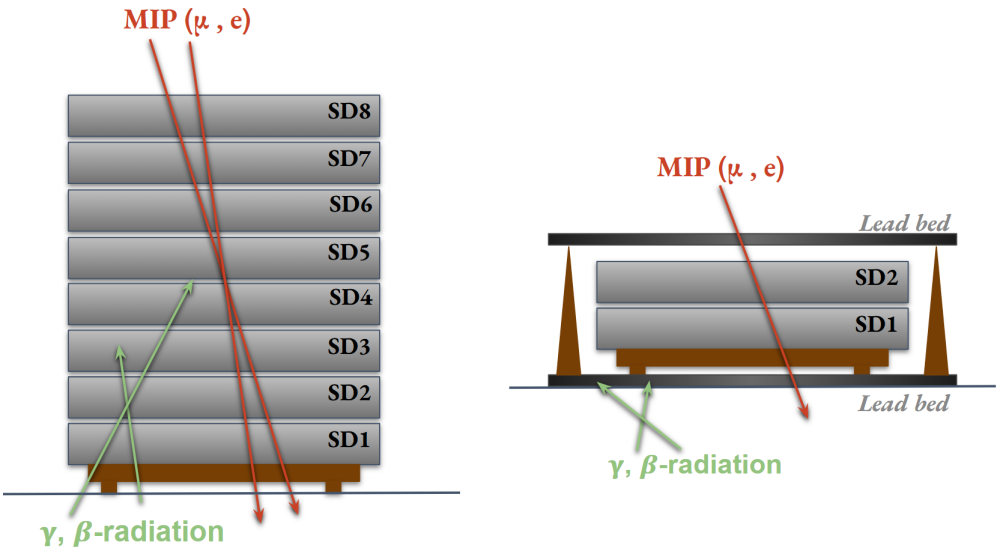

Figure 4.32: The configurations implemented for the validation measurements. Left: Eight detectors stacked on top of each other (Hodoscope). No lead shielding is employed in this setup. Right: Two detectors are placed on a movable bench between two layers of lead. The expected behavior of MIPs and local radiation due to natural radioactivity is also shown in both configurations.

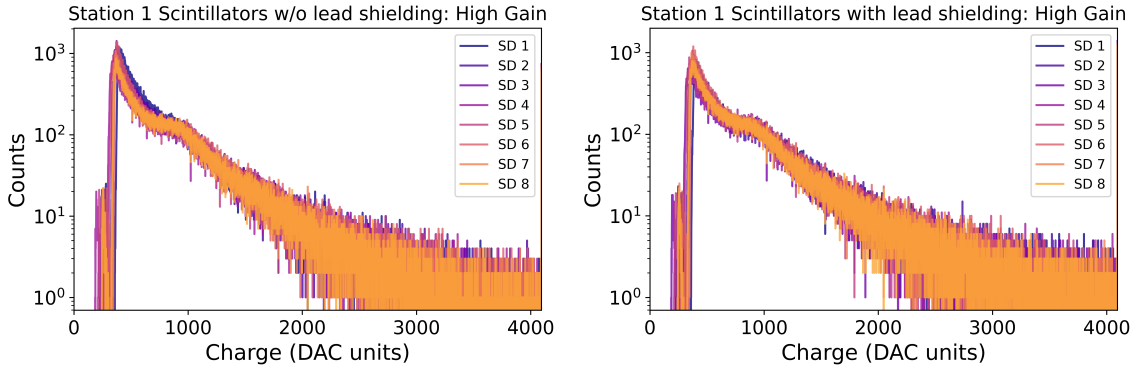

Figure 4.33: Histogram measurements of the eight scintillation detectors in station 1: without lead shielding (left) and with lead shielding (right). The improvement in background suppression with height (left) and the uniform suppression across detectors due to external shielding (right) are visible in the valley region.

To quantify the MIP peak, the charge spectra from the high-gain channel were fit using a Landau distribution convoluted with an exponential background (expo+Landau):

$$f(x) = \frac{A}{1+\exp(x/\lambda)} + B \cdot \sigma \cdot \frac{1}{\sqrt{2\pi}} \exp\left(-\frac{1}{2}\left(\frac{x-x_0}{\sigma} + e^{-\frac{x-x_0}{\sigma}}\right)\right) \tag{4.8}$$

where A is the normalization constant for the exponential background. λ controls the steepness of the background suppression. B is the scaling factor for the Landau component. x_0 is the most probable value of the Landau function. And finally, σ is the width parameter of the Landau distribution. The observed pedestal was characterized by a Gaussian fit of the form Eq. (4.7). While a double exponential model was also tested, it yielded negligible improvement over the single exponential and was therefore not used for final analysis. Figure 4.34 shows an example fit for one detector. The MIP peak position was determined to be 847.69 ± 1.1 ADCs. The fit quality was evaluated using the reduced chi-squared metric, defined as

$$\chi^2 = \frac{1}{\text{ndof}} \sum \frac{(O-E)^2}{E} \tag{4.9}$$

where O and E denote observed and expected counts, respectively. Elevated χ^2 values can be attributed to the slight suppression of the MIP peak due to lower gain at room temperature, and also the noisy nature of the short histogram measurement.

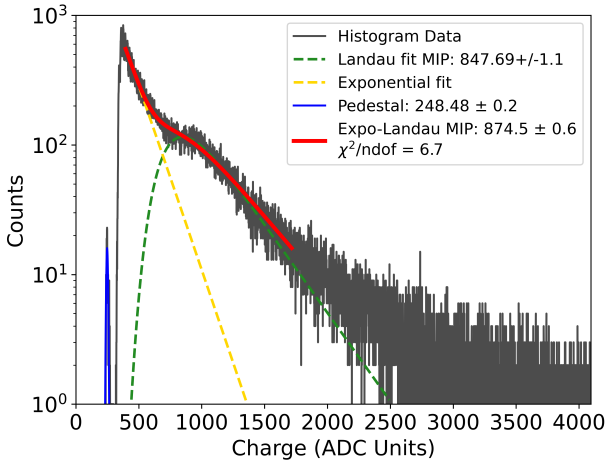

Figure 4.34: Example fit to a charge histogram from a scintillation detector, showing the pedestal (blue), Landau component of the MIP signal (green dashed), exponential background (yellow dashed), and combined expo+Landau fit (red).

This fitting procedure was applied to all 48 scintillation detectors across the six stations. The resulting MIP peak positions are summarized in Figure 4.35. The observed variation among detectors is consistent with expected differences in detector response due to gain variations, bias voltage settings, and environmental effects such as temperature fluctuations. Each detector was measured twice under the same conditions, and the repeated measurements show strong internal consistency, thereby validating the stability of the method already at this preliminary calibration stage.

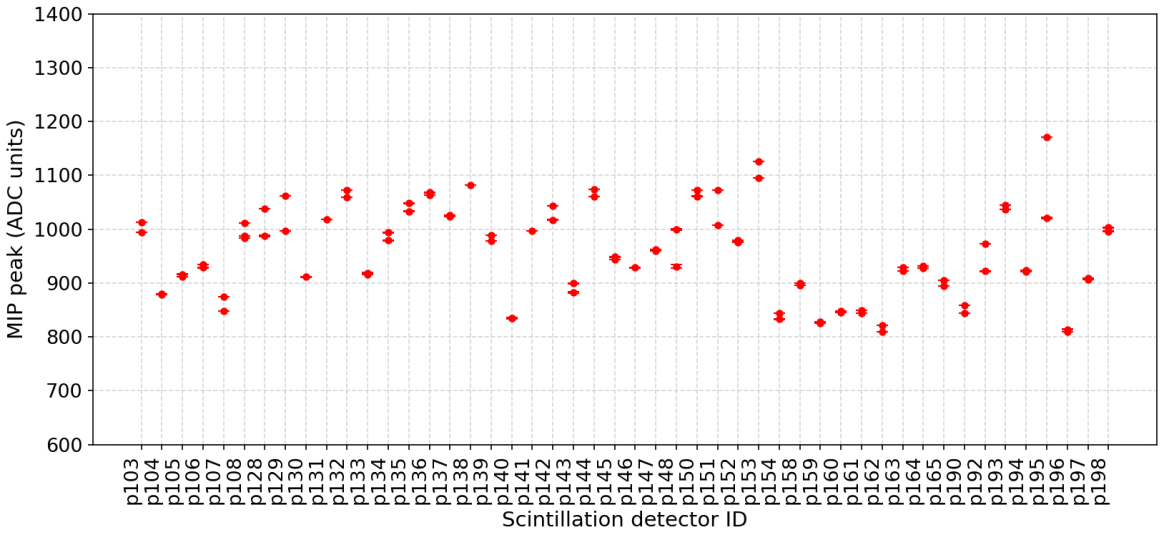

Figure 4.35: Extracted MIP peak positions for all 48 scintillation detectors across six stations. The two points per detector correspond to two repetitions of the same measurement to ensure reproducibility. The variation in peak values arises from differences in detector gain and environmental temperature during measurement.

Hitbuffer Measurements

The MIP peak characterization was further corroborated using the hitbuffer measurements performed in the hodoscope condition 4.32. This method enabled event-level background suppression through multiplicity-based coincidence filtering. A multiplicity of 8 was required, meaning that coincident hits in all 8 scintillation detectors had to occur within a 200 ns window. This criteria isolated the true MIP events while filtering out the background noise. The filtered charge spectra were then analyzed by fitting a Landau distribution of the form 4.6 to the remaining peak region, excluding the pedestal and residual background. An example of such a filtered histogram for station 1 is shown in Figure 4.36 [18]. The background contribution is significantly suppressed, resulting in a much-improved fit quality evident with the reduced χ^2 value. The MIP peak position extracted from this fit, 838.4 ± 0.3 ADCs, is in close agreement with the value obtained using the standalone histogram method (847.69 ± 1.1 ADCs), thereby confirming the consistency and robustness of the peak localization across independent measurement techniques.

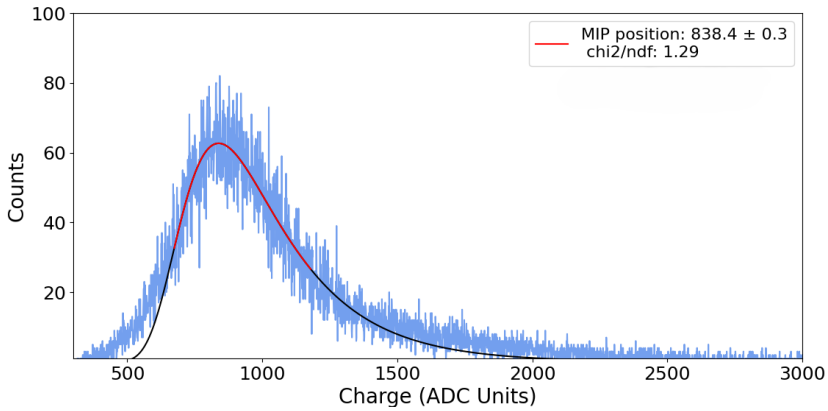

Figure 4.36: Filtered charge histogram using hitbuffer data from station 1 with multiplicity-based coincidence requirement. The improved signal-to-noise ratio leads to a clearer MIP peak and a more reliable Landau fit.

Threshold Scans

A threshold scan was performed for each of the 48 scintillation detector units to map their performance in the entire threshold range in the hodoscope scenario. Each scan consisted of 110-second hitbuffer measurements taken at discrete threshold settings between 0 and 4095 DAC units, with an increment step of 10 DAC. The event rate for each discrete threshold was deduced from the total triggers observed during the measurement interval.

A fixed bias voltage of 2650 DAC was used for all threshold scans. This value was selected based on a prior voltage scan conducted at a constant threshold of 1350 DAC (data presented in Fig 4.37). This preliminary analysis demonstrated that the SiPM transitions into its Geiger-mode operation at a bias of approximately 2500 DAC and exhibits a linear increase in event rate up to approximately 2750 DAC. Beyond this point, a non-linear rise toward saturation was observed, likely due to limitations of the readout electronics. Thus, a bias of 2650 DAC was chosen to ensure a robust Geiger-mode operation while mitigating the effects of electronic saturation, a selection corroborated by the manufacturer's specification of ≈ 5V above breakdown [90].

The results of these threshold scans for all six stations are presented in Fig. 4.38. Below a threshold of approximately 1300 DAC, the event rate remains negligible, consistent with a discriminator level below the electronic baseline. At approximately 1300 DAC, a sharp increase

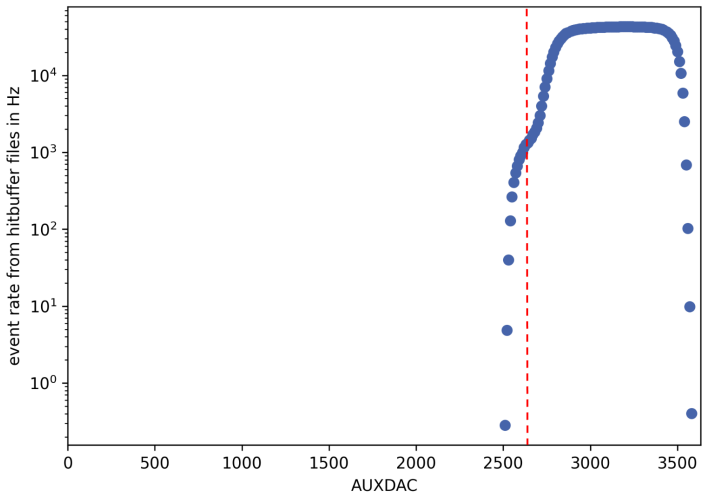

Figure 4.37: Voltage scan performed at room temperature for one of the scintillation detectors. The SiPM pixels enter the Geiger mode around 2500 DAC units. The red line corresponds to the 2650 DAC operating point used in the threshold scans.

in the event rate is observed. This phenomenon corresponds to the threshold level intersecting the baseline, leading to the detection of dark counts and electronic noise. As the threshold is increased further, the event rate exhibits a predictable decrease, as only events corresponding to greater energy depositions can satisfy the trigger condition. This characteristic trend is observed across all scintillation detector units. Minor variations in the response curves between detectors are attributed to slight differences in their respective electronics, which are addressed during subsequent operational calibrations. Furthermore, discrepancies in the event rates can be ascribed to local variations in the ambient background from natural radioactivity.

Air Shower Measurements

The final validation stage involved air-shower measurements using the full station components, representative of the planned station at the South Pole. Each station comprised eight scintillation detectors connected to a central data acquisition system (TAXI), along with three radio antennas positioned approximately 10 m apart outside the test bench building at KIT. The scintillation detectors were positioned in the previously mentioned hodoscope condition within the test bench building.

This measurement campaign aimed to evaluate the performance of the scintillation detectors in triggering radio counterparts under realistic air-shower conditions. To suppress uncorrelated background events, a high discriminator threshold of 4095 was applied. Given the hodoscope configuration, this threshold ensured that only events with at least five or more minimally ionizing particles (MIPs) crossing the station within 1 μs would produce a trigger, corresponding to genuine air-shower events. Figure 4.39 shows the rate at which radio antennas were triggered as a function of scintillator multiplicity. This information is obtained from the radio readout frequency. As expected, the rate decreases exponentially with increasing multiplicity requirement, reflecting the reduced probability of accidental coincidences and the increased likelihood of registering only true air-shower events. The trigger rate is observed to have a much lower rate than that observed in the threshold scans. This can be explained by the deadtime of the radio readout, which is 71 μs, which leads to saturation for multiplicity up to 3 [105].

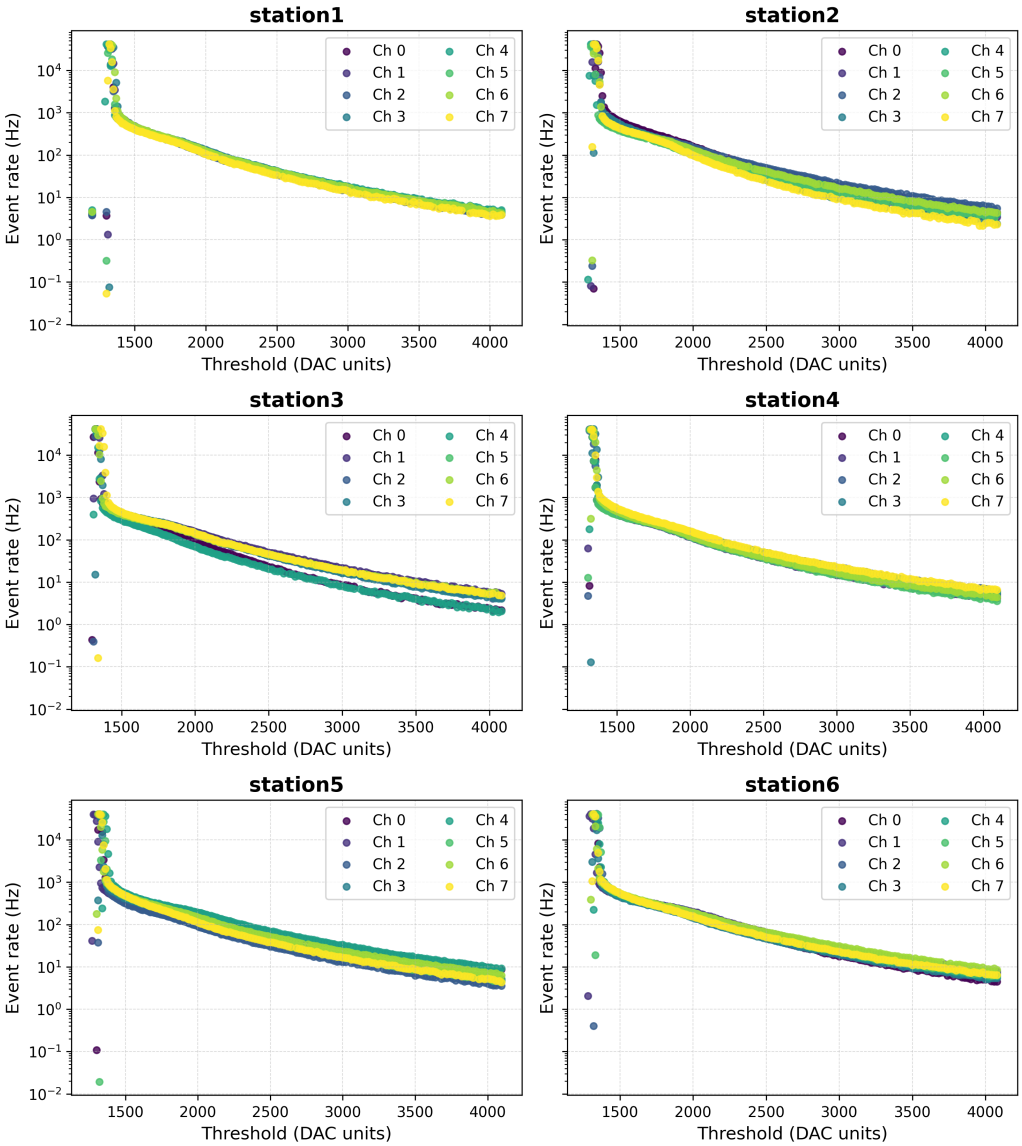

Figure 4.38: Threshold scans covering the entire range of trigger threshold for all scintillation detectors for the 6 stations. Each color corresponds to a unique scintillation detector within a station.

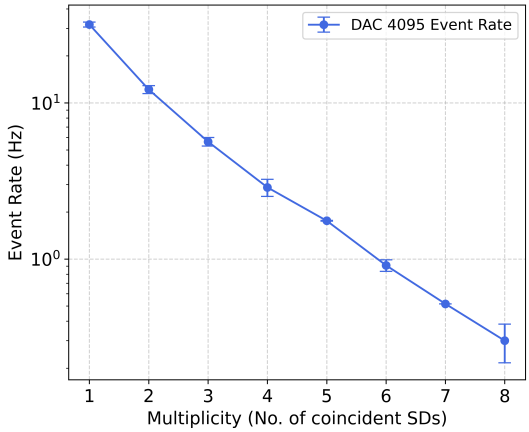

Figure 4.39: Rate at which the radio antennas are triggered as a function of required scintillator multiplicity for DAC threshold 4095.

Chapter Summary:

In this chapter, the production and validation of scintillation detectors for the Surface Array Enhancement is discussed. Scintillators for seven stations intended for deployment at the South Pole were tested using a dedicated setup designed with consideration of baseline requirements influenced by environmental conditions such as natural radioactivity and radio-frequency interference (RFI). Both field tests and measurements with radioactive sources were conducted. A key outcome is the experimental confirmation that minimum ionizing particles (MIPs) deposit approximately $1.7\,\mathrm{MeV}$ in the scintillators, verifying the detectors' low-energy threshold and their suitability for enhancing the sensitivity of the IceCube surface array to lower-energy events.

Chapter 5

Commissioning and Calibration of the first SAE station

The prototype station of the SAE at the South Pole has been upgraded over the period from 2018 to 2023, leading to station 0 as the first station with all components in final configuration planned for the Surface Array Enhancement. For the consistent operation of the scintillation detectors, a detailed temperature calibration is essential due to the strong dependence of SiPM gain on ambient temperature.

This chapter presents details on the calibration of the Station 0 scintillation detectors during the commissioning period following the Jan-2023 update of the prototype station (section 5.3). The detectors are calibrated in units of minimum ionizing particles (MIP), as discussed in Section 2.4. Calibration validation is achieved through a study of timing and charge correlation between neighbouring detectors, owing to the unique station geometry featuring 5 m spacing between scintillators, allowing them to sample approximately the same part of the observed air-showers. The dynamic range of the upgraded detectors is also characterized, with the calibration results contributing to future real-time temperature corrections aimed at maintaining a stable operational range.

The data processing framework, particularly for scintillator data, is described in Section 5.4, including its evolution over multiple firmwares used for data taking. Temperature correlation with data from nearby weather stations to recover missing temperature readings during air-shower measurements is achieved. The chapter concludes with the preparation of an air-shower dataset comprising coincident events with IceTop following integration in the full processing framework.

5.1 Prototype Station

A prototype station of the Surface Array Enhancement has been collecting air-shower data at the South Pole since early 2020, following a commissioning period [85]. While the prototype station has already demonstrated its capability to detect showers in a 3-fold coincidence with IceTop, reinforcing its advantages and proof of principle [106], there remained scope for improving its dynamic range and measurement uptime. An example event with a 3-fold coincidence is shown in Fig. 5.1(Top). The circles represent the deposited signal observed by the scintillators, with their colour scheme indicating the relative timing of the signals, providing an intuitive sense of the shower's arrival direction. Additionally, the radio antennas with their corresponding waveforms for the event are included. The arrows illustrate the reconstructed directions obtained from the three detection channels: IceTop, scintillators, and radio. A good agreement among these reconstructions is clearly visible.

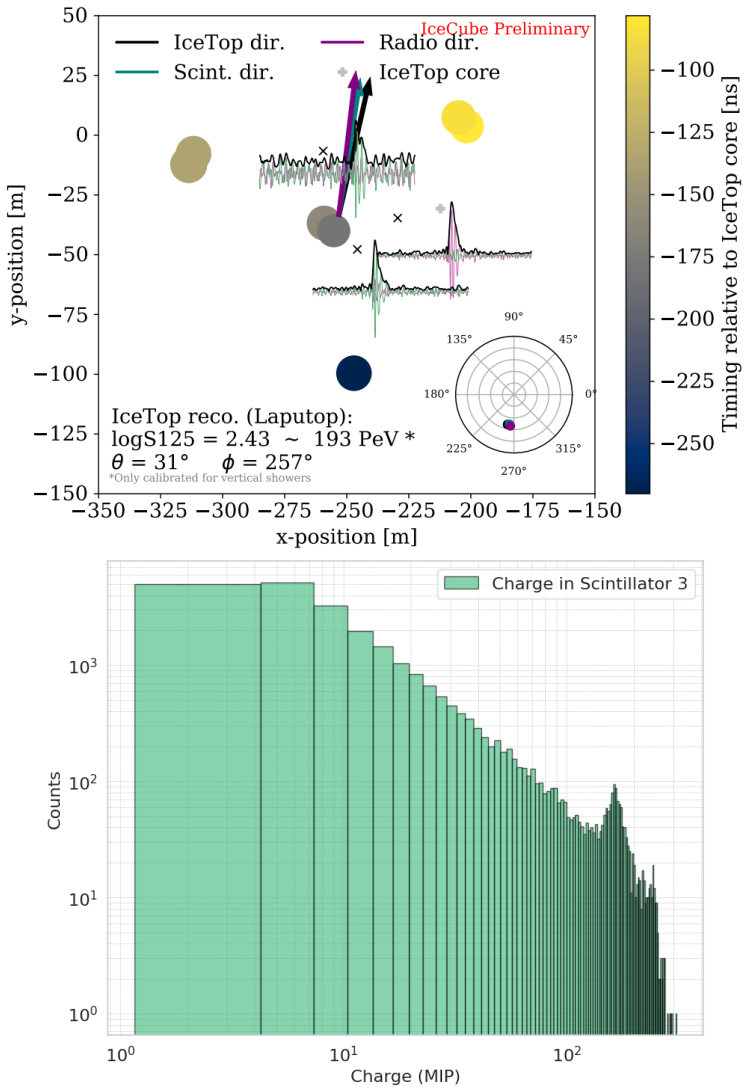

Figure 5.1: Top: An example air shower event observed in all 3 detection channels. Taken from:[106] Bottom: Dynamic range of the scintillators of the prototype station.

The limited dynamic range of the prototype station's scintillation detectors, observed to be approximately 200 MIPs, was already identified in previous work [85] and is evident in Fig. 5.1(Bottom). In particular, a saturation effect in the form of a pile-up was observed around 160 MIPs. Based on these findings, active efforts were made to expand the observation window, leading to key improvements implemented in the latest deployment in 2023.

5.2 Station 0

The latest upgrade of the prototype station of the SAE was carried out in January 2023, leading to the first SAE station with all detector components in the final configuration, called Station 0. It featured a complete replacement of the existing scintillation detectors and one of the radio antennas. The new scintillators incorporated an updated version (V4.1a) of the readout electronics, known as uDAQs (Sec. 4.1.3).

Additionally, the hardware assembly of the scintillation detectors was improved to enhance durability in the harsh South Pole environment. A 2K-Silicone Sealant (OTTOCOLL S 610-BLACK) was applied along the edges of the detector housing, in addition to the previous

riveting method. This upgrade ensures the detectors remain both light- and water-tight, preventing potential damage from wear and tear over time. To facilitate easier maintenance, the original sideways-opening design was replaced with a top-side opening, allowing for more convenient access to the internal components. The connector position was also moved to the smaller edge of the detector, optimising cable management. Furthermore, the military-grade connector used for cabling was upgraded from an L-shape to a straight joint, eliminating potential misalignment issues and simplifying assembly during deployment.

A major feature of the new uDAQs was an expansion in the dynamic range, allowing observation of up to 800 MIPs opposed to the limited range of 200 MIPs with the previous electronics [18, 85]. Consequently, this allowed for a wider detection range in the energy regime. The exchanged antenna was deployed on a custom mount [50] with a pre-calibrated low-noise amplifier (LNA). The remaining antennas were already in this configuration from the previous deployments [18]. To mitigate snow accumulation in the coming years, the scintillation detectors and the fieldhub were elevated to approximately 1.5 metres. Figure 5.2 illustrates the deployment of the upgraded antenna and one of the new scintillator panels.

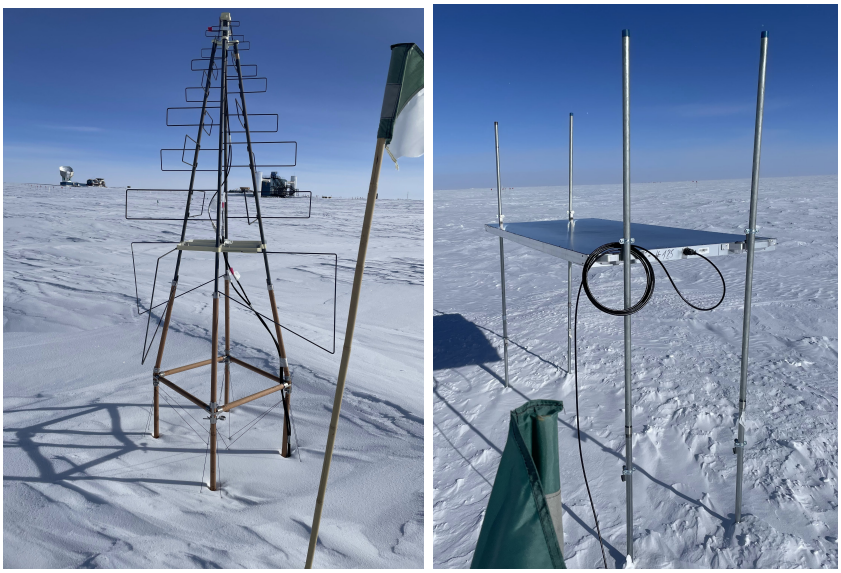

Figure 5.2: Left: The new deployed antenna with the custom mount by Roxanne Turcotte in 2023; Right: One of the new scintillation detectors from the 2023 deployment.

5.3 Commissioning and Calibration of Station 0

Following the upgrade of the prototype station, a commissioning period was conducted to characterise Station 0. A key focus of this characterisation was the temperature calibration of the newly deployed scintillation detectors. This calibration was necessary because the light generated within the scintillators by a passing MIP is measured using temperature-sensitive photosensors called Silicon Photomultipliers (SiPMs). Additionally, studies were carried out on charge deposition as well as timing correlations between neighbouring detectors, in addition to baseline stability checks. These analyses were essential to ensuring a uniform measurement environment. This section will discuss these topics in detail. A brief discussion on the characterisation of the Radio antennas is also included.

The configuration settings for scintillator measurements, such as bias voltage and threshold, were well understood from previous studies [85] and pre-calibration measurements conducted after production. Therefore, these aspects are not discussed in detail in this chapter, but comprise an important part of the characterisation process during the commissioning of a

station. The data utilised for the commissioning and calibration steps is from 10th January - 30th June 2023, from the South Pole.

5.3.1 Scintillator Characterization

Baseline Studies

Studying the baseline in a particle detector is crucial for accurate signal detection, as it represents the detector's response in the absence of a signal. Any fluctuations or drifts in the baseline can affect the identification of real measured events, making baseline stability essential for maintaining consistent trigger conditions and ensuring reliable, uniform measurements over time. A well-understood baseline is also necessary for choosing the correct measurement settings, such as determining the trigger threshold. To evaluate the baseline of the uDAQs, CPU-triggered hits are collected through software-triggered readouts approximately once per second. This soft-trigger is referred to as a Fixed Rate Trigger (FRT). The FRT hits are stored in the hitbuffer file alongside signal-over-threshold triggered hits, with a flag indicating the trigger condition.

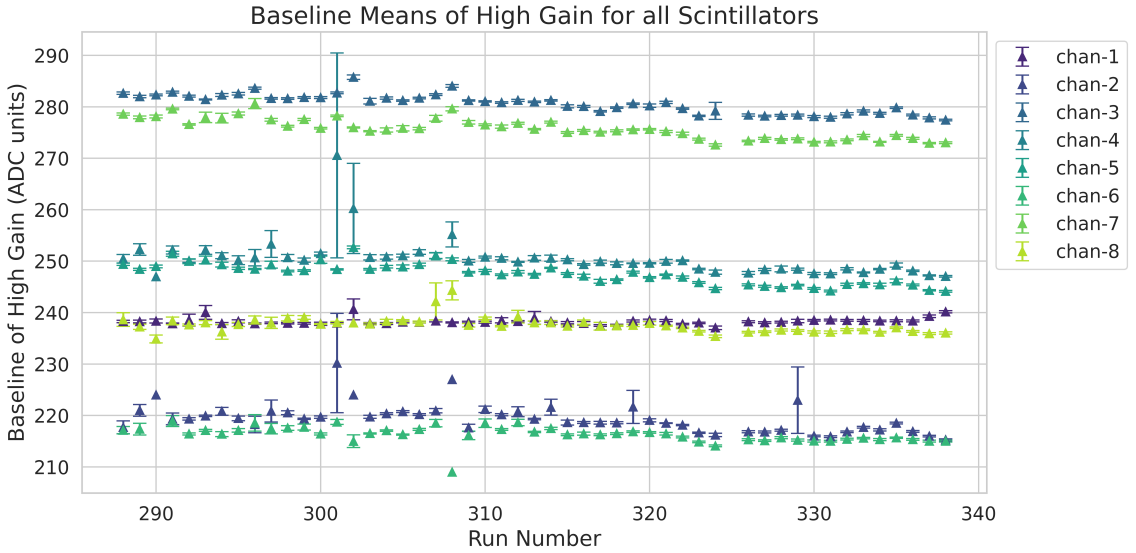

Figure 5.3: Baseline of the 8 detectors in High gain of Station 0 for 50 days. The Run Number corresponds to the measurement run, each signifying data taken on a single day.

A study of the baselines through the summer months of Jan-Feb, 2023 is presented in Fig. 5.3 for all 8 scintillators of station 0. The baseline was also investigated in the medium and low gain, and is included in the Appendix B.1. It is apparent that the mean baseline value for all scintillators is stable over the entire period. The individual baselines are slightly varying due to the difference in gain response of the SiPMs for the fixed bias voltage setting (2650 ADC units[1]) used across all detectors. This can be explained by the SiPM I-V curve measurements discussed in 4.16. All the baselines are well contained between 200-300 ADC units. Some outliers were observed at higher ADC units, accounting for 0.2% of the data. This can be explained by the arrival of the MIP when the FRT is being recorded, and is therefore not a true FRT. The baseline from each measurement is taken into account for calibration of the air shower data during data processing, which will be discussed later in Sec. 5.4.

[1] ADC units correspond to the Analog Voltage setting converted to a Digital channel

Temperature and MIP Calibration

To ensure uniform measurements across all scintillators, it is essential to understand the behaviour of the gain output by SiPMs at a given bias voltage and temperature. However, owing to the similar behaviour of the SiPMs even prior to calibration (Fig. 5.4), air shower measurements (hitbuffer measurements) were conducted in addition to the calibration measurements (histogram measurements) during the commissioning period. Temperature corrections were applied later during offline data processing (Sec. 5.4). Fig. 5.4 presents an example charge histogram measurement with all 8 scintillation detectors recorded in the high-gain channel of their respective uDAQs. The peaks visible at the beginning of the charge spectra are the single photo-electron peaks (also called the finger spectrum), which are distinguishable when the SiPM gain is large enough. The distance between these single p.e peaks correspond to the gain of the SiPM, and provide an estimate of the number of photo-electrons generated per passing MIP, which is visible as the broad peak around ~ 1500 ADCs.

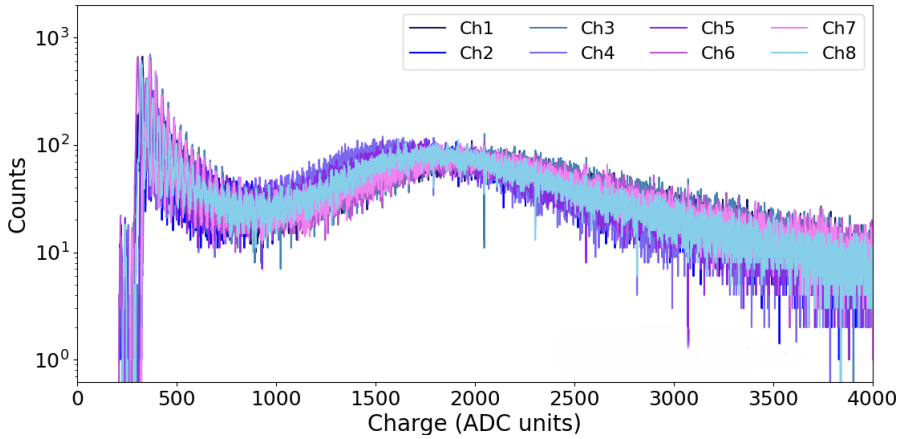

Figure 5.4: Charge histogram data for the 8 scintillation detectors in high gain prior to calibration. A near uniform behaviour is evident from the plot [18].

For the air shower measurements during commissioning, the threshold was set to the highest digital channel of 3600 ADC units, where the threshold in all detectors is roughly a few MIPs. This threshold value is derived from the ADC to DAC relation studied in [85], and is shown in Fig. 5.5. This high threshold was favourable for cleaner radio data, as the radio detectors have a higher detection threshold, and the lower trigger threshold from scintillators would result in increasingly noisy data. In addition, a trigger was implemented, where a signal exceeding the threshold in at least six scintillation detectors triggered a readout from the radio antennas, ensuring they were only read-out during air shower events.

The SiPM board (Fig. 4.7) includes an integrated temperature sensor. Due to the extremely cold conditions at the South Pole (-40°C to -70°C), SiPMs are particularly well-suited for scintillator readout, as their gain increases with decreasing temperature, as shown in Fig. 5.6(a). Additionally, the gain of the SiPM depends on the supplied bias voltage. Increasing the bias voltage beyond the breakdown voltage leads to a gain increase but also results in a higher dark count rate, which must be considered (Fig. 5.6(b)). Therefore, understanding the relationship between gain, bias voltage, and temperature is crucial for properly calibrating each scintillator and optimising the measurement configuration settings.

For calibration measurements, the threshold was set as low as 1350 ADC units in order to characterise both the MIP peak (~ 1700 ADCs) and the finger spectra ($\sim 300 - 500$ ADCs). During these calibration runs, a voltage scan was performed between 2550 and 2750 DAC units (corresponding to 53.3V to 57.5V) with 110-second measurements in steps of 10 DAC units. These runs were conducted daily for the first three months after deployment and later

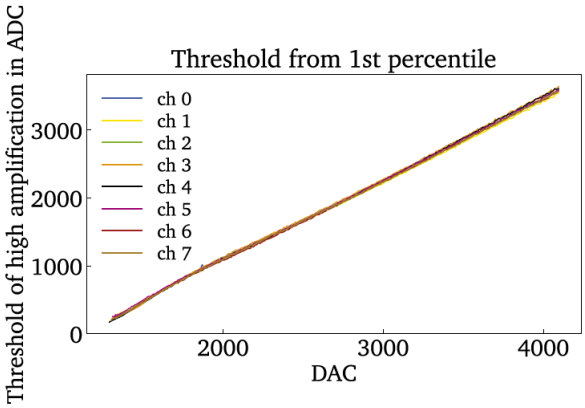

Figure 5.5: Relation of the Threshold set in DAC units to ADC units. Taken from [85].

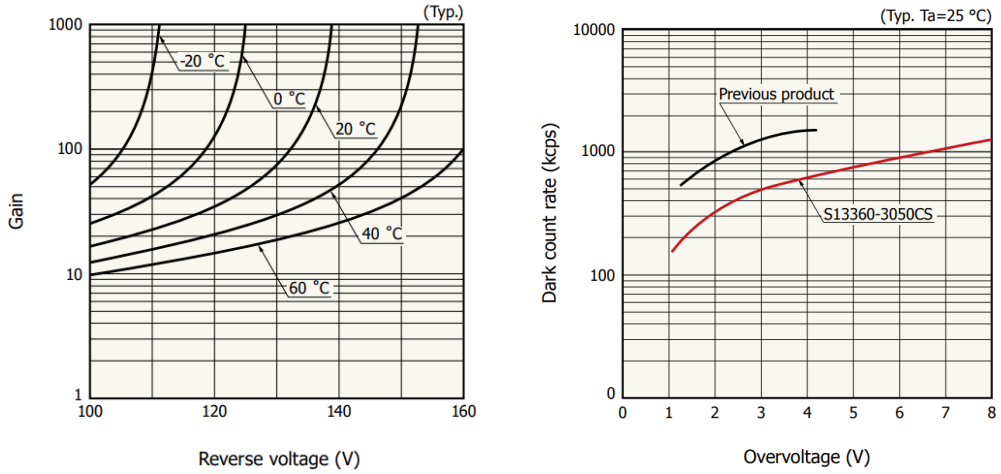

Figure 5.6: Left: Gain dependence on supplied Bias voltage and temperature for Multi-Pixel Photon Counter SiPMs; Right: Dark count rate with respect to OverVoltage [91].

at lower frequencies. Each calibration run took approximately 2.5 hours, with the remaining time allocated to air shower measurements. Figure 5.7 presents an example of a calibration run, showing charge histograms across all three gain channels for the entire voltage scan range for a single scintillation detector. As expected, an increase in bias voltage shifts the MIP peak to higher ADC values due to increased gain. At higher voltages, the MIP peak flattens, and single photoelectron peaks become smeared.

Gain Calibration: To extract the gain, the single photoelectron peaks at the start of the charge spectrum were individually fit with a Gaussian function. These peaks are expected to be equidistant, with their spacing indicating the SiPM gain as visible in Fig. 5.8 (left). To correctly estimate this gain, the initially peak is removed from the fit data, as it can overlap with the electronic pedestal in some cases. In addition, a threshold for significance of the peaks was applied to avoid inaccurate gain calculations due to smeared-out peaks. Fig.5.8 (right) presents the observed gain values over a full calibration run for one of the scintillators. The gain exhibits a linear dependence on the bias voltage in the measured range, as expected.

To calibrate the gain dependence of the SiPM on bias voltage and ambient temperature, the three quantities were studied over a period of 5.5months from January 15th to June 30th, 2023. This was done to cover the entire range of temperatures at the South Pole, with the Antarctic summer covered in January to March period, and the winter period covered by April

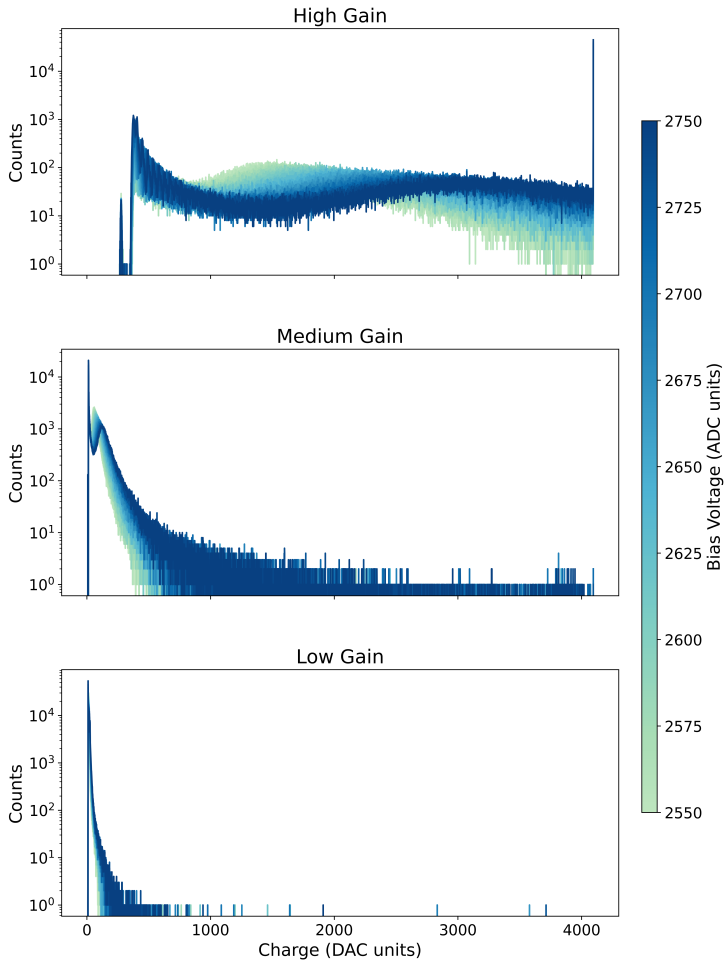

Figure 5.7: Charge histogram observed in the 3 gain channels of one of the scintillation detectors for a full calibration run before calibration is implemented. The colour bar represents the supplied bias voltage in units of ADC, varied with a step size of 10 ADC units.

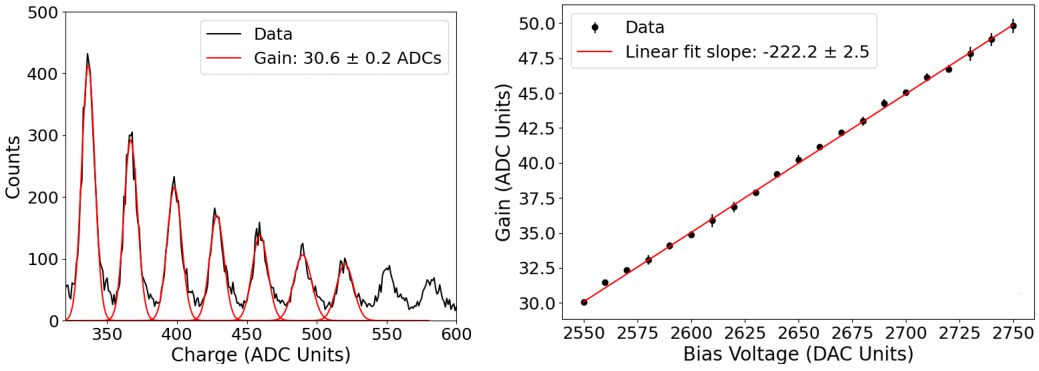

Figure 5.8: Features of the charge histogram data from the scintillation detectors. Left: Single Photo Electron (SPE) peaks; Right: Gain versus Bias Voltage for a single calibration run.

to June months. The dependence was modelled with a 2D plane of the form:

$$\text{Gain} = a * \text{V} + b * \text{T} + c, \tag{5.1}$$

where T is the temperature in °C and V is the output voltage. Figure 5.9 (Top) shows the output for one of the scintillation detectors. For the presented dataset, the best-fit parameters

are:

$$a = -0.352 \pm 0.001,$$
$$b = 0.100 \pm 0.0003,$$
$$c = -243.884 \pm 0.217.$$

This analysis was repeated for all scintillation detectors to stabilise their gain. Fig 5.9(Bottom) presents a histogram of residuals observed between the expected and observed data. The 2D plane fit agrees very well with the data, indicating a standard deviation of 0.17ADCs.

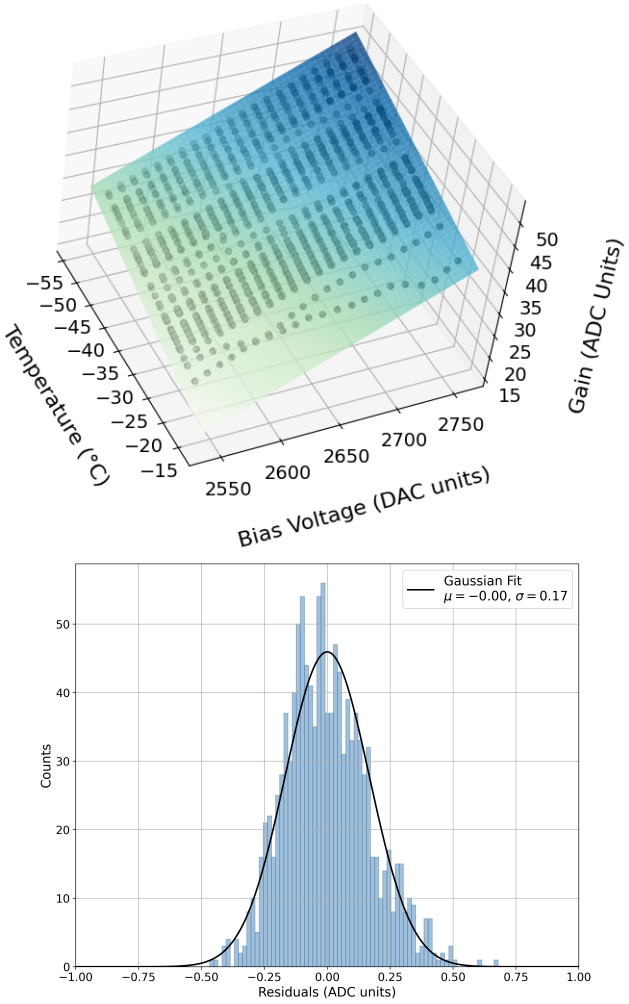

Figure 5.9: Top: Gain as a function of the temperature and bias voltage deduced from the calibration data. Bottom: A residual histogram to show the agreement between the data and 2D fit.

MIP peak calibration: As mentioned in Chapter 4, the uDAQ is equipped with 3 gain channels in order to measure cosmic ray secondary particles in a wide dynamic range. The deposited charge in each of the gain channels must be converted into a detector-independent quantity, which can then be utilised as a measure of the intensity of the shower at the detector location. This is done by characterising the MIP peak in all three gain channels as shown in Fig. 5.10.

When a minimally ionising particle (MIP) passes through a scintillation detector, it ionises the scintillation material but does not deposit all of its kinetic energy. The most probable energy loss per unit distance can be described by the Bethe-Bloch equation 2.8. Due to the thinness of the scintillation bars, the energy deposition exhibits intrinsic fluctuations, resulting

in a broad distribution rather than a sharp peak. Additionally, the occasional production of δ-rays (delta radiation), which is caused by single fast electrons, creates a characteristic tail in the distribution. This behaviour is well described by Landau's theory. Therefore, the MIP peak in all gain channels is characterised by a Landau function (ref. to 4.6). There is a visible background before the MIP peak in the charge spectrum, mainly from electromagnetic cascade particles from low-energy air showers and the dark spectrum of the SiPMs. This is characterised by an exponential function. The full charge spectrum in the high and medium gains is consequently modelled with a modified expo-landau function of the form equation 4.8. The exponential background fit is omitted in the lowest gain channel, due to the limited resolution of the exponential background in this gain channel. Finally, the pedestal or baseline is characterised by a Gaussian function.

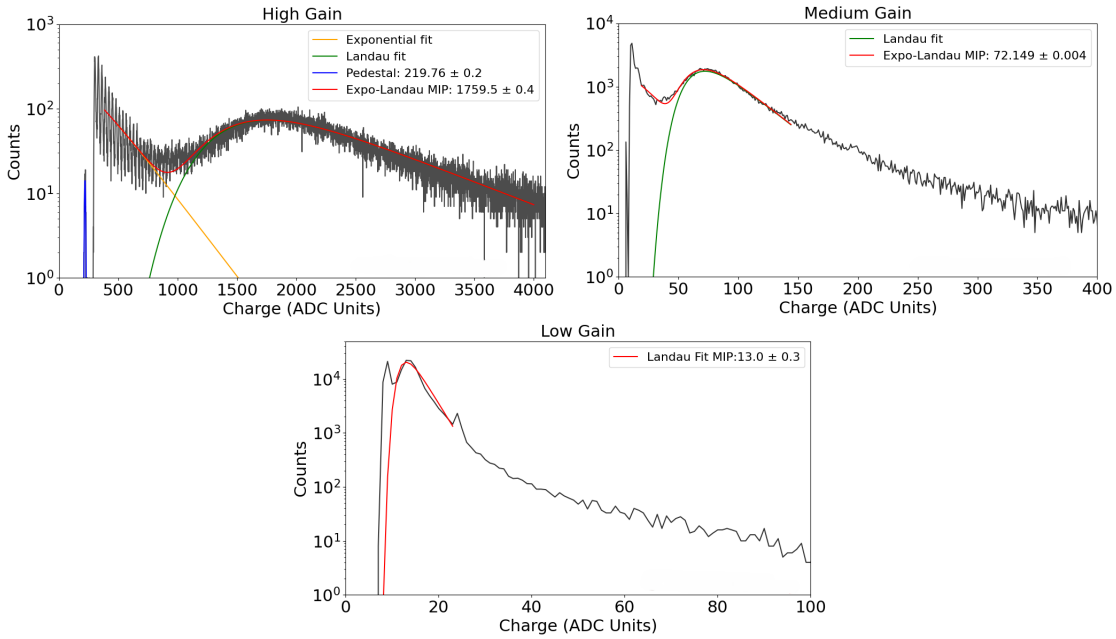

Figure 5.10: Example charge histograms in the three uDAQ gains for one of the scintillation detectors after calibration is performed. The high and medium gains are fit with an expo-landau function, whereas for the low gain, only the MIP peak is fit with a Landau function. Note the different x-axis ranges. The peak in the lowest gain at ~ 20 ADCs is expected to be a consequence of high gain to lowest gain transition, and is a uDAQ board artefact which must be further investigated.

Combining the gain and the MIP peak information, the light yield can be determined. This process involves correcting the MIP position relative to the pedestal peak, followed by deducing the fraction of the number of ADCs per unit MIP and the corresponding gain. The light yield is defined as α:

$$\alpha = \frac{\text{MIP} - \text{pedestal}}{\text{gain}} \tag{5.2}$$

where all three quantities are in ADC units.

The recorded signal is sampled by each of the gain channel ADCs on uDAQ simultaneously. In case the highest gain channel saturates, the medium gain and similarly the lowest gain can be leveraged for determining an accurate number of MIPs, allowing for a wide dynamic range. Therefore, the amplification factors between the three ADCs should be well known. These scaling factors can be determined by comparing the pedestal-corrected MIP peak positions in each channel. Figure 5.11 shows the obtained scaling factors for the medium and low gains. A scaling factor of 11.74 is obtained from low to medium gain. The medium to high gain exhibits a scaling of 23.73. Consequently, the low to high gain amplification is 280.

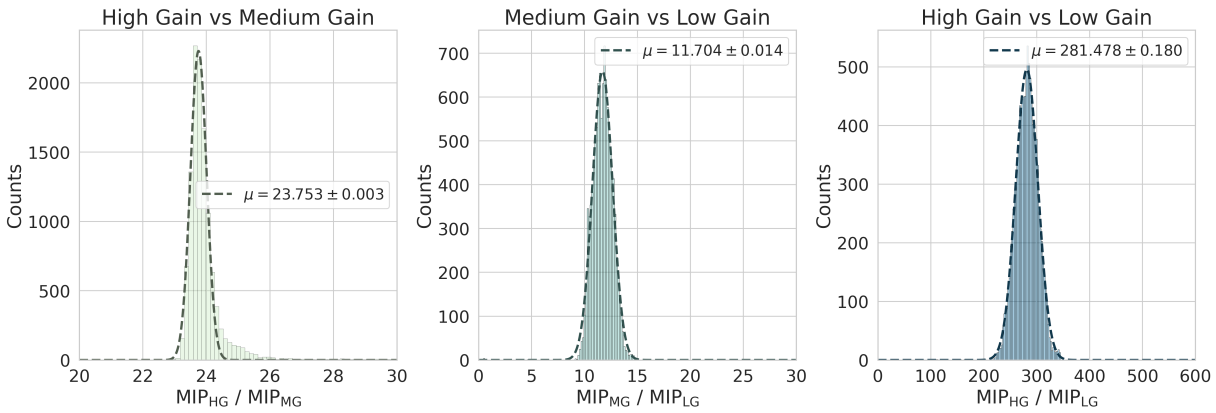

Figure 5.11: The scaling factors for the 3 gain channels are obtained and presented

Consequently, the temperature dependence can be investigated in relation to the number of MIPs through all gain channels. The conversion of ADC hits into units of MIP for all gain channels can be expressed by the equation 5.3, where the scaling factor for high gain is simply 1:

$$\text{Hit in MIP} = \frac{\text{Hit in ADC-Pedestal}}{\alpha * gain * scalingfactor} \tag{5.3}$$

Finally, the temperature calibration with respect to the MIP in units of p.es and applied bias voltage can be achieved. In this case, a second-order polynomial plane, of the form:

$$\text{MIP} = a\text{T}^2 + b\text{V}^2 + c\text{T} \cdot \text{V} + d\text{T} + e\text{V} + f, \tag{5.4}$$

is utilized for modelling the dependence. Figure 5.12 presents the modelled data on the plane. This approach accounts for the expected non-linear behaviour of the SiPM's photon detection efficiency as a function of over-voltage [91]. The agreement of the 3D fit with the data is shown in Fig. 5.12(top). An overall acceptable agreement is visible with a standard deviation of 0.38 MIPs. Some deviations from the fit are observed as a tail on the left of the plot Fig. 5.12(bottom). This can be attributed to the larger error in the MIP peak fits at higher bias voltages, when the MIP flattens out significantly. The best-fit parameters for the quadratic fit to the presented data are:

$$\begin{aligned} a &= -0.0054 \pm 0.0003 \\ b &= -0.0004 \pm 0.0006 \\ c &= 0.0024 \pm 0.0001 \\ d &= -6.8053 \pm 0.0831 \\ e &= 2.0499 \pm 0.0262 \\ f &= -2837.264 \pm 35.0371 \end{aligned}$$

Following this complete calibration chain, the raw data from the measurements is converted into the detector-independent, physical quantity called MIP. Following this, the Dynamic Range of the detectors can be determined to estimate the high end of their energy threshold.

Saturation and Dynamic Range

Following the temperature and MIP calibration, the air shower data is investigated for further studies on saturation and dynamic range of the detector system. The dynamic range of a

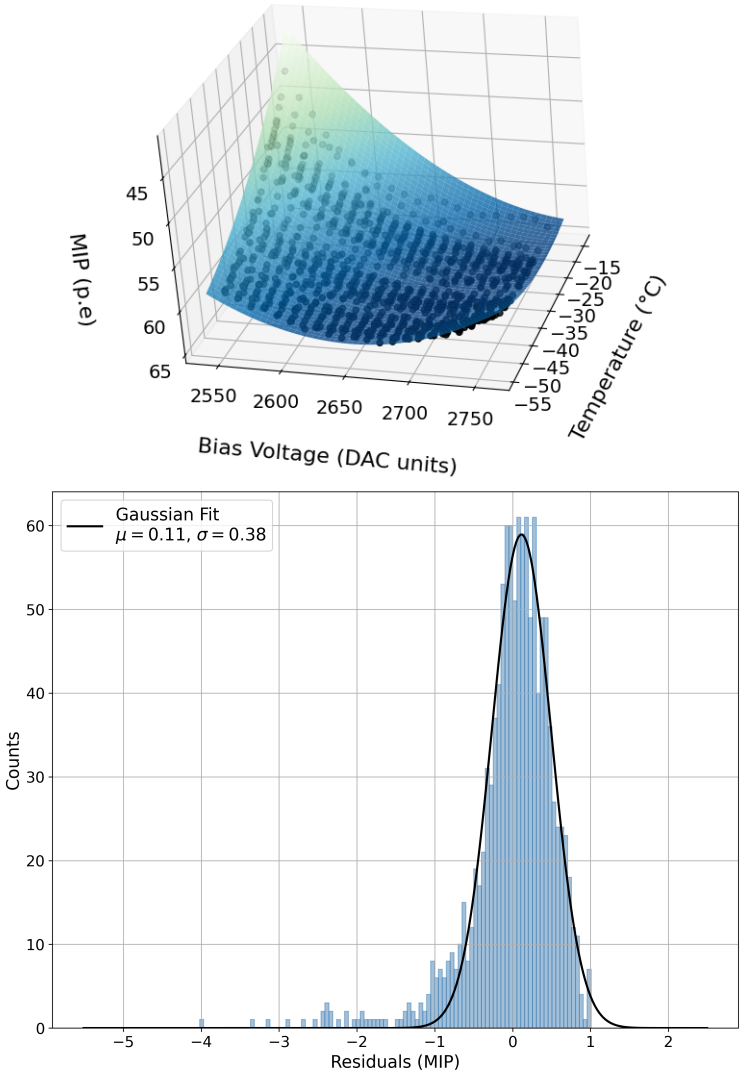

Figure 5.12: Top: A 3D representation of MIP-Temp-Voltage dependence. Bottom: The residuals of the fit are investigated to show agreement between observed and expected data.

detector defines the range of signal magnitudes it can accurately measure. As already elaborated, in the uDAQs this range is extended by incorporating three gain channels, where each successive channel increases the amplification factor. A theoretical estimate of the dynamic range can be obtained from the pedestal-corrected MIP peak position in the lowest gain channel and the total available ADC channels. Since the three gain ADCs are 12-bit, the total number of channels available is 4095 in each channel. A MIP corresponds to 5 ADC counts in the lowest gain, as illustrated in Fig. 5.10 at the operational bias voltage of 2550 in ADC units. Therefore, the dynamic range of the new uDAQs is expected to be approximately 800 MIPs for the gain of 30 ADCs.

However, a realistic estimation of the dynamic range can be achieved by examining the operational configuration of the dataset and, consequently, the gain at those configurations. One must further account for the saturation effects across the ADC channels. While the theoretical range assumes that saturation occurs only at the highest ADC of each gain channel, in practice, signals approaching the 12-bit limit may exhibit a distribution of saturation effects across the last few ADC channels. This occurs due to variations in signal response, non-linearity at high intensities, and potential electronic limitations. Additionally, an overlap between the three gain ranges is necessary to ensure smooth transitions and avoid gaps in measurement,

particularly where one gain channel saturates while the next has not yet become fully effective. Moreover, the SiPM itself can contribute to saturation effects, as its response becomes non-linear for a high number of incident photoelectrons [107]. This must be considered when determining the overall measured dynamic range.

For the data recorded throughout 2023, the bias voltage for shower measurements was set at 2650 ADCs, which is the mean setting of the voltage range in the calibration runs. This was done to maintain a nominal gain of the SiPMs throughout the possible temperature range. Fig 5.13 (a) shows the gain response as a function of bias voltage with temperature as colour. The gain ranging from 30 to 40 ADCs is observed. The observed MIP peak in high gain for this range corresponds to roughly 2500 ADCs as shown in Fig. 5.13 (b). This results in the light yield of 55-60 p.es per MIP. Keeping the scaling factors in mind, this corresponds to a dynamic range of 500-716 MIPs (dependent on temperature variations). This corresponds to a light yield of up to 39K p.es. The SiPMs are expected to exhibit slight deviations from linearity starting at 30K p.es [107]. The slight deviation from linearity is also visible in the same plot starting roughly around 2500 ADCs. This can contribute to the saturation of the SiPM.

Dynamic Range overlap study: The raw charge deposited in the three gain channels of the uDAQs was analysed to investigate gain continuity and saturation behaviour. Figure 5.14 shows the charge distribution in the medium and low gain channels for the period of January–June 2023. The medium gain channel exhibits saturation around 3800 ADCs, likely due to limitations in the readout electronics, as the SiPM response is expected to remain linear in this range. In contrast, the lowest gain channel shows no signs of saturation.

To further ensure continuity between gain channels, the same air-shower hits sampled by the three ADCs were compared, as shown in Figure 5.15. The saturated region of the medium gain was observed to be fully covered by the low gain channel, which begins sampling around 300 ADCs. This overlap confirms that a continuous and reliable dynamic range is maintained across the gain channels.

The conversion from ADC counts to MIPs is performed using the appropriate gain channel, depending on saturation. If the highest gain channel is saturated, the conversion is done using the medium gain. And if that too is saturated, the lowest gain channel is used. If all three gain channels are saturated, only a lower limit on the shower size can be estimated. To investigate SiPM saturation, the charge deposits were analysed in units of MIPs. Figure 5.16 presents the resulting charge spectrum. A saturation feature is observed around 500 MIPs, likely corresponding to the onset of non-linear behaviour in the SiPM response. This saturation threshold can be extended up to approximately 800 MIPs by lowering the SiPM gain and maintaining it at a stable value that corresponds to around 40 photoelectrons per MIP. The calibration discussed in this section will be used for this stabilization in the future with a uDAQ firmware that features real-time temperature correction. A test version of such a firmware was already utilized in the 2024 measurements.

Charge in neighbours

Following the saturation and calibration studies, the charge deposited in neighbouring scintillators should exhibit a 1:1 correlation. This is because both scintillators in each pair are positioned at a 5 m distance, which is small enough to observe the same region of the shower, ensuring that they detect similar particle flux. As shown in Fig. 5.17, this correlation is evident in the deposited charge between neighbouring stations. This serves as proof of similar functionality of the neighbour scintillators in the air-showers measurement mode and indicates that a good MIP calibration is achieved.

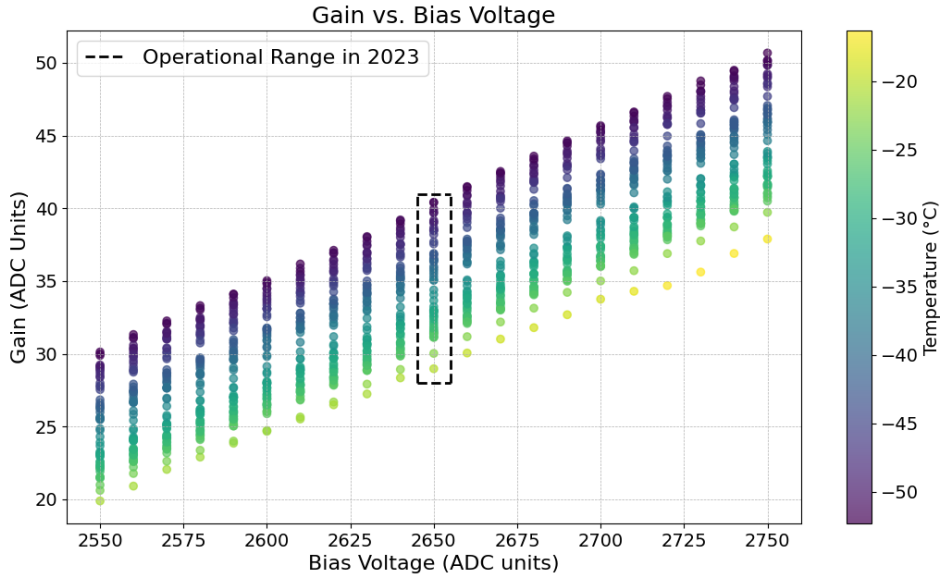

(a)

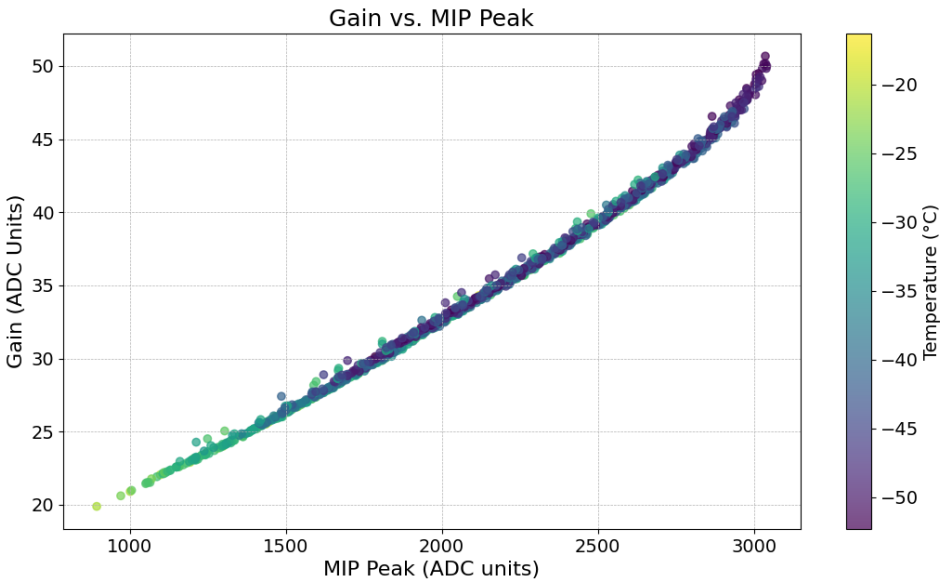

(b)

Figure 5.13: (a) The operational range for measurements in 2023 is highlighted by the dotted square. The plot represents the gain dependence on ambient temperature and supplied bias voltage in a 2D format. The temperature is represented by the colour bar. (b) The observed gain of the SiPM as a function of ADCs per MIP for varying bias voltage and temperature is presented.

The spread of $\Delta S = S1 - S2$, from this correlation, can be attributed to fluctuations in the shower's particle density and the error on deposited charge in an individual scintillation detector. These fluctuations arise due to the broad nature of the shower far away from the core position, where particles from various parts of the shower contribute to the signal. The observed standard deviation of 8 MIPs can be explained by these fluctuations in particle density, which lead to variations in the amount of charge deposited in each scintillator. This behaviour reflects the inherent variability in the shower geometry and the distribution of particles across the detection area. Further studies on the charge fluctuations to model the signal uncertainty from the individual detectors, as well as the influence of factors like shower size, zenith angle of incidence, and core distance, will be discussed in the following chapters.

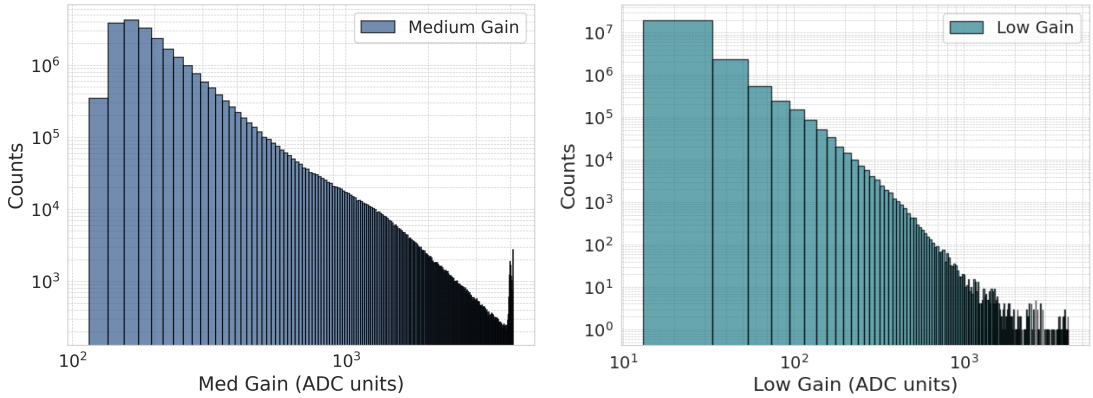

Figure 5.14: The saturation observed in the medium (left) and low (right) gain channels.

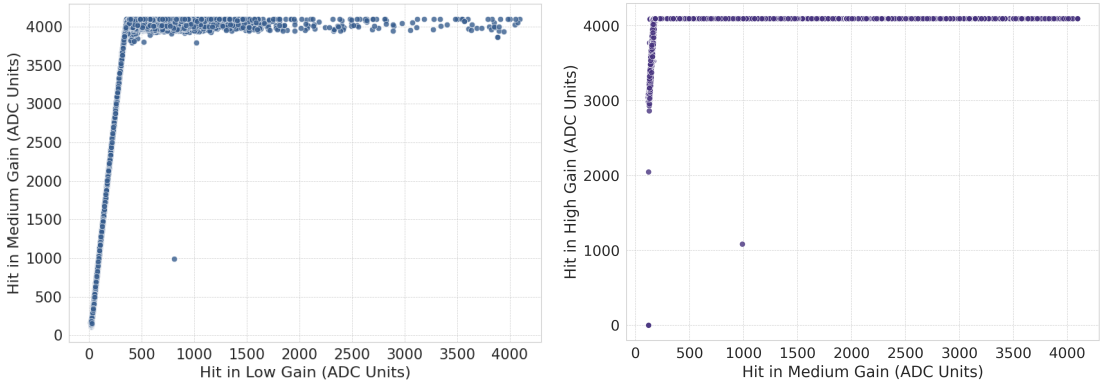

Figure 5.15: Medium-low gain (left) and high-medium gain (right) exhibit an overlap in the detection range. The highest gain channel is fully covered in the medium gain channel. The lowest gain channel also covers the medium gain fully.

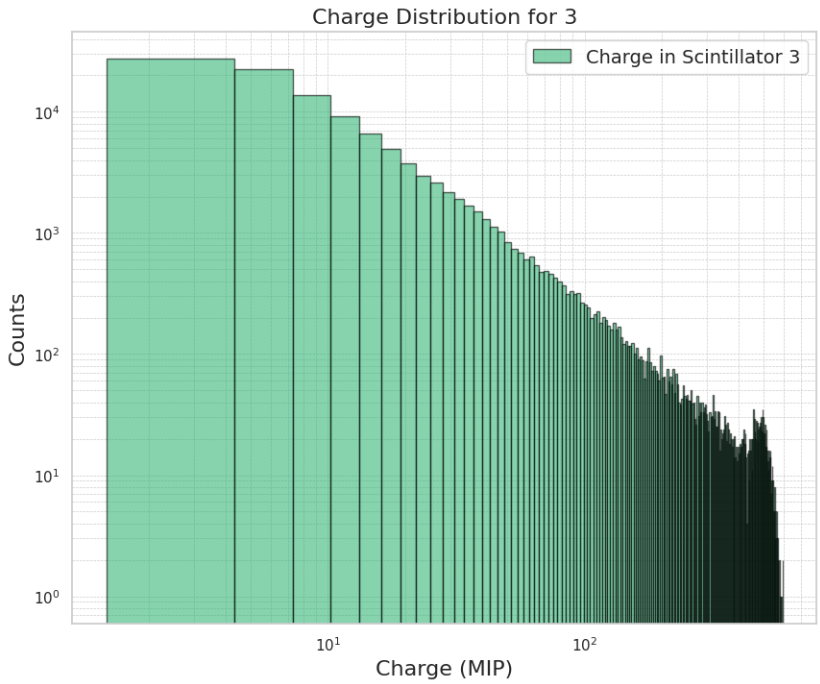

Figure 5.16: Charge spectrum observed in units of MIP after the MIP calibration.

Timing in neighbours

Similar to charge deposition, neighbouring scintillators are expected to register particle hits nearly simultaneously when detecting air showers, reflecting the spatial and temporal coherence

Figure 5.17: An example of charge correlation in neighbouring scintillators following the calibration in units of MIPs. The dashed line represents the best fit.

of particles within an air shower. Accurate timing between these detectors is critical for the precise reconstruction of shower properties. Consequently, a study was conducted to examine the relative timing between neighbouring scintillators.

Several factors can influence the timing of charge deposition, including the distance of the shower core from the detectors, the amount of deposited charge, the zenith angle of the incoming particles, and inherent electronic delays in the system. For the prototype scintillator stations, such electronic delays were identified and corrected in [85].

This analysis was revisited for the scintillators of Station 0 using data collected between January and November 2023. A total of approximately 16,000 showers were selected based on the following criteria:

- Events in which all eight scintillation detectors recorded hits within 1μs.
- Coincident detection with IceTop (will be discussed in Sec. 5.4).
- Shower cores reconstructed by IceTop to lie within 100 m of the FieldHub.
- Zenith angles reconstructed by IceTop up to 25°.

Figure 5.18 shows the mean time differences (Δt) between neighbouring scintillators. For all four pairs, the mean values lie well within 1ns, consistent with the timing precision expected from the uDAQ system. The observed spread in the distributions likely arises from variations in deposited charge, which can reflect the distance from the shower core and the stochastic nature of particle arrival. Additional contributions may include propagation effects within the scintillators and the 5 m separation between neighbouring detectors. Pair 0-1 is the central pair, which is expected to be at an average closer to the shower core than the remaining 3

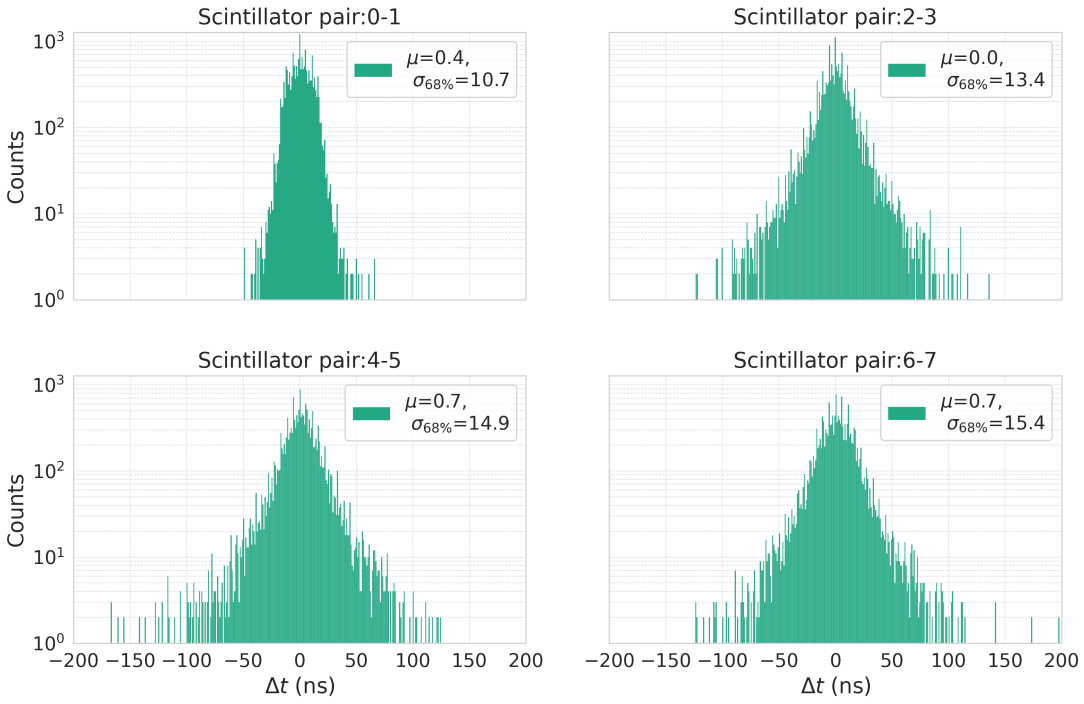

Figure 5.18: Difference in timing for particles detected from the same shower by neighbouring scintillators.

pairs. This explains the smaller standard deviation for this pair. This result also presents proof of the uniform functionality of the neighbouring scintillators.

To further investigate the accuracy and factors affecting timing between neighbours, the Δt distributions were analysed with respect to deposited charge, core distance, zenith angle, and the shower size parameter S_{125}. These dependencies are explored in detail in the following chapter.

5.3.2 Radio Characterization

While temperature calibration was necessary for the scintillation detectors, it was not required for the swapped antenna, as its new electronics were pre-calibrated and exhibited minimal temperature variation [50]

The radio signal from air showers is frequency dependent, with lower frequencies having higher signal amplitude. A stable gain translates to a well-understood signal with lower systematic uncertainty. All components in the electronics chain used for recording the radio signals are characterised in the laboratory to ensure that all features in the gain are included in the electronics response. Figure 5.19 illustrates the gain as a function of frequency. It is evident that the gains of the Low Noise Amplifier (LNA), the cable, and the radioTad (the filtering and amplifying board) remain relatively constant within the desired frequency range of 70 MHz to 350 MHz.

The overall gain behaviour of the system is accounted for in the analysis of the radio signals [82]. The overall gain behaviour is shown in the figure, but it is the individual component gain that is independently included in the electronics response. The overall gain is only for representative purposes. Also, the LNA is +40dB than shown in the figure, and so is the overall gain. The calibration of data measured with the radio antennas was also performed during the commissioning period within a parallel work at KIT, but was not the focus of this thesis.

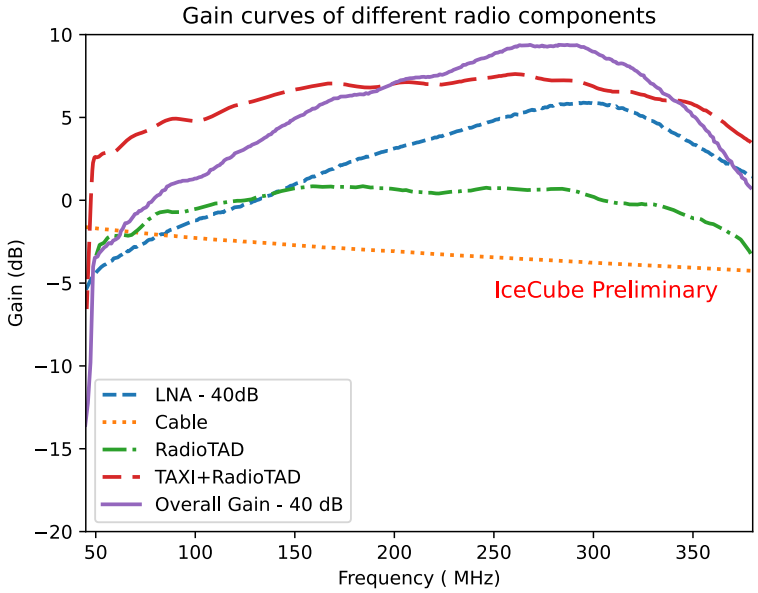

Figure 5.19: Electronics response radio components. Taken from [82]

5.4 SAE data processing

Following the calibration of individual detector data, it is crucial to establish a robust and scalable software pipeline for processing and merging data within the standard IceCube framework. This will facilitate analysis that can be done on a multi-detector level, for example, coincidence measurements with the IceTop array, and even In-Ice data.

The foundation of this framework was originally developed for processing data from the prototype station, involving the initial uDAQ firmware, which changed significantly in August 2022. Within this thesis, significant modifications have been made to adapt the pipeline to new uDAQ firmware versions, which featured updated data formats and readout. A major focus of this thesis has been the scintillator data processing, where most of the core modifications were implemented.

5.4.1 Processing Workflow

The flowchart in Fig. 5.20 outlines the structure in which SAE data is handled, beginning with raw data collection, followed by pre-processing, and followed by merging of the data from both detector types. This is currently developed for a single station data, but it is scalable for the full array. The workflow is explained as follows:

- **Data Acquisition:** The process starts with three primary datasets described below. It is foreseen to also include in-ice information in the future, but it is omitted here because the pipeline is in the development and validation stage, which requires IceTop for benchmarking.
  - Scintillator Data: from the scintillation detectors
  - Radio Data: from the radio antennas
  - IceTop L3 Data: data from the IceTop array already reconstructed and processed
- **Processing of the individual dataset:** The data from scintillation and radio detectors is converted into i3 files, which are the standard file format used within the IceCube

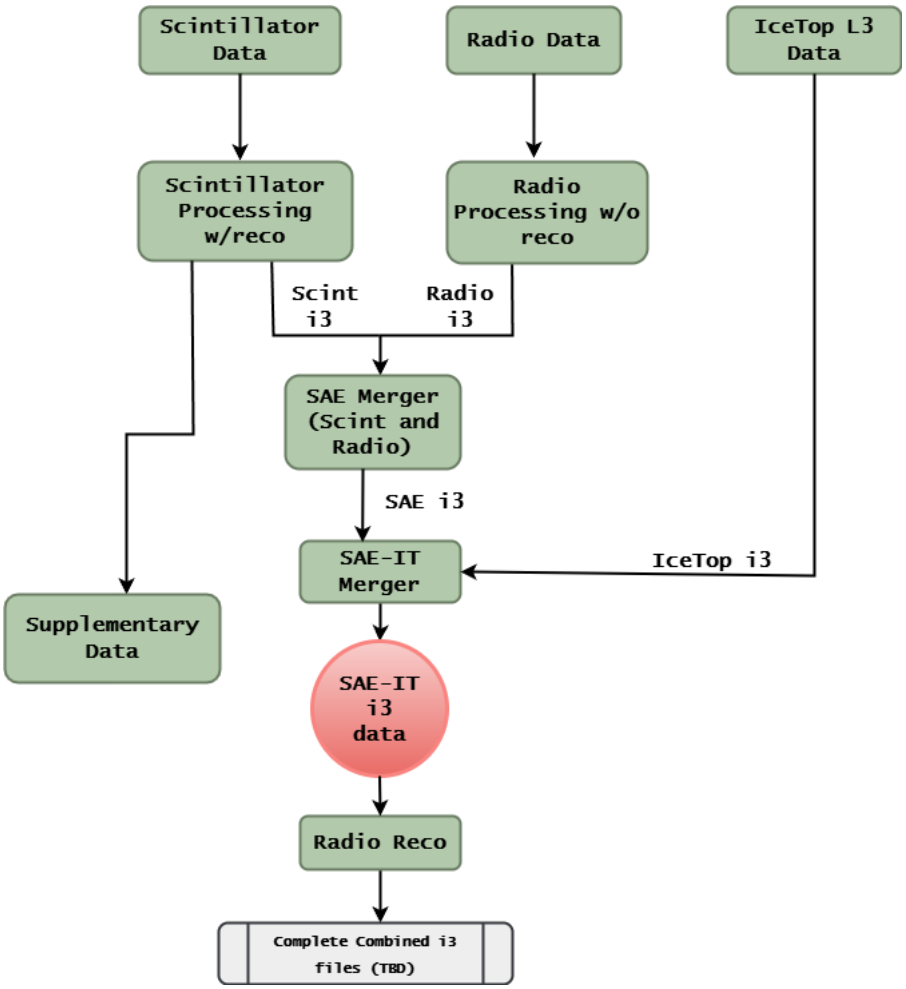

Figure 5.20: The processing workflow of the SAE data is described with this flowchart. The data from the 2 detector types, scintillators and radio antennas, is processed in parallel in combined into air showers. These are further checked for coincidences with IceTop data, and result in a combined dataset with 3-fold coincidences. Currently, the radio reconstruction module is not incorporated into the combined pipeline, but it is well developed and foreseen in the near future.

collaboration for serial processing of data. The data is assigned the same run numbers as IceCube runs by matching the time of the measurements with a goodrunlist.

- Scintillator Data undergoes a multi-step processing, which will be discussed in detail in Fig. 5.21. This includes calibration and reconstruction of the measured air showers. Supplementary information like baseline, configuration settings, etc. are also converted and stored at this stage.
- Radio Data is processed without reconstruction at this stage into i3 files, maintaining raw signal integrity for later steps. The timestamps of the Radio data is shifted by a constant of $+0.089s$ (Appendix B.3). This offset is due to the TAXI electronics, as the timestamp is sent to the scintillators via a fanout board, which could cause an additional delay.

- **SAE Merger:**
  - The SAE Merger combines Scintillator and Radio data into a unified dataset, producing an SAE i3 output file for each run. The events are combined based on a $10\mu s$ coincidence window.

- **Integration with IceTop Data:**
  - The SAE i3 dataset is further merged with IceTop L3 (level3) data via the SAE-IT Merger, generating a combined SAE-IT dataset. This is implemented for events with a start time falling within a corresponding IT event start-stop time. A typical IT event is generally $20\mu s$ long.
- **Radio Reconstruction:**
  - For the selected candidate, Radio events within coincidence with the scintillator and IceTop data, a reconstruction is performed using the module called radcube. This reconstruction step is not performed at an earlier stage at the moment. This will be combined at the pre-processing stage in the future.

5.4.2 Scintillator Data Processing

This section provides a detailed description of the scintillator data processing framework. As part of this thesis, the processing pipeline was modified to accommodate the uDAQ firmware update implemented in August 2022. These modifications ensured compatibility with all firmware versions used until 2023. While minor adjustments will be necessary for the 2024 firmware versions, the overall structure of the output remains largely unchanged. In addition, the framework discussed in this section is for 1 station, but is developed in a way that it can be scaled for multi-station data for future deployments.

uDAQ Firmware Update

In August 2022, the firmware of the uDAQs was updated for the prototype station, which was also used for Station 0 measurements in 2023. The newly implemented firmware developed by Tim Bendfelt [108] was `udaq-dist-mar_15_2022_b`. This update introduced changes in the output files for hitbuffer measurements and completely removed the histogram measurement mode. It served as an intermediate step towards automated temperature correction measurements, planned for future firmware versions. The main improvements introduced by this firmware are outlined below:

- **Transition to a Multi-threaded DAQ System:** The new firmware, named FieldHub (FH), was designed as a multi-threaded DAQ application, capable of executing a single data-taking run for all scintillators simultaneously. In contrast, the previous firmware operated sequentially, requiring a shell script to activate each scintillator one by one.
- **Extended Measurement Duration:** The previous firmware limited measurements to 110 seconds due to buffer constraints, which required periodic emptying before the next measurement could begin. In the FieldHub firmware, this limitation was eliminated, allowing significantly longer measurement runs of up to 23 h / day (approximately $\times 2$ longer). This was implemented by replacing the user-space serial driver with a kernel-space driver, increasing the overall throughput of uDAQ readout. In addition, the uDAQ hit buffer was expanded from 32Kbs to 64Kbs, which in turn increased readout resilience to occasional long CPU scheduling pauses [109].
- **Changes in Data Storage and Formatting**
  - The output run file includes both soft-trigger (baseline) hits and particle hits as before, stored in a COBS[2]-decoded format within a binary file for each channel. Previously, data was COBS-encoded.

[2]Constant Overhead Byte Stuffing

  - The monitoring data for each run was stored as a text file per channel with the FieldHub firmware, containing the configuration settings, run duration, and a single temperature readout at the start of the measurement. Previously, this information was stored in an encoded binary file. However, since only a single temperature measurement is recorded per run, temperature monitoring data is lost during long measurement sessions using the FieldHub firmware.

- **Change in Channel Classification/Numbering:** The previous firmware assigned for each scintillator 0-7 channel numbers. The FieldHub firmware assignment ranges from 1 to 8 channels.

Processing Workflow

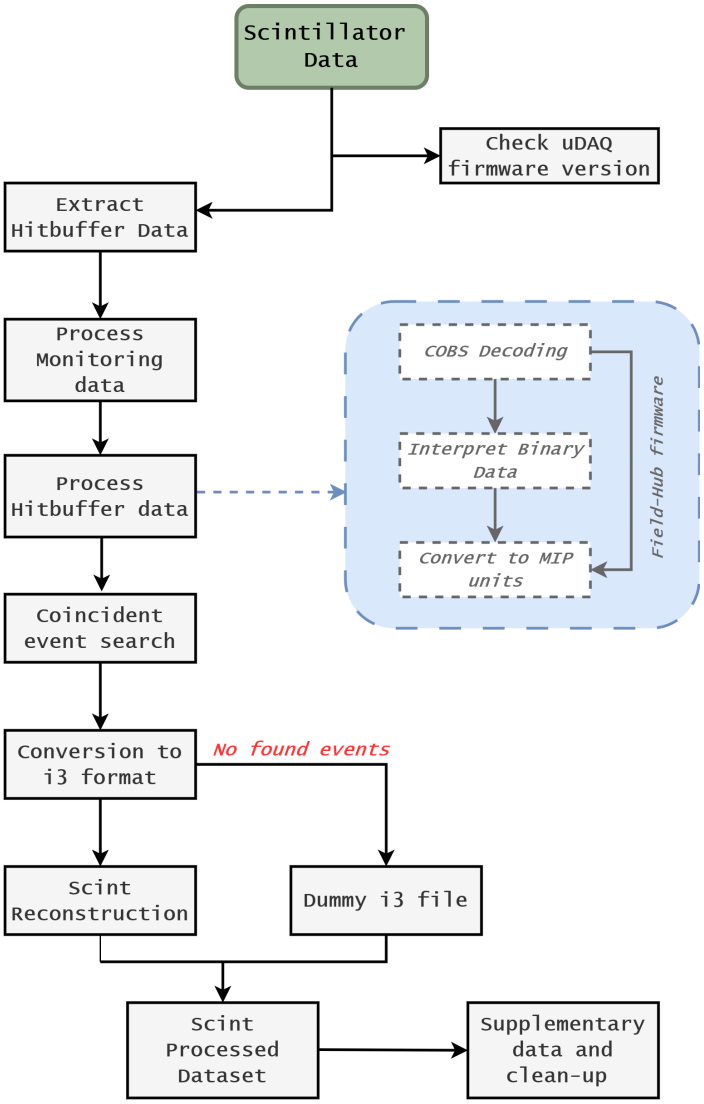

Figure 5.21: The processing workflow of the scintillator data. The green box labeled "Scintillator Data" is the same as one of the data streams introduced in Fig. 5.20.

The flow chart in Fig. 5.21 illustrates the data processing pipeline for scintillator data. Key stages include:

- **Firmware Classification and Hitbuffer Data Extraction:** Data extraction is performed using separate custom functions depending on the firmware version.

- **Monitoring Data Processing:** The monitoring data from both firmware versions is handled separately. The bin file (old firmware) is COBS-encoded and undergoes a checksum validation for each frame to extract monitoring data such as temperature and timestamps. The text file (new firmware) is directly read for monitoring information. Both outputs are then standardised for further processing.

- **Hitbuffer Data Processing:** This step converts raw ADC data from the uDAQ into physical units of MIPs. For both firmware versions, binary data is interpreted, with an additional COBS decoding step for the old firmware. Temperature information from monitoring files and MIP calibration data (Sec. 5.3.1) are used to convert raw ADC counts into MIPs. The detector baseline is accounted for in each measurement to ensure accurate MIP classification.

- **Coincident Event Search:** A sorting algorithm groups particle hits arriving within a $1\,\mu s$ time window into single air-shower events.

- **Conversion to i3 Format:** Identified events are structured into frames, forming an i3 file. If no events are found, a dummy i3 file is created.

- **Scintillator Reconstruction:** Air-shower candidate events undergo a three-step reconstruction process previously developed by Agnieszka Leszczynska [78] for the SAE. The reconstruction results are added to the corresponding frames in the i3 file. Further details on the method and its performance are discussed in the following chapters.

- **Supplementary Dataset and Clean-up:** The framework includes a debug mode that allows saving metadata such as baseline data, raw ADC values, and intermediate processing steps. This also gives a unique possibility to keep the calibrated data and utilise it for individual studies, for example, coincidences with In-Ice, muon density calculations, etc.

Temperature Correlation with Weather Station

Due to the limited temperature readout from the FH firmware, an alternative source for scintillator temperature data was explored. Since the relevant temperatures correspond to the ambient conditions surrounding the scintillation detectors, a nearby facility with regular temperature monitoring could be used. The temperature data from the South Pole Atmospheric Research Observatory (ARO) is utilised as part of the IceCube Live information and was also used for scintillator temperature calibration.

In austral winter, the temperatures at the weather station and the scintillation detectors are expected to be similar. However, in austral summer, solar exposure can create an offset between the temperatures recorded by the ARO weather station and those of the scintillators. To account for seasonal variations, the temperature data from the period of 2021 and 2022 during which regular temperature monitoring was available was taken. It was divided into winter (March–September) and summer (October–February) periods.

Figure 5.22 shows the correlation between IceCube Live temperature data and scintillator temperature sensor measurements. To reduce the impact of outliers, a Random Sample Consensus (RANSAC) algorithm was applied, providing a robust linear fit for both the slope and intercept. A slope of approximately 1 suggests strong agreement between the two datasets. Notably, the intercept value in the summer months reveals an offset of about 9°C. This offset is incorporated into the temperature calibration within the processing framework for the summer months.

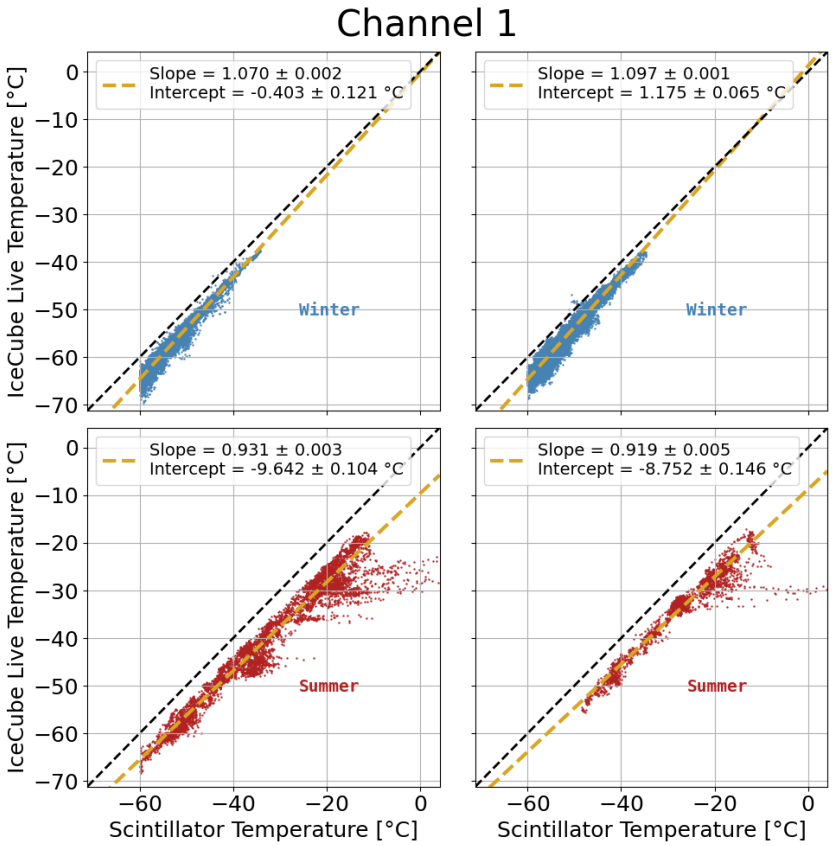

Figure 5.22: The IceCube Live Temperature observed in the winter (top) and summer (bottom) periods of data taking before the uDAQ firmware update, for the years of 2021 (left) and 2022 (right) without FieldHub. A correlation between the two temperature monitoring datasets is studied. An offset of approx. 10° is observed for the summer months. The yellow lines indicate a linear fit.

Coincidence Offset in 2023

For the merger of SAE data with IceTop data, it is crucial to search for coincidences within the correct time window. In the 2023 dataset, approximately $500K$ showers were recorded with Station 0, with a scintillator multiplicity greater than 5. However, the number of detected coincident events was negligible, indicating a possible search window mismatch or time offset. To investigate this, a sorting algorithm was implemented to search for six nearest IceTop neighbours for each SAE event, using the starting timestamp of the SAE event as a reference. Only those IceTop events were included for this search that met the $IceTopSTA5$ condition. This is 5 5-station trigger condition which indicates that a shower was observed by at least 5 stations of IceTop, which is more likely to be observed by the SAE station as well.

Figure 5.23(top) presents the deviation between the reference SAE event time and the nearest IceTop event start times. Since a typical IceTop event lasts approximately 20 μs, compared to an SAE event lasting around 2 μs, the expected distribution should exhibit a peak centred around zero. However, for the 2023 data, this peak was observed at a 1 second offset. To validate the method, the same approach was applied to the 2022 dataset, where SAE-IceTop coincidences were successfully identified. As shown in Figure 5.23(bottom), the expected peak appears at 0 seconds. Therefore, for the 2023 dataset, an additional 1 second offset was applied to the SAE timestamps, resulting in a significant increase in detected coincident events. This offset was later traced back to a White Rabbit firmware bug, which was identified and fixed in 2024.

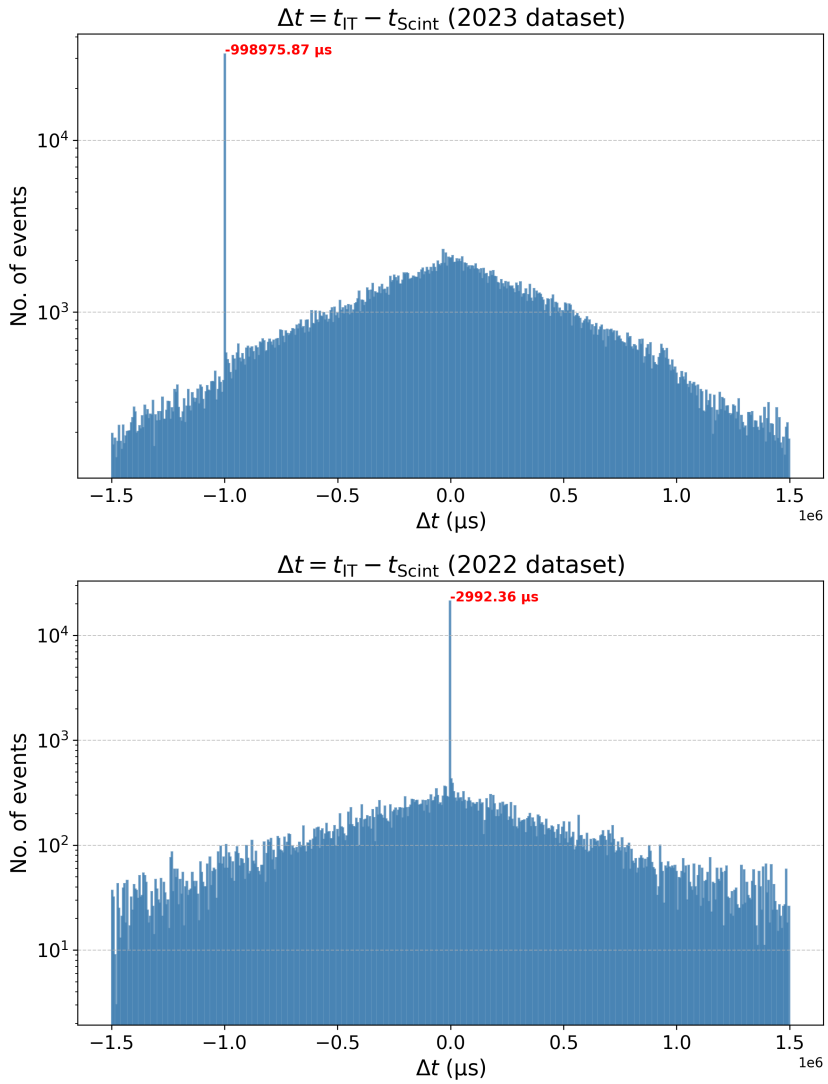

Figure 5.23: (Top) Deviation of reference SAE event time from the nearest IceTop event start times in 2023, showing a 1s offset. (Bottom) Expected peak at 0s in 2022 data, confirming correct time alignment.

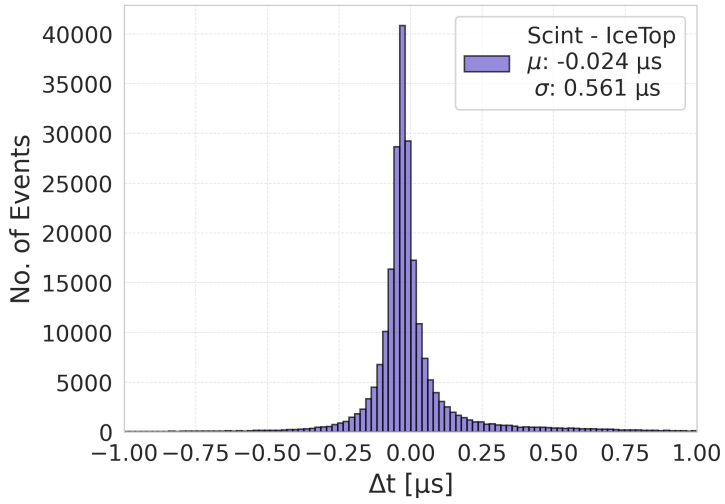

Figure 5.24: The plot shows the difference in the arrival time of the shower core seen by SAE and IT.

After applying the coincidence offset corrections, the SAE-IT coincidences were found. A total of 227,228 coincidences were found for the period of January-November 2023. The difference in their core times is shown in Fig. 5.24. This distribution in Fig. 5.24 has been offset corrected, to show that the events are observed within $2\mu s$ window. In reality, a constant offset of $195ns$ between the SAE and IT timing is present. This is primarily due to the electronics difference between IT and SAE, as a universal clock is not shared by the two systems. The uncorrected distribution is included in the Appendix B.5.

Chapter Summary:

Following the upgrade of the prototype station with the scintillation detectors produced within this work (chapter 4), a thorough on-ice calibration was performed using the calibration data from the first half of the year 2023. The baseline stability has been verified. In addition, the SiPM gain, and consequently the light yield with temperature variations, was characterised to achieve air-shower data in physical units of MIP. The dynamic range of the detectors was also studied with a realistic reach of 500 MIPs with the current setup. Furthermore, a scalable data processing for the scintillation detectors was improved. Finally, after resolving the timing of scintillation detectors with respect to the IceTop timing, a sizeable dataset of 227 K events with greater than 5 multiplicity was obtained for the period of Jan-Nov 2023.

Chapter 6

Data-driven Reconstruction of Air Showers

Since cosmic-ray detection with surface-based detectors is indirect, the spatial and temporal signal distributions are essential to infer the properties of the air shower and identify the primary particle. The calibrated data from the scintillation detectors is reconstructed using an established method previously introduced in the processing pipeline (see Fig. 5.21). This reconstruction technique was originally developed in [78] based on simulations of the entire planned surface array using the `RockBottom` framework [110], and its functionality was subsequently verified with 3 months of prototype station data from the year of 2021 in [85]. In this work, the existing method was further optimised through a data-driven parametrisation of key shower observables, namely the lateral distribution, signal variance, and timing model. This parametrisation was performed using data collected with Station 0 scintillation detectors within the entire year of 2023. This chapter outlines the reconstruction methodology, including the event selection criteria relevant to the subsequent studies, additions to the existing reconstruction applied to improve the quality of the air-shower dataset, and the data-driven parametrizations developed to enhance reconstruction performance.

6.1 Air Shower Reconstruction

Following the first interaction of a high-energy cosmic ray with the atmospheric particles, an extensive air shower develops both longitudinally along the shower axis and laterally due to transverse momentum in hadronic interactions and Coulomb scattering [20]. While the bulk of the particles follow the direction of the primary particle, these transverse effects cause a lateral spread, with particles farther from the shower axis arriving later at ground level. This time delay arises from both geometric path length differences and variations in particle production heights. As a result, the shower front assumes a curved shape. The curvature becomes more pronounced at larger radial distances from the core. Figure 6.1 illustrates the main components of an air shower, including the curved shower front. The point where

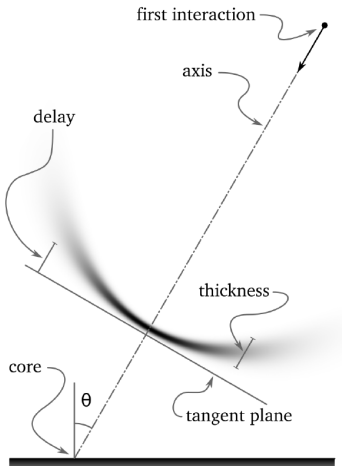

Figure 6.1: Schematic view of an air shower and its key features. The dotted line represents the shower axis. The curved shower front follows the axis of the primary particle. Taken from [78].

the shower axis intersects the ground is referred to as the *shower core*. By using an array of detectors, it is possible to measure the fluctuations in signal arrival times and their spatial spread. With sufficient spatial and temporal information, a reconstruction method can be applied to determine key shower parameters, including the core position, arrival direction, and lateral distribution. The employed air shower reconstruction follows a three-step iterative procedure. Each step minimises a negative log-likelihood function by fitting the observed spatial or temporal or both distributions, with a suitable model function.

First Estimates

A good initial guess for the core position and shower direction is critical for achieving a reliable reconstruction. As a first guess, the shower core is estimated as the signal-weighted average position of all triggered detectors [78]:

$$\vec{r}_{\text{core}} = \frac{\sum_i S_i \vec{r}_i}{\sum_i S_i}, \tag{6.1}$$

where S_i are the recorded charge in MIPs, and r_i are the scintillation detector positions. A planar approximation is used for the shower front, yielding the zenith and azimuth through the direction vector $\vec{n} = (\vec{n_x}, \vec{n_y})$ as well as the core time(t_0) through a χ^2 minimisation:

$$\chi^2 = \sum_i \left(\frac{t_i - t_0 + \frac{1}{c}(x_i n_x + y_i n_y)}{\sigma_i} \right)^2, \tag{6.2}$$

where t_i are the times of hits and x_i, y_i are the positions of the detectors. The z component is ignored as the scintillation detectors are roughly at the same height.

Lateral Distribution

The lateral distribution of the deposited signals is modelled using a Double Logarithmic Parabola (DLP) function, parametrised by a reference signal S_{ref} (signal at a reference distance R_{ref}) and a slope parameter β [78]. The curvature of the shower is described by the κ parameter. This function captures both the radial normalization and curvature of the signal profile in the detector plane:

$$S(r) = S_{\text{ref}} \left(\frac{r}{R_{\text{ref}}} \right)^{-\beta - \kappa \log_{10}(r/R_{\text{ref}})}, \tag{6.3}$$

The R_{ref} in this case is the expected distance from the shower core, at which the shower-to-shower fluctuations are stabilized for the geometry of the detector array. For the IceTop array, this is 125 m. In order to compare the scintillator response to IceTop and leverage a similar array footprint, the same reference distance is utilized in the scintillator reconstruction.

The reconstruction employs a minimisation of the sum of the log likelihoods, taking into account different charge deposit scenarios for a given air shower. The full log-likelihood function consists of three terms,

$$\ln L = \ln L_{\text{tr}} + \ln L_{\text{sa}} + \ln L_{\text{si}}, \tag{6.4}$$

as follows [78]:

- ***Triggered Detectors:*** The signals above 2 MIP are expected to have a Gaussian distribution, while smaller signals can deviate from this; therefore, the likelihood is

defined separately as, For $S_i \geq 2$ MIP:

$$\ln L_{\mathrm{tr}} = -\sum_i \left[\frac{1}{2} \left(\frac{S_i - S_i^{\mathrm{LDF}}}{\sigma_i} \right)^2 + \ln\left(\sqrt{2\pi}\sigma_i\right) \right] \tag{6.5}$$

For $S_i < 2$ MIP:

$$\ln L_{\mathrm{tr}} = -\sum_i \left[S_i^{\mathrm{LDF}} - S_i \ln\left(S_i^{\mathrm{LDF}}\right) + \ln \Gamma(S_i + 1) \right] \tag{6.6}$$

- ***Saturated Detectors:*** For detectors that record signals above the measurable range, a saturated probability based on the error function is used

$$\ln L_{\mathrm{sa}} = \sum_i \ln \left[\frac{1}{2} \operatorname{erfc} \left(\frac{S_{\max} - S_i^{\mathrm{LDF}}}{\sqrt{2}\sigma_{\mathrm{sa},i}} \right) \right] \tag{6.7}$$

- ***Silent Detectors:*** These are detectors expected to not record a signal due to the expected signal to be below the detector threshold. Their contribution is modelled through a non-detection probability:

$$\ln L_{\mathrm{si}} = \sum_i \ln(1 - P_{\mathrm{hit}}), \tag{6.8}$$

where S_i is the signal recorded by the i^{th} detector, S_{LDF} is the expected signal based on the chosen LDF model, DLP in our case, and σ is the square root of the signal variance. P_{hit} is the probability that a detector is triggered based on the expected signal strength relative to its threshold [78]. Signal variance weighting accounts for intrinsic detector fluctuations, allowing a distinction between variations originating from the detector and those inherent to the air shower itself, such as stochastic effects in shower development and deviations related to the shape of the lateral distribution. It is therefore essential to develop a realistic signal model based on data, in order to account for possible inaccuracies in detector simulations.

Timing Distribution (Shower Front)

The time of arrival of the shower front is modelled with a parabolic function, where r is the distance to the shower core.

$$\Delta t(r) = ar^2 + b \tag{6.9}$$

The associated timing likelihood is given by the following equation. It accounts for signal-weighted timing residuals as well as corresponding signal fluctuations:

$$\ln L_t = -\sum_i \sqrt{S_i} \left[\frac{1}{2} \left(\frac{\Delta t_i}{\sigma_{t_i}} \right)^2 + \ln\left(\sqrt{2\pi}\sigma_{t,i}\right) \right] \tag{6.10}$$

Table 6.1 summarises the parameter settings used in the three-step iterative air-shower reconstruction procedure. Each step involves different configurations of fixed and free parameters, step sizes, and boundary conditions to ensure stable minimisation and accurate reconstruction.

Table 6.1: Overview of the iterative reconstruction steps. Taken from [78]

Step	Free Parameters	Fixed Parameters	Likelihood Minimized
1	$x, y, S_{\text{ref}}, \beta$	θ, ϕ, t_0, a_t	LDF only
2	$\theta, \phi, t_0, a_t, S_{\text{ref}}, \beta$	x, y	LDF + Timing
3	$x, y, S_{\text{ref}}, \beta$	θ, ϕ, t_0, a_t	LDF only

6.1.1 Proposed Optimization

Although the reconstruction method described above is well established, there remains room for improvement in both the dataset preparation to account for the influence of uncorrelated particles and the determination of the core position, which is estimated using a relatively small number of detectors in the case of a single station. To address these limitations, a pulse cleaning was applied to remove uncorrelated particles, possibly muons, which have a longer path length, often unidentified in coincidence searches, which could otherwise bias the reconstruction results. Furthermore, a fourth step was introduced in the reconstruction sequence, and called L2 reconstruction for clarity. This step involved a repetition of the time-front minimisation using the core position provided by the IceTop reconstruction.

Temporal Pulse Cleaning

For efficient identification of coincident air shower signals, a maximum expected time delay must be considered. This includes both (i) the time a shower takes to cross the entire station, and (ii) the projected time difference between detectors due to the shower inclination.

The total extent of the SAE prototype station is approximately 135 m, corresponding to a maximum shower crossing time of about 500 ns for horizontal showers. Including electronics and shower front uncertainties, coincidences are therefore searched within a 1 μs time window during event building [85]. For pulse cleaning, however, the relevant delay arises from detector-to-detector projection along the shower front. For two detectors separated by a distance d, the maximum expected delay is

$$\delta t = \frac{d \cdot \sin\theta}{c}, \tag{6.11}$$

where c is the speed of light. Although the full detector separation is 135 m, the shower front typically intersects near the geometric center of the triangle. Thus, the effective maximum delay is governed by the station's arm distance, i.e., $d \approx 70$ m, yielding $\delta t \approx 230$ ns for horizontal showers. However, highly inclined showers are geometrically disfavored and inefficiently detected due to the reduced effective area ($A_{\text{eff}} = A \cdot \cos\theta$) and the thin (1 cm) vertical profile of the scintillator bars. Consequently, practical reconstruction is limited to zenith angles $\theta \leq 45°$, where the corresponding delay reduces to ~ 150 ns for the actual arm length of 66m for Station 0.

To accommodate shower front curvature and timing uncertainties, a conservative pulse cleaning threshold of 200 ns is applied. A pulse is rejected if no other detector in the event registers a signal within 200 ns of its arrival time. That is, pulses that are temporally isolated from the rest are considered likely noise or unrelated secondaries. This cut is applied relative to the expected arrival time based on the reconstructed core and shower front geometry. The cleaned set of pulses is then used in the three-step reconstruction process. Figure 6.2 (left) shows the time residuals before and after pulse cleaning, with IceTop tank pulses included for reference. A marked improvement in temporal consistency is visible.

To validate the improvement, the reconstructed zenith angle is compared to that from IceTop.

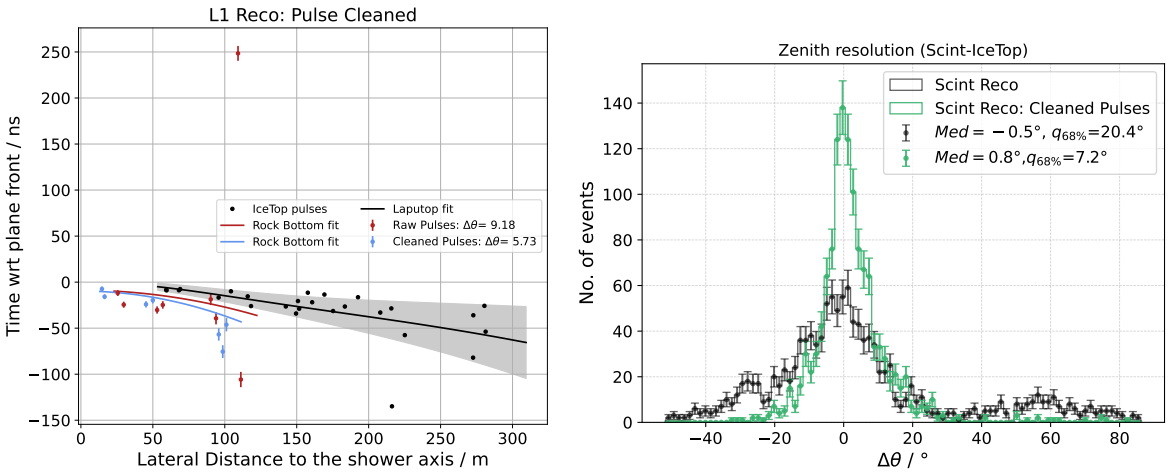

Figure 6.2: Left: Time residuals of pulses with respect to the reconstructed shower front as a function of lateral distance to the shower axis, before and after pulse cleaning. IceTop timing is shown for comparison. Right: Zenith angle resolution after cleaning, using IceTop as the reference. Only events with six or more scintillator hits are included.

As shown in Fig. 6.2 (right), a $\sim 65\%$ enhancement in angular resolution is achieved. Although only 0.5% of events required cleaning in the current dataset, this method will be increasingly important as more stations are deployed.

L2-Reconstruction

Accurate core reconstruction is essential for determining the shower geometry, especially its direction and size. For the scintillators of SAE station 0, this task is particularly challenging. In the best-case scenario, only 8 detectors per event are available. Out of these, only four sample the more distant parts of the shower, due to the pairs being spaced within 5 m of each other. This effectively limits the core fit to four spatially meaningful points. In addition, the reconstruction minimization involves up to five free parameters for such limited input. As a result, the fit is under-constrained and prone to systematic bias, especially near array edges or low-multiplicity events. Conversely, IceTop requires at least 5 HLC hits (i.e., 10 detectors) for reconstruction. The higher station multiplicity, as well as a larger footprint, naturally yield a more uniform and reliable core estimate.

Figure 6.3 (top row) shows a comparison of the reconstructed IceTop and Scintillator core positions with measured data. IceTop cores are spatially uniform with slight biases towards the detectors. In contrast, the scintillator cores cluster at the array centre and fixed peripheral zones, pointing to minimizer bias due to the geometry. These patterns point back to the center-of-gravity (CoG) seed used to initialize the core position as a first estimate. With sparse detector coverage, the CoG estimate likely pushes the minimizer into local minima. This is also visible as asymmetry in the reconstructed cores from scintillators around $\sim -400m$. This effect is visible as an asymmetry in the reconstructed cores from scintillators, around ~ 400 m on the plot. The asymmetry arises due to the central scintillator pairs being positioned slightly away from the geometrical center of the array.

The bottom plots in Fig. 6.3 quantify the radial core differences. The left histogram shows the radial offset between IceTop and scintillator cores: the 68% containment radius is 73.6 m, which is significant. In contrast, the core-uncertainty for IceTop reconstruction is observed to be ≤ 20 m, as presented in Fig. 3.7, which is valuable information that can be utilised. The right plot shows the core resolution with respect to the true energy from simulations. It is evident that the resolution gets worse with energy due to the size of the station, and

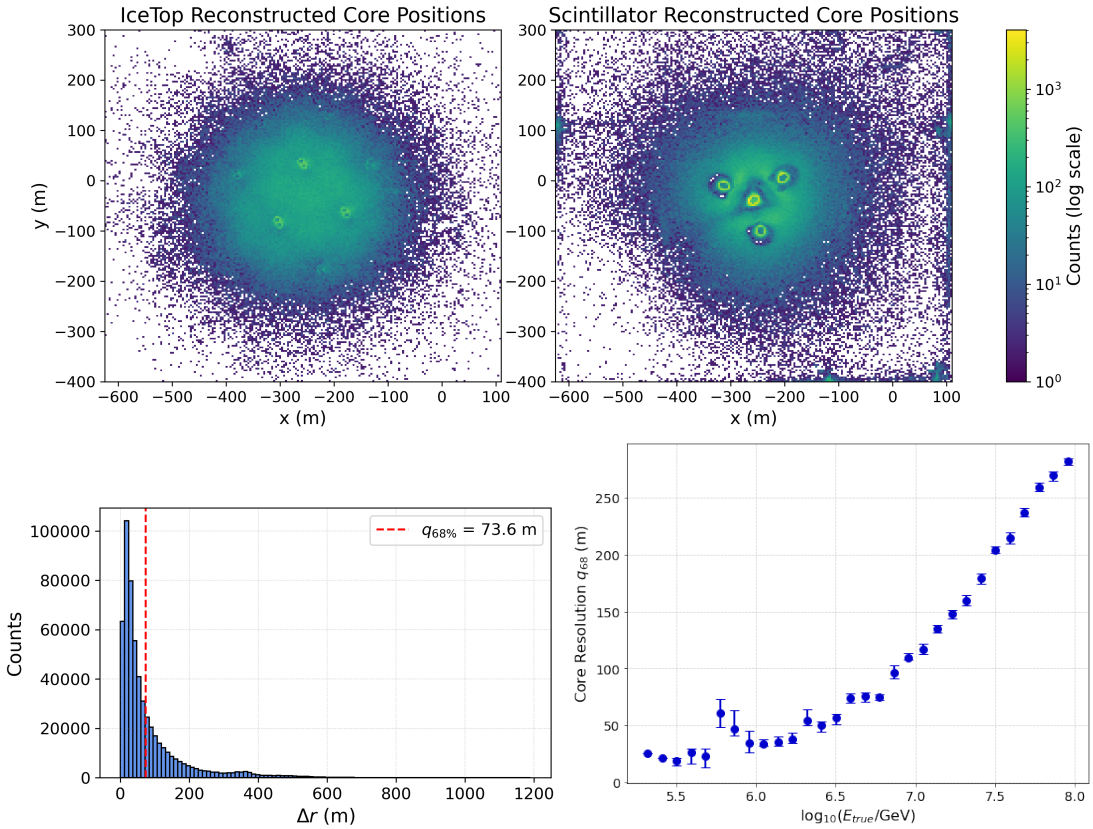

Figure 6.3: Comparison of reconstructed core positions for coincident events observed by IceTop and the scintillator array. Top: reconstructed core distributions from data. Bottom:(left) radial core difference histogram for IceTop–Scintillator obtained from data, and (right) core resolution of scintillators with respect to true energy obtained from simulations.

is nearly 50 m or more in the region of interest covering the PeV region. Cumulatively, it can be confirmed that the stand-alone core resolution of the scintillators of a single station is unreliable.

An inaccurate core position leads to wrong timing corrections, since signal times are shifted relative to the assumed core. This, in turn, biases the shower front fit and hence the angular resolution. Furthermore, lateral signal scaling and thus shower size are also affected. A mis-reconstructed core thus degrades every subsequent step. Therefore, a Level-2 (L2) reconstruction was performed to repeat the second step of reconstruction using the IceTop core as input. Figure 6.4 presents the same example event presented in Fig. 6.2, after performing L2 reconstruction on the cleaned event. A cumulative improvement of $\Delta\theta = 7.32°$ for the presented event, in the zenith resolution with respect to IceTop, is observed. Further studies on the performance of the reconstruction are presented in the next chapter.

6.2 Single Station Simulations

Although this thesis primarily focuses on the analysis of measured data, a dedicated simulation set for the prototype station geometry was also available for validation and comparison purposes. These simulations are particularly useful in performance studies and have also been employed to validate the signal variance of the scintillation detectors, as discussed in Sec. 6.3.3.

The simulations were produced by Agnieszka Leszczyńska [78] using the CORSIKA framework [111], and include air showers induced by proton and iron primaries, based on the hadronic

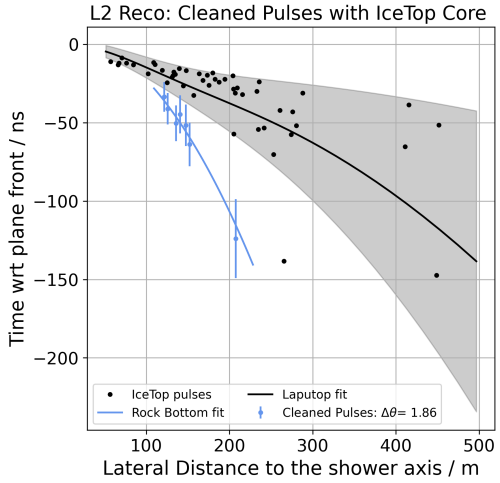

Figure 6.4: Example air shower event after pulse cleaning and L2 reconstruction, observed by the SAE station 0 scintillators, presenting their distance to the core with respect to the timing.

interaction model Sibyll [112]. Showers are simulated with zenith angles up to 71.6°, binned in intervals of $\sin^2\theta = 0.1$. The primary energy spans $13.0 < \log_{10}(E/\mathrm{eV}) < 16.7$ in steps of 0.1 in log-scale, thus covering the lower-energy portion of the cosmic-ray spectrum. Each shower core is randomly placed within a 500 m radius around the centre of the SAE prototype station. The detector layout reflects the GPS-surveyed positions from 2020 [85], and the detector response is modelled using the parametrisation described in [78]. For each energy–zenith bin, 100 showers were simulated and resampled 5 times. To emulate a realistic cosmic-ray flux, events are weighted in energy and mass according to the H4a model [19].

Figure 6.5 shows the resulting distributions for shower energy and core position. The energy distribution (Top) combines proton and iron primaries and is shown after H4a weighting (arbitrary normalisation). The spatial core distribution (Bottom) confirms a uniform spread within the 500 m radius around the station. The positions of the scintillator detectors and field hub are overlaid for reference.

The timing resolution obtained from simulation is illustrated in Fig. 6.6, showing the standard deviation of arrival time differences between neighbouring detectors for events with at least eight hits. While the resolution is slightly worse than that observed in data (by approximately 10 ns 5.18), it remains within 25 ns. This discrepancy may stem from simplifications in the detector response modelling used in the simulation and is expected to improve for higher-energy showers. Such differences will influence the resolution studies presented later in this work.

6.3 Data-driven Reconstruction Parametrization

While the simulations provide a robust foundation for detector and reconstruction development, measured data is essential for validating and refining key modelling aspects, particularly the detector response and shower observables. To this end, data from the 2023 SAE prototype dataset was used to derive a data-driven parametrisation for the air shower reconstruction. This included a validation of the timing model currently used for shower front reconstruction. Both single-event and multi-event approaches were employed to characterise the shape and fluctuations of the shower front more accurately. In addition, a realistic model of the signal variance as a function of signal size was developed. This variance model plays a crucial role in the lateral distribution function (LDF) reconstruction, as it determines the appropriate

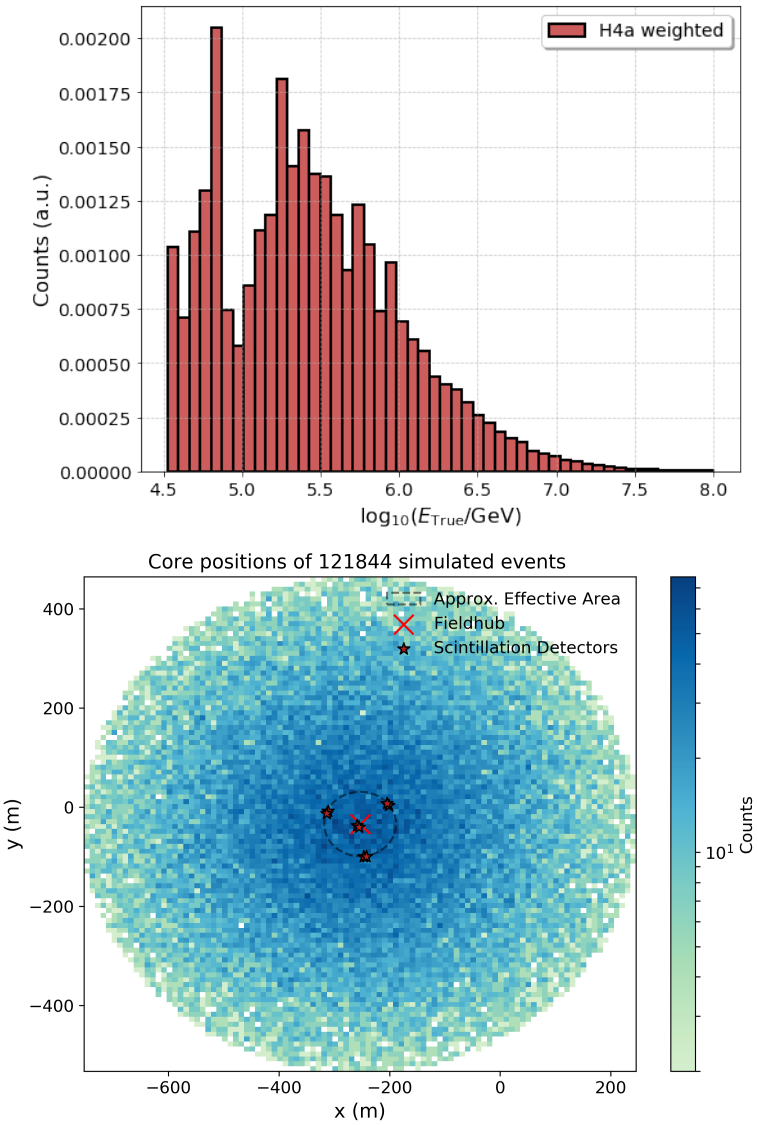

Figure 6.5: Top: Simulated energy distribution after applying H4a weighting. Bottom: Core position distribution of simulated showers projected onto the ground. The scintillator detectors and the field hub of the prototype station are also shown.

weighting of individual pulse amplitudes. Finally, the refined signal model was applied in both event-wise and binned approaches to extract parameters of the lateral distribution. The fits were performed by minimising the residuals of the LDF for individual events by aggregating events within bins of shower size and zenith angle.

6.3.1 Selection Criteria

In real data, the true air-shower parameters are unknown, so a careful event selection is critical for a robust parametrisation. Coincidences with IceTop provide significant benefits here, as its reconstruction leverages the full array, along with well-validated simulations and over a decade of calibration and refinement. As mentioned in Chapter 5, a total of about 227 K events were found in coincidence with IceTop, recorded with a scintillator multiplicity greater than five. In order to ensure both reconstruction quality and statistical significance, the coincident events that met the following criteria were selected:

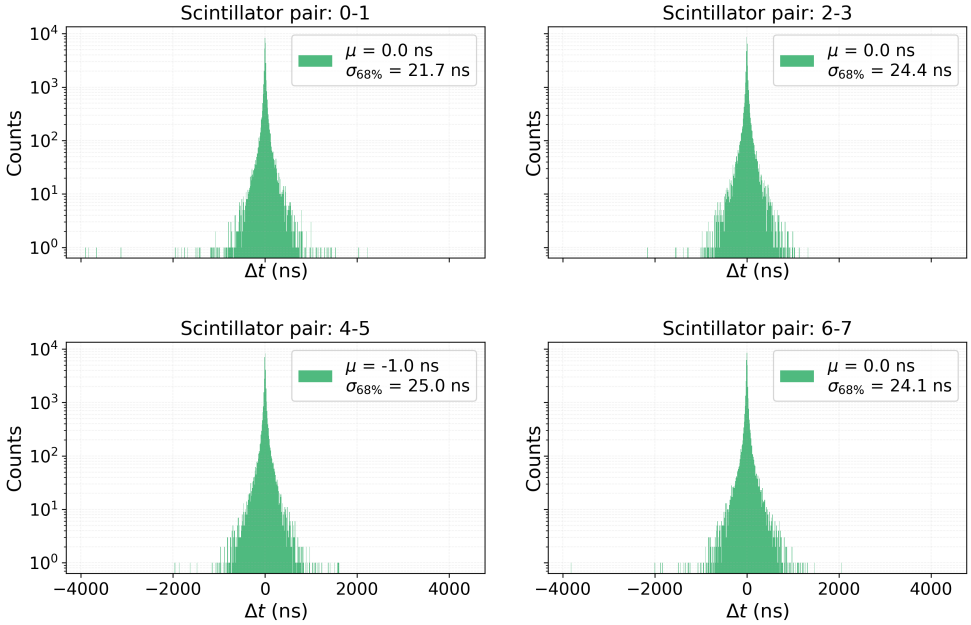

Figure 6.6: Timing resolution between neighbouring detectors for simulated events with multiplicity of ≥ 8. The resolution is defined as the standard deviation of the arrival time differences and remains within 20 ns.

- Events had to be successfully reconstructed by both the scintillator reconstruction and IceTop. This ensures a well-defined geometry and timing for each shower.

- Only events with a scintillator multiplicity of 8 were selected. Given the compactness of the prototype station and the complexity of the reconstruction, which involves multi-parameter (up to 5 in one step) minimisation over timing and lateral signals, this high multiplicity provides the best constraints.

- Events were retained only if the IceTop-reconstructed zenith angle was below 37°, a regime where IceTop's angular reconstruction is reliable [62].

- A containment cut was applied to the IceTop-reconstructed core, requiring it to lie within 250 m of the prototype station's central DAQ unit (fieldhub). This eliminates edge and uncontained events, which bias core and angular fits.

- An additional cut was placed on the scintillator-reconstructed zenith angle, removing showers with $\theta > 70°$, to reject mis-reconstructed events.

The relationship between scintillator multiplicity and reconstruction success is illustrated in Fig. 6.7. Below multiplicity 5, the failure rate increases sharply, largely due to uncorrelated or noisy pulses. From multiplicity 5 onward, the reconstruction success rate improves significantly, though the number of events drops exponentially as expected.

After applying all cuts, a final data sample of 58,387 events remained. The distribution of these events in $\log_{10}(S_{125}/\text{VEM})$ and core position from the IceTop reconstruction is shown in Fig. 6.8. The uniform spatial distribution reflects good containment, with most of the event being localised near the station. The energy proxy ($\log_{10}(S_{125}/\text{VEM})$) shows broad coverage across the low-energy range, down to 1 PeV with the majority of the sample lying before 3 PeV, in the knee region, and where IceTop reaches maximum efficiency.

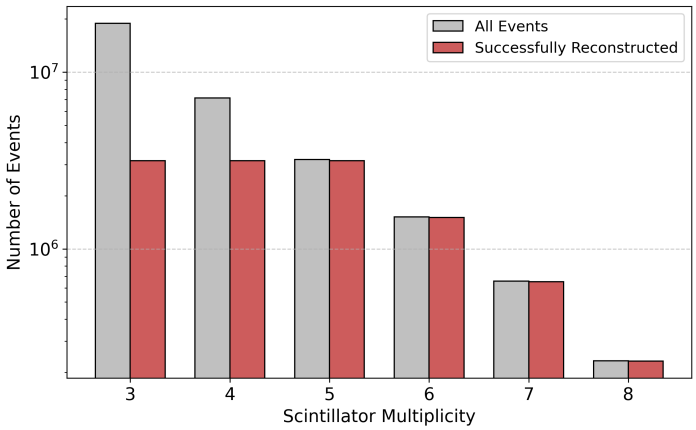

Figure 6.7: Number of all found events and successfully reconstructed scintillator events as a function of detector multiplicity. The reconstruction success rate improves with multiplicity, while the event rate drops, as expected for a threshold-limited station.

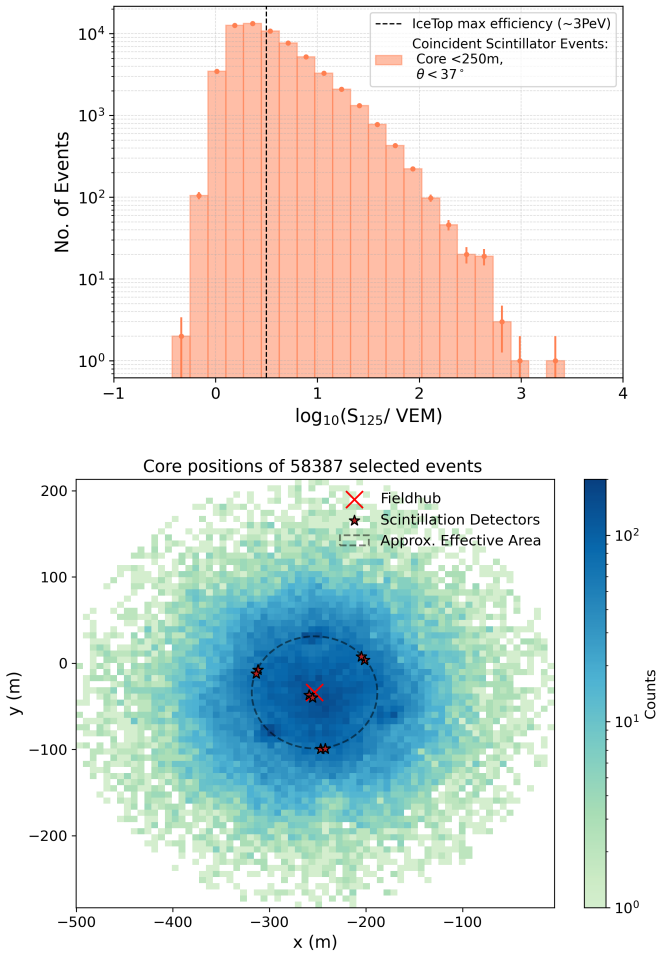

Figure 6.8: Top: Distribution of IceTop-reconstructed shower size ($\log_{10}(S_{125}/\mathrm{VEM})$) for the selected events. Bottom: Core positions of selected events, overlaid with the station layout. The central DAQ (fieldhub) and scintillator locations are marked.

6.3.2 Timing Parametrization

The temporal profile of air-shower signals in the scintillators was parametrised using the pulse time delay (t_{Delay}) as a function of lateral distance r from the reconstructed shower core.

Two complementary approaches were applied: an event-wise fitting procedure and a binned multi-event statistical analysis.

Event-by-event analysis: Each selected air-shower event was fitted with a parabolic model describing the curvature of the shower front, accounting for timing uncertainties arising from shower thickness [78]. The functional form used was $t_{\mathrm{Delay}}(r) = ar^2 + b$, where a represents the curvature of the front and b an overall time offset. An example of such a fit was shown previously in Fig. 6.4.

Only events passing a quality criterion based on the reduced χ^2 of the fit were retained for further analysis. The resulting distributions of the parameters a and b are shown in Fig. 6.9. The curvature parameter a displays a pronounced positive skewness, indicative of intrinsic variations in shower development, such as differences in the altitude of the shower maximum. Deeper developing showers, often initiated by lighter primaries, result in a more curved shower front at the ground. The offset parameter b, representing a relative timing shift, is centred around zero and approximately Gaussian in shape, consistent with expectations from symmetric electronic and geometric delays.

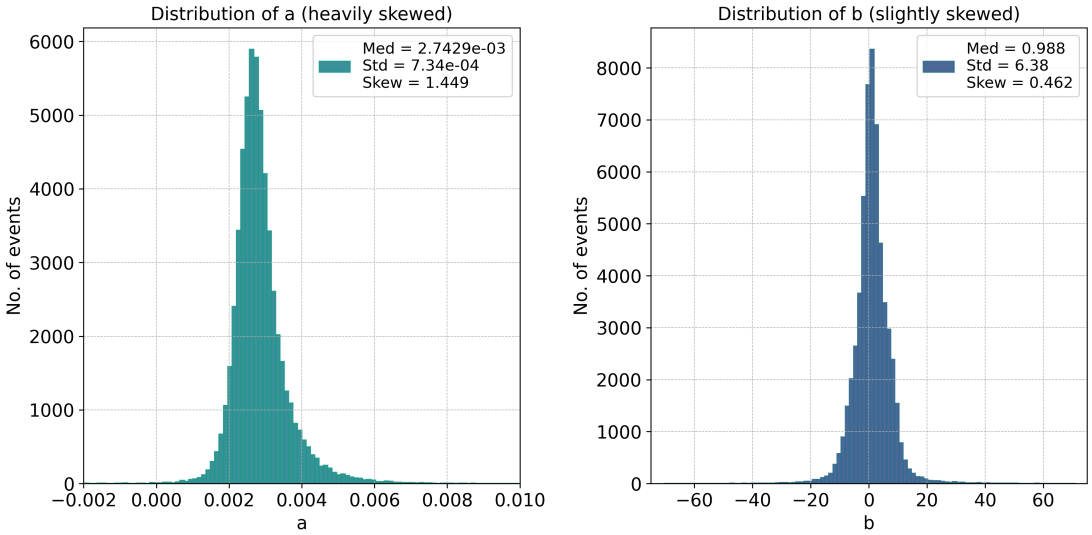

Figure 6.9: Distributions of the shower front fit parameters from the event-wise analysis: curvature a (left) and time offset b (right).

Multi-event binned analysis: To statistically extract the mean behaviour of the shower front, all valid events were combined and binned in lateral distance. Within each radial bin, the distribution of t_{Delay} was fitted with an Exponentially Modified Gaussian (EMG) function (binned plot included in Appendix C):

$$f(x) = \frac{A\lambda}{2} \exp\left[\frac{\lambda}{2}(2\mu + \lambda\sigma^2 - 2x)\right] \cdot \left[1 - \mathrm{erf}\left(\frac{\mu + \lambda\sigma^2 - x}{\sqrt{2}\sigma}\right)\right],$$

where μ, σ, and λ are the Gaussian mean, width, and exponential decay parameters, respectively. From this, an adjusted mean $\mu_{\mathrm{adj}} = \mu + \frac{1}{\lambda}$ and standard deviation $\sigma_{\mathrm{adj}} = \sqrt{\sigma^2 + \left(\frac{1}{\lambda}\right)^2}$ were calculated to characterise the time delay per bin.

While a Gaussian fit was also tested and found to yield consistent results (see Appendix C), the EMG model provides a better description of the tail behaviour, especially for the full detector array where fluctuations are more pronounced. A parabola was then fitted to the adjusted

mean time delays across bins:

$$\mu_{\text{adj}}(r) = ar^2 + b,$$

with uncertainties propagated from σ_{adj}. A 3σ confidence band is included to reflect the uncertainty on the fit. Figure 6.10 presents the data and resulting parabola.

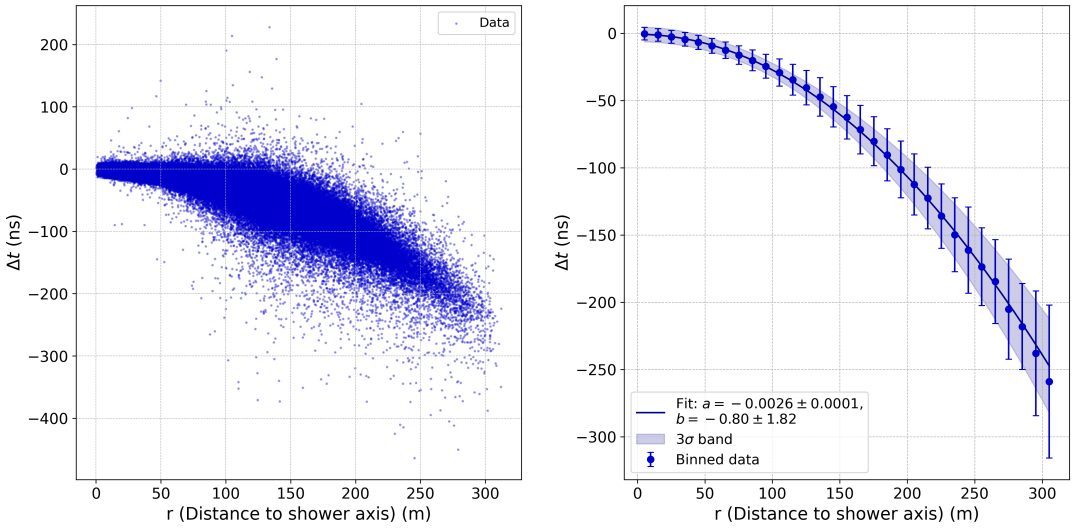

Figure 6.10: Left: Pulse time delay versus lateral distance r for all events. Right: Fitted parabola to adjusted EMG means with 3σ uncertainty band.

Parametrization choice for reconstruction: The a and b parameters obtained from the event-wise and binned approaches were found to be consistent within 1σ of each other. For practical implementation in the reconstruction algorithm, a fixed value of $a = 0.0028$ was adopted, corresponding to the mean curvature from the binned fit. The offset b was treated as a free parameter, initialised at 0.9 and allowed to vary within a 3σ range based on its observed distribution. This hybrid approach improves both the stability and accuracy of the timing model during lateral distribution reconstruction.

6.3.3 Signal Variance Model

Signal fluctuations in individual detectors arise from two primary sources: (i) intrinsic variations in the development of the air shower, and (ii) detector-related effects such as light yield statistics, electronic noise, and calibration uncertainties. When detector effects are minimised and the signal originates from discrete particle counts, fluctuations are expected to follow Poisson statistics [113]. Specifically, if a detector registers N particles, the standard deviation of the measured signal theoretically scales as $\sigma \propto \sqrt{N}$. In the case of scintillators, where each traversing charged particle deposits energy stochastically but within a narrow distribution, the total charge approximately tracks the number of particles, resulting in Poisson-like behaviour in the signal spread.

To investigate this, a signal fluctuation analysis using experimental data from Station 0 was performed. This method has previously been used in simulation-based signal variance studies for the Scintillator Air-shower Extension (SAE) of IceCube [78], and similarly in IceTop [114] and IceCube-Gen2 surface array [115], as well as experiments like Pierre-Auger Observatory [113]. The method leverages the fact that two neighbouring detectors, separated by 5 m, sample nearly the same lateral distance from the shower core and thus measure the same underlying particle density. This allows for a quasi-independent double measurement of the signal.

By comparing the signals S_1 and S_2 from neighboring panels, the intrinsic spread of a single detector can be approximated using the relative difference:

$$\Delta S_{\text{rel}} = \frac{S_1 - S_2}{\sqrt{2}},$$

assuming Gaussian-distributed fluctuations and independence between detectors [115]. This distribution was evaluated with respect to the average signal in the two detectors,

$$\langle S \rangle = \frac{S_1 + S_2}{2},$$

and the widths of these distributions were fit with Gaussians to extract the signal spread as a function of the average signal strength. Figure 6.11 shows the distribution of signals in neighbouring detectors.

To ensure the validity of the point-like double measurement assumption and stable core reconstruction, two additional quality cuts were applied:

- Events were required to have at least 8 hit detectors, ensuring stable core and direction reconstruction. This also selects higher-energy events, where the array is expected to operate at full efficiency [78].
- Only scintillator pairs located at radial distances $> 50\,\text{m}$ from the reconstructed shower core were used. At small core distances ($< 50\,\text{m}$), the lateral distribution function (LDF) increases steeply, causing significant signal differences even over short ($5\,\text{m}$) separations, which would artificially inflate the estimated fluctuations.

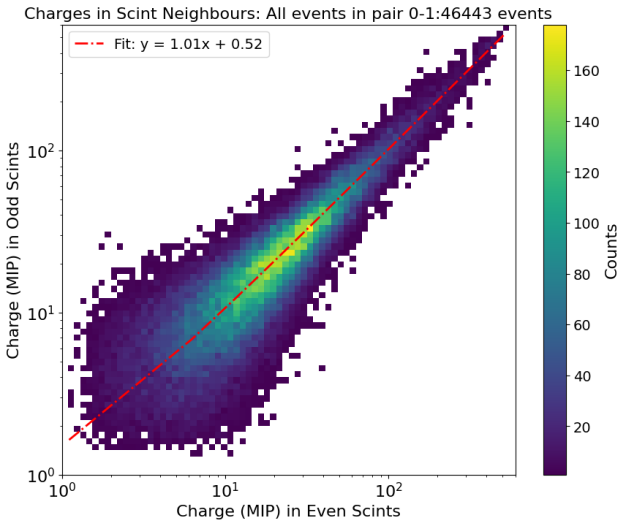

Figure 6.11: Charge deposited in neighbouring panels of Station 0, illustrating the double-measurement principle. A linear fit is applied to show the agreement in the neighbours.

Figure 6.12 presents the extracted signal spread as a function of mean signal $\langle S \rangle$ for all four pairs in Station 0. The plots are shown in log-log scale, where a linear relationship indicates a power-law behaviour:

$$\sigma_{\frac{S_1 - S_2}{\sqrt{2}}} = \langle S \rangle^{\alpha}.$$

Below the threshold, the range of possible signal fluctuations is artificially constrained, leading to an apparent decrease in the spread, as shown in Fig. 6.12. The linear fits were therefore performed for $\langle S \rangle > 10\,\text{MIP}$, which lies above the detector threshold region. The observed slope is $\alpha \approx 0.54$ across all pairs, which is consistent with near-Poissonian behaviour. For the signal model, the contribution from all pairs was combined to deduce the value of $\alpha = 0.545$. This data-driven behavior was also reproduced in dedicated single-station simulations of the prototype geometry which rendered a slope of 0.533 [116].

A small deviation from pure Poisson scaling may arise due to residual LDF gradients even at $5\,\text{m}$ separation as well as the detector response. This is demonstrated in Fig. 6.13, which shows the relative signal difference as a function of distance from the core. The relative difference maximises at the detector spacing of $5\,\text{m}$. Ideally, the slope of this trend should be zero, and

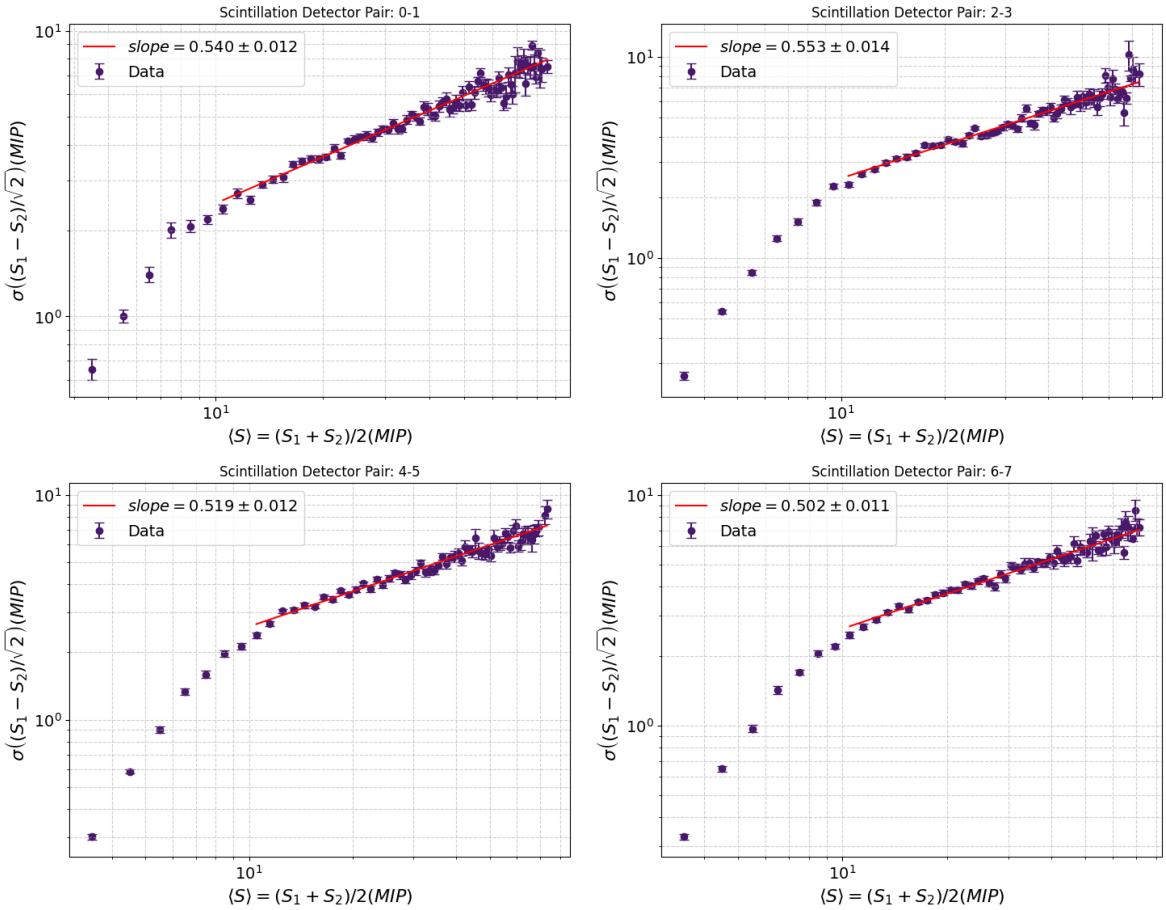

Figure 6.12: Measured signal spread versus mean signal size for the four detector pairs in Station 0. The log-log slope is approximately 0.54 in each case, indicating nearly Poissonian behavior.

correcting for this LDF-induced slope would yield a more accurate estimate of the shower fluctuations. However, since such corrections are model-dependent and could introduce bias into reconstruction, they were not applied in this work. A further study investigating whether this slope decreases with mean signal is presented in Appendix C, and was found true as per the above-mentioned expectation.

Zenith Dependence

Signal fluctuations are also expected to depend on the zenith angle of the incoming shower. As inclined showers traverse more atmosphere, the longitudinal development is more developed, potentially increasing intrinsic fluctuations. To investigate this, data from all panel pairs were grouped into three zenith angle bins using $\sin^2\theta$, and the same fluctuation analysis was performed in each bin.

Example Gaussian fits to the ΔS_{rel} distributions in two selected $\langle S \rangle$ bins are shown in Fig. 6.14. The extracted spread as a function of signal for the different zenith bins is shown in Fig. 6.15. The overall shape of the dependence remains a power law, but with a changing normalisation (intercept in log-log space), denoted as the "spectral factor" $f(\theta)$. The spectral factor a was fitted as a function of $\sin^2\theta$, yielding:

$$f(\theta) = (0.39 \pm 0.02)\sin^2\theta + 0.66.$$

Combining the zenith dependence with the power-law behaviour gives the full fluctuation

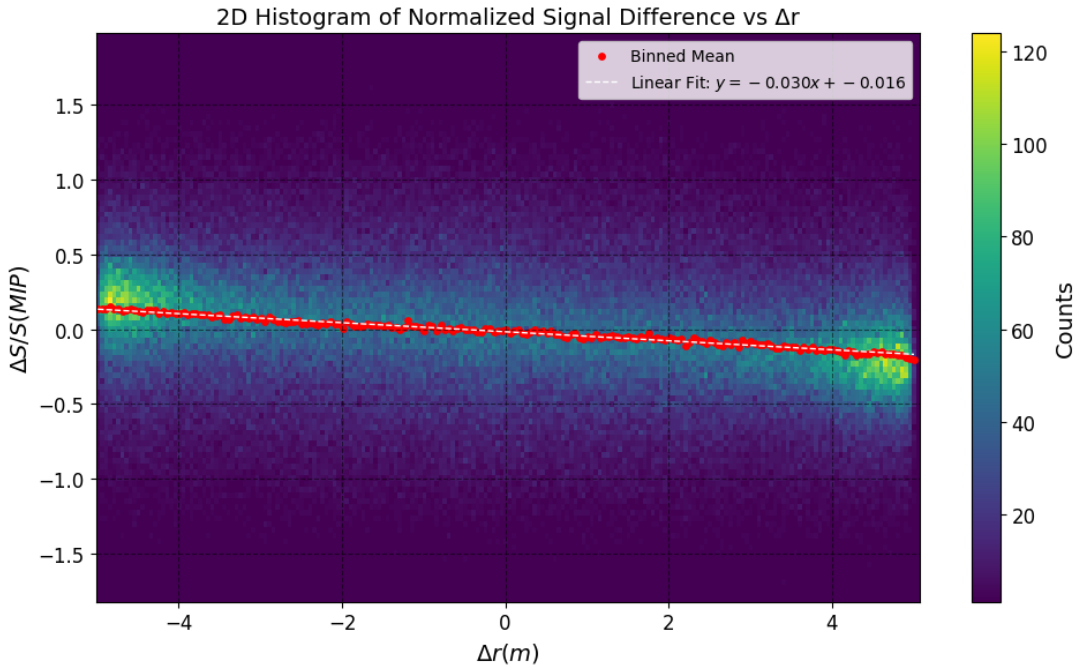

Figure 6.13: Relative signal difference between neighbouring panels as a function of lateral distance from the shower core, illustrating residual LDF gradients.

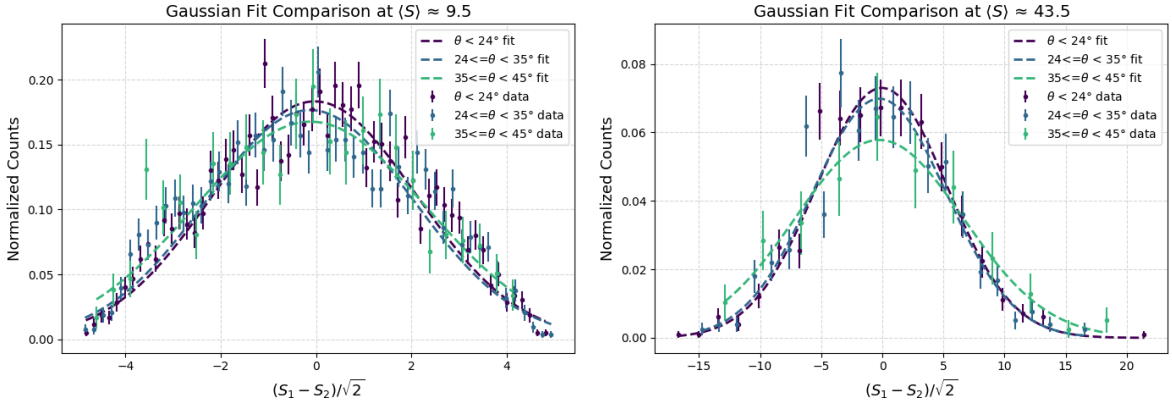

Figure 6.14: Example of Gaussian fits to ΔS_{rel} distributions in two different $\langle S \rangle$ bins for one zenith angle bin.

model:

$$\sigma_S = \langle S \rangle^{0.545} \cdot \left[0.39 \sin^2 \theta + 0.66\right].$$

6.3.4 Lateral Distribution Parametrization

The lateral distribution of signals in an air shower provides essential information about the spatial variation of particle densities as a function of distance from the shower core. This distribution is sensitive to the energy and arrival direction of the primary cosmic ray, making it a key tool in reconstructing air-shower parameters. The lateral distribution function (LDF) is commonly used to extract important quantities such as the core location and a reference signal S_{125} in this case, which correlates with the primary energy.

Event-by-event LDF fitting The LDF was modelled using the Double Log-Parabola function with a minimisation method that includes contributions from triggered, saturated, and

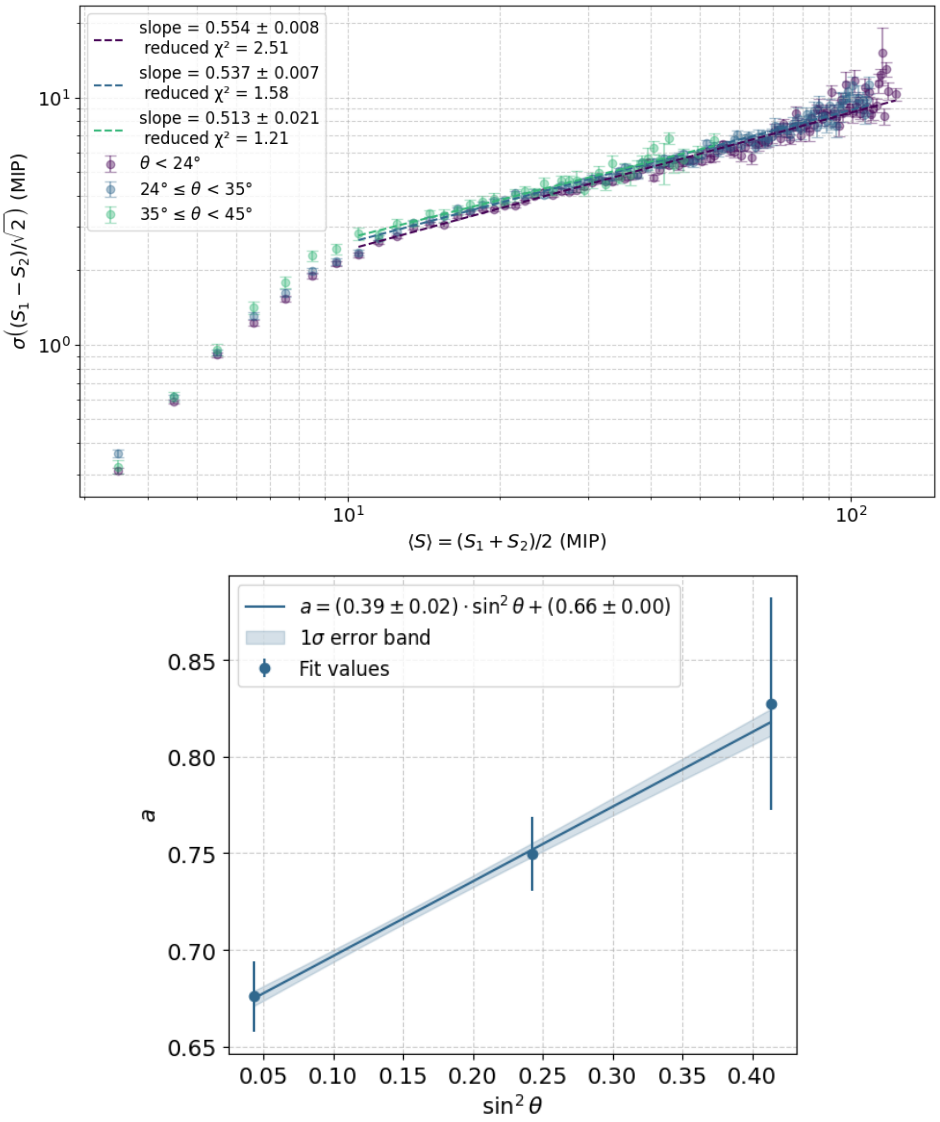

Figure 6.15: Top: Signal fluctuation as a function of signal strength for different zenith angle bins. Bottom: Spectral factor a vs. $\sin^2\theta$, showing increasing fluctuations with zenith.

silent detectors, as described in Section 6.1. However, in this study, single-station events were analysed, and the silent detector term was omitted due to the limited number of stations and their reduced constraining power in such sparse configurations.

A best-fit DLP function was obtained for each event individually by minimizing the difference between measured and modelled signals. Because of the limited number of data points per event (maximum 8 points per event), a quality selection based on the reduced chi-squared χ^2_ν was applied, retaining fits with values between 0.8 and 2.0. The reduced chi-squared was defined as

$$\chi^2_\nu = \frac{1}{N - n_{\text{fit}}} \sum_{i=1}^{N} \left(\frac{S_i^{\text{meas}} - S_i^{\text{fit}}}{\sigma_i} \right)^2 , \tag{6.12}$$

where N is the number of signal points, n_{fit} the number of fit parameters, S_i^{meas} the measured signal, S_i^{fit} the fitted value, and σ_i the measured signal uncertainty derived from the variance model. This formulation ensures that the fit quality accounts for both residuals and expected fluctuations, independent of the shower size.

During minimization, the curvature parameter κ in Eq. (6.3) was fixed at 0.35 based on simulation studies to reduce fit complexity. Additionally, a constraint enforcing a monotonically decreasing signal expectation with distance was applied to maintain a physically sensible LDF shape. Figure 6.16 illustrates an example single-event LDF fit, the distribution of reduced χ^2_ν versus β, and the β distribution for selected events with a Gaussian fit used to extract mean and 3σ bounds.

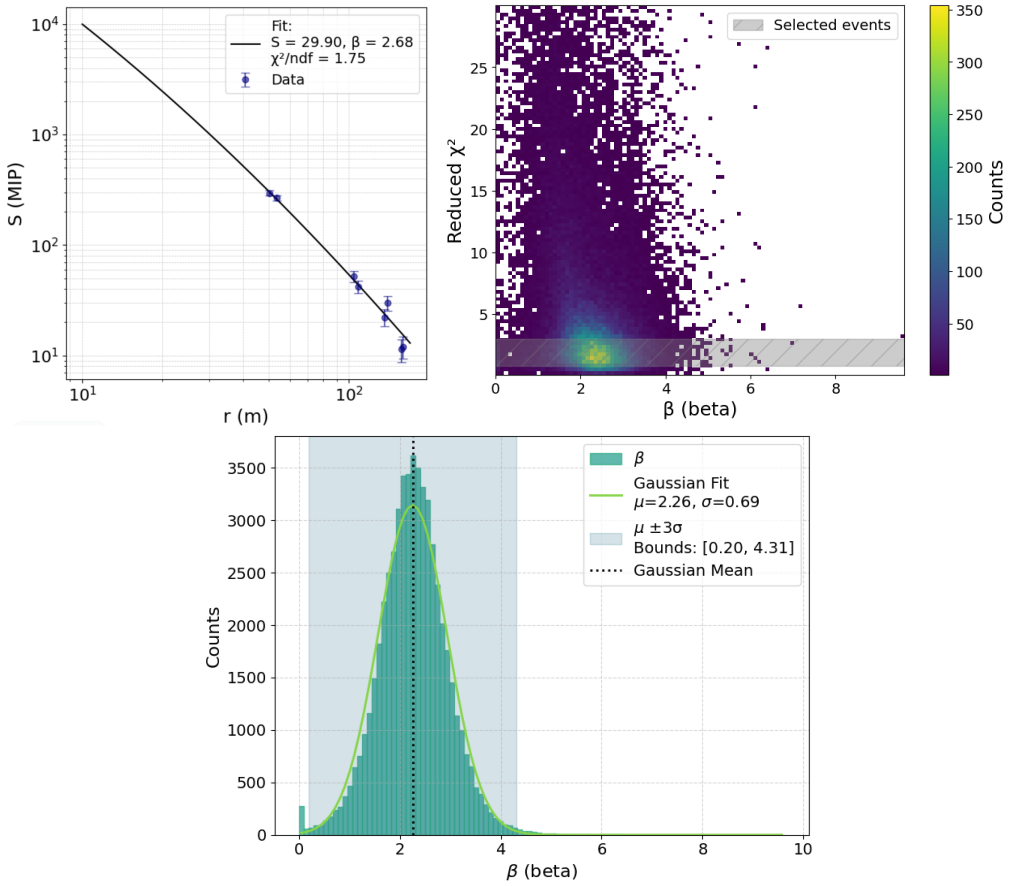

Figure 6.16: (Top-left) Example of a single-event LDF fit. (Top-right) Reduced chi-squared values versus β parameter from the fit; the grey band indicates selected events. (Bottom) Distribution of β values from selected events with a Gaussian fit.

Multi-event binned LDF analysis Due to the limited information content of single events, a complementary multi-event approach was developed. Recognising the LDF's sensitivity to both shower size and geometry, events were binned in two dimensions based on S_{125} and zenith angle θ, as shown in Fig. 6.17. The binning was done in $\cos\theta$ from 0.5 to 0.9 in steps of 0.05, and in $\log_{10}(S_{125})$ with bins of width 0.1. The distribution of the $\log_{10}(S_{125})$ for the selected events is also presented. For each $(\log_{10}(S_{125}), \cos\theta)$ bin, the lateral distribution $S(r)$ was constructed by aggregating all events and dividing the data into radial bins of 5 m width, considering only distances greater than 50 m to avoid saturation effects. Within each radial bin, the mean signal was computed using a log-normal distribution. Radial bins with mean signals below 6 MIPs were excluded to minimise threshold bias.

An example of a binned LDF from a well-populated bin is shown in Fig. 6.18 (left). More examples can be found in the Appendix C.3. In bins with insufficient statistics, the LDF was fit directly to the unbinned data. The distribution of β values extracted from all bins is shown in Fig. 6.18 (right). The observed slight skewness motivated using the median β as the best

estimate and defining the uncertainty via the 3σ spread. These binned results are consistent with the event-by-event analysis.

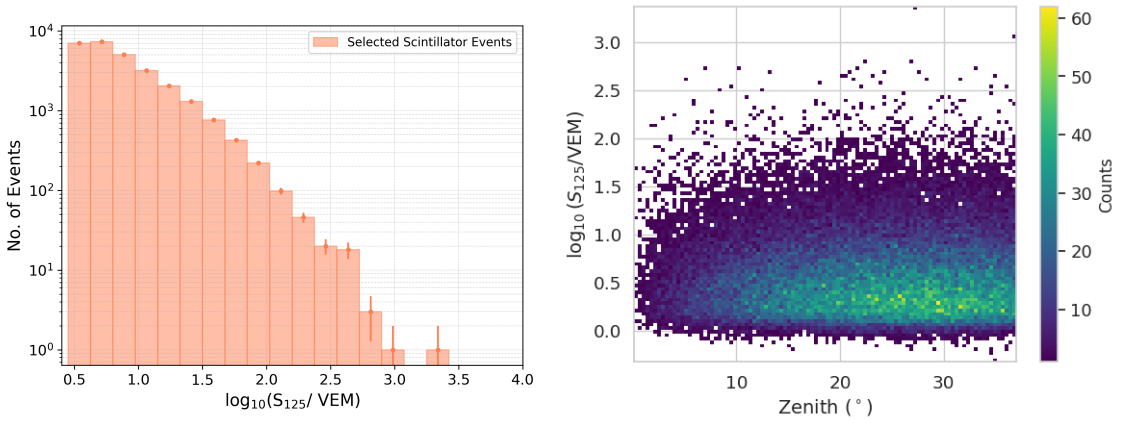

Figure 6.17: 2D distribution of $\log_{10}(S_{125})$ vs $\cos\theta$ for selected events used in binned LDF analysis.

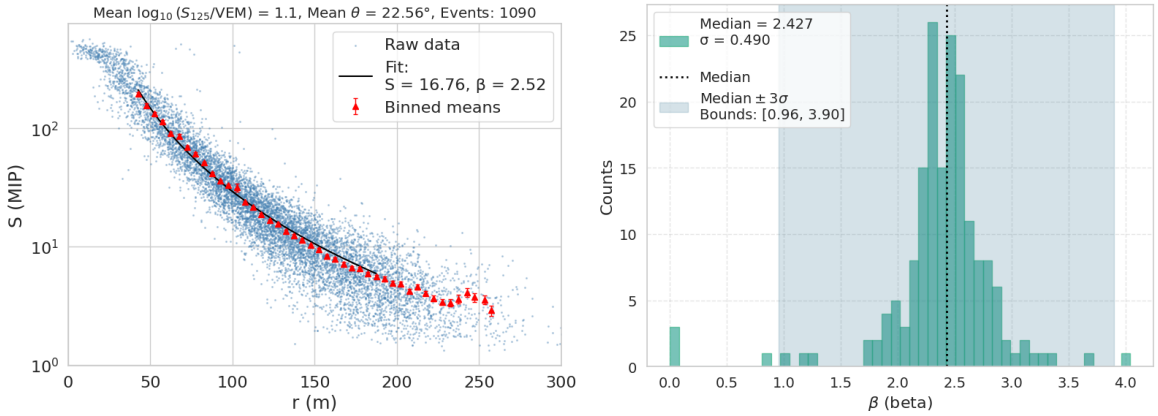

Figure 6.18: Left: Example binned LDF for one $\log_{10}(S_{125}), \cos\theta)$ bin. Right: Distribution of fitted β values across all bins.

Chosen parametrization and fit constraints Based on these studies, the final reconstruction strategy constrains β within the derived 3σ interval from the multi-event analysis, while keeping the curvature parameter κ fixed at 0.35. This approach balances fit stability with physical fidelity, given the limited data per event, and ensures consistent lateral distribution shapes across the dataset.

6.3.5 Energy Estimator

Since the reference signal from the LDF is used as an energy proxy, the quality of the energy reconstruction is closely tied to the choice of the reference distance. A large contribution to the uncertainty in the energy reconstruction stems from the uncertainty in the LDF slope. Therefore, for the choice of the optimal reference distance, the correlation of β and the reference signal can be minimized [115].

In IceTop analyses, a reference distance of 125 m is used. Hence, the same nominal value has been utilized in this study to enable direct comparison and benchmarking against established results. The optimal reference distance can be obtained by examining the covariance between the shape parameter β and the signal at different distances in the LDF. Minimising this

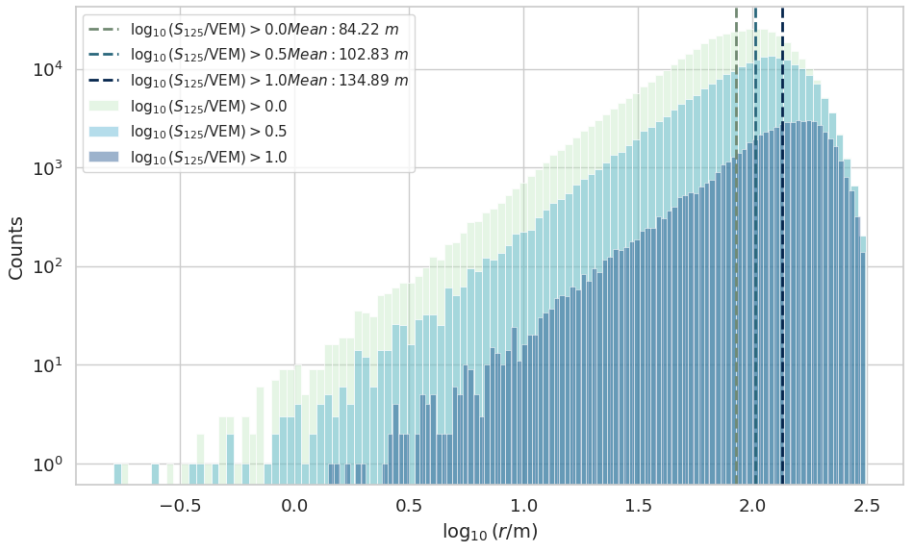

Figure 6.19: Distribution of $\log_{10}(r)$, the logarithm of the distance from the shower core, for various event selections based on $\log_{10}(S_{125})$. The peak shifts toward larger distances for higher-energy showers, indicating an energy-dependent optimal reference distance for the lateral distribution function.

covariance effectively identifies the distance where the signal is least affected by shower-to-shower fluctuations in β. In the case of the DLP function, this corresponds roughly to the peak in the distribution of $\log(r)$ [115]. Figure 6.19 shows the distribution of $\log_{10}(r)$ for different subsets of events: all events, events with $\log_{10}(S_{125}/\mathrm{VEM}) > 0.5$, and events with $\log_{10}(S_{125}/\mathrm{VEM}) > 1$. The peak of this distribution shifts toward larger distances as shower energy increases, reflecting the energy dependence of the optimal reference distance. For events with $\log_{10}(S_{125}/\mathrm{VEM}) > 0.5$, the peak is found near 102 m. Since IceTop reaches a maximum detection efficiency around $\log_{10}(S_{125}/\mathrm{VEM}) \approx 0.5$, using 125 m as a nominal reference distance remains a practical choice for comparison and analysis. However, it is worth noting that this distance should ideally be optimised in future work with more stations, to improve the performance of energy reconstruction, as it is highly dependent on the type of the detector and the layout of the array.

Chapter Summary

In this chapter, the reconstruction method applied to the scintillation detectors was introduced. To enhance the dataset quality, a pulse cleaning procedure and a Level-2 (L2) reconstruction step were added to the existing framework. Additionally, the signal fluctuations, the timing of the shower front, and the lateral distribution function were parametrized using data from the scintillators of Station 0. These developments enable a more accurate assessment of the reconstruction performance and provide a foundation for further improvements based on a realistic detector response.

Chapter 7

First Performance Studies

This chapter presents a performance evaluation of the scintillation detectors at Station 0 after the complete data processing chain, including calibration, pulse cleaning, Level-2 (L2) reconstruction, and the data-driven parametrization introduced in the previous chapters. The event selection follows the criteria outlined in Section 6.3.1. The performance is benchmarked against IceTop (IT) data, and therefore reflects both the intrinsic resolution of the scintillation detectors and systematic effects arising from IT. To reduce the influence of IT uncertainties, a cut on reconstructed shower size is applied, requiring $\log_{10}(S_{125}/\mathrm{VEM}) > 0.5$. In this regime, IT operates with maximum efficiency [62] and achieves an angular resolution of approximately $0.5°$. Following this selection, the dataset contains 27.2 K events.

Furthermore, the behaviour of the lateral distribution function's slope parameter, β, is briefly examined as a function of shower size. Given the limited number of detectors per number of degrees of freedom (dof = 6), β exhibits significant sensitivity and instability, especially at higher energies. To isolate the functionality of the new signal model, β is fixed at 2.4 in the S_{125} reconstruction for this study.

The timing accuracy of the scintillation detectors is studied by comparing time delays between neighbouring detectors and the reconstructed shower front. This analysis is performed as a function of shower observables, namely, shower size, core distance, and mean signal. A more stringent containment (100 m) region is explored in this study to efficiently derive the timing resolution of the scintillation detectors.

Finally, a preliminary comparison of the reconstructed S_{125} values from the scintillators and IceTop detectors is presented. The level of agreement between the two measurement systems is evaluated, and directions for further studies are outlined. Additionally, the measured signals from individual detectors are compared based on their spatial vicinity, focusing on neighbouring pairs of IceTop tanks and scintillation detectors.

7.1 Directional Resolution

An important feature of ground-based particle detector arrays is the reconstruction of the air-shower arrival direction, which corresponds to the trajectory of the primary cosmic-ray particle. Accurate directional reconstruction is essential for identifying anisotropies in the cosmic-ray sky and for probing their astrophysical origins. Furthermore, precise geometric reconstruction facilitates improved signal reconstruction, which is vital for accurately determining the shower size, a key parameter closely related to the primary particle's energy, and for characterizing the overall shower development.

To investigate the pointing resolution of the scintillation detectors, the angular difference is quantified by studying the deviations in the reconstructed zenith (θ) and azimuth (ϕ) angles

with respect to the IceTop reconstructed quantities. These quantities are then combined to compute the angular separation between the expected[1]. Figure 7.1 presents the corresponding distributions for the case of IceTop reconstructed directions subtracted from Scintillator reconstructed directions as zenith ($\Delta\theta$), azimuth ($\Delta\phi$), and space angle (ω). Reasonable agreement is observed in both the zenith and azimuthal angles, with resolutions of 2.8° and 8.6°, respectively. The larger azimuthal resolution is expected, as for vertical showers (which are included in this dataset), even small deviations in zenith can lead to amplified changes in the reconstructed azimuth due to the projection of the shower direction onto the horizontal plane. In such cases, the arc length traced at larger zenith angles corresponds to larger azimuthal shifts, effectively increasing the angular uncertainty in ϕ. It is important to note that this resolution also includes the uncertainty from IceTop reconstruction, which is of the order of 0.5° in the region of interest for this dataset (ref. to Fig. 3.7). Consolidating the information from the individual parameters, a combined resolution of 2.3° is observed in the space angle. For the resolution calculation, the 68th percentile of the distribution is used, which corresponds to the 1σ interval in a Gaussian distribution. This method is more robust than relying on Gaussian fits, as it avoids overestimating the resolution due to outliers and underestimating it in the presence of skewness in the distributions.

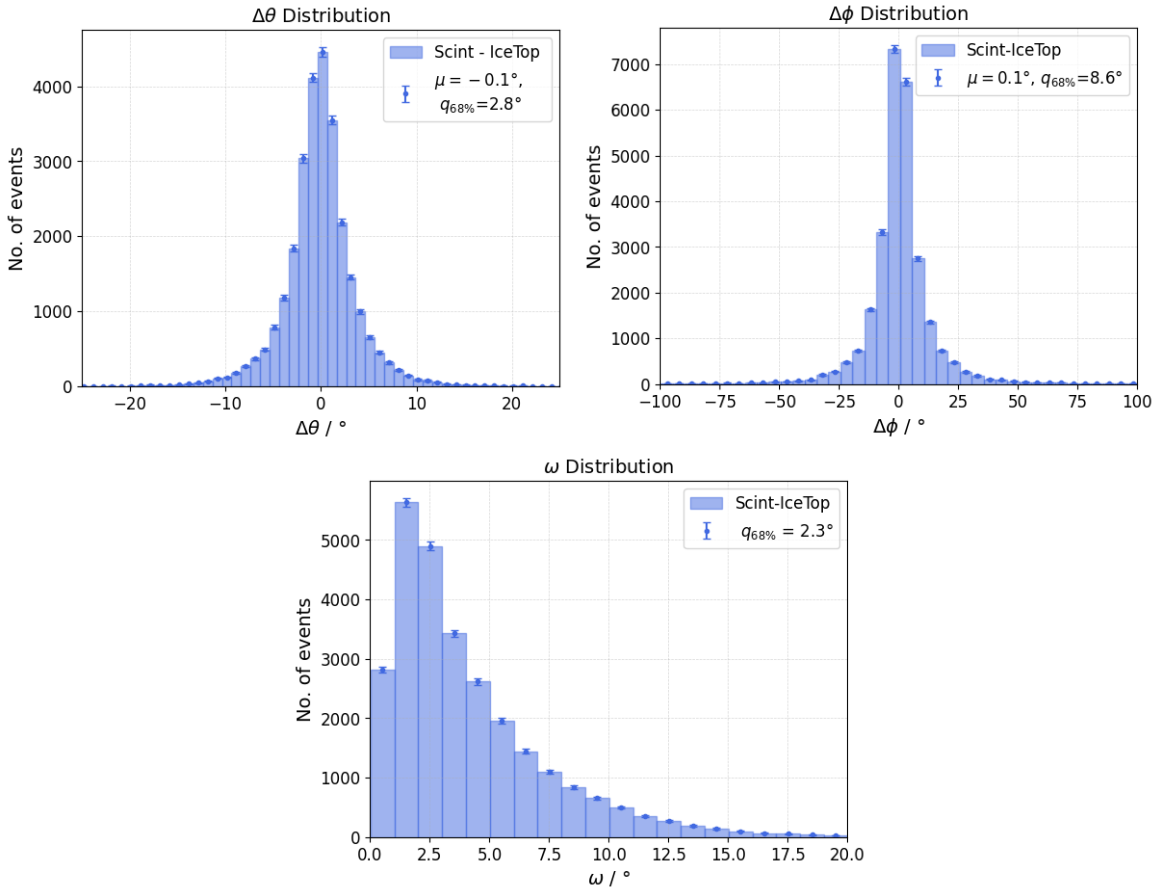

Figure 7.1: Angular resolution observed with Scintillation detector reconstruction in comparison to IceTop reconstruction in zenith (θ), azimuth (ϕ), and angle between the two reconstructed directions (ω)

Since this dataset includes events with shower cores located outside the station footprint, the resulting resolution reflects a conservative estimate and is worse than the intrinsic capabil-

[1]In this case, the reference arrival direction is taken from IceTop. In the case of simulations, the method relies on the single station's simulated true direction as reference.

ity of the detectors. Figure 7.2 presents the angular resolution as a function of shower size ($\log_{10}(S_{125}/\mathrm{VEM})$) reconstructed by IceTop, for different core-containment regions. For each scenario, the distribution of angular deviation (ω) is computed in bins of shower size, and the resolution is defined as the 68th percentile of the distribution in each bin with reasonable statistics. Statistical uncertainties on resolution are obtained via bootstrap resampling. For events with cores within 250 m of the station, the resolution increases from approximately 1.8° at low S_{125} to around 4°, and then plateaus with the bulk of the events lying in the lower energy bins. In contrast, for tighter core-containment regions within 125 m and 70 m the resolution remains more stable, around 1.6° and 1.2° respectively. This trend confirms that the angular resolution is significantly better when the shower core is closer to the station, where timing and signal geometry are better constrained.

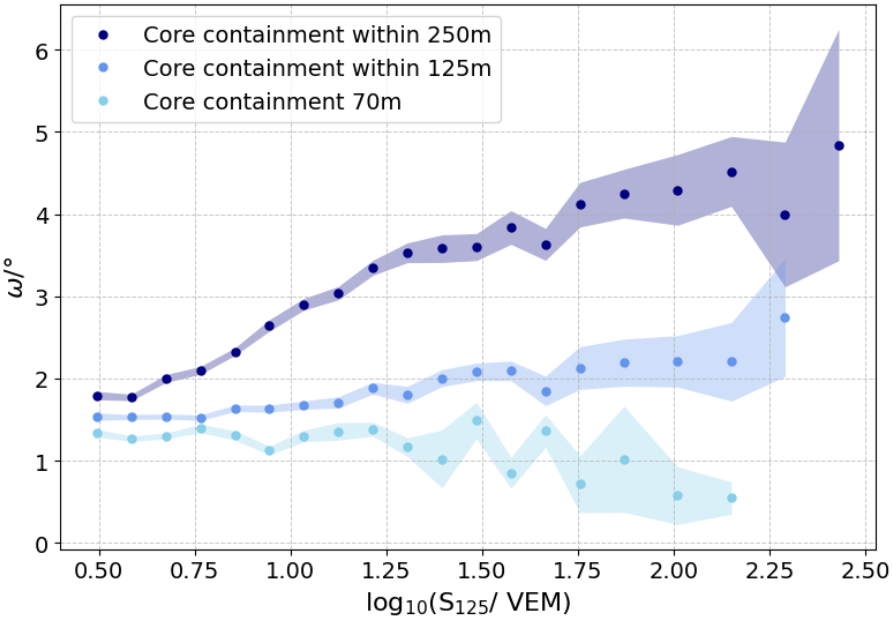

Figure 7.2: Angular resolution (ω) as a function of shower size ($\log_{10}(S_{125}/\mathrm{VEM})$) for different core-containment radii from the Fieldhub.

To evaluate the impact of the reconstruction method on the angular resolution, a comparison is made between the preliminary reconstruction[2] and the data-driven reconstruction for the space angle. This analysis is restricted to events with cores contained within 100 m of the station, where geometric constraints are minimized and reconstruction performance can be fairly assessed. Beyond this containment, additional effects such as timing delays and sparse signal geometry begin to dominate, requiring further dedicated optimization. The results presented in Fig. 7.3 show that the data-driven reconstruction provides significantly improved and more stable angular resolution across the full range of shower sizes. The improvement is especially pronounced at lower shower sizes, which correspond to the lower-energy end of the cosmic-ray spectrum precisely where the scintillator detector is expected to contribute significantly. This reinforces the potential of SAE stations to enhance sensitivity in the low-energy regime.

The angular resolution was also studied using the available simulation dataset with the data-driven reconstruction method. Although the core reconstruction uncertainty in simulations is higher (see Fig. 6.3), the obtained resolutions are observed to be within reasonable limits. Figure 7.4 shows the observed angular resolution for both data and simulations. It is important to note that this is not a one-to-one comparison, as the data resolution includes IceTop

[2]This is the reconstruction driven by simulations in [97]

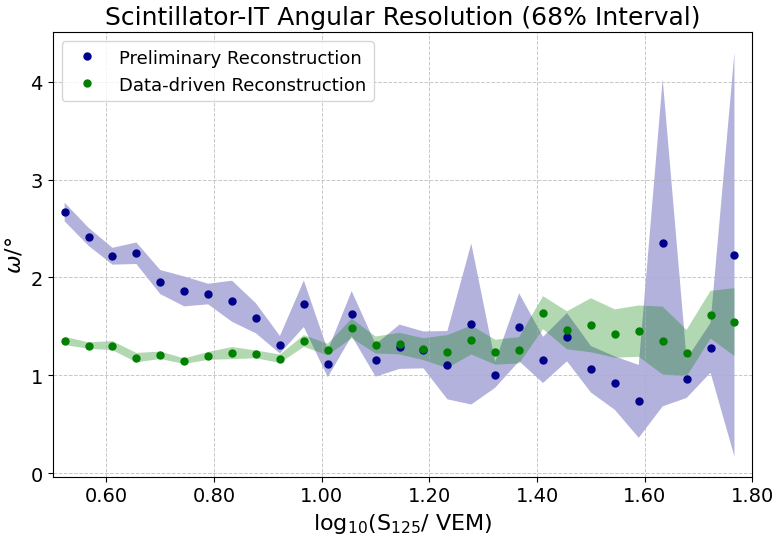

Figure 7.3: Space angle as a function of $\log_{10}(S_{125}/\text{VEM})$ for the preliminary and data-driven method. The data-driven reconstruction exhibits a more stable resolution with a significant improvement in the lower energy bins.

uncertainties, while the simulations exhibit slightly worse core reconstruction as well as worse timing resolution (see Fig. 6.6) than the data. This is due to the previously mentioned limitations in core reconstruction for a single station, as well as a limited detector response accuracy in simulation.

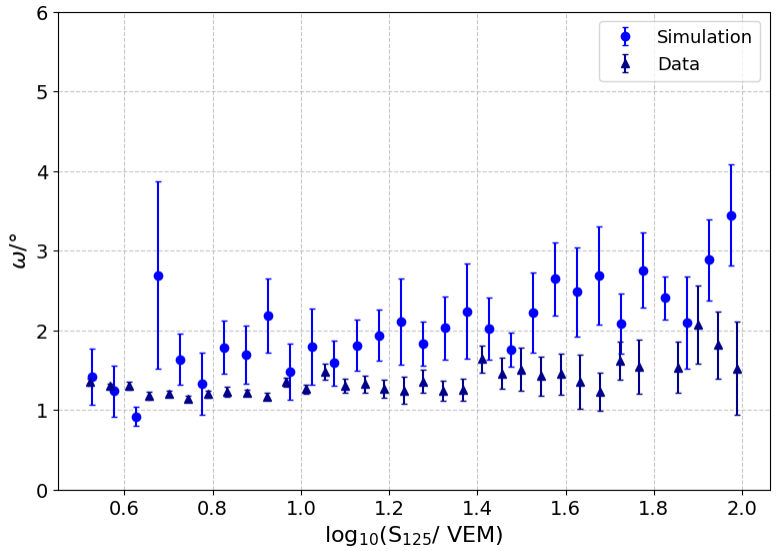

Figure 7.4: Comparison of the observed angular resolution between data and simulations. The reconstruction method demonstrates consistent performance across the angular range for both cases, although the comparison is not strictly one-to-one.

7.2 Timing Resolution

The measured time spread between all four scintillator pairs was observed to exhibit a spread of up to 15 ns for air showers contained within 100 m of the centre of the station and inclined up to 25° (see Fig. 5.18). Considering the typical detector separation of approximately 5 m, the expected geometric time delay between two panels can be up to 8 ns. This theoretical value

can be further influenced by electronic delays arising at various levels of the data acquisition chain. Additionally, while the detector efficiency scales with $\cos\theta$, the primary cosmic ray flux is approximately isotropic. As a result, the majority of detected showers originate from the near-vertical direction, reinforcing the expectation that the geometric delay is typically around 8 ns or lower. This is visible in Fig. 7.5, which shows the zenith distribution of the selected events used for the performance studies in this chapter.

To further characterize the timing performance of the scintillation detectors, a dedicated study was carried out to evaluate the intrinsic time resolution of the neighbouring detector pairs. This was achieved by examining the spread in the measured timing differences between neighbouring detectors with respect to key air-shower observables, namely, the distance of the detectors to the shower core, reconstructed shower size (S_{125}), and mean recorded charge in the pairs. The same methodology was applied to the reconstructed timing from the shower front model to investigate the performance of the reconstruction.

Figure 7.6 presents the measured time resolution between neighbouring panels as a function of (i) mean recorded charge, (ii) shower size $log_{10}(S_{125}/\text{VEM}$, and (iii) distance to the reconstructed shower core. In each panel, the 68th percentile spread of the measured time difference between neighbouring detectors is shown, along with the same metric for the reconstructed time delays (tDelay) relative to the core time. Data from all four scintillator pairs have been combined in this analysis, as the observed trends are broadly consistent across all pairs, and the goal is to characterize the overall timing resolution.

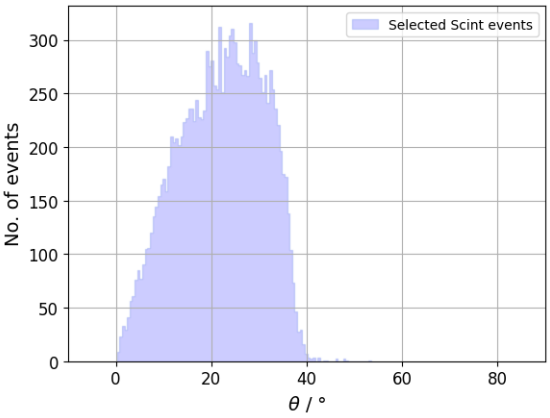

Figure 7.5: Distribution of the reconstructed zenith angles of the selected scintillator events.

From the mean charge plot, it is observed that the timing spread exhibits significant fluctuations at very low charges, which gradually reduces and plateaus around ~ 10 ns. This is expected, as at low signal levels the panels are likely sampling the outer, less dense regions of the air shower, where particle arrival times are more stochastic, and one detector in the pair may trigger while the other does not. In contrast, at higher charge values, both panels are more likely to sample the same dense region of the shower, leading to improved timing coincidence. A good agreement is observed between the raw timestamp resolution and the tDelay resolution, with the latter reaching slightly higher values around 10 ns, suggesting that the underlying time resolution of the system is approximately 10 ns. This minor discrepancy may indicate small residual electronic delays or model imperfections, but overall suggests robust performance.

For the $log_{10}(S_{125}/\text{VEM})$ dependence, the timing resolution improves with increasing shower size. This trend mirrors the one observed with charge, since higher-energy showers are more likely to produce dense particle footprints in the detectors, improving the temporal correlation between neighbouring modules. Notably, the worst-case timing spread at low S_{125} values is observed at 12.5 ns, which improves to approximately 7 ns at the highest shower sizes, indicating promising timing resolution. As previously observed, the simulated and measured timing agree well.

Lastly, the dependence on distance to the shower core shows that the optimal resolution is achieved when the scintillator pair lies close to the core, with the resolution deteriorating beyond $\sim$70 m. This is consistent with expectations. Detectors far from the core sample more spread-out regions of the shower front, where particle arrival times exhibit more variation.

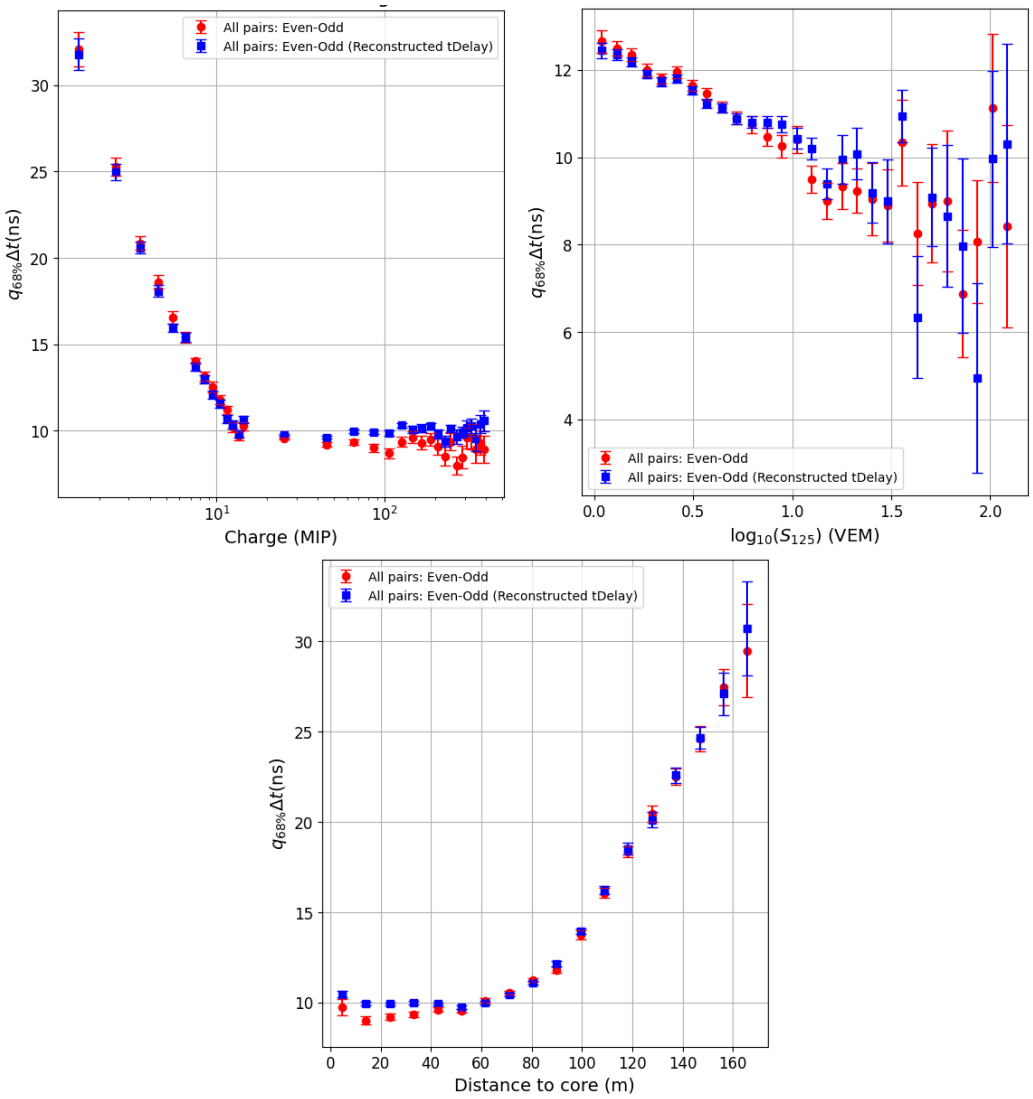

Figure 7.6: Measured timing resolution between neighbouring scintillator panels, shown as a function of mean recorded charge, reconstructed shower size ($log_{10}(S_{125}$/VEM), and distance to the shower core (bottom). In each case, both raw timestamp differences and reconstructed time delays relative to core time are shown.

The 70 m scale also roughly corresponds to the arm length of an SAE station, indicating that timing resolution naturally degrades at the array periphery. Again, the reconstructed tDelay values consistently track the raw timestamp resolution, supporting the reliability of the reconstruction. However, the difference in the measured timing at closest distances can be attributed to shower fluctuations due to the shape of the LDF. It is important to note that each bin in these distributions includes all zenith angles in the selected range. Since more inclined events exhibit greater shower front curvature and thus increased timing spread, part of the observed resolution degradation is attributable to inclination effects.

To investigate the influence of zenith direction of the shower core, a comparison of the standard deviation[3] of the measured time difference, Δt, for events with highly vertical ($0° - 10°$), up to inclined ($30° - 40°$) zenith angles was performed. Fig. 7.7 presents the timing with respect to mean charge for both measured (left) and reconstructed (right) scenarios.

A clear zenith dependence on the resolution is visible in the measured scenario. For high mean

[3] In this case, the full standard deviation is used due to limited statistics in these bins

charges, this spread decreases to approximately 7 ns for vertical showers. For the inclined showers, the resolution reaches about 9 ns. For the reconstructed time front, this spread in the resolution minimizes, and a resolution of $\sim$ 7ns is consistently achieved for all zenith angles. This is due to the applied time variance model, which accounts for the zenith dependence of the showers. These results collectively indicate a timing resolution of a few ns for the scintillation detectors in both instrumentation and reconstruction, which is comparable to the reported IceTop resolutions.

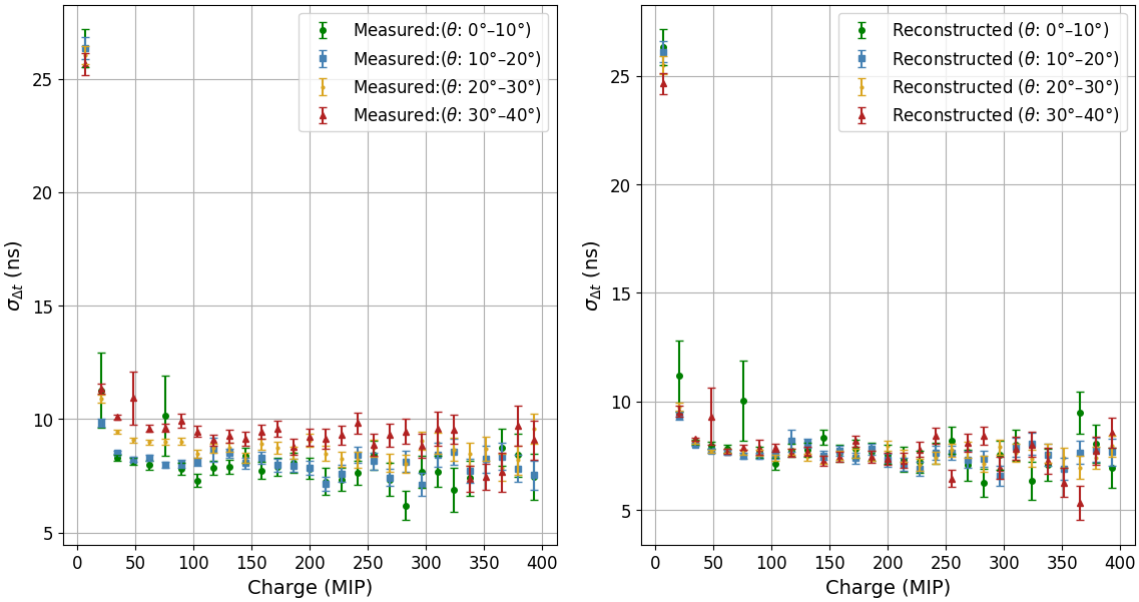

Figure 7.7: The time resolution in scintillator pairs with respect to mean deposited charge in distinct zenith bins ranging from vertical to inclined showers. The left plot depicts the measured resolution, and the right plot shows the reconstructed time resolution.

7.3 S_{125} Reconstruction and Comparison to IceTop

7.3.1 Shower Size

An essential component of the air-shower reconstruction is the estimation of the shower size, S_{125}, which serves as a proxy for the energy of the primary cosmic ray. Since S_{125} is derived from a lateral distribution function (LDF) fit, it is particularly sensitive to the stability of the LDF slope parameter, β. To better understand this sensitivity, the distribution of reconstructed β values was studied as a function of the $log_{10}(S_{125}/\text{VEM})$, taken from the IceTop reconstruction.

Figure 7.8 presents the β distributions in different bins of $\log_{10}(S_{125}/\text{VEM})$ in the form of violin plots. While a mean trend is observed, indicating a slight increase in β with shower size, each bin shows a wide spread in values, suggesting that β is not well constrained in a single-station reconstruction. This is expected given the high number of degrees of freedom in the LDF minimization, which involves fitting up to six parameters. Given this instability, a fixed value of $\beta = 2.4$, derived from the LDF parametrization discussed earlier, is used to reconstruct the shower size for the following study. Since the β parameter mainly affects the LDF reconstruction, the angular resolutions with the fixed β are comparable to ones discussed above.

Given the fixed β parameter, the signal model derived in the previous chapter can then be evaluated more closely. A preliminary comparison of the resulting S_{125} values with those from

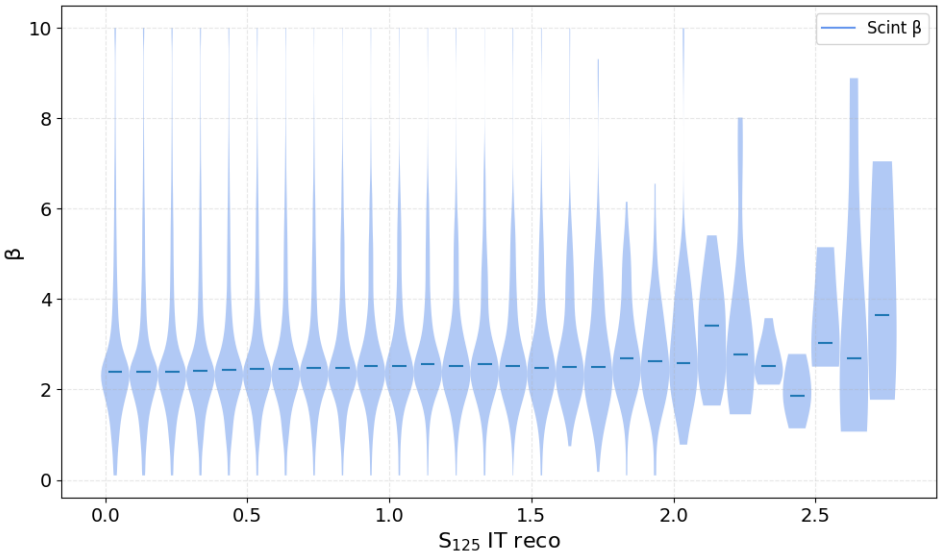

Figure 7.8: Violin plots showing the distribution of reconstructed β values as a function of $\log_{10}(S_{125}/\text{VEM})$ (IceTop). The mean value in each bin is marked. Although a trend is visible, the distributions are broad, reflecting the instability of β in single-station reconstructions.

the preliminary reconstruction, based on a non-Poisson model, shows a good agreement, along with a reduced number of edge events. This suggests that the signal model introduced earlier is reliable. These findings are encouraging, and further investigations based on this approach, especially with more stations, should be taken into account.

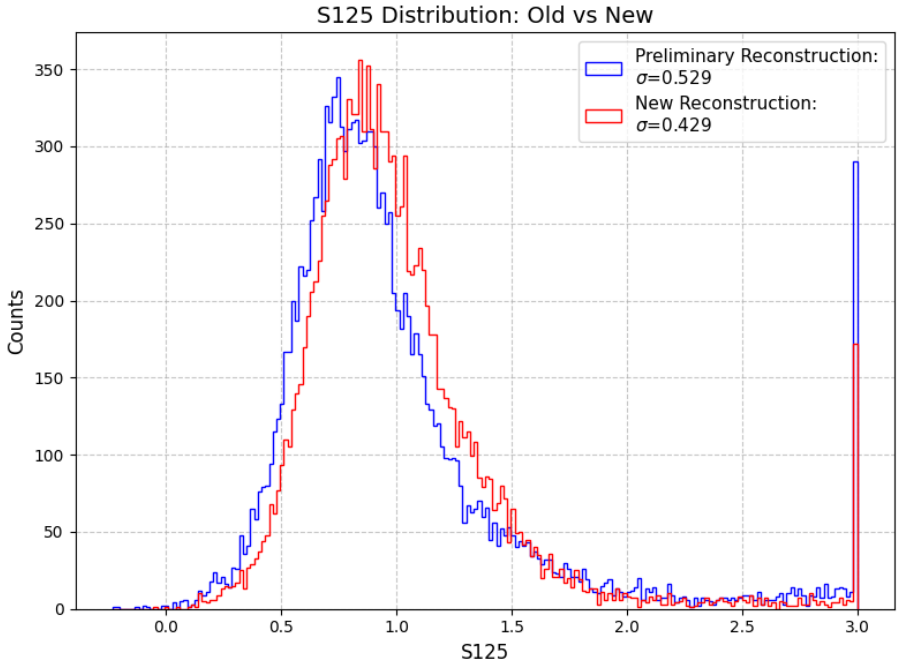

Figure 7.9: Comparison of reconstructed S_{125} from the scintillator station with the data-driven reconstruction (with fixed $\beta = 2.4$) to the preliminary reconstruction.

7.3.2 Comparison to IceTop

A preliminary comparison of the reconstructed $\log_{10}(S_{125})$ from both the IceTop and scintillation detectors was performed. Since both detector systems sample the same air showers, this

comparison is a valuable first step toward cross-calibration. An illustrative event, showing the lateral distribution observed by both detector types, is presented in Fig. 7.10. The markers indicate the measured charges in individual detectors. The lateral distribution function (LDF) reconstruction is performed using RockBottom [110] for the scintillators and Laputop [4] for IceTop. The IceTop reconstruction includes current snow correction model, which compensates for signal attenuation due to accumulated snow on top of the tanks. This correction is evident in the difference between the fit and observed charges in the plot.

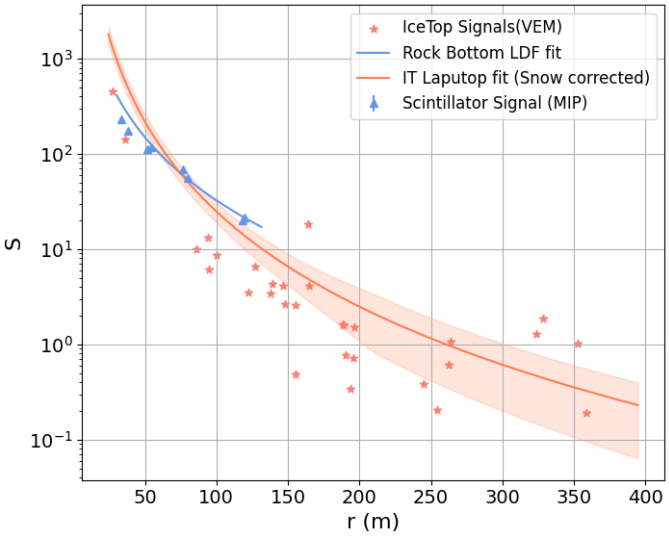

Figure 7.10: Lateral distribution function (LDF) for a representative event, comparing signal sizes from scintillators and IceTop. The discrepancy between the fit and measured IceTop signals is due to the snow correction applied in the Laputop reconstruction.

The charge measured by the scintillation detectors primarily originates from the electromagnetic component of air showers. This is a consequence of the 1 cm thickness of the scintillator bars, which makes them most sensitive to high-energy electrons observed as minimum ionizing particles (MIPs), with comparatively lower contributions from muons as they deposit less energy per unit length. Because scintillators are sensitive to minimally ionizing particles, their detection threshold is lower, resulting in a larger number of observed signals. For IceTop, both electromagnetic and muonic components contribute significantly. Snow accumulation further attenuates signals in IceTop, enhancing this difference. This attenuation can be studied by monitoring the difference in the deposited signal in these detectors over time, especially across periods of significant snow accumulation. Two main studies were conducted:

Comparison of S_{125} Values: As a first step, the S_{125} values reconstructed by each detector system were compared. The reconstructed S_{125} values for IceTop are in units of VEM, which corresponds to the signal generated in the detector by a Vertical Equivalent Muon passing through it, while in the scintillation detectors it corresponds to the vertical passing Minimally Ionizing Particles. Both correspond to the vertical sensitive area of the detectors. Since they differ in a sensitive area ($1.5\,\mathrm{m}^2$ for scintillators vs. $3.5\,\mathrm{m}^2$ for IceTop tanks), appropriate correction was applied to obtain per meter square signals. While a zenith angle correction should ideally be included, this preliminary analysis is restricted to nearly vertical showers ($\theta < 10°$).

The deduced comparison is shown in Fig. 7.11. A shift in the mean deposited signal is expected due to the difference in the detectors' response. A factor of approximately 3 is observed,

[4] The reconstruction framework used for IceTop

pointing to the difference in the two detectors' response due to the scintillation detector's lower energy threshold and higher sensitivity to the electromagnetic component. Although the scintillator reconstruction will improve with more stations, this is already a good indication for future studies aimed at disentangling the electromagnetic and muonic components of the same Extensive Air Showers.

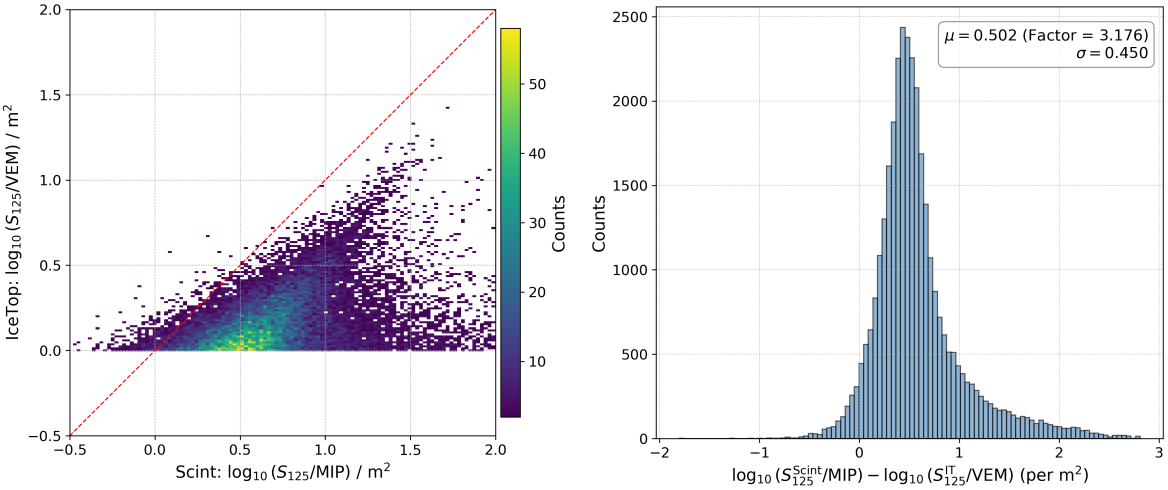

Figure 7.11: Left: 2D histogram comparing S_{125} from scintillators and IceTop, scaled by detector area. Right: Distribution of the difference between the two S_{125} values. A significant offset suggests limitations in the current snow correction model.

Comparison of the measured Signals As a step further, the measured signals in the two detectors can be compared. This is motivated by an objective to monitor how the IceTop tanks respond to the attenuated signals with increasing snow accumulation. The charge measured by each edge scintillator pair was compared to that of the two nearest IceTop tanks. While each detector samples a different region of the shower, the large containment area and statistical averaging should mitigate such effects. An advantage of the SAE geometry is the positioning of the scintillation detectors at roughly the same distance $\sim$ 60m from the IceTop tanks (see Fig. 3.18). This allows a rough comparison of charge deposits over time, potentially indicating snow accumulation effects. The area correction was also applied in this case, but no snow correction was done.

The obtained difference in the $log_{10}(S_{125})$ of Scintillators and IceTop is shown in Fig. 7.12. For comparison, the mean charge deposited in the two tanks of a station and the two neighbouring scintillators is taken. The two plots per detector combination present measurements over two-month intervals at the beginning (Jan-Mar) and end of 2023 (Sept-Nov). A slight increase in the scintillator to IceTop signal factor is observed between the two periods for IceTop stations 33 and 34; however, for station 43, a slight decrease is observed. The deposited snow heights measurements from Nov-2022, and Nov-2023 show an increase of snow depth by $\sim$ 20 cm for all the stations. Therefore, such a study needs to be further investigated. Nonetheless, overall, it can be a promising approach, especially over a longer period of time and with more detectors to compare.

Chapter Summary:

In this chapter, the performance of the scintillators of SAE Station 0 is evaluated using the data of the first year of operation, following the full calibration and reconstruction procedure. The performance is benchmarked with respect to IceTop array data. The key points include

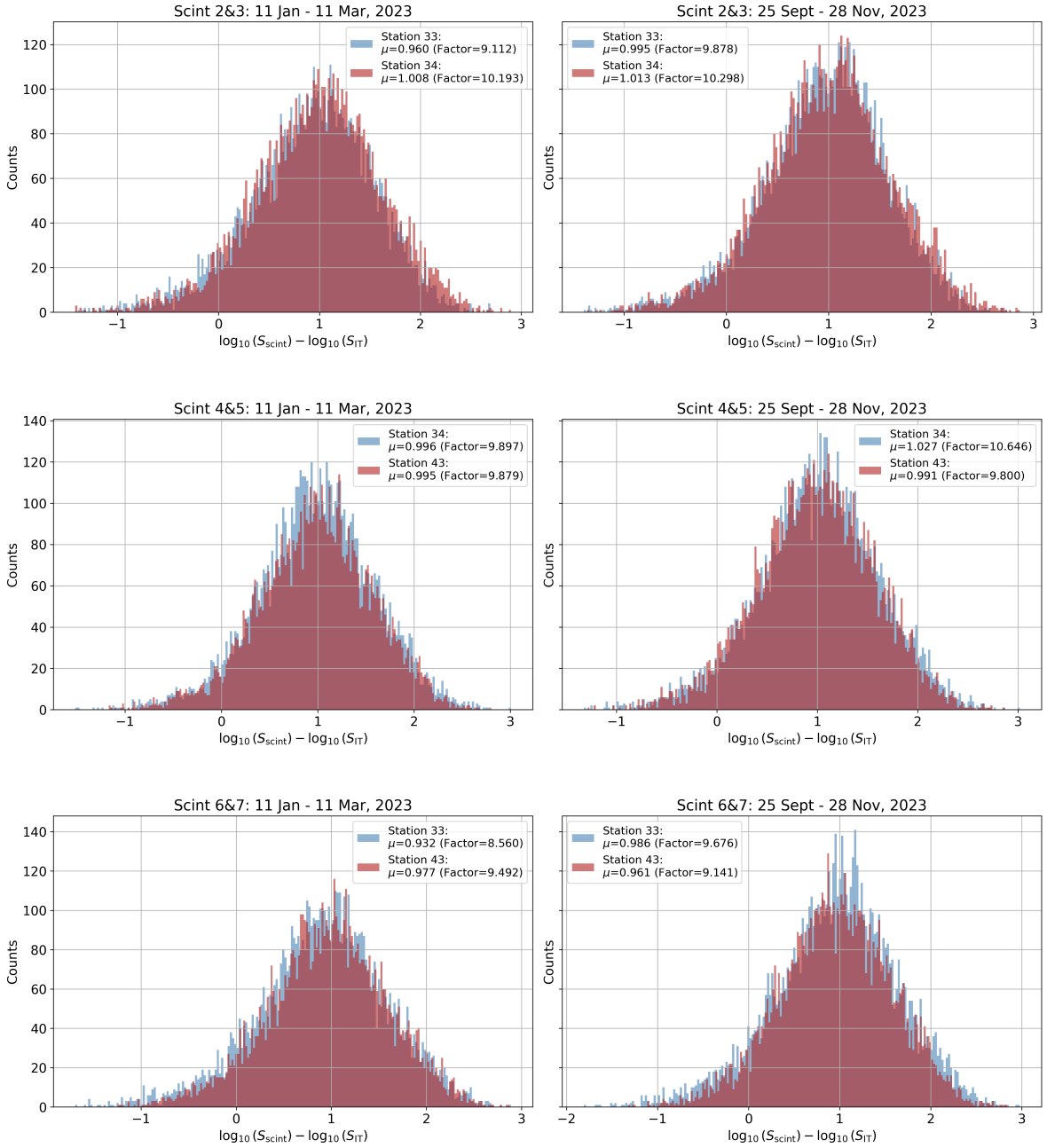

Figure 7.12: Seasonal variation in the ratio of measured charges between scintillators and nearby IceTop stations for three edge detector pairs. Each plot shows data binned in two-month intervals. Slight increases in the charge ratio over time may indicate effects from snow accumulation.

determination of the angular resolution, timing accuracy of the detectors, as well as the reconstruction procedure. An angular resolution of 2.3° is observed with a significant improvement for contained events within 70 m of the station centre. The dependence of the spread in the arrival timing of the air-shower particles at the scintillation detector neighbours is well understood and accounted for in the reconstruction, reaching a resolution of 7 ns for the given detectors at 5 m distance, which indicates the ns accuracy of the instrument. Finally, a preliminary comparison of the reconstructed shower size $log_{10}(S_{125})$ observed with Scintillators and IceTop tanks was performed, which pointed to a factor ≈ 3 excess in the scintillators, confirming their lower threshold and electromagnetic component sampling response. This can motivate future discrimination studies of the muonic and electromagnetic components of EAS

with a combination of the two particle detectors. Finally, a comparison of the raw signals of both detector types was performed, hinting at the possibility of monitoring the snow accumulation on the IceTop tanks.

Chapter 8

Summary

The origin of cosmic rays and their journey to Earth have been studied for over a century. While cosmic rays with energies up to a few hundred TeV are believed to originate from galactic sources such as supernova remnants, the higher-energy part of the spectrum remains veiled due to limitations on the direct measurements at higher energies on account of drastic drop in the flux. This transition region from TeV to PeV energies and beyond, also referred to as the first knee, is particularly intriguing, as it marks the upper energy limit of cosmic rays originating from galactic sources. Understanding this transition is crucial for identifying the underlying acceleration mechanisms and the astrophysical environments responsible for producing the highest-energy particles in the Milky Way Galaxy.

The IceCube Neutrino Observatory is uniquely positioned to probe the knee region of the cosmic-ray spectrum, enabling detection of the highest energy galactic cosmic rays. It acts as one of the leading cosmic-ray detector arrays in the Southern Hemisphere owing to its surface component, IceTop. Despite it's successful operation for over 13 years, IceTop's placement directly on the surface has posed challenges due to non-uniform snow accumulation. This effectively increases uncertainties and raises the detection threshold. To mitigate these effects, lower the energy threshold, and enable multi-channel air-shower observations, a major enhancement effort is underway, involving the deployment of additional particle detectors and radio antennas. This is called the IceCube Surface Array Enhancement (SAE).

This work was focused on the Scintillation detectors of the SAE. It includes the full production and characterization of the scintillator panels, detailed laboratory and in-situ calibration procedures, especially for temperature-sensitive Silicon Photomultipliers (SiPMs), and validation of their response to cosmic-ray-induced Minimally Ionising Particles (MIPs). Initial performance evaluations from the deployed station demonstrated promising timing resolution, detector uniformity, and reconstruction capabilities, laying the groundwork for precision cosmic-ray studies of the highest-energy galactic cosmic rays.

Production A dedicated pre-calibration and validation framework was developed to support the production of scintillation detectors for the full SAE, which is planned to consist of 32 stations, each equipped with 8 scintillation detectors. As part of the preparation for the initial deployment phase, detectors for 7 stations were produced, calibrated, and qualified. Among these, one station replaced the prototype station's scintillators, becoming the first fully instrumented final-configuration SAE station. Two additional stations have been deployed at the South Pole since January 2025. To ensure uniformity in production and validation, a dedicated test bench was established at KIT. This setup enabled systematic pre-calibration, energy response characterization, and background assessment for each detector unit. Environmental noise in the test bench vicinity, primarily from natural radioactivity in concrete and

electromagnetic interference was effectively mitigated using lead shielding and a metal-walled enclosure, resulting in a stable and reproducible test environment. A key outcome of the validation campaign was the confirmation that cosmic-ray induced MIPs deposit approximately 1.7 MeV in the scintillation detectors, in agreement with expectations from simulations (using radioactive source measurements). This served as a fundamental benchmark for detector calibration and demonstrated the ability of the detectors to identify relativistic particles even in unshielded conditions. The calibration stability was further cross-validated using independent approaches. MIP peaks determined from stand-alone charge histograms were in good agreement with results obtained from hitbuffer-based multiplicity filtering. Threshold scans additionally confirmed reliable Geiger-mode operation across the entire production series, with consistent behaviour observed across all detector units. These efforts collectively demonstrate the technical readiness and scientific reliability of the scintillation detectors for operation in the extreme environment of the South Pole and represent a major milestone in the successful realisation of the SAE.

Calibration and On-Ice Commissioning The first final-configuration station of the SAE, Station 0, was deployed at the South Pole in early 2023. It was equipped with updated scintillation detector modules and the latest data acquisition boards uDAQ 4.1a, which offered a significantly expanded dynamic range and enhanced data acquisition capabilities. To ensure robust calibration under the extreme and variable conditions at the South Pole, a gain calibration procedure was developed for the SiPMs. This calibration relied on the position of the MIP peak in the presence of electromagnetic background and was performed across all three uDAQ gain channels over the full expected temperature range. The resulting calibration allowed raw ADC signals to be reliably converted into physical MIP units for each scintillation detector. The observed dynamic range of the scintillation detectors covers the range from 0.5 to 500 $\sim$ 700 MIPs, dependent on the ambient temperature. This calibration will be incorporated into real-time corrections in the future uDAQ firmware. Post-deployment performance studies confirmed the uniformity and stability of the detector response across Station 0, indicating successful calibration. Neighbouring scintillators showed a near 1:1 correlation in measured charge, with observed fluctuations primarily due to differences in air-shower particle densities rather than hardware inconsistencies. Timing studies revealed excellent resolution. A few nanoseconds-level timing precision was achieved, with the time resolution in measured air-showers reaching $\sim$10 ns and improving to $\sim$7 ns for larger showers for the 5 m distant detectors. Such timing precision is essential for accurate air-shower front reconstruction and effective background suppression. A scalable data processing and reconstruction pipeline was also partially developed, enabling scintillator data to be calibrated, filtered, and merged with coincident IceTop and radio detector events. During commissioning, a $\sim$1-second time offset between SAE and IceTop was identified in the 2023 dataset and traced to a firmware issue in the White Rabbit timing system. This correction ensures the temporal alignment required for high-quality hybrid event reconstruction across the enhanced surface array. Together, these calibration and commissioning efforts confirm the scintillator system's readiness for long-term operation and scientific use within IceCube's surface enhancement programme.

Data-Driven Reconstruction and Performance Studies A comprehensive data-driven parametrization for air shower reconstruction was developed using data from Station 0, refining and optimizing reconstruction previously derived from simulations. A temporal pulse cleaning was implemented to effectively remove uncorrelated particles to improve the angular resolution accuracy. To overcome limitations of single-station core reconstruction, a L2-reconstruction step was introduced that leveraged the more reliable core position estimates from IceTop. This step was crucial in enhancing angular resolution and overall reconstruction quality. Ad-

ditionally, a realistic signal variance model was established, exhibiting near-Poisson behaviour ($\sigma_S \propto \langle S \rangle^{0.545}$). This model plays a vital role in properly weighting signals during Lateral Distribution Function (LDF) reconstruction, directly impacting the precision of energy and composition measurements.

The data-driven reconstruction achieved a space angle resolution of 2.3° (zenith 2.8°, azimuth 8.6°) when benchmarked against IceTop, with the resolution improving significantly to 1.2° for shower cores located within 70 m of the stations center. This improvement is especially significant at lower shower energies, underscoring the enhanced sensitivity provided by SAE. Timing performance studies confirmed the intrinsic timing resolution between neighbouring scintillation detectors plateaued near ∼10 ns at high charges and improved to ∼7 ns at the largest shower sizes. A clear dependence on the arrival direction was observed, with timing resolutions of approximately 6 ns for vertical showers and 9 ns for inclined showers. However, the reconstructed shower front consistently achieved ∼7 ns resolution, demonstrating excellent time modelling critical for precise air-shower reconstruction.

A preliminary comparison of the reconstructed shower size proxy, S_{125}, between the scintillators and IceTop revealed a factor of approximately 3. This dependence validates the expected difference in the response of the two detector types, with scintillation detection predominantly sampling the electromagnetic component of the observed air showers. Over a longer period of time and a bigger SAE array, this can be used for dedicated studies to disentangle the electromagnetic and muonic components of the Extensive Air Showers. Further seasonal analyses of measured signals in the two detectors indicated subtle variations in the scintillator-to-IceTop signal ratio, likely linked to snow accumulation effects. A similarly elaborated study can be used to monitor the snow accumulation on the individual IceTop detectors in the future. These results achieved with one year of data from a single SAE station highlight important avenues for improving long-term cosmic-ray data quality and interpretation within the IceCube surface array.

Appendix A

Supplementary Measurements: Pre-Calibration

A.1 SiPM calibration: Disqualified unit

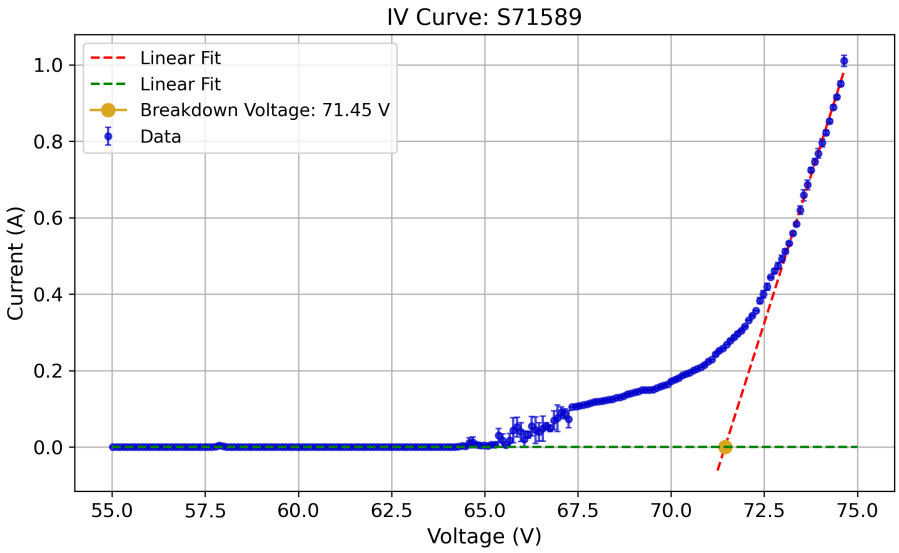

Figure A.1: One of the SiPMs failed the IV-curve calibration due to an abnormal increase in current observed before reaching the expected breakdown voltage. This atypical behavior suggests potential defects or damage in the device, which could compromise its performance and reliability in operation.

A.2 Field Tests: Low Temperature measurements

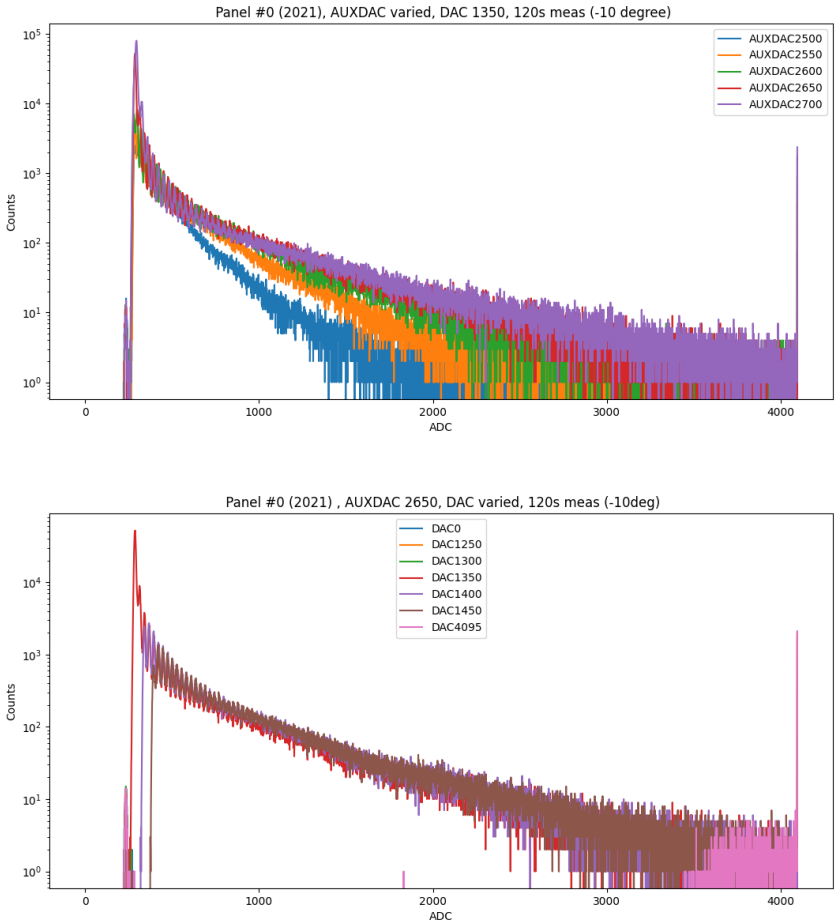

Figure A.2: Measurements were conducted to determine the optimal bias voltage and threshold settings for operating the scintillation detectors. The top panel displays charge histograms from a voltage scan near the expected optimal operating range, illustrating how detector response varies with different bias voltages. The bottom panel presents charge histograms from a threshold scan, including the lowest and highest achievable thresholds.

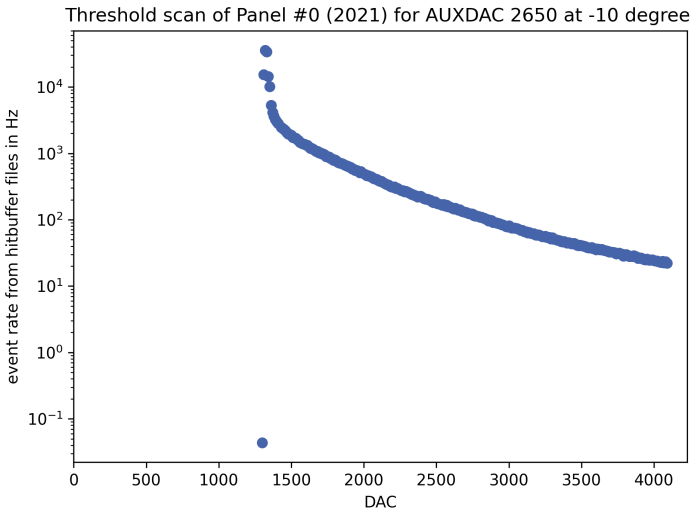

Figure A.3: Threshold scan covering the entire range. The avalanche condition is met at roughly 1300 DAC units.

A.3 Radioactive Source Measurements

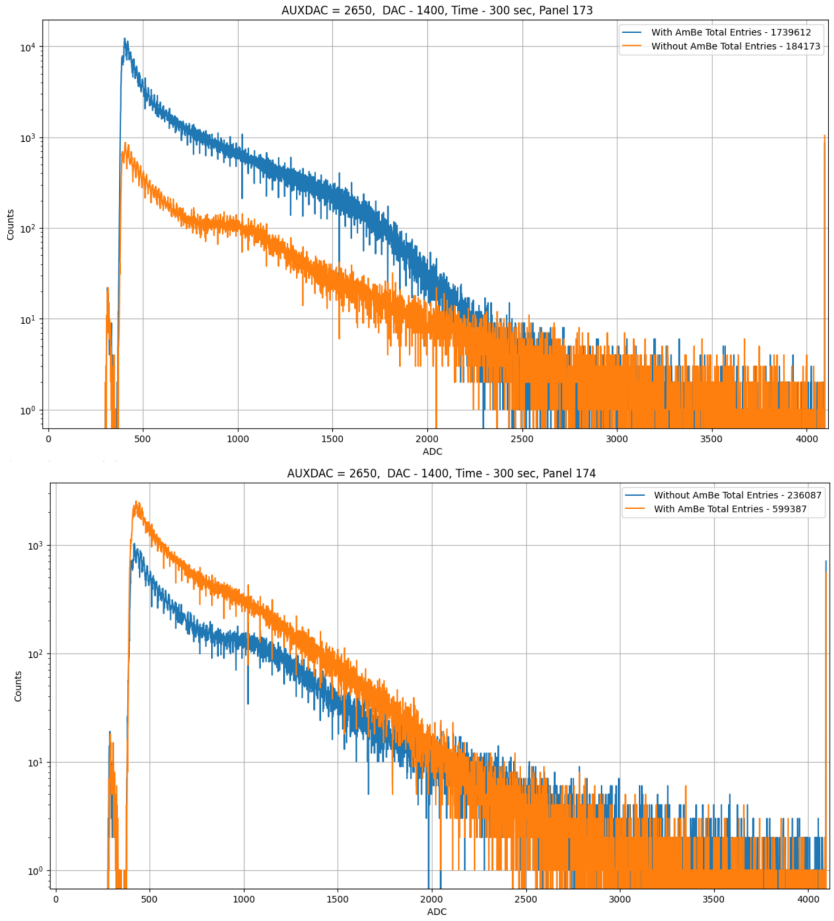

Figure A.4: The charge histogram measurement taken with the AmBe neutron source revealed that its intensity was so high that it completely obscured the minimum ionizing particle (MIP) peak, even in Panel 174, which was positioned above the boron carbide and lead shielding. The Compton edges, typically used as spectral features for energy calibration, were not distinguishable in the spectrum, indicating that the detector response was dominated by the high neutron flux rather than distinct energy depositions.

A.4 Local Radioactivity Measurements

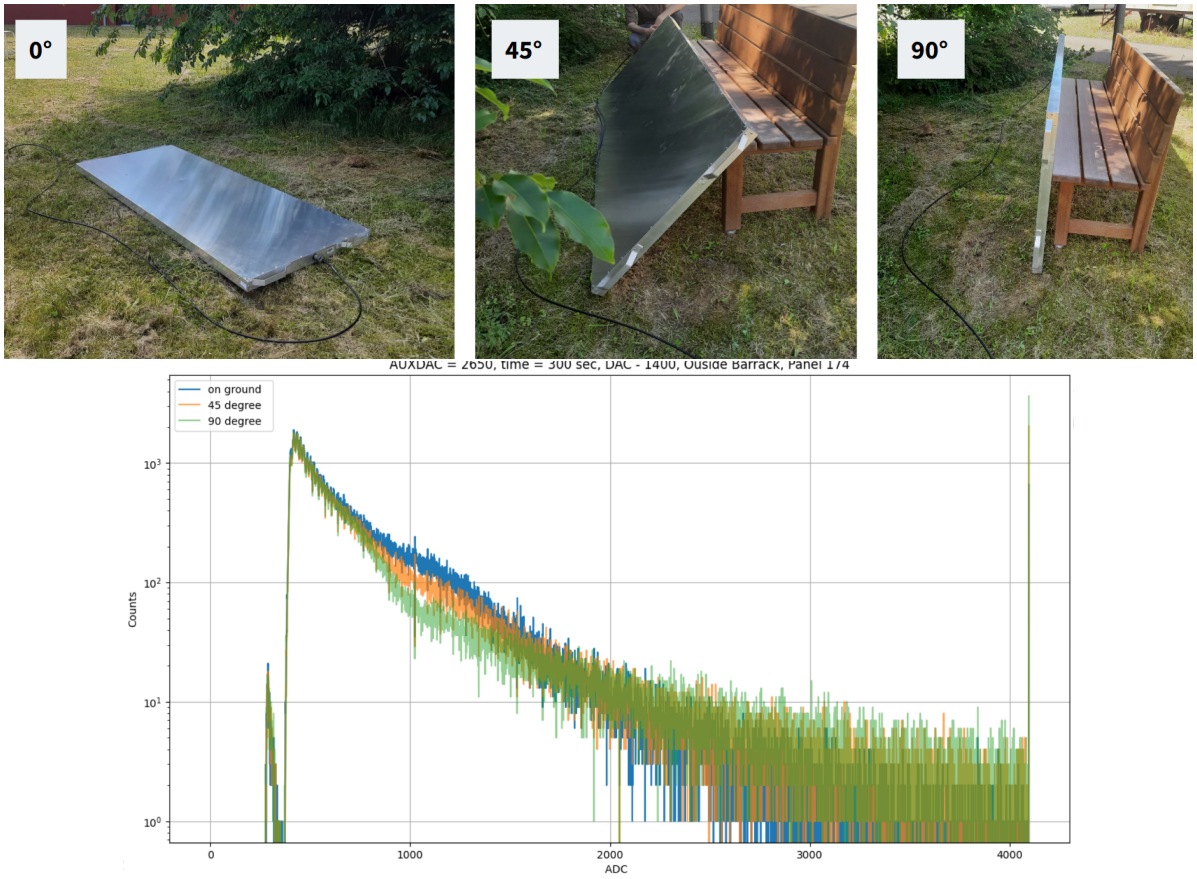

Figure A.5: The response of the scintillation detectors was measured at three different angles relative to the ground to isolate the contribution of local background from natural radioactivity. At 90 degrees, the detectors primarily sampled stray beta and gamma particles from the atmosphere, resulting in a prominent bump in the expected background region.

Appendix B

Supplementary Measurements: On-Ice Calibration and comissioning

B.1 Baseline Studies

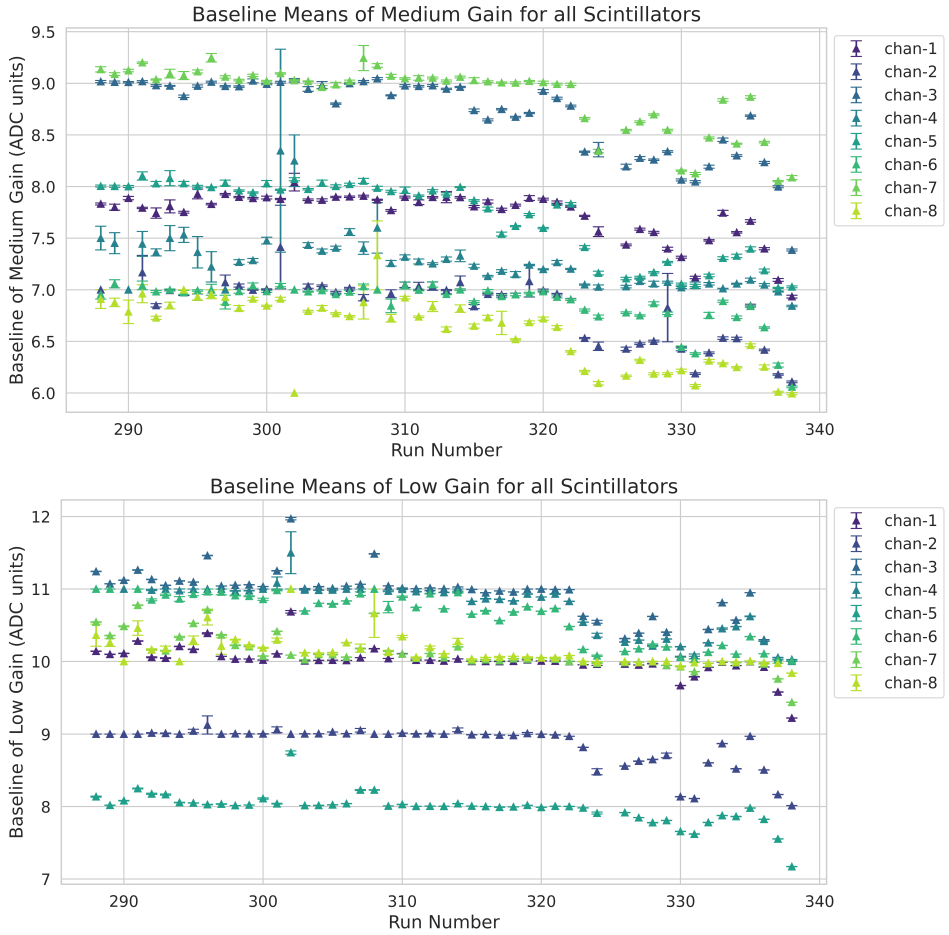

Figure B.1: The baseline of the 8 scintillation detectors as seen in medium and low gain channels. The variations are likely due to the weather transition from summer to winter, affecting the SiPM response.

B.2 Time offset: Radio-IT

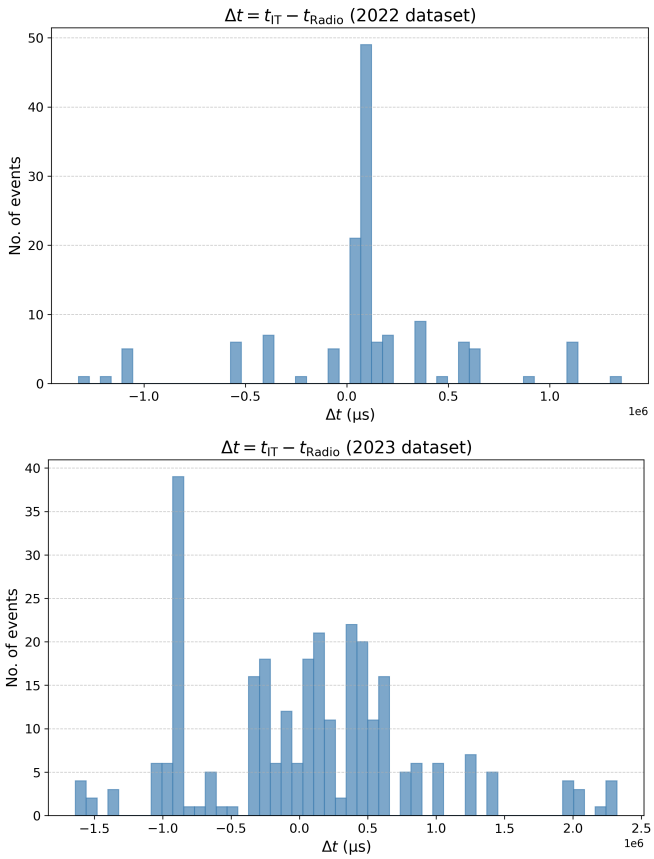

Figure B.2: A 1-second timing offset was observed in the 2023 data relative to IceTop, indicating a synchronization issue. A comparison of time offsets between IceTop and the Radio array for both 2022 and 2023 shows consistent alignment in 2022, while the 2023 data reveals a clear shift in the Radio system.

B.3 Time offset: Radio-Scint

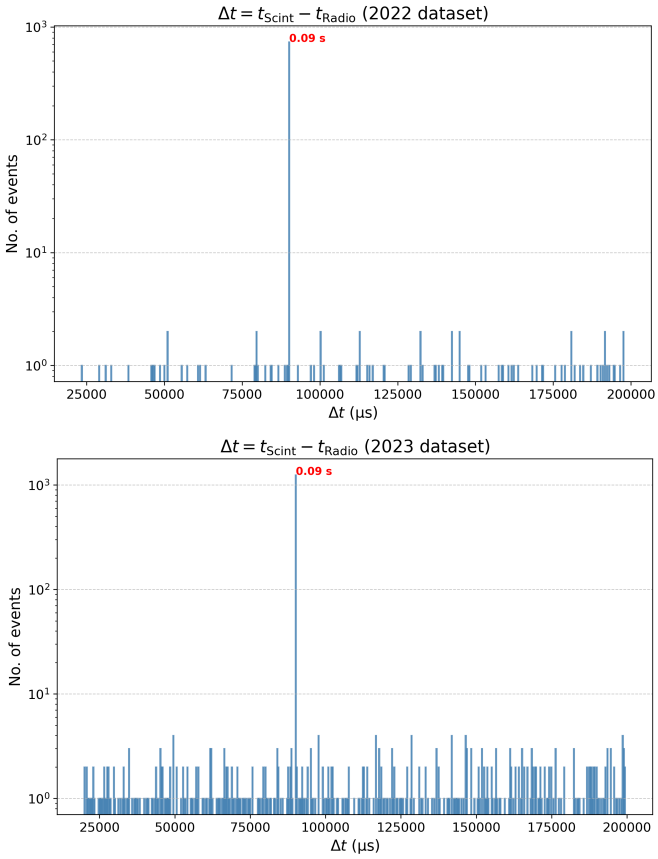

Figure B.3: The time offset between the scintillators and the radio detectors was confirmed to be stable over the years, consistently measuring around 0.09 seconds. This persistent offset suggests a systematic timing difference between the two systems, which is accounted for in joint analyses to ensure accurate event matching and reconstruction.

B.4 Temperature Co-relation

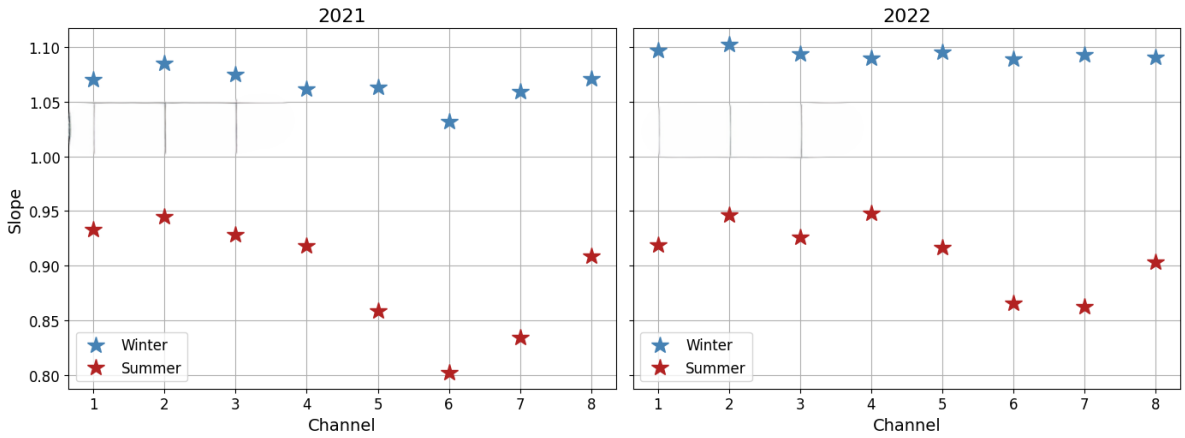

	2021 Winter	2021 Summer	2021 All	2022 no FH Winter	2022 no FH Summer	2022 no FH All
0	1.07	0.933	0.896	1.097	0.918	0.962
1	1.086	0.945	0.908	1.102	0.948	0.959
2	1.075	0.929	0.895	1.094	0.926	0.969
3	1.061	0.921	0.884	1.09	0.948	0.971
4	1.063	0.862	0.845	1.095	0.918	0.933
5	1.032	0.804	0.781	1.089	0.865	0.911
6	1.059	0.831	0.814	1.093	0.864	0.91
7	1.071	0.909	0.878	1.091	0.903	0.955

Figure B.4: The slopes for all eight channels, representing the correlation between scintillator temperature and the nearby weather station readings, were evaluated separately for the summer and winter periods. The results are summarized in a table.

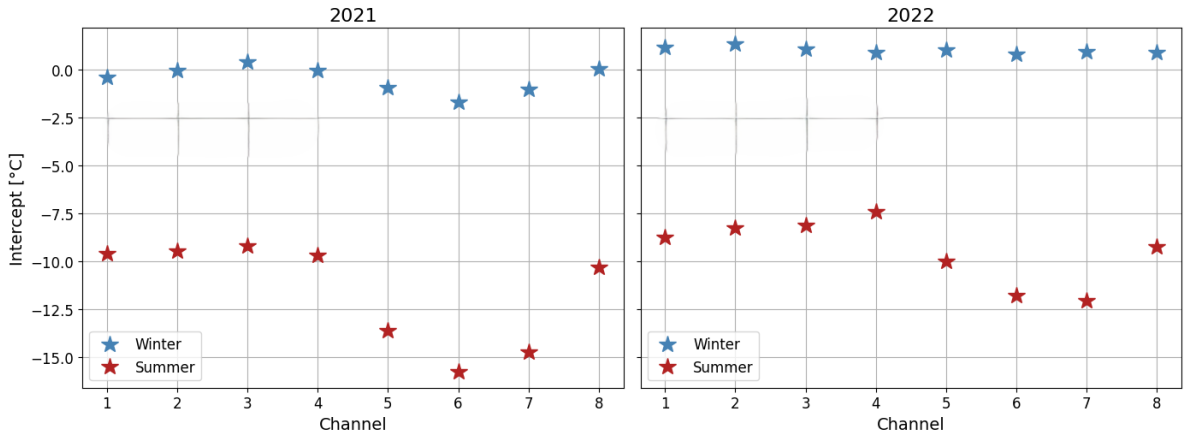

	2021 Winter	2021 Summer	2021 All	2022 no FH Winter	2022 no FH Summer	2022 no FH All
0	-0.399	-9.581	-10.09	1.175	-8.78	-5.899
1	-0.043	-9.427	-9.932	1.341	-8.213	-6.138
2	0.416	-9.202	-9.649	1.09	-8.139	-5.423
3	-0.045	-9.548	-10.002	0.924	-7.387	-5.29
4	-0.911	-13.459	-12.965	1.04	-9.967	-7.434
5	-1.666	-15.674	-15.594	0.823	-11.822	-8.471
6	-1.0	-14.882	-14.545	0.972	-12.013	-8.604
7	0.079	-10.279	-10.686	0.912	-9.257	-6.175

Figure B.5: The offset observed for all eight channels, representing the correlation between scintillator temperature and the nearby weather station readings, were evaluated separately for the summer and winter periods. The results are summarized in a table. The summer months experience 9° offset which is corrected for in the processing.

B.5 SAE-IT Coincidences

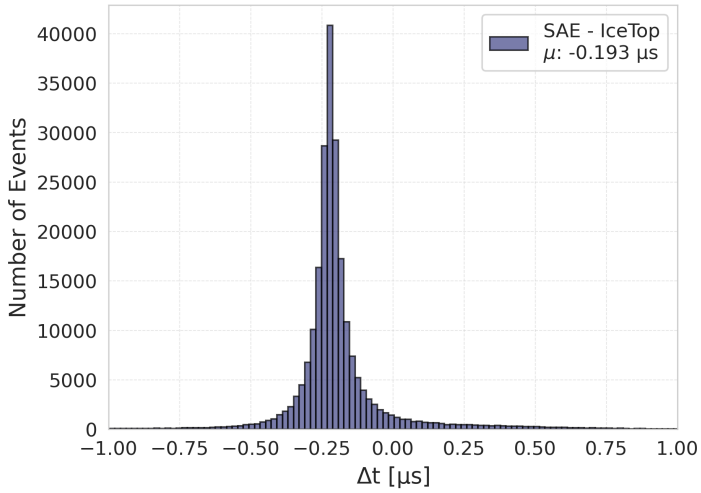

Figure B.6: The uncorrected timing offset between scintillator and IceTop coincident events shows a mean value around 193 ns, which is likely caused by differences in their global clock systems.

Appendix C

Supplementary material: Data Driven Parametrization

C.1 EMG-Gaussian Time bin model

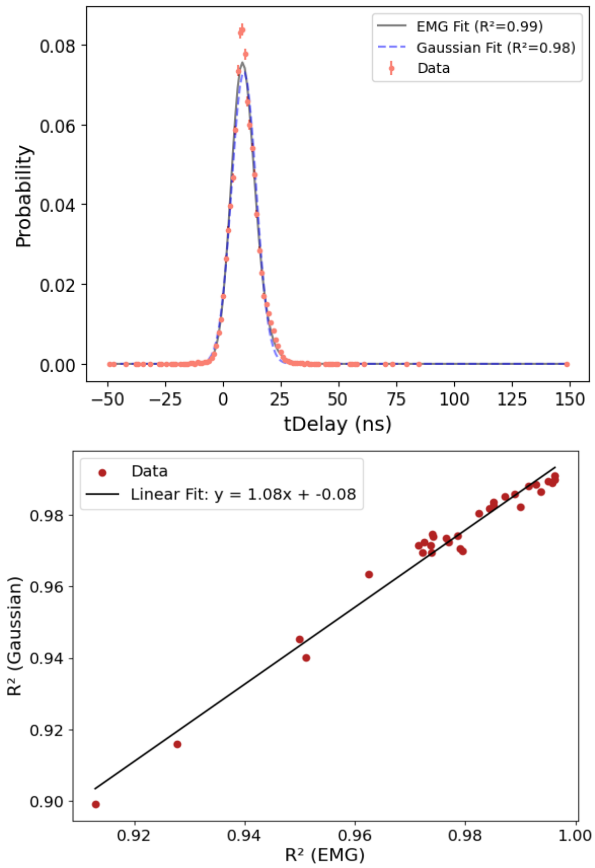

Figure C.1: The binned timing with respect to the shower front, is modelled with exponetially modified and gaussian function. Both fits seem to agree with reason, so the existing gaussian approach is taken. The lower plot shows the corelation plot in the R2 goodness of fit for both. The slope is 1.08

C.2 Slope vs Measured Signal

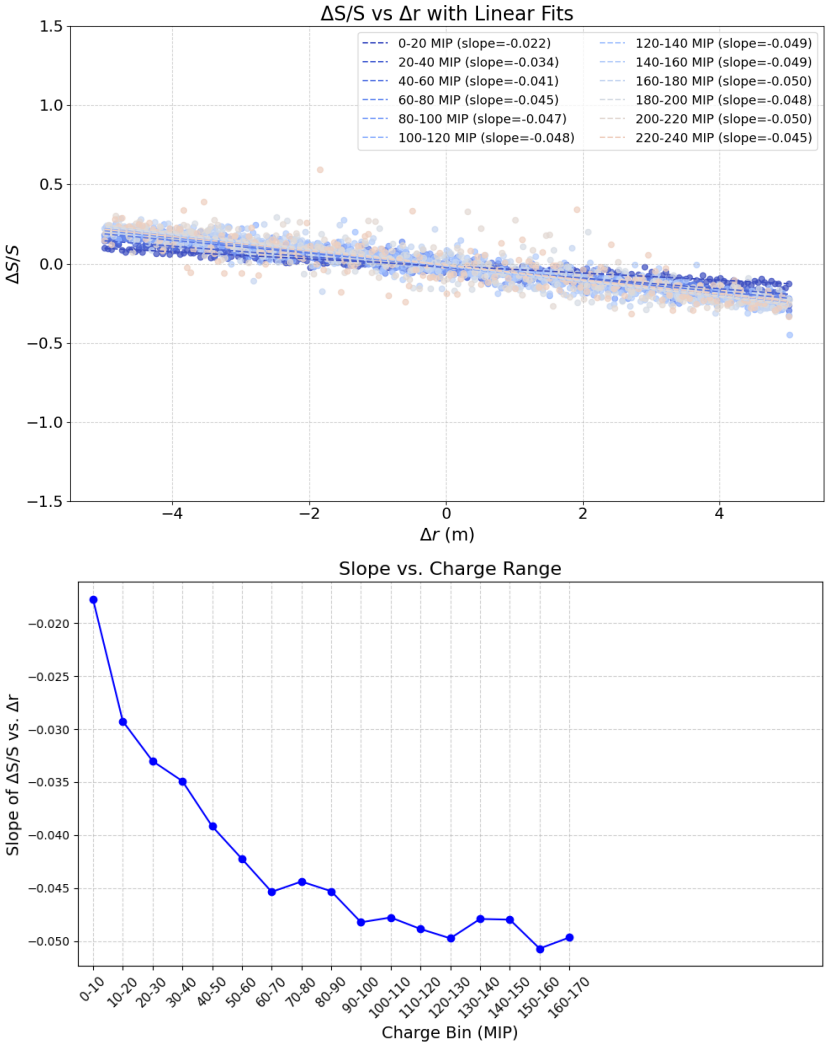

Figure C.2: The increase in relative fluctuations between neighbouring panels as a function of mean charge was studied, revealing that the slope of the $\Delta S/S$ (relative signal difference) versus distance to the shower core decreases with increasing mean charge.

C.3 More examples of LDF Binned Data

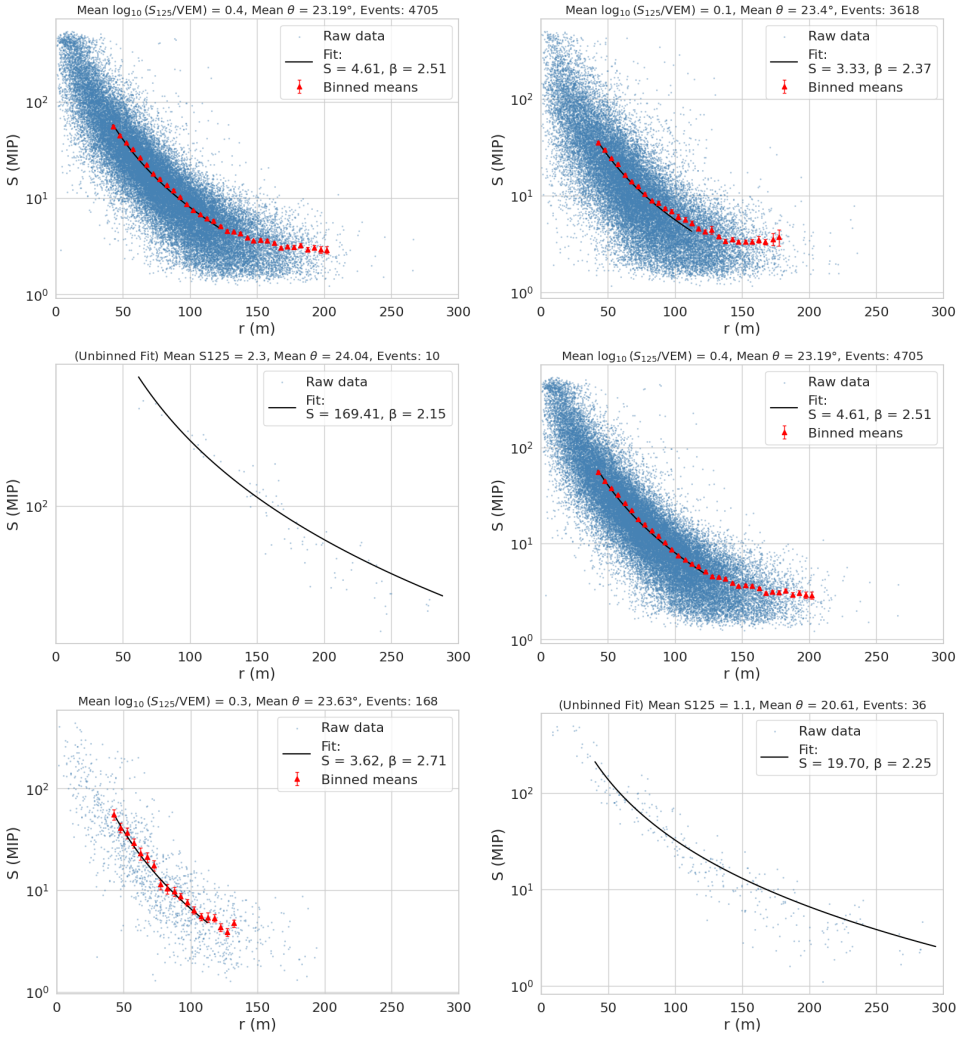

Figure C.3: Lateral Distribution Function (LDF) fits using binned parameterization are presented for various zenith angle and shower size bins, showing a clear flattening of the slope parameter β at higher energies. In cases with insufficient statistics, radial binning was omitted, and the LDF fit was applied to the full dataset to ensure reliable parameter estimation despite limited event counts.

Bibliography

[1] D. Pacini, *Penetrating Radiation at the Surface of and in Water*, *Nuovo Cim.* **8** (1912) 93 [1002.1810].

[2] V.F. Hess, *Über Beobachtungen der durchdringenden Strahlung bei sieben Freiballonfahrten*, *Phys. Z.* **13** (1912) 1084 [1808.02927].

[3] P. Mertsch, *Rapporteur talk: Cosmic ray direct*, *arXiv:2110.03325* (2021) [2110.03325].

[4] F.G. Schröder, *News from Cosmic Ray Air Showers (Cosmic Ray Indirect - CRI Rapporteur)*, *PoS* **ICRC2019** (2020) 030 [1910.03721].

[5] Y.-H. Chang, *Latest Results from the AMS Experiment*, *JPS Conf. Proc.* **39** (2023) 011006.

[6] W. Menn, O. Adriani, G. Barbarino, G. Bazilevskaya, R. Bellotti, M. Boezio et al., *The PAMELA space experiment*, *Advances in Space Research* **51** (2013) 209.

[7] Pierre Auger collaboration, *Constraining the sources of ultra-high-energy cosmic rays across and above the ankle with the spectrum and composition data measured at the Pierre Auger Observatory*, *JCAP* **05** (2023) 024 [2211.02857].

[8] A.D. Supanitsky, A. Cobos and A. Etchegoyen, *Origin of the light cosmic ray component below the ankle*, *Phys. Rev. D* **98** (2018) 103016 [1810.12367].

[9] IceCube collaboration, *Observation of Cosmic-Ray Anisotropy in the Southern Hemisphere with 12 yr of Data Collected by the IceCube Neutrino Observatory*, *Astrophys. J.* **981** (2025) 182 [2412.05046].

[10] KASCADE-Grande collaboration, *The KASCADE-Grande energy spectrum of cosmic rays and the role of hadronic interaction models*, *Adv. Space Res.* **53** (2014) 1456.

[11] GRAPES-3 collaboration, *A large area muon tracking detector for ultra-high energy cosmic ray astrophysics—the GRAPES-3 experiment*, *Nuclear Instruments and Methods in Physics Research Section A: Accelerators, Spectrometers, Detectors and Associated Equipment* **545** (2005) 643.

[12] Telescope Array collaboration, *Telescope Array Experiment*, *Nuclear Physics B - Proceedings Supplements* **175-176** (2008) 221.

[13] Pierre Auger collaboration, *AugerPrime: the Pierre Auger Observatory Upgrade*, *EPJ Web Conf.* **210** (2019) 06002 [1905.04472].

[14] IceCube collaboration, IceCube. https://icecube.wisc.edu/science/icecube/.

[15] IceCube collaboration, *IceTop: The surface component of IceCube*, *Nucl. Instrum. Meth. A* **700** (2013) 188 [1207.6326].

[16] IceCube collaboration, *Accounting for changing snow over 10 years of icetop, and its impact on the all-particle cosmic ray spectrum*, in *38th International Cosmic Ray Conference (ICRC2023) - Cosmic-Ray Physics (Indirect, CRI)*, vol. 444 of *Proceedings of Science*, pp. Art.–Nr.: 377, Scuola Internazionale Superiore di Studi Avanzati (SISSA), 2023, DOI.

[17] IceCube collaboration, *A Scintillator and Radio Enhancement of the IceCube Surface Detector Array*, *EPJ Web Conf.* **210** (2019) 06009 [1903.04117].

[18] S. Shefali, F. Schröder, R. Abbasi, M. Ackermann, J. Adams, S.K. Agarwalla et al., *Status and plans for the instrumentation of the IceCube Surface Array Enhancement*, in *Proceedings of 38th International Cosmic Ray Conference — PoS(ICRC2023)*, vol. 444, p. 342, 2023, DOI.

[19] T.K. Gaisser, R. Engel and E. Resconi, *Cosmic Rays and Particle Physics*, Cambridge University Press, 2 ed. (2016).

[20] P. Grieder, *Extensive Air Showers: High Energy Phenomena and Astrophysical Aspects - A Tutorial, Reference Manual and Data Book*, Springer Berlin Heidelberg (2011).

[21] J. Bland-Hawthorn and O. Gerhard, *The galaxy in context: Structural, kinematic, and integrated properties*, *Annual Review of Astronomy and Astrophysics* **54** (2016) 529–596.

[22] S.D. Wick, C.D. Dermer and A. Atoyan, *High-energy cosmic rays from gamma-ray bursts*, *Astroparticle Physics* **21** (2004) 125.

[23] E. Fermi, *On the origin of the cosmic radiation*, *Phys. Rev.* **75** (1949) 1169.

[24] M. Bustamante, G. Carrillo Montoya, W. de Paula, J.A. Duarte Chavez, A.M. Gago, H. Hakobyan et al., *High-energy cosmic-ray acceleration*, *2009 CERN - Latin-American School of High-Energy Physics* (2010) 533.

[25] K. Greisen, *End to the cosmic-ray spectrum?*, *Phys. Rev. Lett.* **16** (1966) 748.

[26] G.T. Zatsepin and V.A. Kuzmin, *Upper limit of the spectrum of cosmic rays*, *JETP Lett.* **4** (1966) 78.

[27] B.G. Keilhauer, *Investigation of atmospheric effects on the development of extensive air showers and their detection with the Pierre Auger Observatory*, Ph.D. thesis, Karlsruher Institut für Technologie, 2004. 10.5445/IR/4512003.

[28] F.G. Schröder, *Radio detection of cosmic-ray air showers and high-energy neutrinos*, *Progress in Particle and Nuclear Physics* **93** (2017) 1.

[29] J. Matthews, *A Heitler model of extensive air showers*, *Astroparticle Physics* **22** (2005) 387.

[30] H.P. Dembinski, R. Engel, A. Fedynitch, T. Gaisser, F. Riehn and T. Stanev, *Data-driven model of the cosmic-ray flux and mass composition from 10 GeV to* 10^{11} *GeV*, *PoS* **ICRC2017** (2018) 533 [1711.11432].

[31] B. Peters, *Primary cosmic radiation and extensive air showers*, *Nuovo Cim.* **22** (1961) 800.

[32] W.D. Apel et al., *KASCADE-Grande measurements of energy spectra for elemental groups of cosmic rays*, *Astropart. Phys.* **47** (2013) 54 [1306.6283].

[33] Pierre Auger collaboration, *Measurement of the cosmic ray flux near the second knee with the Pierre Auger Observatory*, *PoS* **ICRC2019** (2020) 225.

[34] V. Berezinsky, A.Z. Gazizov and S.I. Grigorieva, *On astrophysical solution to ultrahigh-energy cosmic rays*, *Phys. Rev. D* **74** (2006) 043005 [hep-ph/0204357].

[35] E. Guido, P. Abreu, M. Aglietta, J.M. Albury, I. Allekotte, A. Almela et al., *Combined fit of the energy spectrum and mass composition across the ankle with the data measured at the Pierre Auger Observatory*, in *Proceedings of 37th International Cosmic Ray Conference — PoS(ICRC2021)*, vol. 395, p. 311, 2021, DOI.

[36] N. Tomassetti, *Direct Measurements of Galactic Cosmic Rays*, *PoS* **ECRS** (2023) 007 [2301.10255].

[37] DAMPE collaboration, *The DAMPE experiment and its latest results*, *J. Phys. Conf. Ser.* **1390** (2019) 012063.

[38] ISS-CREAM collaboration, *Results from the Cosmic Ray Energetics And Mass for the International Space Station (ISS-CREAM) experiment*, *PoS* **ICRC2021** (2021) 095.

[39] A. Obermeier, M. Ave, P. Boyle, C. Höppner, J. Hörandel and D. Müller, *Energy spectra of primary and secondary cosmic-ray nuclei measured with tracer*, *The Astrophysical Journal* **742** (2011) 14.

[40] Pierre Auger collaboration, *The Surface Detector System of the Pierre Auger Observatory*, *Nucl. Instrum. Meth. A* **586** (2008) 409 [0712.2832].

[41] B.M. Bolotovskii, *Vavilov-cherenkov radiation: its discovery and application*, *Phys. Usp.* **52** (2009) 1099.

[42] D.E. Groom, N.V. Mokhov and S.I. Striganov, *Muon stopping power and range tables 10-MeV to 100-TeV*, *Atom. Data Nucl. Data Tabl.* **78** (2001) 183.

[43] H.E.S.S. collaboration, *The HESS experimental project*, *Nucl. Instrum. Meth. A* **553** (2005) 268.

[44] MAGIC collaboration, *Measurement of the cosmic electron plus positron spectrum with the magic telescopes*, *arXiv preprint arXiv:1110.4008* (2011) .

[45] VERITAS collaboration, *Recent results from the VERITAS multi-messenger program*, *PoS* **ICRC2019** (2020) 782 [1909.05228].

[46] IceCube collaboration, *IceAct, small Imaging Air Cherenkov Telescopes for IceCube*, *PoS* **ICRC2019** (2021) 179 [1908.11177].

[47] F.D. Kahn and I. Lerche, *Radiation from cosmic ray air showers*, *Proceedings of the Royal Society of London. Series A. Mathematical and Physical Sciences* **289** (1966) 206.

[48] G. Askar'Yan, *Coherent radio emission from cosmic showers in air and dense media*, *Zh. Eksperim. i Teor. Fiz.* **48** (1965) .

[49] RNO-G collaboration, *Design and Sensitivity of the Radio Neutrino Observatory in Greenland (RNO-G)*, *JINST* **16** (2021) P03025 [2010.12279].

[50] R. Turcotte-Tardif, *Radio Measurements of Cosmic Rays at the South Pole*, Ph.D. thesis, Karlsruher Institut für Technologie (KIT), 2023. 10.5445/IR/1000160782.

[51] M.G. Aartsen et al., *The IceCube Neutrino Observatory: instrumentation and online systems*, *Journal of Instrumentation* **12** (2017) P03012–P03012.

[52] AMANDA collaboration, *The AMANDA experiment*, in *17th International Conference on Neutrino Physics and Astrophysics*, pp. 518–523, 12, 1996 [astro-ph/9612068].

[53] IceCube collaboration, IceCube, "Neutrinos and Gamma Rays: A Partnership to Explore the Extreme Universe." https://icecube.wisc.edu/news/research/2016/10/neutrinos-and-gamma-rays-partnership-to-explore-extreme-universe/, 2016.

[54] M.G. Aartsen et al., *First observation of pev-energy neutrinos with icecube*, *Phys. Rev. Lett.* **111** (2013) 021103 [1304.5356].

[55] M.G. Aartsen et al., *A combined maximum-likelihood analysis of the high-energy astrophysical neutrino flux measured with icecube*, *Astrophys. J.* **809** (2015) 98 [1507.03991].

[56] IceCube, Fermi-LAT, MAGIC, AGILE, ASAS-SN, HAWC, H.E.S.S., INTEGRAL, Kanata, Kiso, Kapteyn, Liverpool Telescope, Subaru, Swift NuSTAR, VERITAS, VLA/17B-403 collaboration, *Multimessenger observations of a flaring blazar coincident with high-energy neutrino IceCube-170922A*, *Science* **361** (2018) eaat1378 [1807.08816].

[57] M.G. Aartsen and others [IceCube Collaboration], *Neutrino emission from the direction of the blazar txs 0506+056 prior to the icecube-170922a alert*, *Science* **361** (2018) 147.

[58] IceCube collaboration, *Detection of a particle shower at the Glashow resonance with IceCube*, *Nature* **591** (2021) 220 [2110.15051].

[59] IceCube collaboration, *Evidence for neutrino emission from the nearby active galaxy NGC 1068*, *Science* **378** (2022) abg3395.

[60] IceCube collaboration, *Observation of high-energy neutrinos from the Galactic plane*, *Science* **380** (2023) adc9818 [2307.04427].

[61] M.G. Aartsen et al., *Observation and characterization of the cosmic-ray anisotropy with icecube*, *Astrophys. J.* **826** (2016) 220 [1603.01227].

[62] IceCube collaboration, *Cosmic ray spectrum and composition from PeV to EeV using 3 years of data from IceTop and IceCube*, *Phys. Rev. D* **100** (2019) 082002 [1906.04317].

[63] IceCube collaboration, *Multiplicity of TeV muons in extensive air showers detected with IceTop and IceCube*, *PoS* **ICRC2023** (2023) 207 [2307.14689].

[64] IceCube collaboration, *Search for PeV Gamma-Ray Emission from the Southern Hemisphere with 5 Years of Data from the IceCube Observatory*, *Astrophys. J.* **891** (2019) 9 [1908.09918].

[65] IceCube, HESS, MAGIC collaboration, *Joint searches by FACT, H.E.S.S., MAGIC and VERITAS for VHE gamma-ray emission associated with neutrinos detected by IceCube*, *PoS* **ICRC2023** (2023) 1501 [2309.15469].

[66] IceCube collaboration, *Neutrino Interferometry for High-Precision Tests of Lorentz Symmetry with IceCube*, *Nature Phys.* **14** (2018) 961 [1709.03434].

[67] IceCube collaboration, *Search for an eV-Scale Sterile Neutrino Using Improved High-Energy $\nu\mu$ Event Reconstruction in IceCube*, *Phys. Rev. Lett.* **133** (2024) 201804 [2405.08070].

[68] IceCube collaboration, *Search for dark matter from the center of the Earth with 10 years of IceCube data*, *Eur. Phys. J. C* **85** (2025) 490 [2412.12972].

[69] IceCube collaboration, *First all-flavor search for transient neutrino emission using 3-years of IceCube DeepCore data*, *JCAP* **01** (2022) 027 [2011.05096].

[70] IceCube collaboration, *Cosmic ray spectrum and composition from PeV to EeV using 3 years of data from IceTop and IceCube*, *Physical Review D* **100** (2019) .

[71] IceCube collaboration, *Cosmic ray measurements with IceCube and IceTop*, *SciPost Phys. Proc.* **13** (2023) 002 [2208.01911].

[72] IceCube collaboration, *The IceCube Upgrade - Design and Science Goals*, *PoS* **ICRC2019** (2021) 1031 [1908.09441].

[73] IceCube collaboration, *Design and performance of the multi-PMT optical module for IceCube Upgrade*, *PoS* **ICRC2021** (2021) 1070 [2107.11383].

[74] IceCube collaboration, *D-Egg: a dual PMT optical module for IceCube*, *JINST* **18** (2023) P04014 [2212.14526].

[75] IceCube collaboration, *Electronics Development for the New Photo-Detectors (PDOM and D-Egg) for IceCube-Upgrade*, *PoS* **ICRC2019** (2020) 966 [1908.11564].

[76] IceCube-Gen2 collaboration, R. Abbasi et al., "IceCube-Gen2 Technical Design Report, Part III." https://icecube-gen2.wisc.edu/science/publications/tdr/, 2024.

[77] T. Huber, J. Kelley, S. Kunwar and D. Tosi, *The IceTop Scintillator Upgrade*, *PoS* **ICRC2017** (2017) 401.

[78] A.S. Leszczyńska, *Potential of the IceTop Enhancement with a Scintillation Detector Array*, Ph.D. thesis, Karlsruher Institut für Technologie (KIT), 2021. 10.5445/IR/1000131245.

[79] IceCube collaboration, *Science Case of a Scintillator and Radio Surface Array at IceCube*, *PoS* **ICRC2019** (2020) 418 [1908.11469].

[80] P.P.M. Jansweijer, H.Z. Peek and E. De Wolf, *White Rabbit: Sub-nanosecond timing over Ethernet*, *Nucl. Instrum. Meth. A* **725** (2013) 187.

[81] E. de Lera Acedo, N. Razavi-Ghods, N. Troop, N. Drought and A.J. Faulkner, *Skala, a log-periodic array antenna for the ska-low instrument: design, simulations, tests and system considerations*, *Experimental Astronomy* **39** (2015) 567–594.

[82] M. Venugopal et al., *Enhancing air-shower observations: Results from an IceCube Surface Array Prototype Station*, in *Proceedings of 10th International Workshop on Acoustic and Radio EeV Neutrino Detection Activities — PoS(ARENA2024)*, vol. 470, p. 038, 2024, DOI.

[83] T. Karg, A. Haungs, M. Kleifges, R. Nahnhauer and K.H. Sulanke, *Introducing TAXI: a Transportable Array for eXtremely large area Instrumentation studies*, in *6th International Workshop on Acoustic and Radio EeV Neutrino Detection Activities*, 10, 2014 [1410.4685].

[84] M. Renschler, *A Prototype Radio Detector for the IceCube Surface Enhancement = Ein Radio-Detektor Prototyp für die Erweiterung des IceCube Oberflächendetektors*, Ph.D. thesis, Karlsruher Institut für Technologie (KIT), 2020. 10.5445/IR/1000104529.

[85] M.J. Oehler, *The Prototype Station for the IceCube Surface Array Enhancement*, Ph.D. thesis, Karlsruher Institut für Technologie (KIT), 2022. 10.5445/IR/1000142813.

[86] Institute for Astroparticle Physics (IAP), "Karlsruhe institute of technology." https://www.iap.kit.edu/english/index.php.

[87] P.D. Group, *Review of particle physics*, *Prog. Theor. Exp. Phys.* **2022** (2022) 083C01.

[88] H. Kolanoski and N. Wermes, *Particle Detectors*, Oxford University Press (6, 2020).

[89] F. Schaufele, I. Demarco and R.N. Day, *4 - FRET imaging in the Wide-Field microscope*, in *Molecular Imaging*, A. Periasmy and R.N. Day, eds., (San Diego), pp. 72–94, American Physiological Society (2005), DOI.

[90] Hamamatsu Photonics K.K., "S13360 series MPPC datasheet." https://www.hamamatsu.com/resources/pdf/ssd/s13360_series_kapd1052e.pdf, 2016.

[91] Hamamatsu Photonics, "Introduction to MPPC (multi-pixel photon counter)." https://hub.hamamatsu.com/content/dam/hamamatsu-photonics/sites/static/hc/resources/TN0014/mppc_kapd9005e.pdf, 2021.

[92] D. Beznosko, A. Bross, A. Dyshkant and P.-D. Rykalin, *FNAL-NICADD extruded scintillator*, in *IEEE Symposium Conference Record Nuclear Science 2004.*, vol. 2, pp. 790–793 Vol. 2, 2004, DOI.

[93] A. Pla-Dalmau, A. Bross and V. Rykalin, *Extruding plastic scintillator at fermilab*, in *2003 IEEE Nuclear Science Symposium. Conference Record (IEEE Cat. No.03CH37515)*, vol. 1, pp. 102–104 Vol.1, 2003, DOI.

[94] Kuraray Co., Ltd., "Plastic scintillating fibers." https://kuraraypsf.jp/pdf/all.pdf.

[95] Pierre Auger collaboration, *The Pierre Auger Observatory Upgrade - Preliminary Design Report*, 1604.03637.

[96] T. Huber, *IceScint : A Scintillation Detector Array for the IceCube IceTop Enhancement*, Ph.D. thesis, Karlsruher Institut für Technologie (KIT), 2021. 10.5445/IR/1000131545.

[97] M. Oehler, *Characterization of SiPMs for the Surface Array Enhancement of IceCube* master's thesis, Karlsruhe Institute of Technology (KIT), Department of Physics, Institute for Nuclear Physics (IKP), Apr., 2017.

[98] C. Wendt, *Private communication*, 2021.

[99] Leasametric GmbH, "Vötsch Vibration and Climate Tester — Configurable Test Chamber." https://www.leasametric.com/en/builder/votsch-en/.

[100] A. Weindl, *Private communication*, 2025.

[101] J.G. Fletcher, *An arithmetic checksum for serial transmissions*, *IEEE Transactions on Communications* **30** (1982) 247.

[102] Institut für Technische Thermodynamik, *Karlsruhe Institute of Technology (KIT), Campus Süd*, 2024.

[103] L. Lehmann, *Energy calibration of the scintillation detectors of the IceCube Surface Array Enhancement* bachelor's thesis, Karlsruhe Institute of Technology (KIT), Department of Physics, Institute for Astroparticle Physics (IAP), Apr., 2023.

[104] European Commission, Joint Research Centre, "European atlas of natural radiation." https://remap.jrc.ec.europa.eu/Atlas.aspx?layerID=9.

[105] N. Goehlke, *An IceCube Surface Array Enhancement station for the deployment at Telescope Array* Master's thesis, Karlsruhe Institute of Technology, 2022, 10.5445/IR/1000153878.

[106] IceCube collaboration, *First air-shower measurements with the prototype station of the IceCube surface enhancement*, *PoS* **ICRC2021** (2021) 314 [2107.08750].

[107] J. Kemp, *Development of a silicon photomultiplier based scintillator detector for cosmic air showers*, dissertation, RWTH Aachen University, Aachen, 2020. 10.18154/RWTH-2020-12243.

[108] T. Bendfelt and M. Kauer, *udaq software personal communication*, 2023.

[109] T. Bendfelt, *Private communication*, 2025.

[110] A. Leszczynska, A. Coleman, M. Plum, D. Soldin, R. Abbasi, M. Ackermann et al., *A multi-detector EAS reconstruction framework for IceCube*, in *Proceedings of 38th International Cosmic Ray Conference — PoS(ICRC2023)*, vol. 444, p. 366, 2023, DOI.

[111] D. Heck, J. Knapp, J.N. Capdevielle, G. Schatz and T. Thouw, *CORSIKA: A Monte Carlo code to simulate extensive air showers*, 2, 1998.

[112] R. Engel, F. Riehn, A. Fedynitch, T.K. Gaisser and T. Stanev, *The hadronic interaction model Sibyll – past, present and future*, *EPJ Web Conf.* **145** (2017) 08001.

[113] M. Ave, P. Bauleo, A. Castellina, A. Chou, J. Harton, R. Knapik et al., *The accuracy of signal measurement with the water cherenkov detectors of the pierre auger observatory*, *Nuclear Instruments and Methods in Physics Research Section A: Accelerators, Spectrometers, Detectors and Associated Equipment* **578** (2007) 180–184.

[114] F. Kislat, *Measurement of the energy spectrum of cosmic rays with the 26 station configuration of the IceTop detector*, Ph.D. thesis, Humboldt-Universität zu Berlin, Mathematisch-Naturwissenschaftliche Fakultät I, 2012. 10.18452/16443.

[115] M. Weyrauch, *Simulation Study for the IceCube-Gen2 Surface Array = Simulationsstudie für den IceCube-Gen2 Oberflächen-Detektor* Master's thesis, Karlsruher Institut für Technologie (KIT), 2021, 10.5445/IR/1000152578.

[116] S. for the IceCube Collaboration, *Performance of the prototype station of the icecube surface array enhancement*, 2025.

Acknowledgements

This work has been a culmination of help and support from many people. It was carried out during the most challenging years of my life, and for all the people who offered their wishes and stood by me, I want to say thank you.

First and foremost, I am truly obliged to Prof. Dr. Ralph Engel for giving me the opportunity to work on this topic, and for all the insightful discussions to probe the topic deeper and refine it to its current state. I am also grateful to Prof. Dr. Frank Simon for graciously taking up the role of my second reviewer.

I would also like to express my deepest gratitude to Dr. Andreas Haungs for being the most positive and motivating advisor I could have imagined. His unwavering support and availability at every stage of my thesis were invaluable. I am especially thankful for the time he dedicated to discussing each topic in great detail and for ensuring that my meticulous plans were actually realised.

This thesis would not have taken off if not for Thomas Huber. He made sure that I was included and not overwhelmed as a newcomer, and when I went through a big loss, he recognised the gravity of the situation and made sure I didn't lose track of my work or my sanity.

Marie and Hrvoje, thank you for helping me in getting started with the know-how of scintillators and answering all my elementary questions with great patience. Roxanne, for clearing all my doubts before moving to Karlsruhe, and the initial good word that she put in for my start. Agnieszka, for helping me navigate my initial days in Karlsruhe, especially when everything was difficult due to COVID. I am thankful for her availability through the analysis portion of my work and for all the valuable suggestions. A special thanks to Paras for asking thoughtful questions about my work and my life, and for keeping me just the right amount of pragmatic. Our shared communication through music and GIFs will always be a fond memory.

Thanks to Andreas Weindl for always being the go-to person whenever I needed help with anything related to scintillator firmware. I am especially grateful for the countless mini-stations we set up together, and for your patient troubleshooting every time something didn't work as expected.

Many thanks to Murat Toron, Heiko Kern, Bernd Hoffmann, and Michael Riegel for their tremendous effort in the production of the scintillators with remarkable teamwork, attention to detail, and dedicated hard work. Sabine, for making my life so much easier by helping with all the administrative things. Doris, for her help in setting up my work stations and maintaining them. Thanks to Anna for always making sure I found appointments at the right time and for being one of the nicest people to talk to. I am also grateful to Raquel and Katrin for their kind support with all things KSETA.

Thanks to Frank Schroeder for the great discussions and inputs on the surface array operations. I would also like to thank David Schmidt and Michael Unger for the very interesting and well-rounded lectures on cosmic-rays that I had the opportunity to attend. I would also like to express my gratitude to Markus for the kind interactions and encouragement during my first ICRC talk. And of course, the entire Auger group, who made the coffee break, and the

conferences we attended together, a pleasant experience.

I would also like to thank the members of my collaboration, beginning with Prof. Dr. Christopher Wiebusch, my Master's thesis supervisor, who continued to check in and encourage me whenever we met during collaboration meetings. I am grateful to Kath and Serap for their kindness and prompt support with all my IceTop related questions. I also value the encouragement and enthusiasm from Hermann Kolanoski throughout my PhD work updates in the cr-wg group calls. I am also thankful to Alan Coleman for his many valuable comments, and support with the processing of the SAE data. Many thanks to Abdul for the excellent cooperation on the combined radio-scintillator analysis. I am also deeply thankful to Matt Kauer, Delia Tosi, Chris Wendt, Tim Bendfelt, and the rest of the scintillator hardware group for generously sharing their knowledge, suggestions, and support on scintillator data and firmware. Thanks also to Dennis for his constructive questions and suggestions during my presentations, which helped me communicate my work more clearly to the community.

A big thanks to my students, with whom I had the chance to work closely. Laura and Anjali for the work on the radioactive sources measurements, Noah for helping narrow down the background by testing the scintillators with me all around campus nord, David for your amazing attempt at calibrating the uDAQs and help with the field tests, Federica for assistance with SiPM calibration, and Lukas for your great work on the temperature correlation at the pole.

I will forever be grateful to Donghwa for being a tremendous emotional support throughout my time at KIT. Her care and consideration for me extended far beyond professional bounds. I am especially thankful for her encouragement during the stressful phase of writing my thesis, and for her help with proofreading and corrections despite her own busy schedule. Thanks also to Fahim for the fruitful discussions, valuable feedback on my analysis, and for bringing his upbeat persona to the group.

I would like to thank my colleagues, my support group, and my close friends at KIT for their constant support and for creating such a friendly atmosphere that made me look forward to coming to work every day. Tista, thank you for the confidence and the initial push to start writing my thesis, for your careful proofreading, and for ensuring that all the indentations were applied properly. Thanks to Megha for consistently checking in on me and for the late nights spent implementing all the corrections. Pranav, thank you for keeping my morale high throughout the writing phase and for reading the thesis many times over with great attention to the flow of the work. Federico, thank you for being a tremendous support when the analysis had to be implemented in a short time, and for the pep talks that kept me going. Jelena, thank you for making sure the subtle mistakes did not go unnoticed, for your help with the cover page, and for being available and ready to help at all times. Mark, thank you for always being willing to explain and patiently re-explain topics from your area of expertise, and for your consistent support across all aspects of the work. To all of you, thank you for making this period truly special for me. Keito, Marvin, Simon, Nikos, Lukas, Carmen, Phillipe, Wenjie, Viktoria, Sara, and Subhadip, thank you for a warm and enjoyable atmosphere during the lunches and in the office. Thanks also to Siva for the much-needed badminton breaks and for the endless supply of delicious food that always lifted all of our spirits.

I would also like to thank the closest group of people I've been fortunate to have by my side over the years. Vrinda, for being my family away from home and for making sure I never felt alone while living in a different part of the world. Yashima and Geeta, my oldest friends, for constantly checking in on me and for their unwavering support and belief in my abilities. Naman, for encouraging me to slow down from time to time. Shivani, for her incredible ability in making everything feel a little lighter. Niko, for being there consistently, patiently, and in all the ways that mattered, both seen and unseen. Andrea and Juergen, for making sure I remember how far I have come and always encouraging me to give my best and to believe in myself.

I would like to acknowledge the ChatGPT and Grammarly tools for their helpful suggestions that improved the clarity of my writing. I also thank Notebook LM for assisting me in reviewing and combining ideas from different texts to better understand the topics.

Last but certainly not least, I am thankful to my family for their unwavering belief in me and their constant support in every aspect of my life. Their love, encouragement, and sacrifices have been the foundation that allowed me to pursue my dreams and overcome every challenge along the way. I could not have reached this milestone without them by my side.

Statutory Declaration

I declare that I have developed and written the enclosed Doctoral Thesis completely by myself, and have not used sources or means without declaration in the text. The Doctoral Thesis was not used in the same or in a similar version to achieve an academic grading or is being published elsewhere.

Date	Shefali